D-33192
Version 3.0

Earth Observing System (EOS)
Tropospheric Emission Spectrometer (TES)

Data Validation Report
(Version F04_04 data)

Editor:

Gregory Osterman

Contributors:

Kevin Bowman, Karen Cady-Pereira, Tony Clough, Annmarie Eldering, Brendan Fisher, Robert Herman, Daniel Jacob, Line Jourdain, Susan Kulawik, Michael Lampel, Qinbin Li, Jennifer Logan, Ming Luo, Inna Megretskaia, Ray Nassar, Gregory Osterman, Susan Paradise, Vivienne Payne, Hank Revercomb, Nigel Richards, Mark Shephard, Dave Tobin, Solene Turquety, Felicia Vilnrotter, Helen Worden, John Worden, Lin Zhang

November 5, 2007

JPL
Jet Propulsion Laboratory
California Institute of Technology
Pasadena, California

Earth Observing System (EOS)
Tropospheric Emission Spectrometer (TES)

Data Validation Report
(Version F04_04 data)

Approved by:

_____	_____
Reinhard Beer	Rob Toaz
TES Principal Investigator	TES Ground Data Systems Manager
Jet Propulsion Laboratory	Jet Propulsion Laboratory

Revision History:

Version	Date	Description/Comments
1.0	8/15/2005	Initial Version of Validation Report for time frame "launch + 1 year"
2.0	1/4/2007	Validation Report for F03_03 data
3.0	11/5/2007	Validation Report for F04_04 data

Acknowledgement:

The research described in the Earth Observing System (EOS) Tropospheric Emission Spectrometer (TES) Data Validation Report was carried out at the Jet Propulsion Laboratory, California Institute of Technology, under a contract with the National Aeronautics and Space Administration.

TABLE OF CONTENTS

LIST OF FIGURES

LIST OF TABLES

1. Overview or TES L2 (Level 2) Product Validation

This document is intended to provide our best determination of the quality of the TES data products based on detailed comparisons between TES L2 data products and other independent data sets.

Validation is defined, for purposes of this report, as comparison between quantities measured by TES and other data products that represent the state of the atmosphere. This definition will evolve as the validation effort matures. Data used in these figures come from processing at the TES Science Computing Facility and are all publicly available.

The TES L2 nadir products have undergone extensive quality control and validation testing. Table 1-1 shows the definitions of data maturity developed by the Terra-MISR (Multi-angle Imaging SpectroRadiometer) team and adopted by the TES team (http://eosweb.larc.nasa.gov/PRODOCS/misr/Quality_Summaries/maturity_def.html).

Using these definitions, the current validation status of the TES L2 data products are given in Table 1-2. Currently, the TES L2 products that are ready for scientific use are the nadir retrievals of ozone, carbon monoxide, temperature and water.

Table 1-1 Definitions of Data Maturity based on those used by the EOS-Terra MISR Team

Term	Definition
Beta	Early release products for users to gain familiarity with data formats and parameters.
Provisional	Limited comparisons with independent sources have been made and obvious artifacts fixed.
Validated Stage 1	Uncertainties are estimated from independent measurements at selected locations and times.
Validated Stage 2	Uncertainties are estimated from more widely distributed independent measurements.
Validated Stage 3	Uncertainties are estimated from independent measurements representing global conditions.
Note: TES L2 retrievals include fully characterized internal error estimates and do not obtain error estimates from external sources. Uncertainty in the TES validation work describes biases when compared to other data sources.	

Table 1-2 Current Validation Status of TES L2 Data Products

Species	Validation Status
Nadir Ozone	Validated Stage 2
Nadir Carbon Monoxide	Validated Stage 2
Nadir Water (Lower/Middle Troposphere)	Validated Stage 2
Nadir Water (Upper Troposphere)	Validated Stage 2
Nadir Temperature	Validated Stage 2
Sea Surface Temperature	Validated Stage 2
Land Surface Temperature/Emissivity	Provisional
Nadir Methane	Provisional
Nadir HDO	Validated Stage 1
Limb Nitric Acid	Provisional
Limb Ozone	Provisional
Limb Temperature	Provisional
Limb Water	Beta

In order to compare TES profile data with other measurements, vertical smoothing and sensitivity must be accounted for by applying the appropriate averaging kernels (such as those supplied with the TES data products). The error estimates included in the L2 data products are meaningful based on the current validation analysis.

The details of validation of products described as "beta" validated in Table 1-2 will be described in the next version of this report.

1.1 Applicable Documents

[1] Osterman, G., (editor), K. Bowman, K. Cady-Pereira, T. Clough, A. Eldering, B. Fisher, R. Herman, D. Jacob, L. Jourdain, S. Kulawik, M. Lampel, Q. Li, J. Logan, M. Luo, I. Megretskaia, R. Nassar, G. Osterman, S. Paradise, V. Payne, H. Revercomb., N. Richards, M. Shephard, D. Tobin, S. Turquety, F. Vilnrotter, H. Worden, J. Worden, and L. Zhang, Tropospheric Emission Spectrometer (TES) Validation Report (Version F03_03 data), Version 2.00, JPL Internal Report D-33192, January 4, 2007.

[2] Osterman, G., (editor), K. Bowman, K. Cady-Pereira, T. Clough, A. Eldering, B. Fisher, R. Herman, D. Jacob, L. Jourdain, S. Kulawik, M. Lampel, Q. Li, J. Logan, M. Luo, I. Megretskaia, G. Osterman, S. Paradise, H. Revercomb., N. Richards, M. Shephard, D. Tobin, S. Turquety, H. Worden, J. Worden, and L. Zhang, Tropospheric Emission Spectrometer (TES) Validation Report, JPL Internal Report D-33192, Version 1.00, August 15, 2005.

[3] Osterman, G., (editor), K. Bowman, A. Eldering, B. Fisher, R. Herman, D. Jacob, L. Jourdain, S. Kulawik, M. Luo, R. Monarrez, G. Osterman, S. Paradise, S. Poosti, N. Richards, D. Rider, D. Shepard, F. Vilnrotter, H. Worden, J. Worden, and H. Yun, Earth Observing System (EOS) Tropospheric Emission Spectrometer (TES) Level 2 (L2) Data User's Guide (Up to & including Version F04_04 data), Version 3.0, JPL Internal Report D-38042, May 4, 2007.

[4] Lewicki, S., TES Science Data Processing Standard and Special Observation Data Products Specifications, Version 10.12 (Science Software Release 10.0), JPL Internal Report D-22993, March 9, 2007.

[5] Lewicki, S., TES Science Data Processing Standard and Special Observation Data Products Specifications, Version 9.1 (Science Software Release 9.3) JPL Internal Report D-22993, May 24, 2006.

2. An Overview of the TES Instrument and Data Products

This section provides information about the TES instrument and the L2 data products. More detailed information on the TES data products is available in the TES L2 Data User's Guide (Osterman et al., 2007) and the TES Data Product Specification Document (Lewicki, 2007).

2.1 Instrument Description

The Tropospheric Emission Spectrometer (TES) on EOS-Aura was designed to measure the global, vertical distribution of tropospheric ozone and ozone precursors such as carbon monoxide (Beer et al., 2001; Beer, 2006). TES is a nadir and limb viewing infrared Fourier transform spectrometer (FTS) (http://tes.jpl.nasa.gov/mission/instrument.cfm). The TES spectral range is from 650 to 3250 cm^{-1}. The apodized resolution for standard TES spectra is 0.10 cm^{-1}, however, finer resolution (0.025 cm^{-1}) is available for special observations. The footprint of each nadir observation is 5 km by 8 km, averaged over detectors. Limb observations (each detector) have a projection around 2.3 km x 23 km (vertical x horizontal).

TES is on the EOS-Aura platform (http://aura.gsfc.nasa.gov/) in a near-polar, sun-synchronous, 705 km altitude orbit. The ascending node equator crossings are near 1:45 pm local solar time.

2.2 TES Observation Modes

TES makes routine observations in a mode referred to as the "global survey". A global survey is run every other day on a predefined schedule and collects 16 orbits (~26 hours) of continuous data. Each orbit consists of a series of repetitive units referred to as a sequence. A sequence is further broken down into scans. Global surveys are always started at the minimum latitude of an Aura orbit.

The at-launch version of the global survey consisted of 1152 sequences (72 per orbit). Each sequence was made up of 2 calibration scans, 2 nadir viewing scans and 3 limb scans. The two nadir scans for this version of the global survey were acquired at the same location on the spacecraft ground track and the radiances averaged, leading to a single TES L2 profile. The along-track distance between the successive nadir scan locations is ~544 km for this version of the global survey.

On May 25, 2005 the global survey was modified to conserve instrument life. The three limb scans were eliminated from the sequences and replaced by an additional nadir scan. In this version the three nadir scans are acquired at locations equally spaced along the spacecraft ground track. The spacecraft ground track distance between successive nadir observations is ~182 km. The radiances of individual scans are not averaged for data acquired with this version of the global survey. As with the original global survey there are 1152 sequences per global survey and with the additional nadir scans there is a maximum of 3456 profiles for these global surveys.

On January 10, 2006 the last sequence in each orbit was replaced with an instrument maintenance operation. All global surveys taken after 1/10/2006 include 1136 sequences per global survey (71 per orbit), meaning a maximum of 3408 L2 profiles. The along-track distance between successive nadir observations was unchanged.

Observations are sometimes scheduled on non-global survey days. In general these are measurements made for validation purposes or with highly focused science objectives. These

non-global survey measurements are referred to as "special observations". The primary special observation modes that have been used to date by TES are summarized in Table 2-1.

Table 2-1 Description of TES Special Observation Modes

Name	Pointing	Sequences	Scans per Sequence	Distance Between Scans	Comments
Step and Stare (prior to Jan 1, 2006)	Nadir	6	25	42 km	Continuous along-track nadir views, ~50 degrees of latitude.
Step and Stare (between Jan 1, 2006 and June 30, 2007)	Nadir	1	125	45 km	Continuous along-track nadir views, ~45 degrees of latitude.
Step and Stare (after June 30, 2007)	Nadir	1	165	45 km	Continuous along-track nadir views, ~45 degrees of latitude.
Transect	Near Nadir	1	40	12 km	Hi density along-track, near nadir views.
Stare	Near Nadir	1	32	0 km	All measurements at a single location.
Limb Only	Limb	1	62	45 km	Continuous along-track limb views, 25 degrees of latitude.
Limb HIRDLS	Limb	142	3	182 km	2 orbits of continuous limb measurements for HIRDLS (High Resolution Dynamics Limb Sounder) comparison

2.3 TES Scan Identification Nomenclature

Each TES scan is uniquely identified by a set of three numbers called the run ID, the sequence ID and the scan ID. Each major unit of observation is assigned a unique run ID. Run IDs increase sequentially with time. The first on-orbit run ID is 2000. The seq ID is assigned to repetitive units of measurements within a run. They start at 1 and are automatically incremented serially by the TES flight software. The scan ID is also incremented by the flight software each time a scan is performed. Each time the sequence is set to 1, the scan ID is reset to 0.

Each time TES makes a set of measurements, that data set is assigned an identification number (referred to as a "run ID"). A calendar of the TES run IDs for global surveys and a list of all TES run IDs (including observation data, time and date) can be found at http://tes.jpl.nasa.gov/science/dataCalendar.cfm .

2.4 Where to Obtain TES Data

There are two locations for obtaining TES data. Links to both locations are available from the TES site at the Langley Atmospheric Science Data Center (ASDC) http://eosweb.larc.nasa.gov/. The supporting documentation necessary to use TES data is also available at the Langley ASDC site.

- The primary location for obtaining TES data is the Earth Observing System (EOS) Data Gateway (http://redhook.gsfc.nasa.gov/~imswww/pub/imswelcome/).
- The second location for obtaining TES data is the Langley ASDC data pool. The data pool has space limitations that make it somewhat dynamic, therefore older versions of TES data may not be available there.

The TES data files are listed in different ways for the different sites. The naming convention is described in Section 2.5 below).

All TES data products are in HDF-EOS 5 format and are completely documented in the TES Data Product Specification documents (Lewicki, 2007 and 2005) referenced in Section 2.7. The site also contains links to the TES documentation mentioned in this manuscript.

2.5 L2 Product File Formats and Data Versions

Information about the TES data file content and format versioning can be found in the L2 product filenames. There are currently four different versions of TES L2 data products publicly available. It is currently planned that the entire TES L2 data product set shall be processed with the latest software release by approximately October 1, 2006. In the meantime it is important to understand the differences in the data versions and file formats.

Table 2-2 provides an explanation of the TES versions strings and more information about the different data versions is provided in the following sections. A change in the format number corresponds to changes in the fields available or minor bug fixes. A change in content number means a major change in the science content of certain fields in the data products. Version F03_03 is the first version to provide limb data results and is a minor upgrade to F03_02. Version F03_02 data was a significant upgrade to the science content in the data products compared to previous versions. The combination of F03_03 and F03_02 are referred to as V02 TES data.

Table 2-2 Description of the TES L2 Data Product Version Labels

TES Version String	Format Version	Science Content Version	Description
F01_01	1	1	The first publicly released L2 data
F02_01	2	1	Bug fixes and additional fields

TES Version String	Format Version	Science Content Version	Description
F03_02	3	2	Some additional fields but major upgrade to scientific quality of data. Known as TES "V002" data.
F03_03	3	3	Minor upgrade to F03_02. Limb data and some bug fixes. Known as TES "V002" data.
F04_04	4	4	Most recent version. Updates to improve nadir temperature products and all limb products. Known as TES "V003" data.

2.6 TES Standard L2 Products

Currently the TES data products available for any given run ID are listed in Table 2-3. The products are separated by species with an ancillary file providing additional data fields applicable to all species. A description of the contents of the product files, information on the Earth Science Data Type names and file organization can be found in the TES DPS (Data Products Specification) document (Lewicki, 2007). The TES methane products are still being improved and should be used with caution.

Table 2-3 Description of the TES L2 Data Product Files Currently Available

TES L2 Standard Data Product	TES View Mode	Description
Ozone	Nadir and Limb	TES ozone profiles and some geolocation information
Temperature	Nadir and Limb	TES atmospheric temperature profiles and some geolocation information.
Water	Nadir and Limb	TES water vapor profiles and some geolocation information
Carbon Monoxide	Nadir	TES nadir carbon monoxide profiles and some geolocation information
HDO	Nadir	TES nadir HDO profiles and some geolocation information
Methane	Nadir	TES nadir methane profiles and some geolocation information

TES L2 Standard Data Product	TES View Mode	Description
Nitric Acid	Limb	TES limb nitric acid profiles and some geolocation information
Ancillary	Nadir	Additional data fields necessary for using retrieved profiles.

TES retrieves surface temperature and it is reported in each species file, however the value in the atmospheric temperature file is the one that should be used for scientific analysis.

The TES L2 Data Products are provided in files separated out by the atmospherics species being measured. An example file name is:

TES-Aura_L2-O3-Nadir_r000002945_F03_03.he5

This particular file contains TES nadir measurements of ozone for run ID 2945 (000002945). The data version number is provided after the "F" in the filename. Additionally there are data files with additional (ancillary) data that are important for working with TES data. These ancillary files can be used with any species data file and contains the string "Anc" in the filename.

2.7 References

[1] Beer, R., T. A. Glavich, and D. M. Rider, Tropospheric emission spectrometer for the Earth Observing System's Aura satellite, *Applied. Optics, 40* (15), 2356-2367, 2001.

[2] Beer, R., TES on the Aura Mission: Scientific Objectives, Measurements and Analysis Overview, *IEEE Transactions on Geoscience and Remote Sensing, 44*, 1102-1105, May 2006.

[3] Lewicki, S., TES Science Data Processing Standard and Special Observation Data Products Specifications, Version 10.12, JPL D-22993, March 9, 2007, for public released data, software release 10.

[4] Lewicki, S., TES Science Data Processing Standard and Special Observation Data Products Specifications, Version 9.0, JPL D-22993, December 13, 2005, for public released data, software release 9.

[5] Osterman, G., (editor), K. Bowman, A. Eldering, B. Fisher, R. Herman, D. Jacob, L. Jourdain, S. Kulawik, M. Luo, R. Monarrez, G. Osterman, S. Paradise, S. Poosti, N. Richards, D. Rider, D. Shepard, F. Vilnrotter, H. Worden, J. Worden, and H. Yun, Earth Observing System (EOS) Tropospheric Emission Spectrometer (TES) Level 2 (L2) Data User's Guide (Up to & including Version F04_04 data), Version 3.0, JPL D-38042, May 4, 2007.

3. Executive Summary

Below is a summary of each data validation section.

- Section 4 – TES L1B Radiances: Version 2 TES data feature an improved Level 1B (L1B) calibration algorithm that brings TES into very good agreement with the aircraft instrument Scanning High-Resolution Interferometer Sounder (S-HIS) and the Atmospheric Infrared Sounder (AIRS) instrument on the National Aeronautics and Space Administration (NASA) Aqua satellite. TES radiances show mean differences of less than 0.3 K at brightness temperatures of 290-295 K, and less than 0.5 K at brightness temperatures of 265-270 K with both Scanning HIS and AIRS. The TES optical bench warm up in December 2005 yielded a four-fold increase in signal-to-noise ratio at higher frequencies (relevant to CO). TES sea surface temperature comparisons to Reynolds Optimally Interpolated product demonstrate radiometric stability.

- Section 5 – Ozone: TES ozone profiles have been compared to ozonesonde and lidar measurements. Comparisons with these other ozone measurements show that TES generally sees higher ozone in the lower and middle troposphere than the sondes and lidar. The magnitude of this difference varies somewhat with different geographic regions. In the Southern low and middle latitudes, in the uppermost troposphere, TES sees lower values than the sondes and lidar. In addition, comparisons of TES total column ozone with OMI (Ozone Monitoring Instrument) show similar global distributions, but TES measures 3-7% more ozone. The source of these biases is currently under investigation.

- Section 6 – Carbon Monoxide: For V003, a major change was relaxed constraints for polar latitude bins, which results in greater variability. Comparisons have been carried out between TES carbon monoxide retrievals and those from a variety of satellite and aircraft instruments. Global patterns of carbon monoxide as measured by TES are in good qualitative agreement with those seen by MOPITT (Measurement Of Pollution In The Troposphere) on the NASA Terra satellite. Comparisons of profiles of CO between TES and MOPITT show good agreement when *a priori* information is accounted for correctly. TES carbon monoxide agrees to within the estimated uncertainty of the aircraft instruments, including both errors and the variability of CO itself.

- Section 7 – Atmospheric Temperature: TES temperature retrievals have been compared extensively with both remote sensing and *in situ* measurements. The V003 retrieval uses additional microwindows in the CO_2 ν2 band (2B1 filter) at 650 to 800 cm^{-1}. V003 temperature bias is improved relative to V002, except for a 0.5 to 2 K cold bias at 400-500 hPa, and warm bias at 800 hPa.

- Section 8 – Sea Surface Temperature: TES measurements of sea surface temperature from V003 have been compared against TES V002 for eight global surveys. The comparison shows a mean difference of 0.2 K with a standard deviation of 2.3 K.

- Section 9 – Water Vapor: TES V003 water vapor shows a 5% improvement over V002 below 500 hPa. Comparisons to CFH (Cryogenic Frostpoint Hygrometer) indicate that

TES is 5-10% wetter below 700 hPa, and 5-40% wetter at 300 to 700 hPa. Conclusions from comparisons of TES water retrievals with sondes and aircraft data are difficult due to atmospheric variability, though radiance closure experiments suggest differences in the middle and upper troposphere cannot be fully accounted for by known systematic errors.

- Section 10 – HDO/H_2O: TES estimates of HDO have undergone preliminary validation by comparison with models and aircraft data. A bias of approximately 5% has been seen, but the distribution of HDO/H_2O as measured by TES and the JPL instrument ALIAS (Aircraft Laser Infrared Absorption Spectrometer) shows good agreement.

- Section 11 – TES Cloud Products: Unlike V002, TES V003 cloud products contain initial guesses at smaller optical depths, which results in more retrievals at low optical depth. V003 also includes filter 2B1, which improves characterization of cloud top pressure for high clouds. TES has been compared with MODIS (Moderate Resolution Imaging Spectroradiometer) and AIRS cloud products.

- Section 12 – Methane: initial comparisons between TES, DACOM (Differential-Absorption Carbon Monoxide Monitor) (DC-8) and ground-based FTIR (Fourier Transform Infrared Spectrometer) indicate that TES is biased ~5% high in column, particularly between 150 and 500 hPa pressure levels.

- Section 13 – Validation of TES Limb Nitric Acid Retrievals: Comparisons have been carried out between TES, Microwave Limb Sounder (MLS), Chemical Ionization Mass Spectrometers (CIMS) (WB-57 aircraft), and Soluble Acidic Gases and Aerosol (SAGA) (on the DC-8 aircraft) during International Chemical Transport Experiment (INTEX)-B. TES has low sensitivity to nitric acid in the troposphere due to clouds. TES stratospheric nitric acid shows similar spatial distributions to these other measurements.

- Section 14 – Comparison of TES Limb Temperature with GMAO: TES limb temperature retrievals have undergone preliminary validation by comparison with GMAO GEOS-5. In the troposphere, TES limb temperature has a bias of -0.08 K relative to GMAO (Global Modeling Assimilation Office). In the stratosphere, TES limb temperature typically has a warm bias that gradually increases with altitude, up to +2 K at 12 hPa.

- Section 15 – Comparison of TES Limb Water with GMAO: TES limb water vapor retrievals have undergone preliminary validation by comparison with GMAO GEOS-5. TES limb retrievals have sensitivity to water in the middle troposphere (biased approximately 4% low relative to GMAO) but little sensitivity at other altitudes

4. Overview of TES L1B Radiance Validation

Though this report is focused primarily on the TES Level 2 data products, it is important to understand that the L1B radiance products have undergone a rigorous validation as well. The following is an outline of the current status of TES L1B nadir radiance comparisons and is taken directly from Shephard et al., (2007) and the reader is referred to this document for more details. The fundamental measurement of the Tropospheric Emission Spectrometer (TES) on board the Aura spacecraft is upwelling infrared spectral radiances. Accurate radiances are critical for both trace gas profile retrievals for air quality as well as radiative forcing for climate (Gauss et al., 2003). For example, any radiometric systematic errors (e.g. calibration) not addressed in the L1B radiances will propagate as errors in the retrieved parameters (Bowman et al., 2006, Worden et al., 2004). In order to ascertain the quality of the TES radiances, comparisons were made between TES spectra and measurements from two other spectrometers, the Atmospheric Infrared Sounder (AIRS) on NASA's Aqua satellite (Aumann et al., 2003) and the Scanning High-Resolution Interferometer Sounder (S-HIS) flown on an aircraft (Revercomb et al. 1988a, 1988b, 1996).

The current version of the L1B radiances is V002 (current version for the L2 products is V003). The V002 radiances were a significant improvement over the version 1 product and led to significant improvements in the Level 2 products (Validation Report, Osterman et al., January 4, 2007). An overview of the improvement in the V002 radiances is provided in Table 4-1.

4.1 Radiance Validations

4.1.1 TES/S-HIS Radiance Comparison

During the Aura Validation Experiment (AVE) there were several S-HIS underflights of TES. We studied two cloud-free scans on November 7, 2004 where S-HIS flew under the TES overpass at an altitude of 18 km over the Gulf of Mexico. The absence of clouds is determined by the zero cloud fraction retrieved by the Moderate Resolution Imaging Spectroradiometer (MODIS) and by the small variability in the 1103-1105 cm^{-1} window brightness temperatures demonstrated in the TES and S-HIS scans in Figure 4-1. The brightness temperatures plotted here have not been corrected for any geometric difference between the two sensors, therefore, given that TES is flying at a much higher altitude the TES brightness temperatures in the window region are expected to be cooler. An average TES spectrum for each scan was obtained by averaging the sixteen TES pixels; a corresponding SHIS spectrum was constructed by averaging the nine closest SHIS scans to the center of the TES scan. The SHIS footprints in Figure 4-1 show the SHIS scans used in the comparisons. Unfortunately, there were no coincident AIRS observations available at this time.

In order to compare the spectra from the different instruments Line-by-Line Radiative Transfer Model (LBLRTM) (Clough et al., 2005) forward model calculations were utilized to account for the differences between altitude and viewing angles (Tobin et al., 2006). Implicit in this procedure is the assumption that the modeled atmosphere between the aircraft altitude and the satellite is representative of the true atmosphere. When the atmosphere specified above the nadir S-HIS observation (18 km) does not represent the true atmospheric state there will be additional residuals in the spectral regions where there is emission above the aircraft.

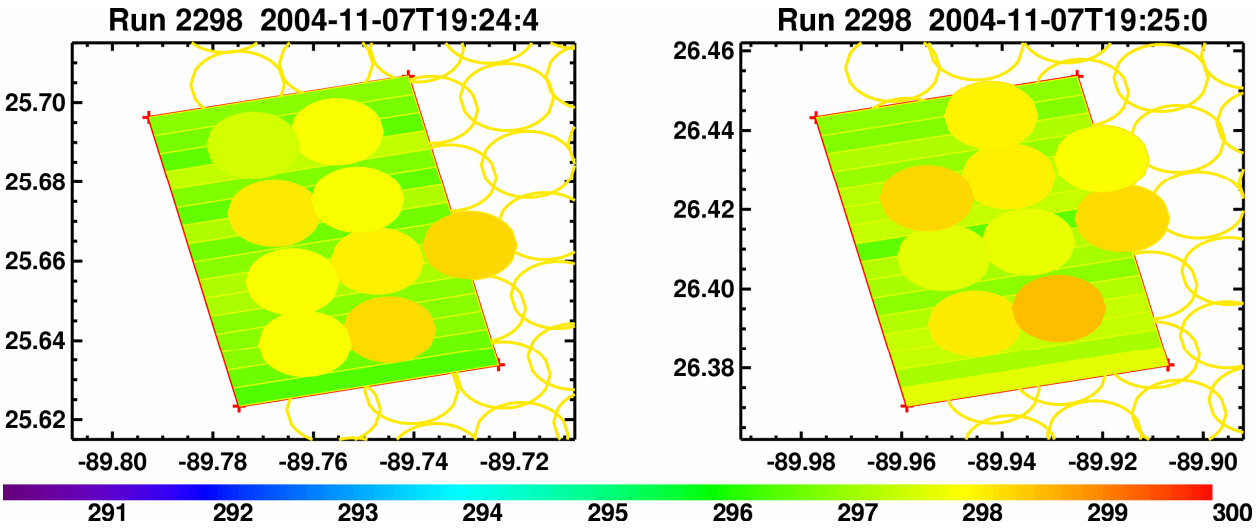

Figure 4-1 Brightness temperature in the 1103-1105 cm^{-1} microwindow for TES nadir-scans (Run 2298, Sequence 3, Scan 8 and Scan 10), each consisting of sixteen 0.5 x 5 km^2 rectangular pixels, and nine S-HIS scans for the corresponding underflight; SHIS scans are ~2 km circles.

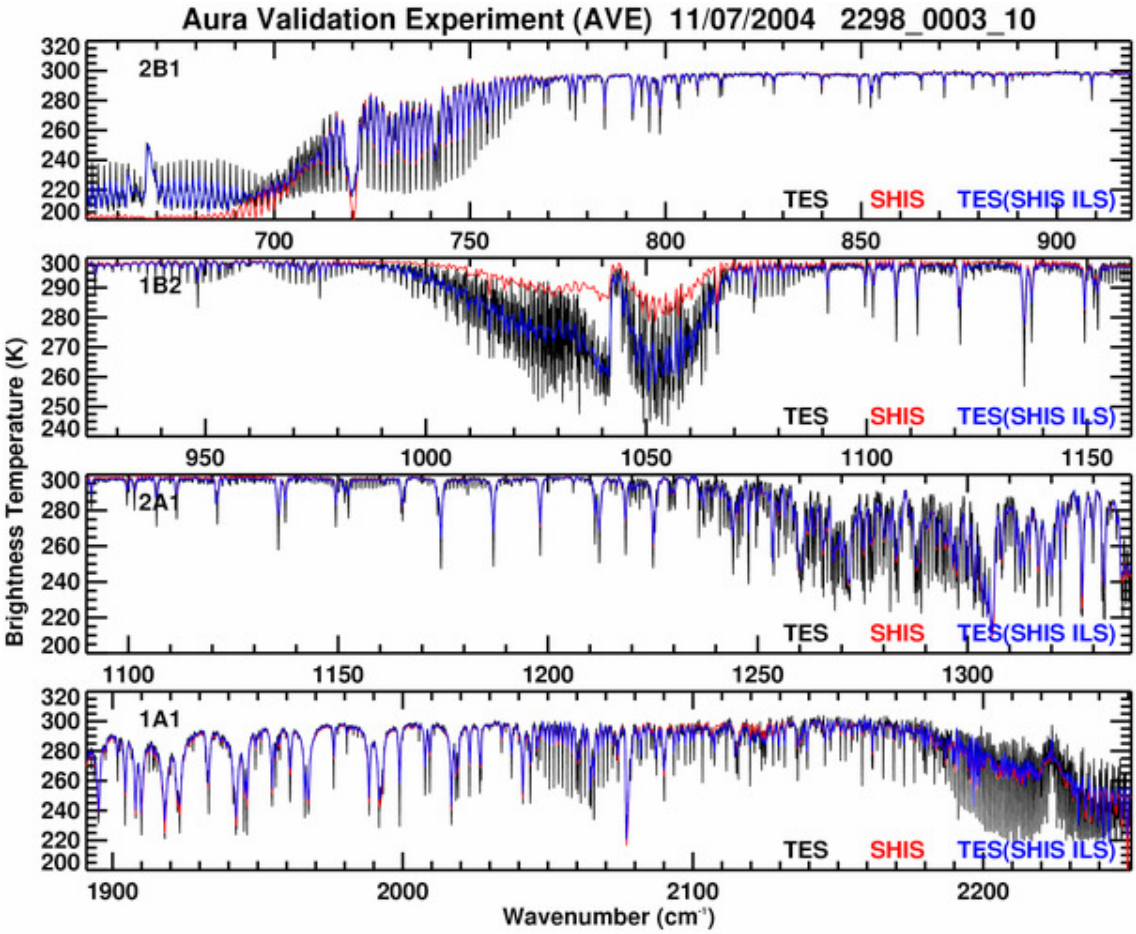

Figure 4-2 TES nadir spectrum from November 7, 2004 for filters 2B1, 1B2, 2A1, and 1A1, with the SHIS (red) and the TES spectral convolved with the SHIS ILS (blue) overplotted.

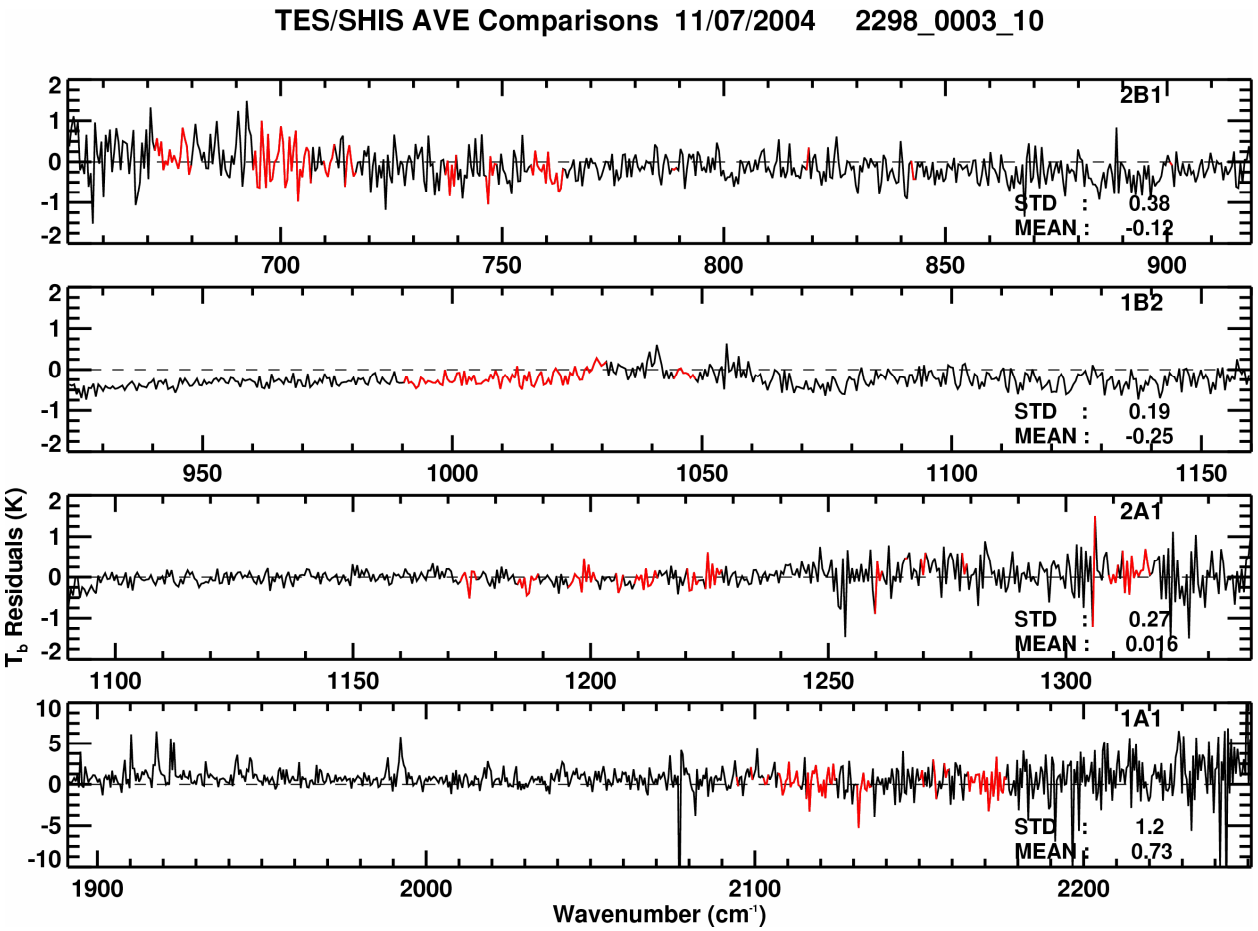

Figure 4-3 Difference between TES and S-HIS brightness temperature residuals for Run 2298, Sequence 3, Scan 10 at the S-HIS resolution, for filters 2B1, 1B2, 2A1, and 1A1. TES V002 L1B radiances were used in this comparison. The red regions are the TES microwindows presently used in TES retrievals.

TES and S-HIS have spectral resolutions of 0.06 cm^{-1} and 0.48 cm^{-1}, respectively. In order to put the two sensors on the same resolution for comparison purposes, TES was convolved with S-HIS Instrument Line Shape (ILS). Figure 4-2 shows a TES, S-HIS, and TES spectra convolved with the S-HIS ILS for TES Run 2298, Sequence 3, Scan 10 on November 7, 2004. Noticeable differences between TES and SHIS are evident in the spectral regions where there is significant emission above the aircraft (e.g. CO2 and O3 spectral regions). An example of the TES-S-HIS spectral comparisons for the 2B1, 1B2, 2A1, and 1A1 TES filters for Scan 10 are shown in Figure 4-3. Note that more detail TES spike remove was performed on the TES observations for these comparisons because the full-filter forward model calculations used to account for the geometric differences were also used to further identify TES spikes; any 4-sigma (TES-LBLRTM) spectral points were removed from the statistics. Over most of the TES spectral regions there is good agreement with S-HIS. The largest residuals are in the regions with significant emission above the aircraft (e.g. CO2 ν2 (~650-700 cm^{-1} in the 2B1), O3 (1020-1060 cm^{-1} in the 1B2), CH4 ν4 (Q-branch at 1306 cm^{-1} in the 2A1), and the start of the CO2 ν3 (the 2180-2251 cm^{-1} in the 1A1)). As stated earlier, incorrect specification of the atmosphere above the aircraft will result in differences beyond the differences in the instrument radiances

themselves. In addition, incorrect specified of the atmosphere in a region in which one sensor is more sensitive to than the other will also generate differences that are not due to radiances themselves. For example, a sensor flying on an aircraft will in general be more sensitive to the atmosphere just below the aircraft than an instrument observing from space (e.g. temperature and ozone). Since there were no coincident and collocated sonde profiles available to specify the atmosphere state, the TES retrieved profile was used in the calculations. The TES a priori profile calculated from the GEOS global transport model maintained at NASA's Global Modeling and Assimilation Office (GMAO) (Bloom et al., 2005) was tried (not shown), however it did not characterize the atmosphere as well as the TES retrieved profile.

Table 4-1 TES V001 and V002 full-filter radiance comparisons

		TES - AIRS			
		Run 2147 9/20/2004 (50 target scenes)		Run 2931 5/21/2005 (320 target scenes)	
TES Filter	Wavenumber (cm^{-1})	Mean Δ BT (K)	STD Δ BT (K)	Mean Δ BT (K)	STD Δ BT (K)
2B1	650 - 920	-0.18 (-0.29)	0.46 (0.86)	-0.13 (-0.31)	0.42 (0.54)
1B2	920 - 1160	0.01 (-0.05)	0.48 (0.52)	-0.12 (-0.19)	0.38 (0.38)
2A1	1090 - 1340	0.34 (1.05)	0.36 (0.37)	0.35 (1.37)	0.32 (0.70)
The evaluation statistics are averaged over the full filter. The values in ( )'s are from TES V001 release.					

Table 4-2 TES V002 Clear-sky radiance comparisons with AIRS and S-HIS

			TES - AIRS		TES - S-HIS	
			Run 2147 9/20/2004 (43 clear-sky scenes)		2298 0003 08 and 2298 0003 10 11/07/2004	
TES Filter	Wavenumber (cm^{-1})	Bright. Temp. (K)	Mean Δ BT (K)	STD Δ BT (K)	Mean Δ BT (K)	STD Δ BT (K)
2B1	650 – 920	290-295	-0.07	0.61	-0.19	0.27
		265-270	0.08	0.56	0.03	0.35
1B2	920 – 1160	290-295	-0.02	0.50	-0.28	0.15
		265-270	0.44	0.45	-0.04	0.21
2A1	1090 – 1340	290-295	0.26	0.59	0.02	0.18
		265-270	0.49	0.41	-0.11	0.36
1A1	1891 - 2251	290-295			0.56	0.94
		265-270			1.03	1.73
The statistics are for 1-sigma.						

Additional insight from these comparisons is obtained from scatter plots of the combined brightness temperature differences from both Scans 8 and 10 as a function of brightness temperature. There are small but systematic differences between the TES and S-HIS at warmer temperatures near the surface (285-300 K); filter 2B1 has a difference of -0.2 K, 1B2 of –0.28 K, 2A1 differences are very close to zero, and the 1A1 band has a systematic difference of 0.5K. The 2B1 differences become slightly positive at wave numbers below 700 cm^{-1}, where emission is mainly from the tropopause region. The 1B2 differences show a distinctive increase with decreasing temperature and wavenumber, as the emission moves into the O3 band. Detailed TES-SHIS comparison statistics for 5K temperature bins at 265-270 K and 290-295 K are in Table 4-2 and shown in Figure 4-4 It should be pointed out that the signal in the 1A1 region is low due to the cold temperatures and drop-off in radiance of the blackbody plank function at these wave numbers and temperatures. Therefore, differences due to noise or spikes in the TES radiances will result in large brightness temperature differences in the 1A1 filter, especially at the high frequencies and cooler temperatures.

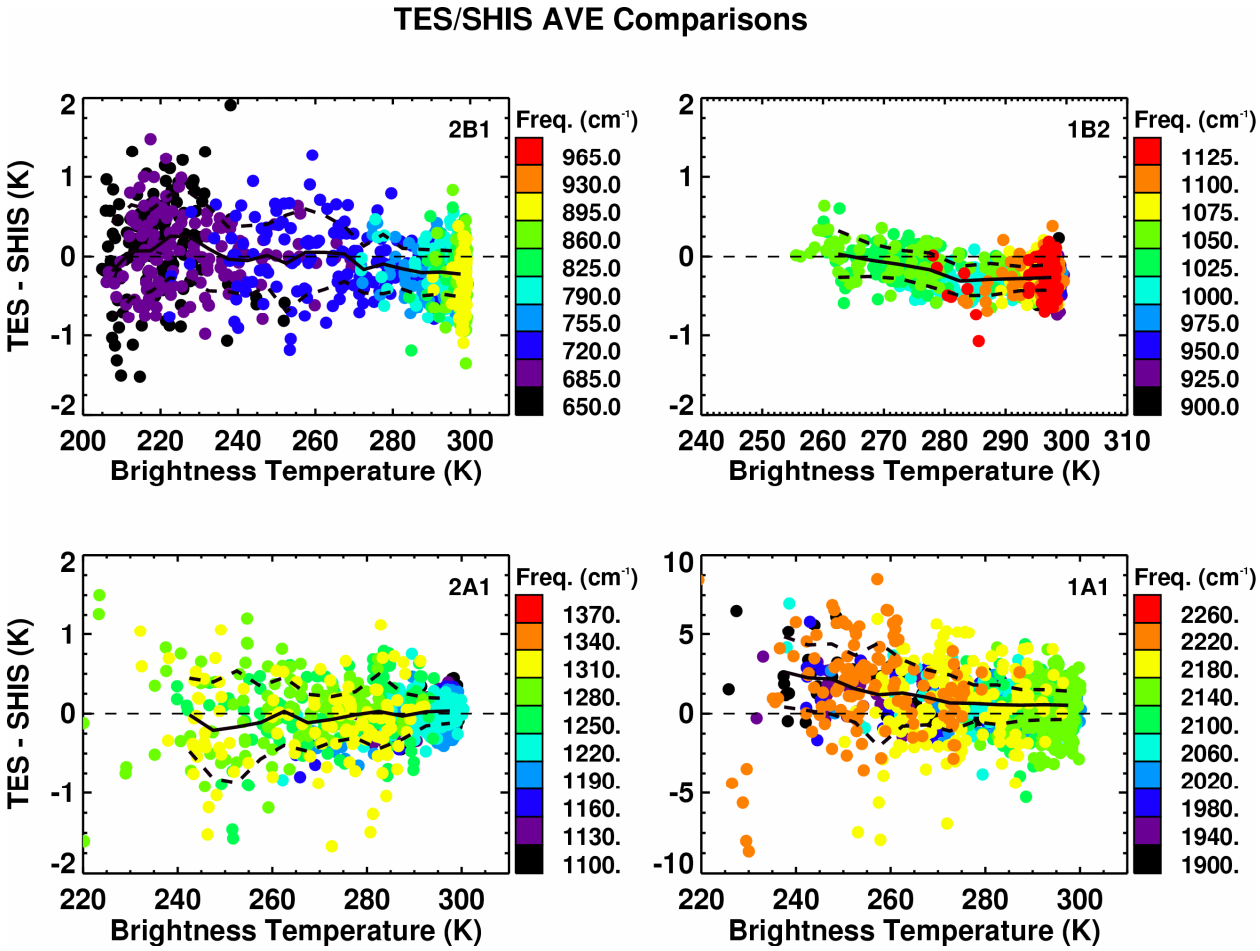

Figure 4-4 Scatter plots of TES-SHIS brightness temperature differences as a function of brightness temperature and color coded in frequency bins, for Run 2298, Sequence 3, Scans 8 and 10. The bold dashed lines are the 1-sigma standard deviation and the solid line is the mean. TES V002 L1B radiances are used in the comparison.

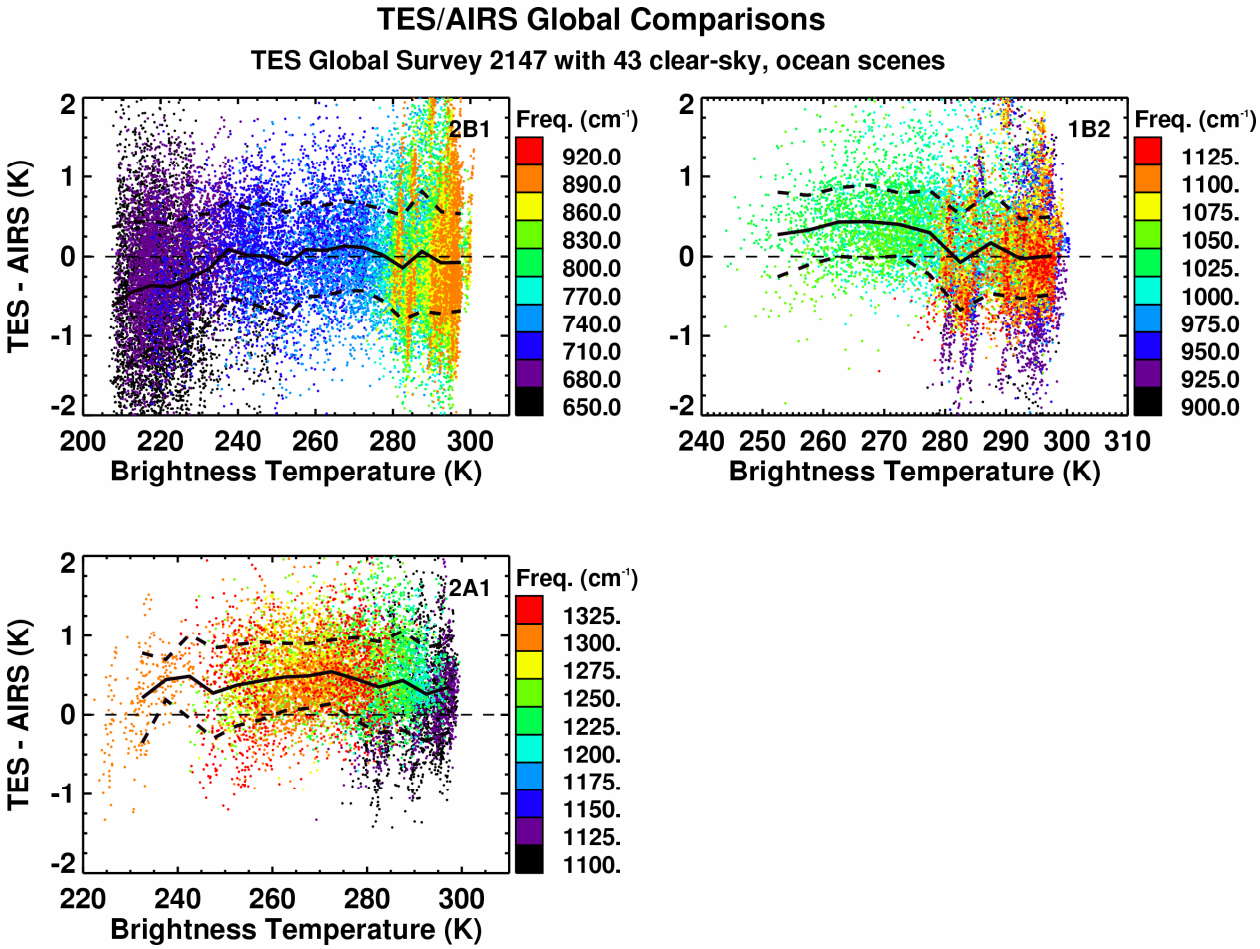

Figure 4-5 Scatter plots of TES-AIRS brightness temperature differences as a function of brightness temperature and color coded in frequency bins, for 43 global clear sky cases over the ocean. The bold dashed lines are the 1-sigma standard deviation and the solid line is the mean.

4.1.2 TES/AIRS Radiance Comparison

TES-AIRS residuals as a function of the TES brightness temperature and frequency are plotted in Figure 4-5. For this analysis only clear sky scenes over ocean were used; a scene was determined to be clear using brightness temperature inter-pixel variability (16-pixel standard deviation <0.25 K), absolute brightness temperature (greater than 273 K), and the lapse rate (greater than 3o C/km). Each of the bands reveals an interesting aspect of the TES-AIRS differences. The 2B1 differences are close to zero across most of the band (from the surface to the tropopause) and become negative at cooler temperatures in the part of the CO2 ν2 (650-680 cm^{-1}) band where the emission is mainly from the tropopause and above. The 1B2 differences are also zero near the surface, but become positive (0.3 K to 0.4 K) at the cooler temperatures associated with the ozone stratospheric emission (1020-1040 cm^{-1}). Finally, the residuals in the 2A1 band are approximately constant over the entire band with average difference values between 0.3 K and 0.5 K, even at the surface, where the residuals in 2B1 and 1B2 are zero. Some of the TES-AIRS comparison differences maybe attributed to the fact that the two observations may not be observing exactly the same atmosphere (e.g. water vapor, unscreened clouds, etc.) as they are not simultaneous measurements (15-minutes apart) and have different field-of-views. Detailed

statistics for 5 K temperature bins at 265-270 K and 290-295 K can be found in Table 4-2. The TES-AIRS standard deviations are larger than the TES-SHIS reported in Table 4-2. This might be due to the fact that TES-AIRS comparison covers a wider range of atmospheric states than the TES-SHIS comparison, and/or that SHIS is a better-calibrated instrument, especially when you consider that nine SHIS footprints are averaged together in one TES scene.

4.1.3 TES Radiance Validation from SST Measurements

In addition to direct AIRS and S-HIS radiance comparisons, TES radiances can be indirectly validated through comparisons of retrieved sea surface temperature (SST) (e.g. *Hagan and Minnett,* 2003; *Aumann et al.,* 2006). These SST comparisons by *Tremblay et al.* (2007) for clear sky radiances (retrieved effective cloud optical depth ≤ 0.05) over two years, demonstrates the long-term stability of TES measurements. It is important to note that the DOFS for the SST retrievals are generally close to 1 for these clear sky cases and therefore the TES SSTs are not biased by the *a priori*. *Tremblay et al.,* (2007) shows the time series of the SST bias with respect to Reynolds Optimally Interpolated (ROI) monthly average SST from November 2004 through November 2006 for nighttime and daytime. The ROI dataset has the advantage that it is insensitive to clouds. In addition, the ROI is a bulk SST measurement allowing for a skin-bulk SST comparison, which can be used to determine the sensitivity of the TES SST retrievals. The average nighttime bias over this period is -0.17 K and the daytime average bias is 0.04 K, which is the expected difference between skin (TES) and bulk (ROI) temperature measurements. This ability to measure a skin-bulk temperature difference that is consistent with the expected physical skin-bulk nighttime bias of ~0.2 K, clearly shows that TES has a sensitivity at the 0.1 K level. RMS differences of ~0.5 K are consistent with the other comparison results shown in this paper. These results demonstrate that TES calibration has been very stable over the two-year period. It is also important to note that *Tremblay et al.,* (2007) provides further evidence that the *a priori* does not bias the SST retrievals under clear sky conditions. They provide a case study in which the *a priori* surface temperatures over Lake Tahoe were 17 K higher than the retrieved values (due to the fact that land surface temperature were used instead of water surface temperatures), however, the retrieved surface temperatures still compare quite well with the in-situ measurements with a bias of –0.11 K and standard deviation of 0.30 K.

4.2 Discussion

Radiance comparison case studies of TES with S-HIS and AIRS are utilized to estimate the in-orbit radiometric calibration of TES. The mean and standard deviation of TES differences with both AIRS and SHIS are presented. TES/S-HIS comparisons show a mean difference of less than 0.3 K with a standard deviation of 0.3 K for brightness temperatures at 290-295 K, except for the 1A1 filter where the reduced signal increases the brightness temperature differences. Note that TES comparisons with both AIRS and S-HIS at these warmer brightness temperatures (near the surface) show that the 2B1 and 1B2 filters agree with each other, but the 2A1 filter is 0.2-0.3 K warmer. If not taken into consideration this systematic error will impact retrievals that use multiple filters (e.g. TES cloud retrieval). The TES/S-HIS comparison results for cooler brightness temperatures show mean differences less than 0.2 K with standard deviation less than 0.4 K at 265-270 K. Since some of these comparisons at the cooler brightness temperatures are from spectral regions where there is significant contribution from the atmospheric emission, it is likely that the differences are greater than the differences in the instrument radiances themselves due to errors in the input profiles used to account for the atmosphere between the aircraft. The

TES/AIRS comparison show a mean difference of less than 0.3K with a standard deviation of 0.6 K at brightness temperatures 290-295 K. Comparisons at cooler brightness temperatures 265-270 K show TES/AIRS mean and standard deviation differences of 0.5 K and 0.6 K, respectively.

It must be noted that TES calibration errors increase significantly within about 10 cm^{-1} of the half-power point frequencies of the optical filters. A study by *Revercomb et al.* (unpublished data, 2006) suggests the errors are likely due to a phase modulation resulting from interferometer velocity variations. These errors are mitigated in the L2 retrieval by the selection of frequency ranges that do not include the filter edges. Table 4-3 lists the useable spectral ranges that were determined based on the radiance comparisons.

Table 4-3 Spectral ranges for TES filters commonly used in the nadir

Filter ID	L1B min.	L1B max.	Suggested min. for L2	Suggested max. for L2
2B1	652	919	660	910
1B2	923	1160	950	1130
2A1	1090	1339	1120	1320

Even though great efforts have been made to obtain coincident and co-located radiance observations under conditions in which the true state of the atmosphere is known, this is a challenging task. In addition, TES radiance validation is on going since instrument properties can change over the mission lifetime. Future radiance comparisons (e.g. with S-HIS) under cloud-free conditions, over water (where the infrared emissivity is well known), and where the atmosphere has been well characterized (e.g. radiosondes, ozonesondes, etc.) would be extremely useful for this validation effort. In addition, TES/AIRS radiance comparison results can be further refined in the future by including more comparison. This article has focused on nadir observations that have a greater potential for coincident measurements. Validation of TES limb radiances will rely heavily on model comparisons and will be addressed in the future.

4.3 References

[1] Aumann, H. H., S. Broberg, D. Elliott, S. Gaiser, and D. Gregorich (2006), Three years of AIRS radiometric calibration validation using sea surface temperatures, *J. Geophys. Res., 111,* doi:10.1029/2005JD006822.

[2] Aumann, H. H., M. T. Chahine, C. Gautier, M. D. Goldberg, E. Kalnay, L. M. McMillin, H. Revercomb, P. W. Rosenkranz, W. L. Smith, D. H. Staelin, L. L. Strow, and J. Susskind (2003), AIRS/AMSU/HSB on the Aqua mission: design, science objectives, data products, and processing systems, IEEE Trans. Geosci. Remote Sensing, 41, 253-264.

[3] Bloom, S., A. da Silva, D. Dee, M. Bosilovich, J.-D. Chern, S. Pawson, S. Schubert, M. Sienkiewicz, I. Stajner, W.-W. Tan, and M.-L. Wu (2005), Documentation and

Validation of the Goddard Earth Observing System (GEOS) Data Assimilation System – Version 4. Technical Report on Global Modeling and Data Assimilation 104606, 26. Available from http://gmao.gsfc.nasa.gov/pubs/docs/Bloom168.

[4] Bowman K. W., C. D. Rodgers, S. S. Kulawik, J. Worden, E. Sarkissian, G. Osterman, T. Steck, M. Lou, A. Eldering, M. Shephard, H. Worden, M. Lampel, S. A. Clough, P. D. Brown, C. P. Rinsland, M. Gunson, and R. Beer (2006), Tropospheric emission spectrometer: Retrieval method and error analysis, IEEE Trans. Geosci. Remote Sens., 44(5), 1297-1307.

[5] Clough, S. A., M. W. Shephard, E. J. Mlawer, J. S. Delamere, M. J. Iacono, K. Cady-Pereira, S. Boukabara, and P. D. Brown (2005), Atmospheric radiative transfer modeling: a summary of the AER codes, Short Communication, J. Quant. Spectrosc. Radiat. Transfer, 91, 233-244.

[6] Gauss M., G. Myhre, G. Pitari, M. J. Prather, I. S. A. Isaksen, T. K. Berntsen, G. P. Brasseur, F. J. Dentener, R. G. Derwent, D. A. Hauglustaine, L. W. Horowitz, D. J. Jacob, M. Johnson, K. S. Law, L. J. Mickley, J.-F. Muller, P.-H. Plantevin, J. A. Pyle, H. L. Rogers, D. S. Stevenson, J. K. Sundet, M. van Weele, and O. Wild (2003), Radiative forcing in the 21st century due to ozone changes in the troposphere and the lower stratosphere. J. Geophys. Res., 108(D9), 4292.

[7] Hagan, D., and P. Minnett (2003), AIRS Radiance Validation Over Ocean From Sea Surface Temperature Measurements, IEEE Trans. Geosci. Remote Sensing, 41, 432-441, 2003.

[8] Revercomb, H., D. L. Buijs, H. B. Howell, W. Smith, and L. Sromovsky (1988a), Radiometric calibration of IR Fourier transform spectrometers: solution to a problem with the high-resolution interferometer sounder, Appl. Opt., 27, 3210.

[9] Revercomb, H. E., D. D. LaPorte, W. L. Smith, H. Buijs, D. G. Murcray, F. J. Murcray, and L.A. Sromovsky (1988b), High-Altitude Aircraft Measurements of Upwelling IR Radiance: Prelude to FTIR from Geosynchronous Satellite, Mikrochimica Acta [Wien], II, 439-444.

[10] Revercomb, H. E., W. L. Smith, F. A. Best, J. Giroux, D. D. LaPorte, R. O. Knuteson, M. W. Werner, J. R. Anderson, N. N. Ciganovich, R. W. Cline, S. D. Ellington, R. G. Dedecker, T. P. Dirkx, R. K. Garcia, and H. B. Howell (1996), Airborne and ground-based Fourier transform spectrometers for meteorology: HIS, AERI and the new AERI-UAV. Proceedings SPIE Optical Instruments for Weather Forecasting, ed. G.W. Kamerman, 2832, 106-117.

[11] Shephard, M. W., H. M. Worden, K. E. Cady-Pereira, M. Lampel, M. Luo, K. W. Bowman, E. Sarkissian, R. Beer, D. M. Rider, D. C. Tobin, H. E. Revercomb, B. M. Fisher, D. Tremblay, S. A. Clough, G. B. Osterman, and M. Gunson, Tropospheric Emission Spectrometer Nadir Spectral Radiance Comparisons, submitted to J. Geophys. Res.

[12] Tobin, D.C., H. E. Revercomb, R. O. Knuteson, F. A. Best, W. L. Smith, N. N. Ciganovich, R. G. Dedecker, S. Dutcher, S. D. Ellington, R. K. Garcia, H. B. Howell, D. D. LaPorte, S. A. Mango, T. S. Pagano, J. K. Taylor, P. van Delst, K. H. Vinson, and M. W. Werner (2006), Radiometric and spectral validation of Atmospheric Infrared Sounder observations with the aircraft-based Scanning High-Resolution Interferometer Sounder, J. Geophys. Res., 111, D09S02, doi:10.1029/2005JD006094.

[13] Tremblay et al. (2007), Validation of Tropospheric Emission Spectrometer (TES) Water Surface Temperature, submitted to J. Geophys. Res.

[14] Worden, J., S. S. Kulawik, M. W. Shephard, S. A. Clough, H. M. Worden, K. Bowman, and A. Goldman (2004), Predicted errors of Tropospheric Emission Spectrometer nadir retrievals from spectral window selection, *J. Geophys. Res., 109*, D09308.

5. Validation of TES Level 2 Nadir Ozone for Data

5.1 Introduction to Nadir Ozone Validation

The TES V003 nadir ozone product differs from V002 as a result of the updates made to improve the atmospheric temperature retrievals. The nature of the difference between V002 and V003 is on average very small, but can be larger for individual retrievals. Figure 5-1, Figure 5-2 and Figure 5-3 show histograms of the percentage difference between the TES retrieved ozone values from the V003 and V002 (V003-V002) for three different pressure levels. Figure 5-1 shows the difference in the ozone for the two data versions at 681 hPa from 12 global surveys spanning the TES data record through late in 2006. The figure shows that the V003 data is on average 4.5% lower than the V002 data. Figure 5-2 shows a similar picture at 261 hPa (V003 is 3% lower) and suggests that the changes made in the algorithm that produce the V003 data could be mitigating slightly the upper tropospheric bias seen in the TES retrievals (see below). The story at 100 hPa (Figure 5-3) is somewhat different in that there is very little change between the versions.

While the changes in nadir ozone seem to be fairly small in the V003 in general, for individual retrievals they can be more significant. Figure 5-4 shows maps of the TES data for July 2006 from both versions of the data. The figure also includes a map of the ratio of the V003 O3 to the V002 data at 618 hPa. The map of the ratio of the two ozone values shows regions of significant differences.

The rest of this section shows a set of validation analyses using the V002 data. The comparisons to ozonesondes, lidar data and of the ozone columns provide a consistent picture of the bias seen in the TES data with respect to correlative data. The sections provide information on the methodology used in validating the TES ozone data product. More information can be found in papers submitted for a special issue of the Journal of Geophysical Research – Atmospheres dedicated to Aura instrument data product validation. There were papers submitted on V002 ozone comparisons to sondes (Nassar et al, 2007), lidar (Richards et al., 2007) and of column values to other satellite instruments (Osterman et al., 2007).

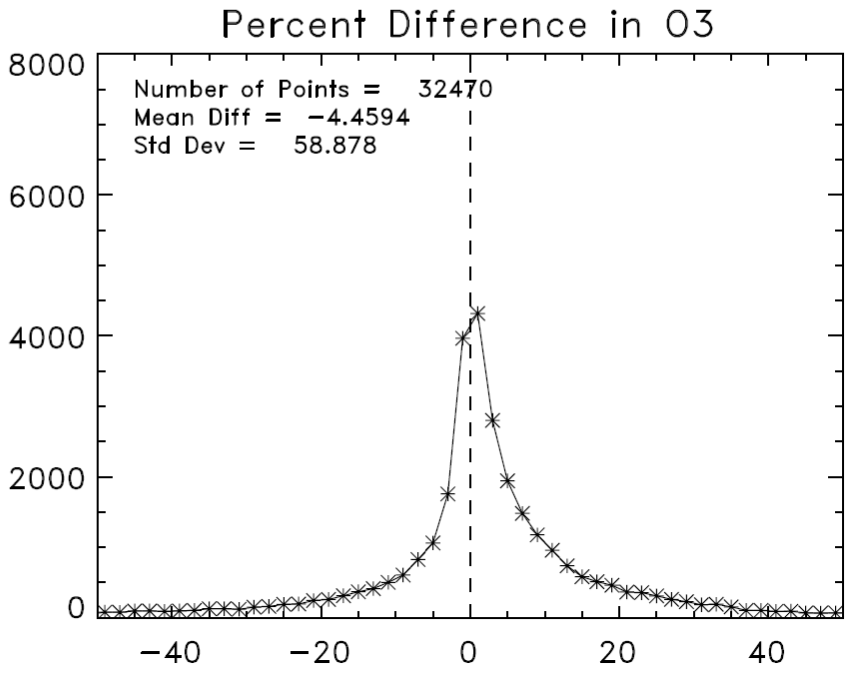

Figure 5-1 The percentage difference (V003-V002)/V003 between the TES data for ozone at 681 hPa. The data have been filtered using the TES "master" quality flag. The V003 data are 4.5% lower than the V002 data at this pressure level.

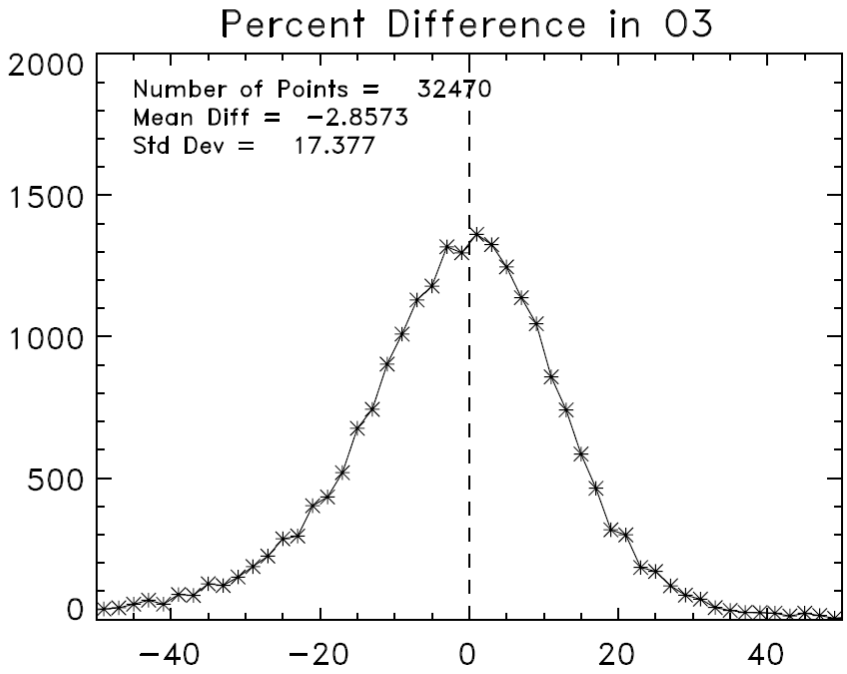

Figure 5-2 The percentage difference (V003-V002)/V003 between the TES data for ozone at 261 hPa. The data have been filtered using the TES "master" quality flag. The V003 data are 2.9% lower than the V002 data at this pressure level.

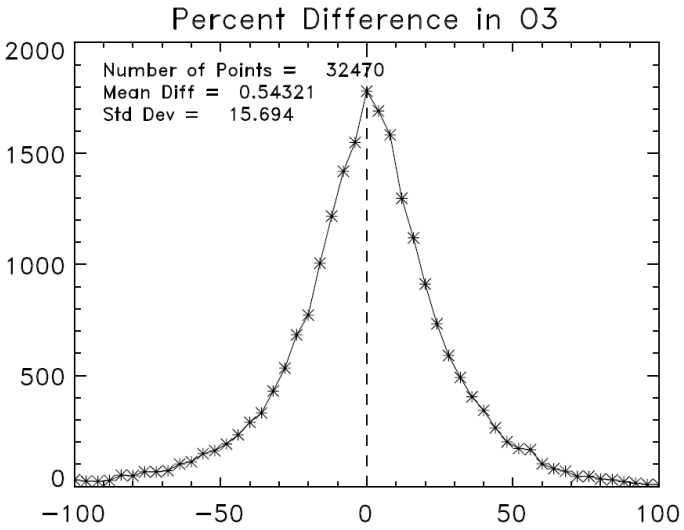

Figure 5-3 The percentage difference (V003-V002)/V003 between the TES data for ozone at 100 hPa. The data have been filtered using the TES "master" quality flag. The V003 data are essentially unchanged from the V002 data at this pressure level.

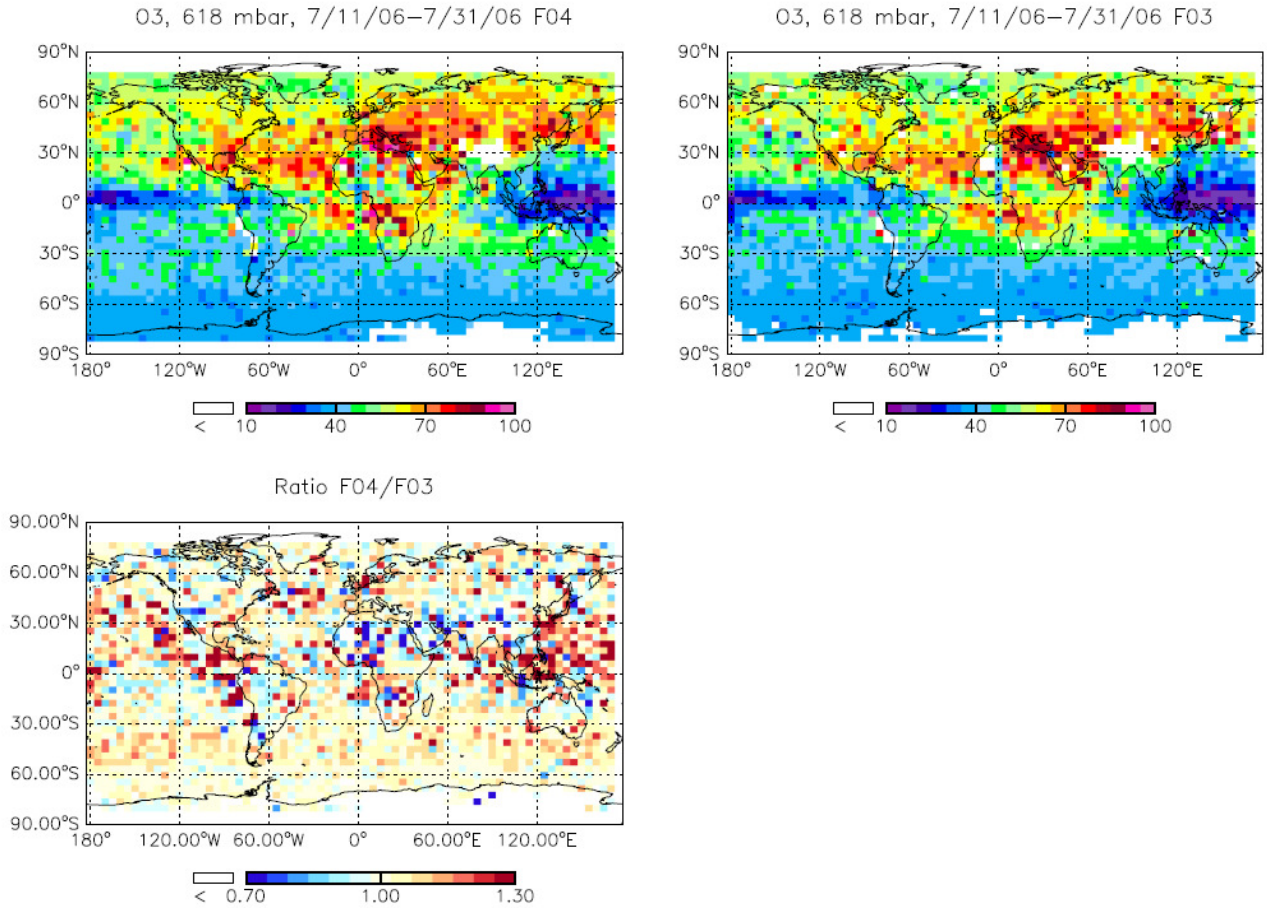

Figure 5-4 Maps of the V003 (left, top) and V002 (right, top) ozone values for July 11-31, 2006 at 618 hPa. The bottom panel shows the ratio of V003/V002 to highlight regions of difference between the two data sets.

5.2 Comparison with Ozonesondes

5.2.1 Introduction

O_3 profiles are retrieved from TES infrared radiances with roughly 6 km vertical resolution for nadir observations. The principal source of validation for TES O_3 measurements is ozonesondes. In some cases, we have sonde data from launches timed to the Aura overpass, such as those taken during the AVE, CR-AVE, SAUNA and IONS-06 campaigns. We also perform comparisons with the data available from the Southern Hemisphere Additional Ozonesondes (SHADOZ) and World Ozone and Ultraviolet Radiation Data Centre (WOUDC) networks. We account for TES measurement sensitivity and vertical resolution by applying the TES averaging kernel and constraint to the ozonesonde data before differencing the profiles. This section gives an update to the comparisons using V001 data, which found a significant high bias for TES ozone compared to sondes in the upper troposphere, especially at mid-latitudes (H. Worden, *et al*, 2007.) We also describe some case studies for specific ozonesonde sites where we have enough statistics to examine coincidence criteria.

5.2.2 Comparison Methods

The procedure for comparing TES to sonde data by applying the averaging kernel and *a priori* constraint vector (hereafter referred to as the TES operator) to the sonde data is described in more detail in H. Worden, *et al*, 2006 and summarized briefly below. It is important to note that accounting for TES sensitivity by applying the TES operator to the sonde data yields a TES-sonde **difference** that is not biased by the TES *a priori.* We can then use the differences to assess systematic errors in the TES calibration and retrieval process, assuming we measure the same airmasses as the sondes.

We process sonde measurements as follows:

1. Map O_3 sonde profile to the TES 65 pressure level grid;

$$X_{sonde}^{pTES} = M_{pTES \Rightarrow Psonde}^{-1} X_{sonde}$$

(Equation 5-1)

2. Apply the TES operator (averaging kernel, A_{TES}, and *a priori* constraint):

$$X_{sonde}^{TES_{AK}} = X_{apriori} + A_{TES}[X_{sonde}^{pTES} - X_{apriori}]$$

(Equation 5-2)

3. Compare to TES profile using the measurement and cross-state error terms. This is denoted as the observational error in the TES data products and does not include the smoothing error term that is included in the total error estimate. Note that we account for smoothing error when we apply the averaging kernel to the sonde profile. Figure 5-5 shows examples of TES nadir ozone averaging kernels. (See C. Rodgers, 2000, J. Worden, *et al*., 2004 and K. Bowman *et al.,* 2006 for more details on error characterization and definitions.)

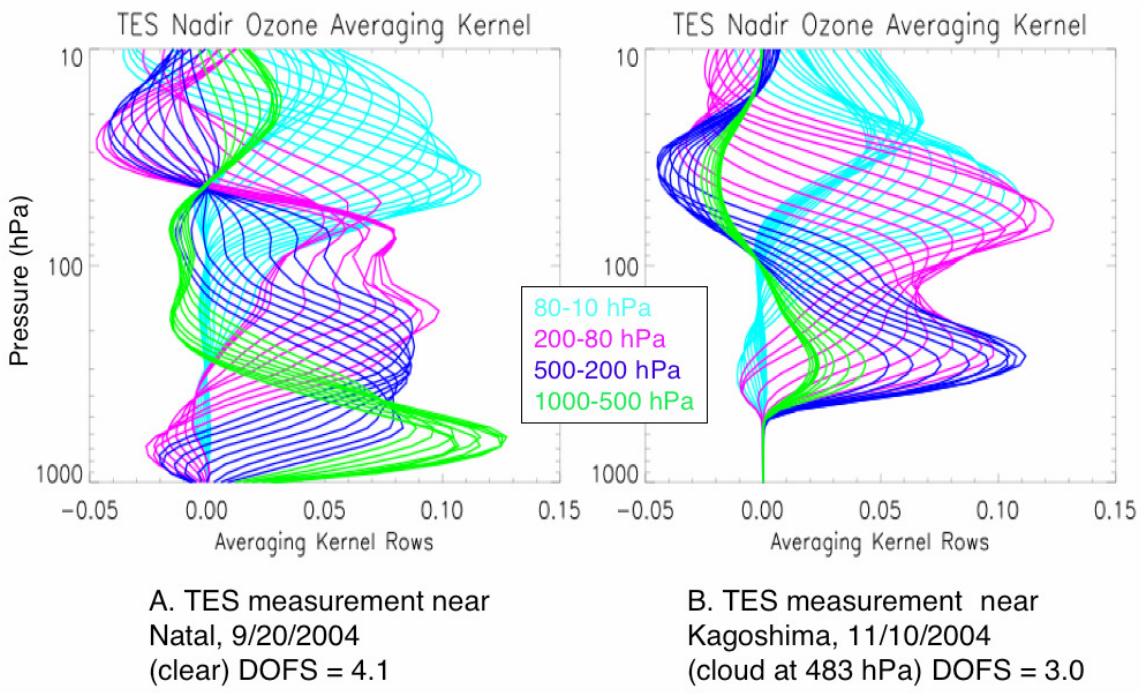

Figure 5-5 Examples of TES Nadir Ozone Averaging Kernels under (A) Clear and (B) Cloudy Conditions. Natal is at 6°S, 35°W and Kagoshima is at 32°N, 131°E. The colors indicate averaging kernel rows corresponding to the pressure levels as noted in the legend. DOFS (Degrees of Freedom for Signal) give the trace of the averaging kernel.

5.2.3 WOUDC and SHADOZ Comparisons

Figure 5-6 shows the coincidence map for TES-sonde sites from the WOUDC (World Ozone and Ultraviolet Data Center) and SHADOZ (Southern Hemisphere Additional Ozonesonde) Archives. Sonde data were screened by the Harvard team and a total of 143 valid matches, with 200 km, 26 hour coincidence criteria, were found for data taken between September 2004 and May 2006. However, some of these were later rejected based on the TES data quality flags (41), the emission layer flag (3) which is explained later, or a temperature difference of greater than 5 K over multiple levels (14) indicating that TES and the sonde may have been measuring different air masses.

Figure 5-7 shows the TES-sonde differences, after applying the TES operator, for the data separated into northern mid-latitudes, tropics and Antarctic latitude ranges. Figure 5-8 gives the bias and Root-Mean-Square (RMS) values for upper and lower troposphere averages for TES vs. sonde (with TES operator) in the different latitude ranges. The apparent outliers in the northern mid-latitude upper troposphere correlations may result from the definition of the tropopause used which may have permitted some stratospheric ozone in the average. These will be investigated further at a later time. Another modification that will be addressed in a future publication is screening for low sensitivity due to either clouds or thermal conditions such as in the lower troposphere Antarctic cases.

To determine the origin of the anomalous low bias shown in the tropics in Figure 5-8, an additional analysis was performed to further separate this region into the inner tropics and subtropics as shown in Figure 5-9. This comparison indicated that the low bias originated almost

entirely from subtropical coincidences; however, the reason for this has not yet been investigated.

Conclusions from WOUDC and SHADOZ analysis:

- TES nadir ozone profiles are typically biased high compared to sondes in all three latitude zones, but this bias has been reduced from that determined in Worden et al. (2006) for V001 data.
- The absolute bias is higher between 10-100 hPa, but the % bias is higher for the troposphere.
- Mean ΔO_3 (TES-sonde) % from the surface to 200 hPa are:
  Northern mid-latitude: 4-17%, Tropical: -5-14%, Antarctic: 0-27%
- The main exception to the high bias in ozone occurs in the subtropics between ~100-300 hPa.
- It is important to note the linearity in ozone abundance for TES-sonde comparisons (Figure 5-8). Although TES ozone has biases with respect to sondes, we have confidence that relative variations in TES ozone are meaningful because of this linearity.

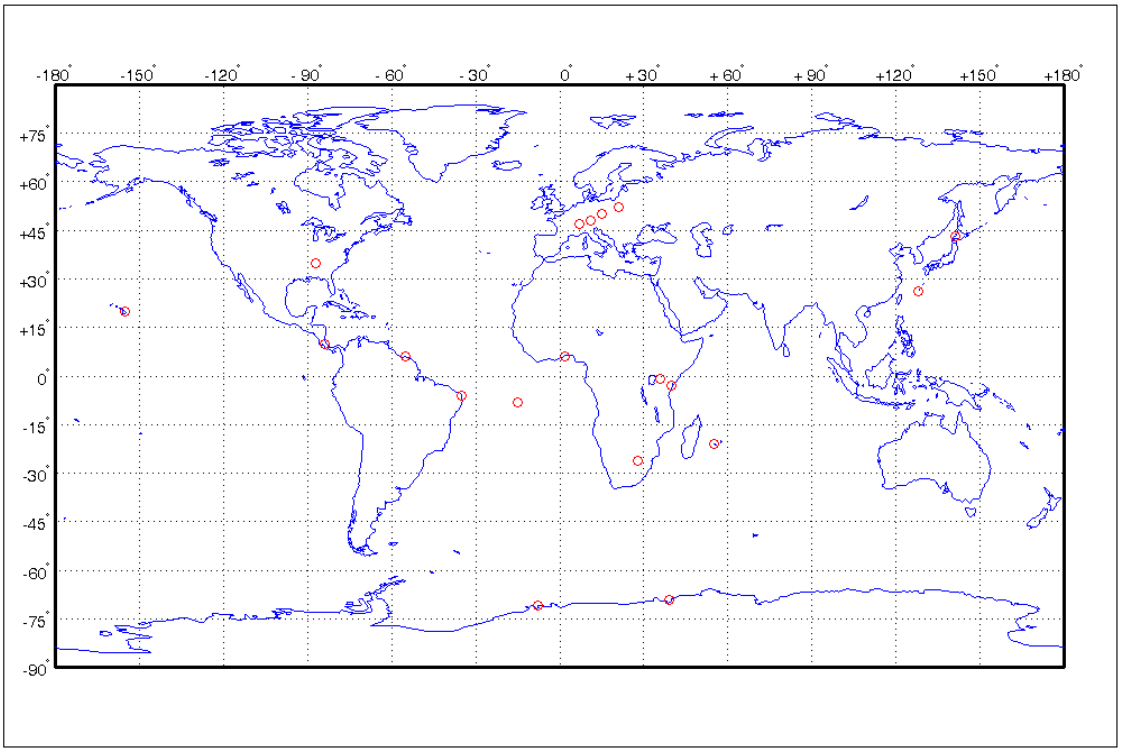

Figure 5-6 WOUDC and SHADOZ Sonde Sites with TES Measurement Coincidences for September 2004 to May 2006.

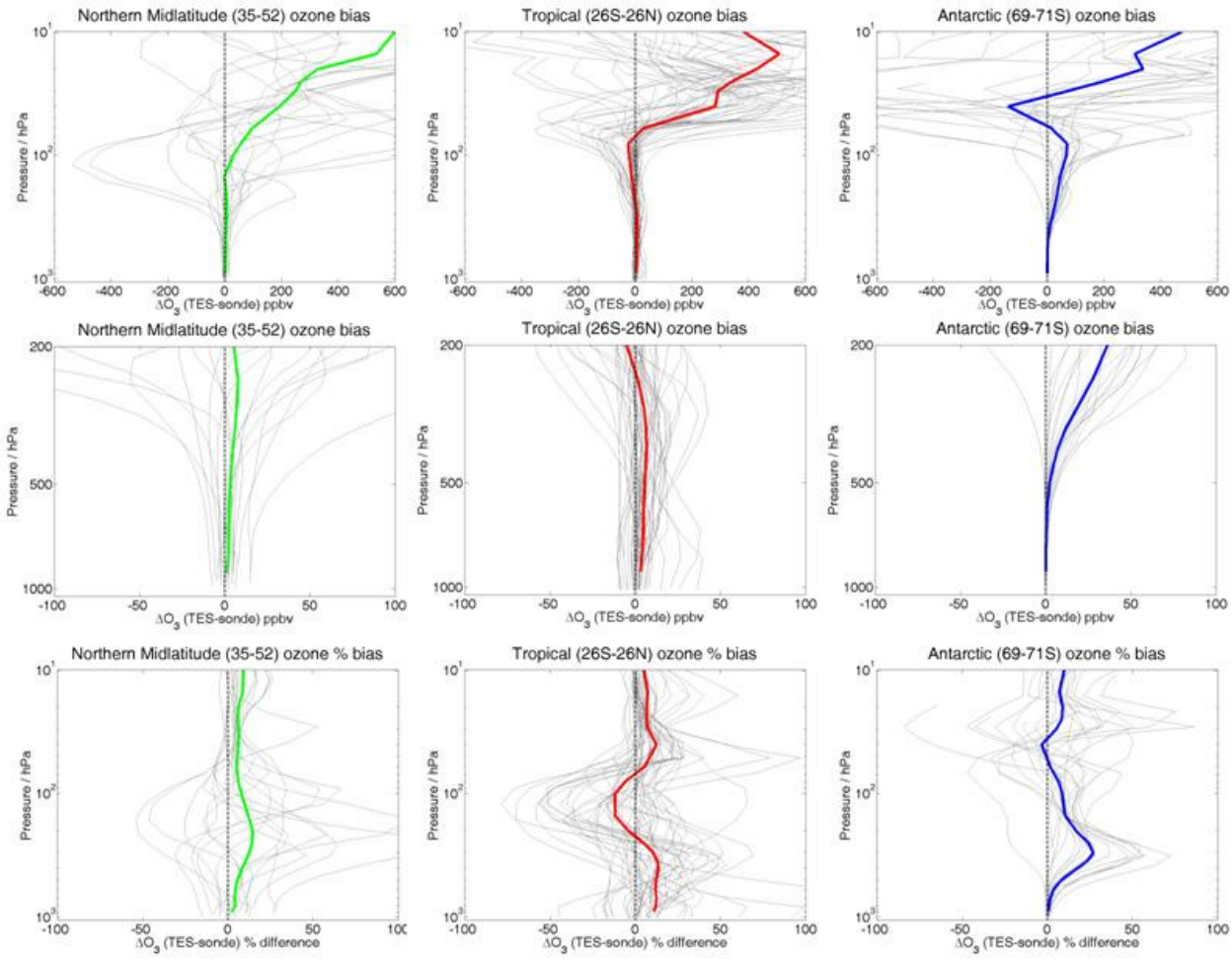

Figure 5-7 TES-Ozonesonde Differences for the Northern Mid-Latitudes, Tropics and Antarctic. Top panels show the difference in ppbv, the middle panels show the same profiles as the top panels in ppbv, but focused on the surface to 200 hPa. Bottom panels show the relative (%) difference for both troposphere and lower stratosphere. The thick red, green and blue lines indicate the zonal averages.

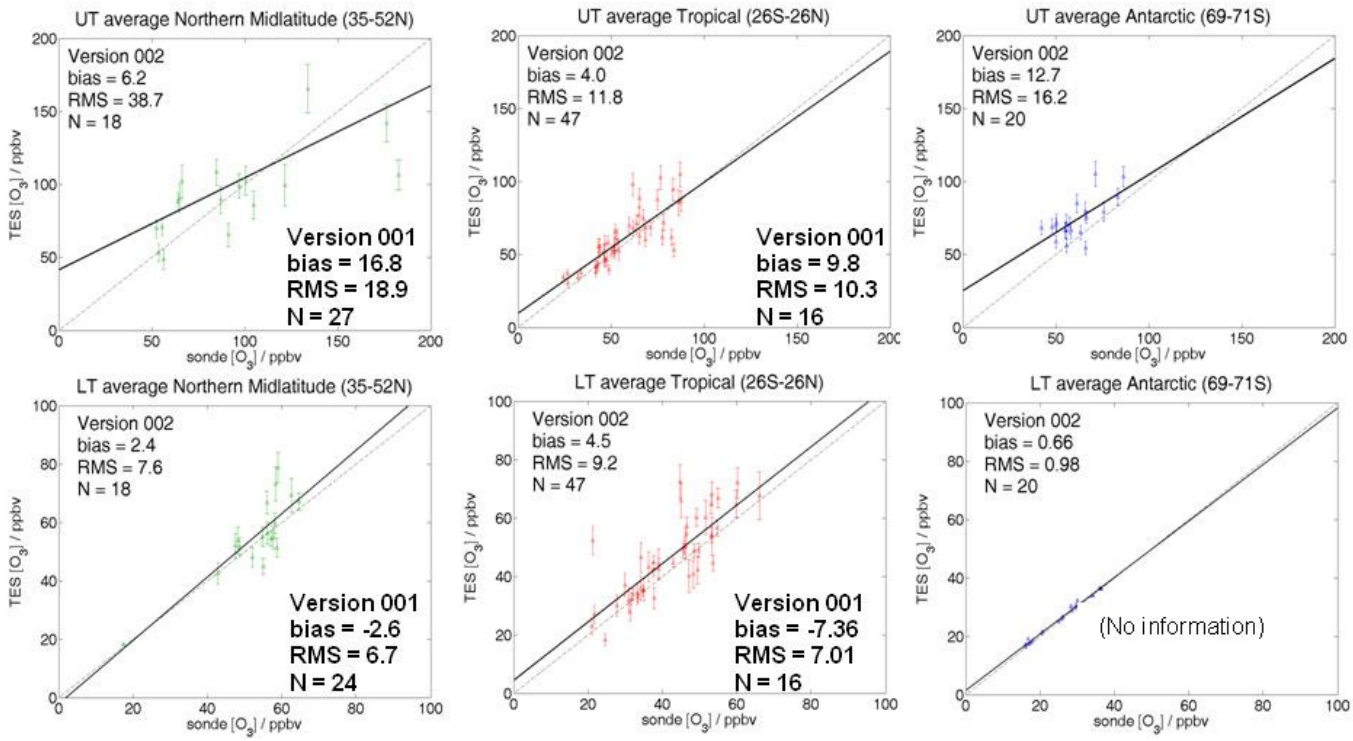

Figure 5-8 TES-Ozonesonde Differences for N. Mid-Latitudes, Tropics and Antarctic. Top panels show average differences for the upper troposphere (500 hPa to 200 hPa or the tropopause, whichever is larger). Bottom panels show average differences for the lower troposphere (surface to 500 hPa). For the Antarctic cases, the comparison in the lower troposphere gives no information due to the lack of TES sensitivity to ozone at those pressures for those latitudes. Bias and RMS values are also given for V001 data, for comparison.

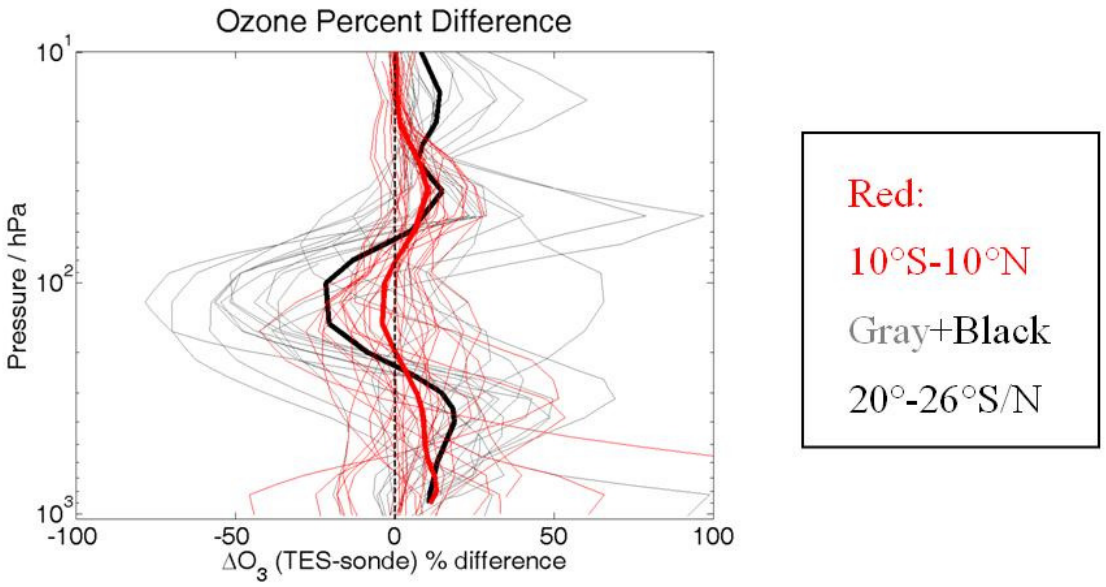

Figure 5-9 Percent Differences in TES-Sonde (with TES Operator). The inner tropics were defined here as coincidences in the 10°S-10°N range and are shown in red. The subtropical (20-26°S/N) coincidences, shown in black are responsible for most of the negative bias between about 100-300 hPa.

5.2.4 Case studies Over Specific Sonde Sites

Ozonesonde campaigns in 2006 with dedicated launches timed for the Aura overpass and corresponding special observations from TES with dense along-track nadir sampling have allowed detailed comparisons and tests of coincidence assumptions.

Two types of TES special observations were used for these campaigns. The TES observations for ARM-SGP and SAUNA were "transects" where the nadir angle changes with scan to allow nearly contiguous footprints with 40 scans covering around 500 km. For the comparisons with IONS-06 ozonesondes launched during the INTEX campaign, "Step and Stare" observations were used for greater coverage with 125 nadir measurements spaced about 40 km apart.

5.2.5 ARM-SGP (36.6°N, 97.5°W) Oklahoma, USA: Identification of "Emission Layer Flag"

Sondes were launched by F. Schmidlin, NASA Wallops from Jan 18 to Feb 16, 2006 for both night and day Aura overpasses at the ARM-SGP site (Southern Great Plains Atmospheric Radiation Measurement facility). The TES comparisons with these sondes have been critical in identifying erroneous retrievals that can sometimes result when the lowest layers of the atmosphere are in emission, *i.e.*, warmer than the surface. The constraints in the retrieval algorithm do not prevent cases with a large ozone abundance in the lowest layers in emission that would radiatively cancel with the layers in absorption above. The retrieval can find a false minimum since the artificially high ozone then suggests higher sensitivity, as seen in the averaging kernel for the lowest layers of these cases. This condition is now identified with the "emission layer flag", set to "bad" when the thermal contrast (T_atm – T_surf) over the lowest 3 layers in our radiative transfer model is > 1K and the ozone in these layers is > 15ppb from the

initial guess. Figure 5-10 shows statistics from the ARM-SGP ozonesonde comparisons (5 night and 4 day transect runs) and demonstrates the effect of the emission layer flag on the night observations, compared to day observations, which did not have emission layer conditions.

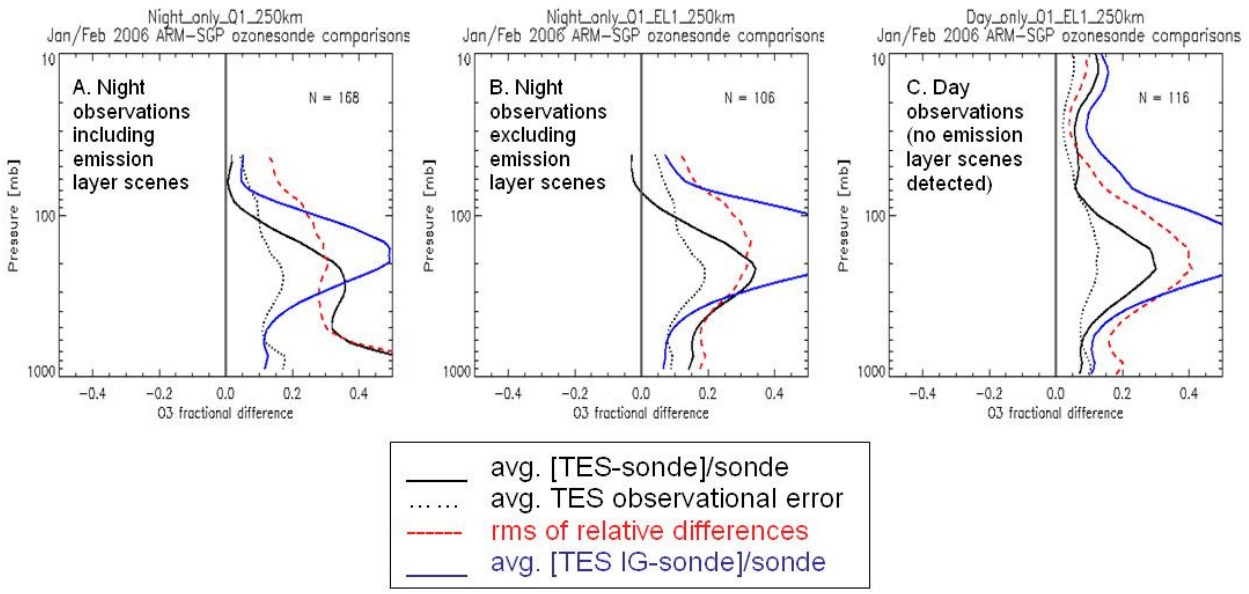

Figure 5-10 Statistics for ARM-SGP TES-Sonde Comparisons. Maximum altitude is determined by the lowest sonde height in the ensemble. Panel A shows the average TES-Sonde (with TES operator) difference and RMS for night observations, screened only by the general quality flag. Note the large values for both average difference and RMS near the surface. Panel B has night observations excluding TES scenes with an emission layer identified. Panel C shows day observations, which did not have any emission layer scenes detected. I.G. indicates initial guess**.**

5.2.6 Sodankyla (67.4°N, 26.6°E) Finland

Sondes were launched as part of SAUNA campaign from March 20 to April 14, 2006. Figure 5-11 shows the location of the TES transects taken during the campaign and a typical curtain plot of averaging kernel diagonals along the transect. The averaging kernels show maximum sensitivity just below the tropopause in these cases. Figure 5-12 shows a TES ozone profile compared to the ozonesonde, the ozonesonde with the TES operator applied and the TES initial guess (same as *a priori*) on the left and the sonde-TES % differences along the TES track as a curtain plot in pressure vs. latitude on the right.

Figure 5-13 shows NOAA-HYSPLIT (Draxler and Rolph, 2003) backward trajectories for both TES measurement locations and sonde site, corresponding to the case shown in Figure 5-12. The larger differences in the curtain plot of sonde-TES are consistent with the changes in the origin of the air masses sampled by TES compared to that sampled by the sonde.

Figure 5-14 gives the statistics of the comparisons as a function of pressure for 3 different coincidence criteria. This figure demonstrates that the average difference for TES-sonde(with TES operator) only varies slightly with the tighter coincidence criteria, while the variance

decreases to where it is mostly explained by the estimate for TES observational error (measurement + cross-state errors).

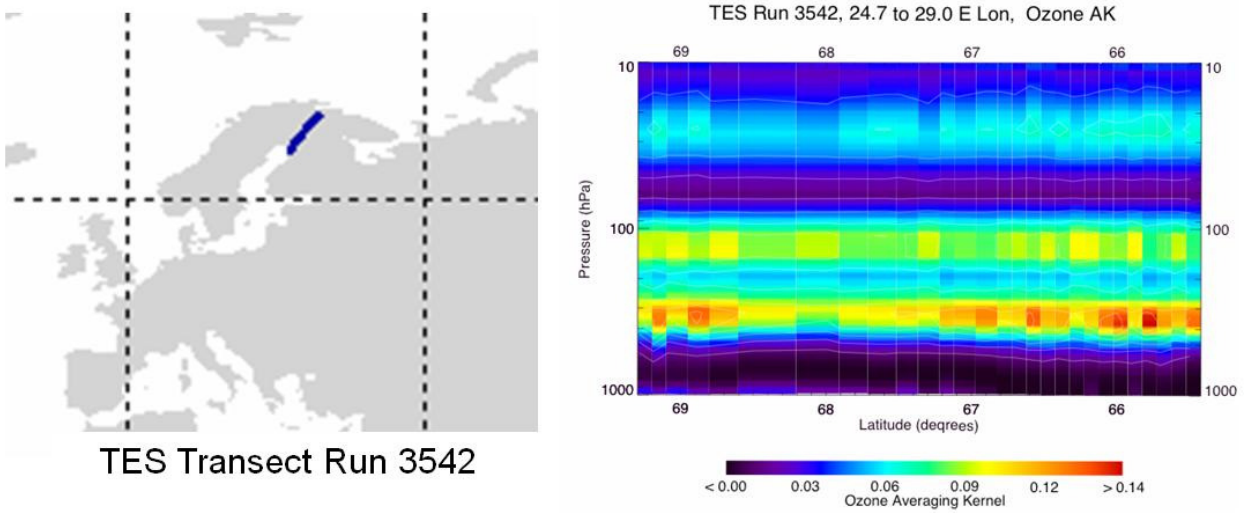

Figure 5-11 Target Locations for TES Transect Observations near Sodankyla and an Example of Averaging Kernel Diagonals vs. Pressure and Latitude Along the Track. The tropopause pressure was around 290 hPa in these measurements.

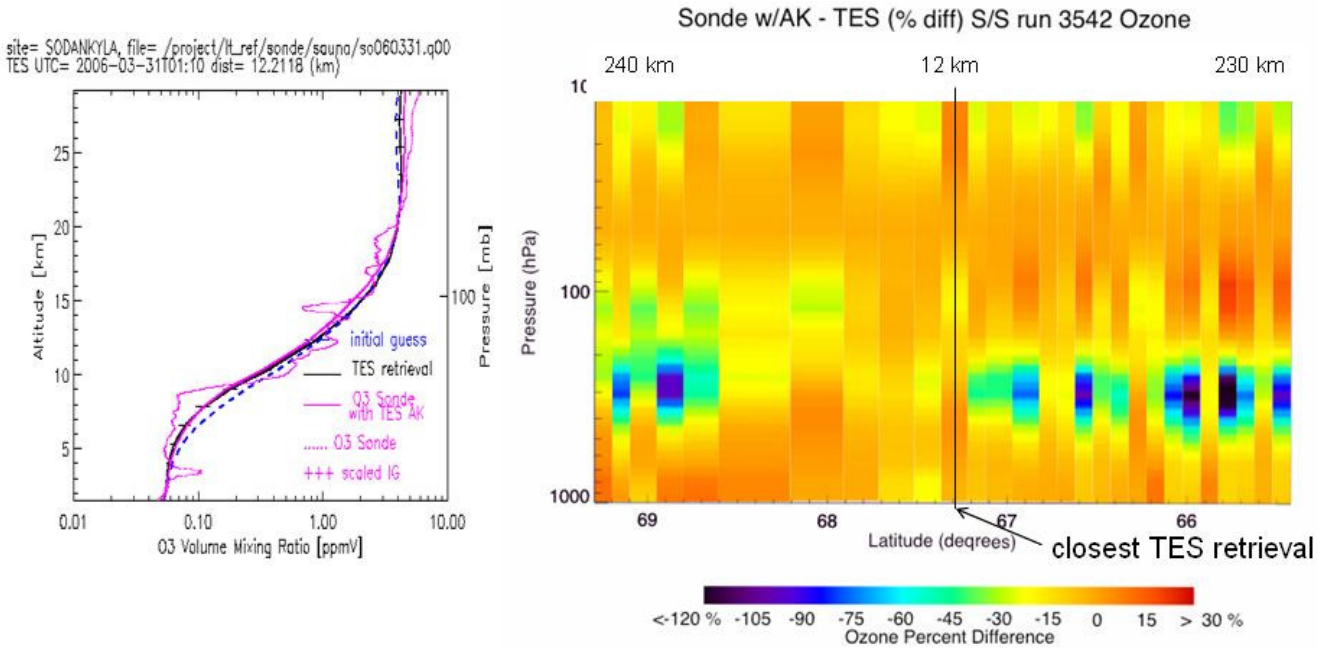

Figure 5-12 Profile Comparison for Closest TES Measurement (12 km) on March 31, 2006 (left) and Curtain Plot of Sonde(w/TES operator) – TES Percent Difference Showing better Agreement Close to the Sonde Site.

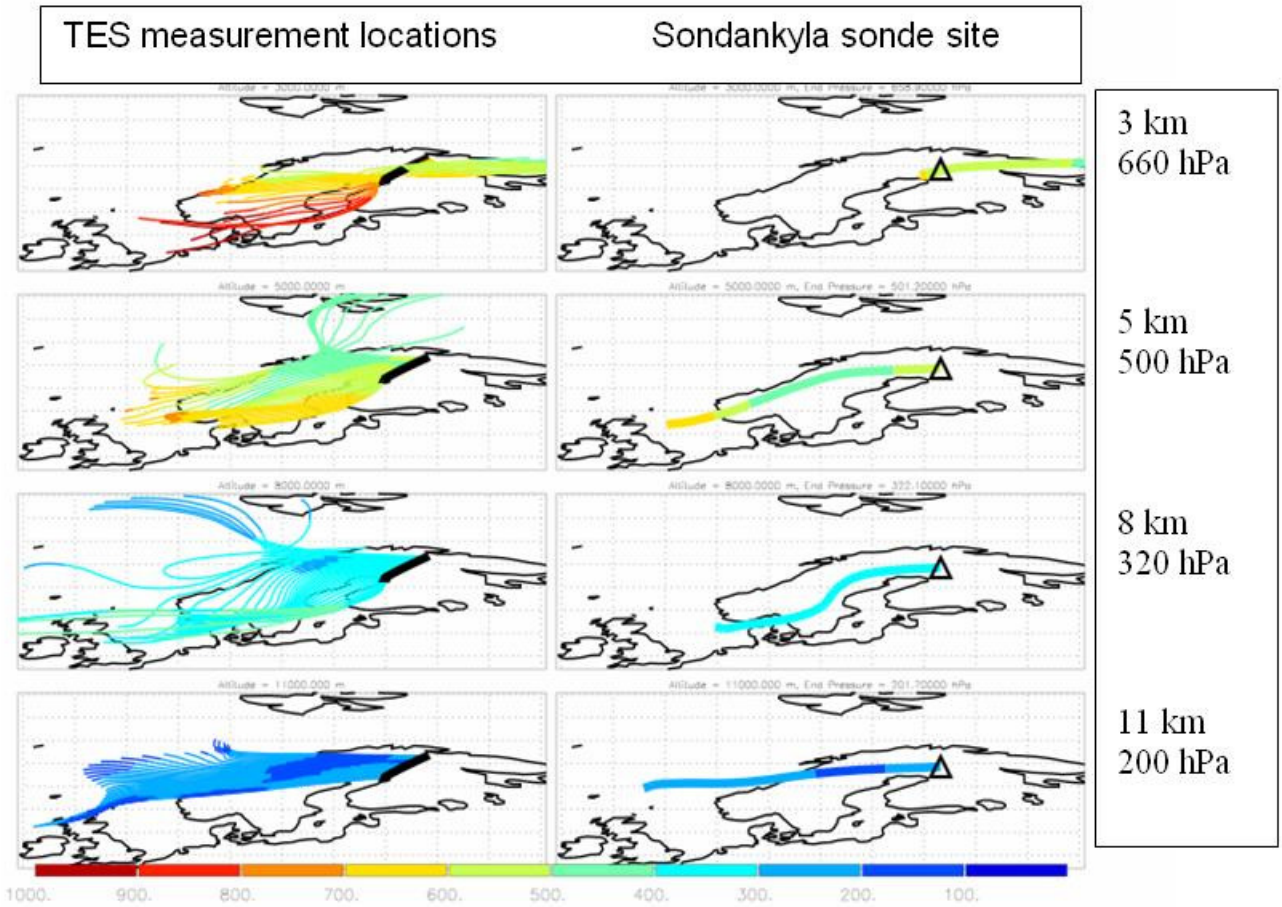

Figure 5-13 72 Hour NOAA-HYSPLIT Backward Trajectories, March 31, 2006, for TES Measurement Locations (Left Panels) and Sodankyla (Right Panels). Pressures of trajectories at the sonde site are shown on the right and colors indicate pressure in hPa along the trajectory.

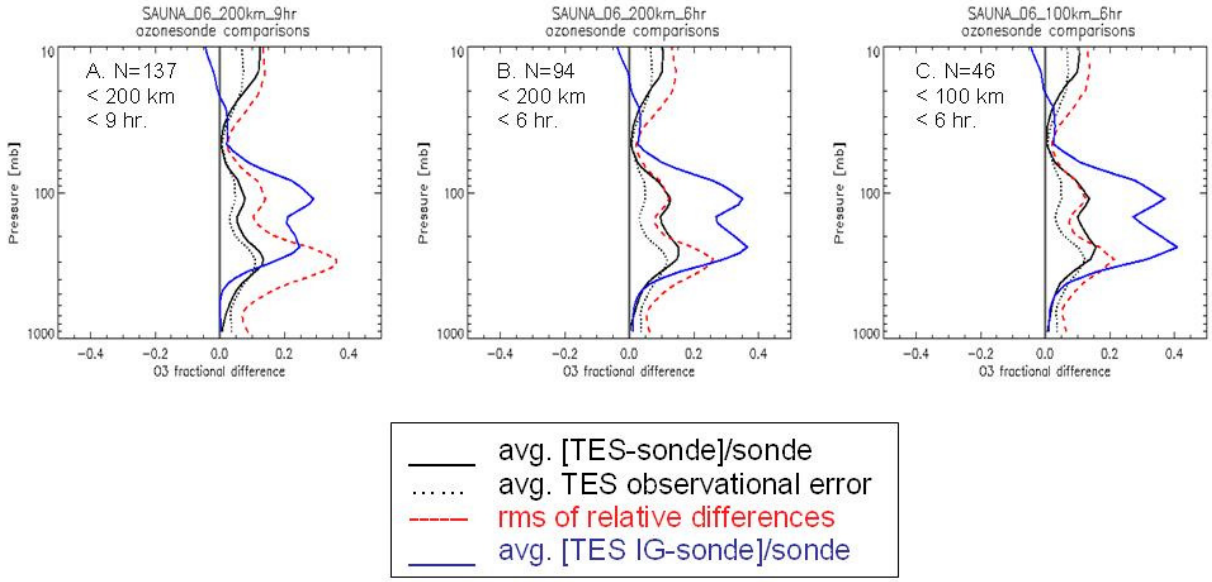

Figure 5-14 Statistics for TES Comparisons to Sodankyla Sondes from the March-April 2006 SAUNA Campaign with Coincidence Criteria as Shown. These plots show that the average fractional difference (avg. [TES-sonde]/sonde) only varies slightly for the different coincident criteria while the rms of fractional differences (red dashed line) decreases to where it is mostly explained by the estimated observational error from TES (black dotted line) for the tightest criteria (panel C: 100 km, 6 hr.).

5.2.7 PNNL (46.2°N, 119.2°W) Richland, Washington, USA

This comparison is with a sonde launched for the IONS-06 campaign on Apr 21, 2006, from the NATIVE (Nittany Atmospheric Trailer and Integrated Validation Experiment) platform at PNNL (Pacific Northwest National Laboratory), A. Thompson (P.I.). Figure 5-15 gives the TES Step/Stare measurement locations and the curtain plot of averaging kernel diagonal along the TES track (between the green bars). The averaging kernel shows that except for the few observations between 43° to 44°N, TES had low sensitivity to the lower troposphere. This is consistent with the retrieved cloud information (effective optical depths > 1 and cloud top pressures around 600 hPa) and demonstrates how application of the averaging kernel accounts for TES sensitivity to clouds. In the presence of optically thick clouds, the TES-sonde comparison gives no information below the cloud, but still allows a valid comparison above. The tropopause for these measurements was around 200 hPa,

Figure 5-16 shows ozone profile comparisons for TES, ozonesonde, ozonesonde with the TES operator and the TES initial guess (same as *a priori*) on the left and a curtain plot of the sonde-TES % differences along the TES track as a curtain plot in pressure vs. latitude on the right. The best TES-sonde agreement appears to be within about 200 km from the sonde site. Figure 5-17 shows NOAA-HYSPLIT (Draxler and Rolph, 2003) backward trajectories for both TES measurement locations and sonde site. Here also the trajectories are consistent with the divergence of the sonde-TES differences observed along the TES track.

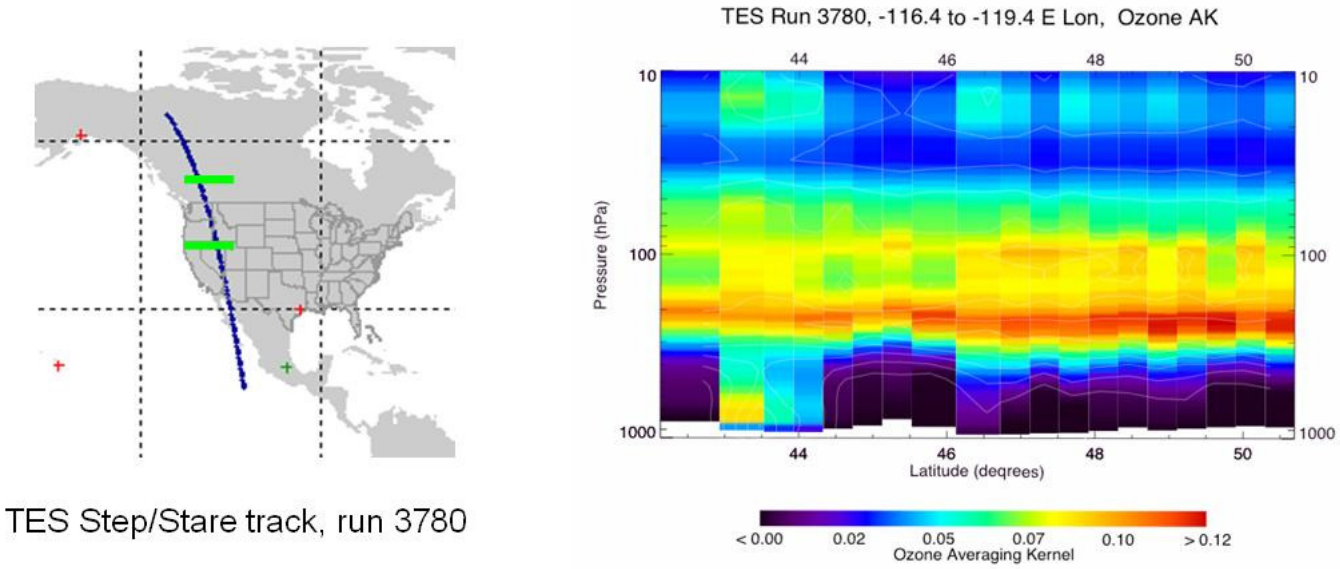

Figure 5-15 TES Measurement Locations (Left) for Closest Run to the IONS NATIVE (PNNL) Sonde on April 21, 2006 and Averaging Kernel Diagonal Curtain Plot (Right) Corresponding to Ozone Profiles Along the Track Between the Green Bars.

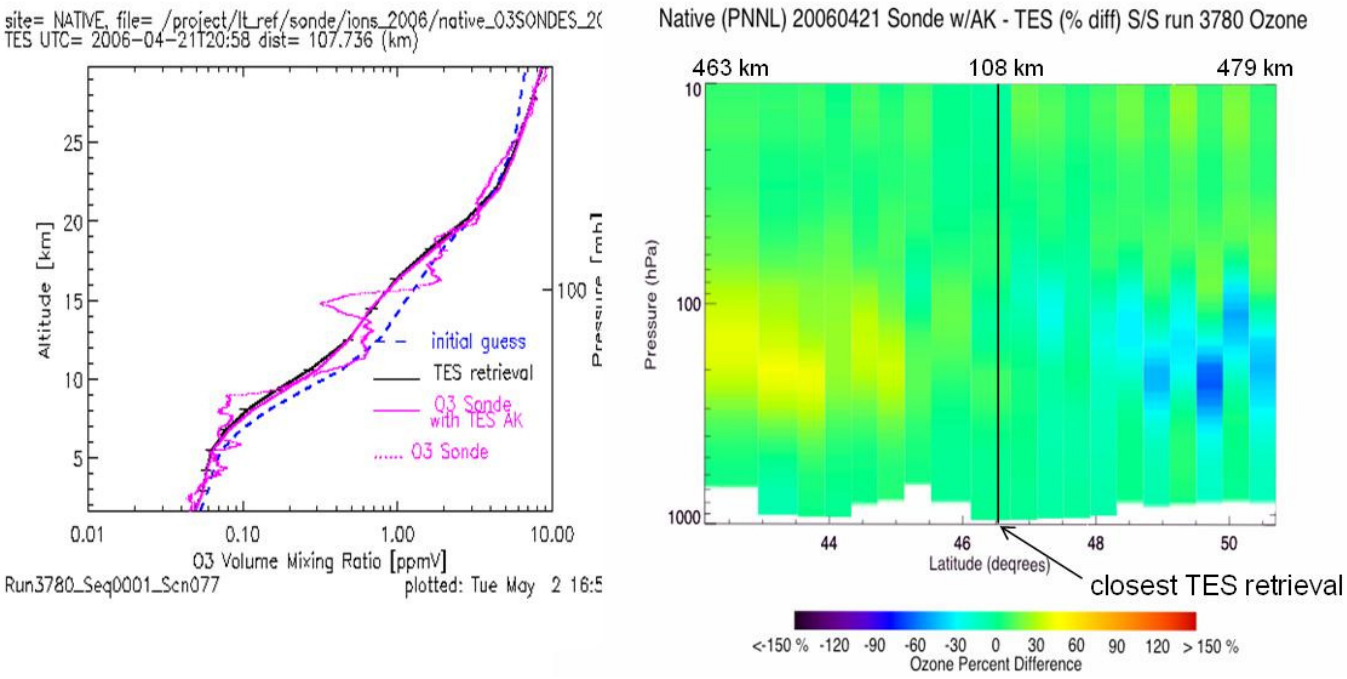

Figure 5-16 Profile Comparison for Closest TES Measurement (108 km) with Sonde, Sonde with TES Operator and TES Initial Guess on April 21, 2006 (left) and Curtain Plot of Sonde(w/TES operator) – TES Percent Difference Showing Better Agreement within about 200 km of the Sonde Site.

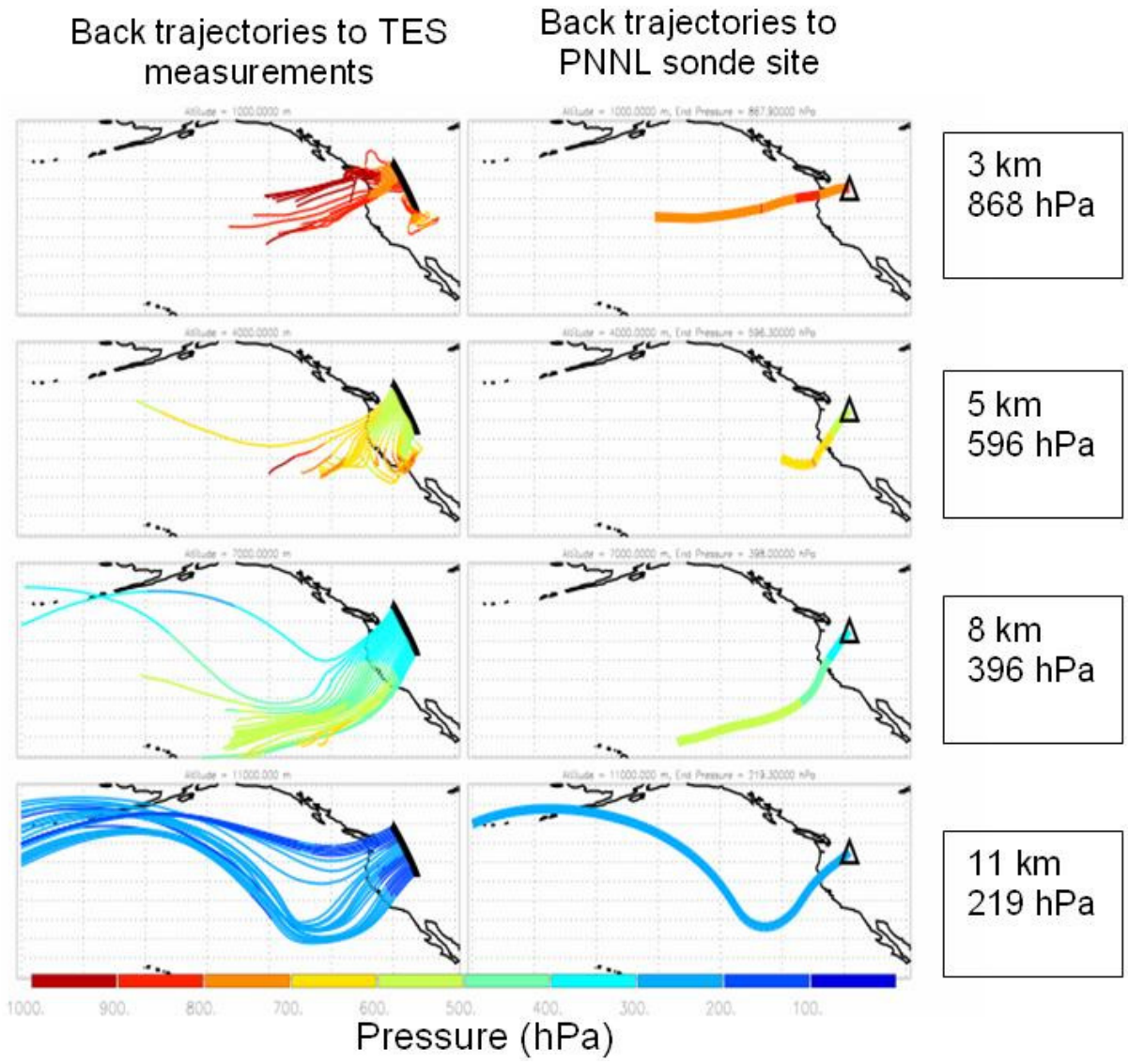

Figure 5-17 72 Hour NOAA-HYSPLIT Backward Trajectories, April 21, 2006, for TES Measurement Locations (Left Panels) and PNNL (right panels). Pressures of trajectories at the sonde site are shown on the right and colors indicate pressure in hPa along the trajectory.

5.2.8 Conclusions from TES-ozonesonde case studies:

- TES data taken near the ARM-SGP site had a high occurrence of emission layer scenes for the night observations. After removing these, the statistics for the night comparisons are much closer to the day comparisons. Both day and night comparisons show a high bias for TES ozone profiles that is larger than the average for northern mid-latitude cases, and is under investigation.
- Sodankyla comparisons represent the highest northern latitude validation obtained so far and exhibit a similar high bias for TES ozone profiles as seen in northern mid-latitude and Antarctic comparisons with WOUDC sonde data.

- Statistical analysis of Sondankyla comparisons shows that tighter coincidence criteria improve the agreement of the relative difference RMS to the estimated TES observational error, but do not make a significant change to the average relative difference [TES-sonde(with TES operator)]/[sonde(with TES operator)].
- Case studies show that 200 km distance criteria, currently applied for the selection of TES data in sonde comparisons, appears to be reasonable for higher northern latitudes.

5.3 Comparison with Lidar Measurements

The following section describes a preliminary version of the validation of the TES ozone profiles by comparison to the Differential Absorption Lidar (DIAL) measurements during INTEX-B. The complete analysis is provided in Richards et al., (2007).

5.3.1 INTEX-B and DIAL Measurements

Validation of remotely sensed constituent profiles is essential before they may be used for scientific studies. Validation seeks to identify and characterize any systematic biases that may be present in the reported mixing ratio profile. Validation is conducted through comparisons with independent measurements of the same parameters. The validation of tropospheric ozone, which has a large degree both spatial and temporal variability, requires that these independent measurements be as close to temporally and spatially coincident with the satellite observations as possible.

The Intercontinental Chemical Transport Experiment – Phase B (INTEX-B) was an intensive aircraft campaign which took place over a 10 week period from March 1 to May 15 2006. Among the objectives of the campaign were to observe Mexico City pollution outflow and the transport of Asian pollution to the United States, as well as obtaining temporally and spatially coincident measurements of trace gas species for the validation of remote sensing instruments on the Aura satellite platform. Measurements were made using NASA's DC-8 aircraft with a range of *in situ* and remote sensing instruments. The campaign was split into two phases, during the first phase, performed in March 2006; the DC-8 was based in Houston, Texas, where it conducted a number of flights over the Gulf of Mexico, in the hope of observing the outflow of pollution from Mexico City. The second phase took place during April and May 2006 with the objective of observing Asian pollution outflow over the Pacific. During the second phase the DC-8 conducted several flights out of Honolulu, Hawaii and Anchorage, Alaska.

During the course of the INTEX-B campaign TES made 243 Step & Stare special observations over the United States, East Asia and the Pacific (see Figure 5-18) in order to try and set a context for the limited spatial extent covered by the aircraft observations. Of the flights conducted, seven were coincident or near-coincident with TES Step & Stare observations, 3 in Houston, 2 in Hawaii and 2 in Alaska, the flight tracks for these flights are shown in Figure 5-19.

During the INTEX-B campaign the NASA Langley Research Center Airborne Differential Absorption Lidar (DIAL) instrument made profiles of ozone both below and above the DC-8 aircraft. The instrument measures ozone using two lasers in the ultraviolet that are tunable to maximize the range and sensitivity of the measurement. An example of a DIAL ozone curtain and the instrument standard error are shown in Figure 5-20 and Figure 5-21 for a DC-8 flight out of Honolulu on April 23, 2006.

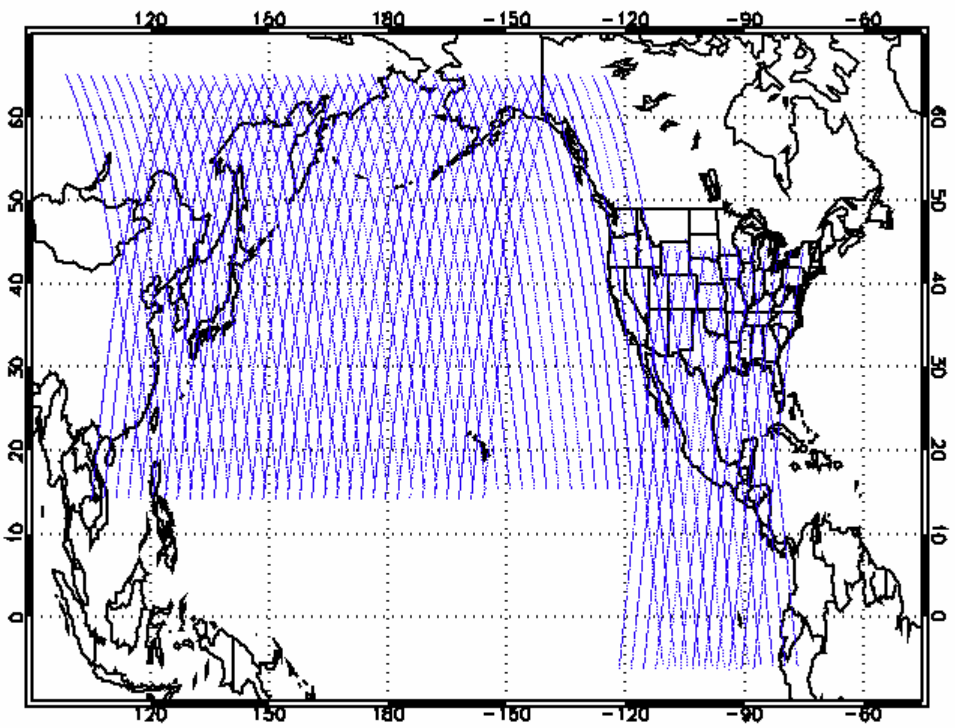

Figure 5-18 The TES step and stare tracks during the INTEX-B campaign.

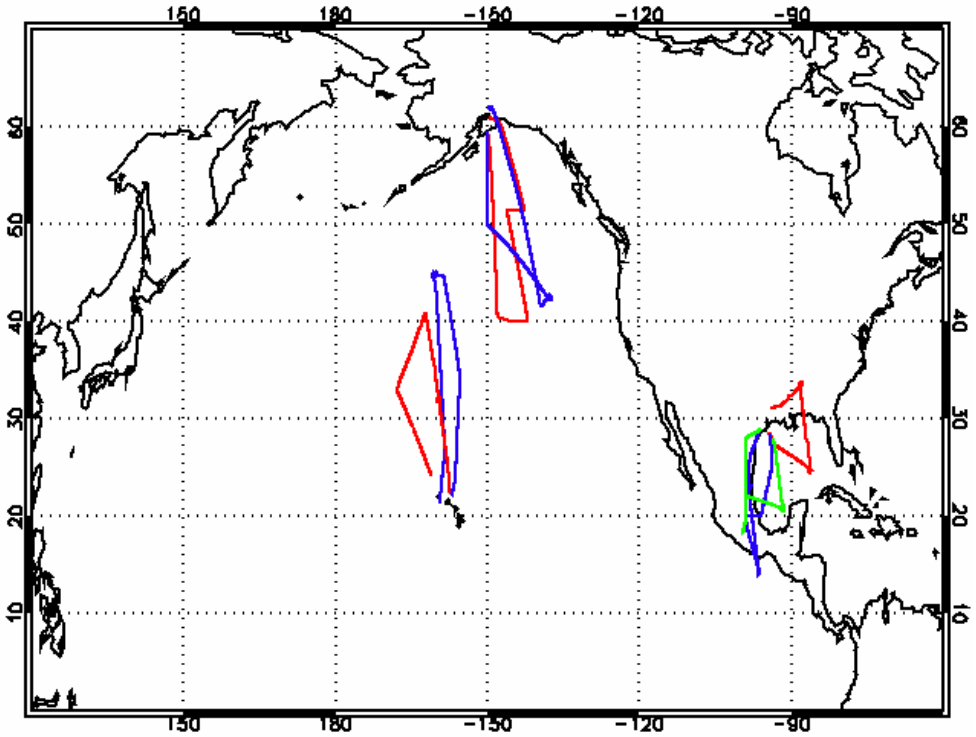

Figure 5-19 The DC-8 flight tracks that provided the best coincidences with TES nadir measurements.

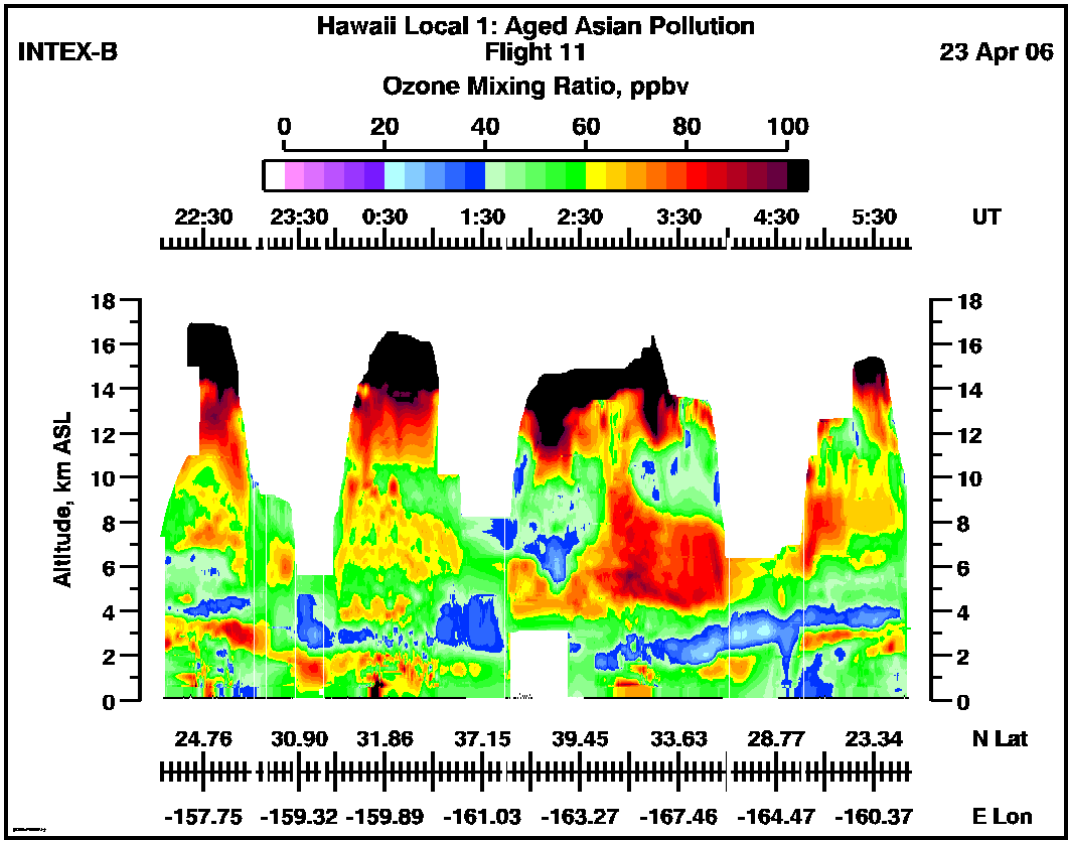

Figure 5-20 A DIAL ozone curtain for the DC-8 flight of April 23, 2006.

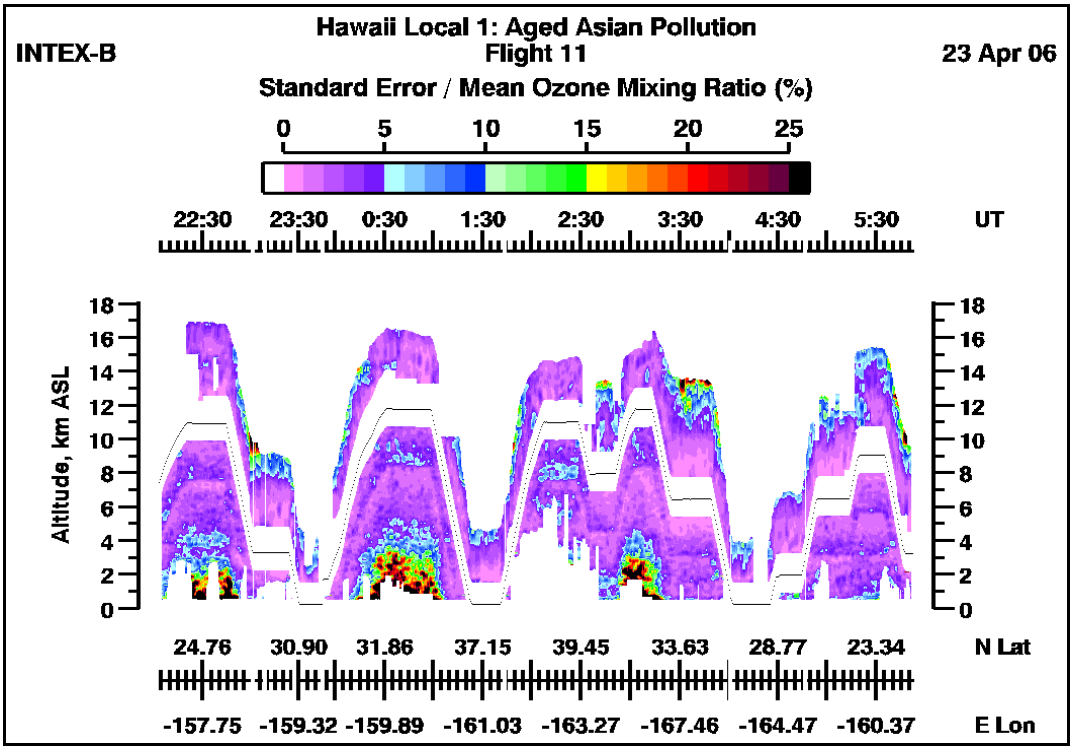

Figure 5-21 The DIAL standard error for the April 23, 2006 DC-8 flight.

5.3.2 DIAL Comparisons with TES

In order to compare profiles obtained from a remote sensing instrument such as TES with *in-situ* data, we must first take into account the limited vertical resolution and the effects of *a priori* information inherent in the retrieved profiles. Averaging kernels intrinsically account for both, and may be used to transform *in-situ* profiles into "TES space" so that they may be directly compared

$$\mathbf{x}_{\mathbf{final}} \equiv \mathbf{x}_{\mathbf{a}} + \mathbf{A}(\mathbf{x}_{\mathrm{DIAL}} - \mathbf{x}_{\mathbf{a}})$$

(Equation 5-3)

An example of how applying the TES averaging kernels affects the DIAL curtain results is given in Figure 5-22. The two panels on the right of Figure 5-22 can be compared directly since the DIAL data is now sampling the atmosphere in a manner similar to TES.

Mean DIAL profiles were calculated to compare to TES special observation profiles. All DIAL observations within 0.15 degrees lat/lon of each TES observation were selected and averaged for comparison with the corresponding TES profile. DIAL profiles were interpolated to the TES pressure grid. In order to apply TES averaging kernels to the DIAL profiles missing data in the DIAL profile were replaced with TES *a priori* information, each profile was also extended to the highest TES pressure level using the *a priori* information used in the TES retrieval. Any profiles which failed the TES QA were discounted from the analysis. Figure 5-23 shows the profile of the difference between TES-DIAL as a function of atmospheric pressure for each of the profiles from DIAL that are coincident with a TES profile. The figure also shows the difference of TES-DIAL for an averaged DIAL profile. The final panel in the figure is the difference profile of TES-DIAL for an average of all coincident DIAL and TES profiles for the Houston based flights during INTEX-B and shows TES to be higher than DIAL by roughly 10-15% over most of the troposphere.

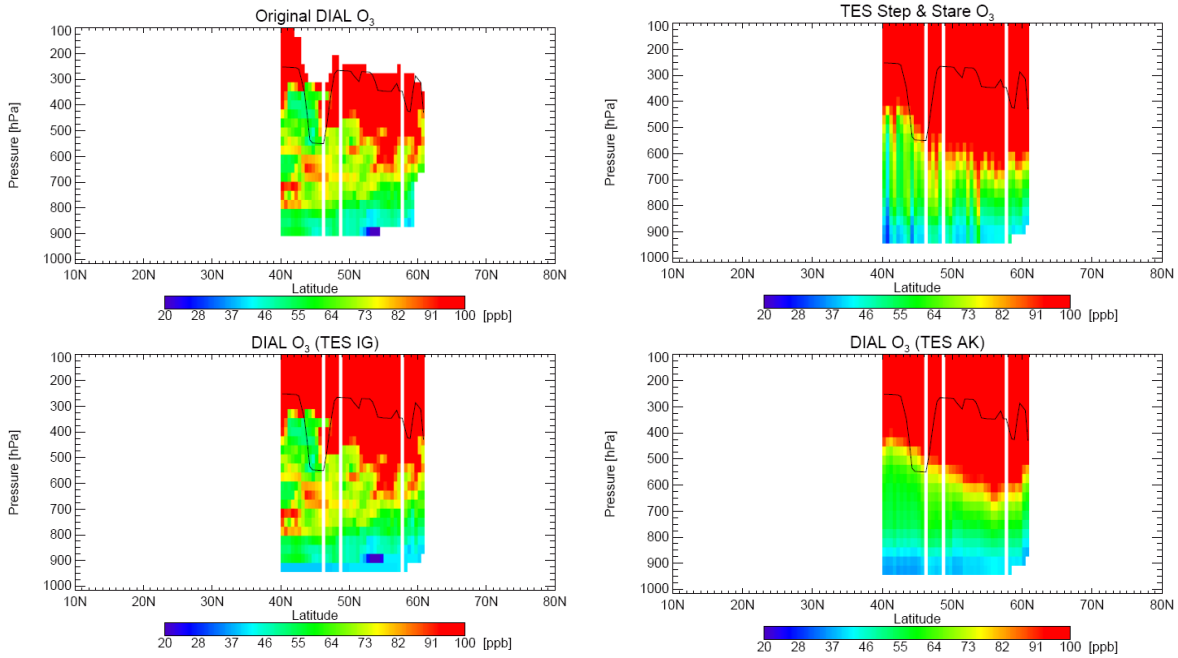

Figure 5-22 The DIAL ozone curtain as measured with the DIAL vertical resolution (upper left). The DIAL ozone curtain with the scaled TES a priori used to extend the profile (lower left). The TES step and stare curtain (upper right) and the DIAL curtain after application of the TES averaging kernel (lower right).

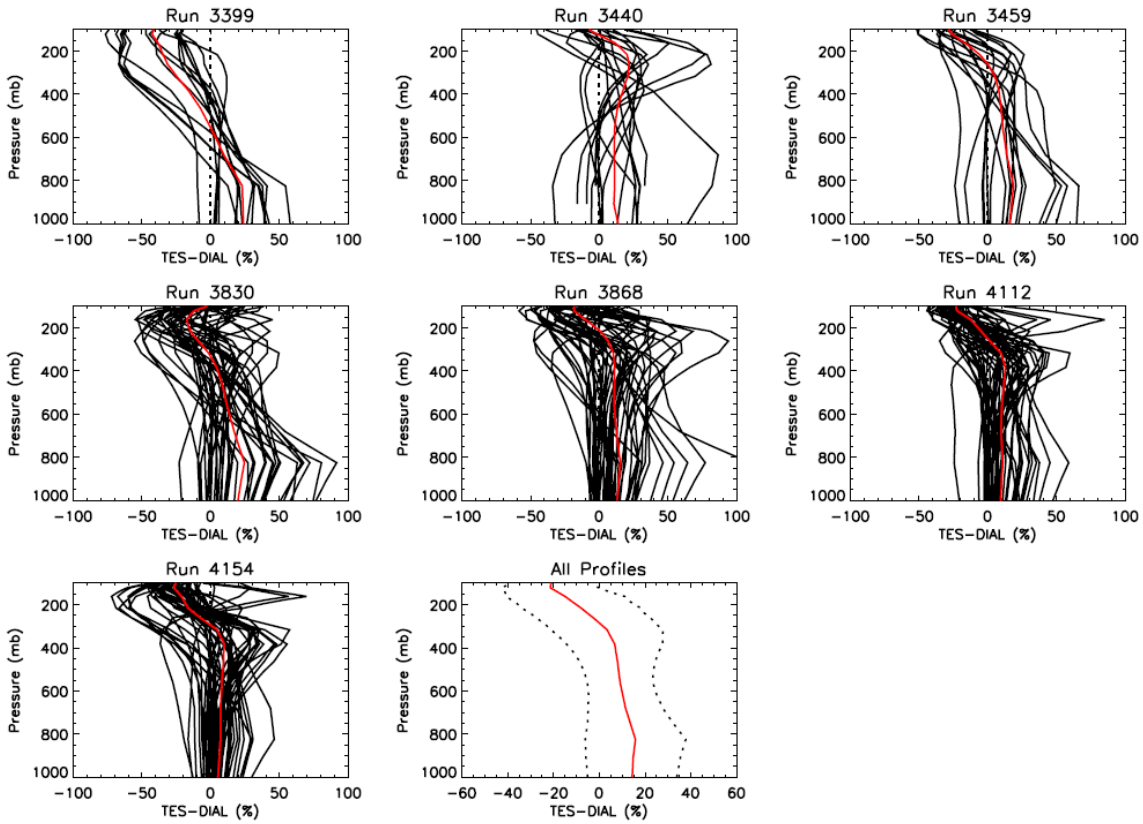

Figure 5-23 Percentage difference between TES and individual (black) and averaged (red) DIAL profiles for different TES step and stare observations. The final plot is the percentage difference between the mean of all TES and DIAL coincident profiles for the Houston based flights of INTEX-B.

5.3.3 Preliminary Conclusions

During the course of INTEX-B 212 coincident profiles were obtained for comparison, these covered the region of the Eastern and Central North Pacific and the Southern United States. A variety of conditions were observed during these observations, from relatively clean air in the Gulf of Mexico to more polluted air in the north eastern Pacific. On average TES exhibits a small positive bias in the middle and lower troposphere of 10-15% and a negative bias of up to 20% in the upper troposphere. Larger differences are observed in cleaner regions than in more polluted regions, this is likely due to the reduced signal available for TES to retrieve profile information. Some of the differences may be due to the temporal mismatch of the DIAL and TES observations since tropospheric Ozone can vary on small spatial and temporal scales.

5.4 Validation of TES Measurements of the Total Ozone Column

5.4.1 TES Total Ozone Column

TES has the measurement sensitivity required to estimate ozone through the regions of the troposphere and stratosphere where the vast majority of total atmospheric column is located. Because of this sensitivity, TES can make a determination of the total column ozone abundance.

In order to examine the quality of the total ozone measured by TES, total column ozone amounts determined by TES have been compared to data from the Ozone Monitoring Instrument (OMI) which like TES is on the NASA Aura spacecraft. The OMI data used is version 2 of the "TOMS" (Total Ozone Mapping Spectrometer) type OMI retrievals. In order to make the best comparison with TES nadir measurements, only the OMI data looking straight down were used in the comparisons. We also compare the ozone column above 100 hPa observed by TES to those measured by the Microwave Limb Sounder (MLS) on the Aura satellite. The analysis described below is basically what is presented in Osterman et al., (2007).

The analysis will focus first on TES/MLS and TES/OMI comparisons for a single "day" of TES data (actually ~26 hours) in July 2006. Then data from three time periods (January – March 2005, October 2005 and July 2006) will be used to understand the differences between column measurements made by the three Aura instruments.

5.4.2 TES – OMI, TES – MLS Comparison for July 3-4, 2006

TES values of the total ozone column are calculated using the logarithm of the retrieved ozone volume mixing ratio (VMR). The integration of the ozone profile uses log(VMR) / log(Pressure) interpolation of the profile between the TES levels (the same interpolation used in the TES retrieval process) and the TES reported air density and altitude for each profile. The column density (molecules/cm^2) can then be defined as:

$$\text{Column density} = \int VMR\rho dz = \sum_{layers} VMR_1 \rho_1 \int_{z_1}^{z_2} e^{-\alpha_{VMR}(z-z_1)} e^{-\alpha_\rho (z-z_1)} \qquad \text{(Equation 5-4)}$$

where ρ is the air density, ρ_1 and VMR_1 are the values at the bottom of the layer, and α_{VMR} and α_ρ are the exponential decay of VMR and ρ, respectively. α_{VMR} can be solved in terms of VMR_1 and VMR_2, similarly for α_ρ. When the integral is integrated and evaluated at the layer boundaries, the equation for the column is:

$$column = \sum_{layers} \frac{(x_1 - x_2)(z_2 - z_1)}{\ln(x_1 / x_2)} \qquad \text{(Equation 5-5)}$$

where

Subscripted values (1) are for the level below the layer

Subscripted values (2) are for the level above the layer

$$x = \frac{airdensity * VMR}{1 + H_2O}$$

(Note the denominator converts to "dry" air density and H_2O is the water volume mixing ratio)

$$z = altitude$$

The error for the column, as discussed in Kulawik et al., 2006), can be calculated by using the chain rule. The reported error matrix for ln(VMR) is converted to an error covariance for VMR by multiplying by the VMR. The linear VMR error matrix is converted to a column error using

the derivative of the column with respect to the VMR for each level. The equation for the column error covariance is shown in (Equation 5-6):

$$S_{column} = \sum_{i,j} VMR_i d_i S_{i,j} d_j VMR_j \qquad \text{(Equation 5-6)}$$

where d_i and d_j are the derivatives of the column with respect to the VMR at levels i and j, and $S_{i,j}$ is the error covariance matrix. This method was used for calculating all the column values described in this analysis. In the case of the TES tropospheric column values, discussed in a later section, the column values were created by integrating the TES reported profile up to the tropopause pressure provided in the NASA Goddard Space Flight Center Global Modeling and Assimilation Office (GMAO) GEOS-4 products (interpolated to the TES measurement location) (Bloom et al., 2005).

Typically, when comparing TES observations to other estimates of the chemical state of the atmosphere such as from ozonesondes, data from other satellite instruments or chemical model fields, the TES averaging kernel and a priori information must be taken into account (Luo et al., 2007, Worden et al., 2007). These initial comparisons of the TES column values to those from OMI and MLS do not take the TES averaging kernel into account. The analysis is an attempt to provide a somewhat less rigorous estimation of the bias between the TES and OMI OMTO3 products. The ideal means of doing comparisons between TES and MLS profiles in the stratosphere would be to take into account the sensitivity of the two measurements (Rodgers and Conner, 2003). This analysis provides users of TES data with preliminary information about the quality of TES ozone retrievals in the stratosphere by comparing column ozone amounts above 100 hPa with those calculated by MLS.

Figure 5-24 (a) shows TES column values calculated from ozone profiles measured during a global survey on July 3-4, 2006. Also plotted in Figure 5-24 (a) are the OMI ozone column values for the same time period. The TES and OMI data were matched in time (scans less than 10 seconds apart) and distance (typically 7-10 km). Using only the nadir data from OMI allows for the best calculation of the absolute difference in the total column in Dobson units (DU) measured by the two instruments. The absolute difference between the matched TES and OMI nadir data is shown in Figure 5-24 (b). The figure provides qualitative evidence of a high TES bias in the total column relative to OMI. The comparison for this particular global survey shows that TES column values are larger by roughly 10 DU (typically a percentage difference of between 2-5%, not shown) compared to OMI.

Figure 5-25 shows a histogram of the absolute difference (TES-OMI) between the two instruments for all matched observations from the July 3-4, 2006 global survey. The data for this 26 hour period shows a mean value for the (TES-OMI) difference of 9.7 DU with a standard deviation of 12.6 DU for 689 matched TES, OMI measurements. A histogram showing the difference between column values calculated from the TES initial guess profiles (instead of the retrieved profiles) and the matched OMI column values is given as the dashed line in Figure 5-25. The TES initial guess column has a 30.3 DU high bias relative to OMI, with a large tail in the distribution at high ozone. There is significant improvement in TES ozone column retrievals relative to the initial guess. This also indicates that anywhere in the TES retrieved profile where information is coming from the *a priori* (due to low sensitivity) that there is likely to be a positive bias in the TES reported retrieved profile, and thus total column values. Therefore, it is

very likely at least part of the positive TES-OMI is attributed to the different sensor sensitivities, especially below ~900 hPa, and not due to retrieval errors.

The data from MLS provides an excellent, thoroughly validated data set for evaluating TES measurements in the stratosphere. Calculating the column above 100 hPa insures that most of the comparisons will be of stratospheric air masses. The MLS stratospheric ozone columns (including those calculated for pressures above 100 hPa) have been validated using data from the SAGE II instrument and average difference between the two measurements is 0.5 DU (Froidevaux et al., 2007). The MLS ozone data have been compared to ozonesondes and agree to better than 1.3 DU at pressure levels at 100 hPa and above (Jiang et al., 2007). The MLS profiles were taken from v2.2 data files and quality controlled as spelled out in the MLS v2.2 Data Guide (Livesey et al., 2006) and the TES and MLS scans closest in time and then distance were matched. The scans were typically made within 400-440 seconds of one another and the distance between the reported locations varied from 8 to 215 km. Figure 5-26 (a) shows a comparison of the MLS and TES column ozone amount above 100 hPa for the July 4-5, 2006 global survey.

The difference between the TES and MLS column values (in DU) above 100 hPa are provided in Figure 5-26 (b). Looking at the TES and MLS stratospheric column values (and their absolute difference) as a function of latitude there is no suggestion of either the clear high bias or the variations with latitude seen in the difference in the TES and OMI comparisons for July 3-4. Figure 5-27 shows histograms similar to those in Figure 5-25 for the difference between the column above 100 hPa between TES and MLS (TES-MLS). Figure 5-27 shows that TES is biased high by 3.7 DU compared to MLS. Comparison of the TES initial guess column values above 100 hPa to MLS shows a mean bias of 10 DU with a standard deviation of 18.9 DU. The improvement in the bias (relative to MLS) from the TES initial guess to the retrieved column value in the stratosphere illustrates the sensitivity of TES retrievals to ozone above 100 hPa.

5.4.3 Data comparisons for January – March 2005, October 2005 and July 2006

The time periods January – March 2005, October 2005 and July 2006 provide a longer time period to examine the column ozone comparisons of TES to OMI and MLS. These time periods were selected because they were the longest periods during which all three satellite instruments had data available processed with the most recent version of the algorithms. The TES data is taken from 25 global surveys, during which nadir scans were averaged and the maximum number of scans was 1152 (January – March 2005), 3456 (October 2005) and 3408 (July 2006). The data from all the global surveys were screened for quality and matched with OMI data in a similar manner to that described in the previous section. Clouds are taken into account in the TES retrievals and are considered in the primary data quality flag that is provided with the TES data products (Osterman et al., 2007). The clouds are accounted for in the retrieval by retrieving a series of frequency dependent cloud parameters and has been shown to work well in the TES retrievals (Kulawik et al., 2006, Eldering et al., 2007), though it should be noted that the retrieval sensitivity is reduced below clouds. The difference in DU between the matched pairs was calculated and then averaged over the globe. The resulting mean bias is 9.84 DU as shown in Figure 5-28. The histogram result and the high bias of TES relative to OMI for the extended analysis time periods is very similar to the one calculated for a smaller sample in July 2006. The analysis from the previous section is repeated also for the comparison between MLS and TES column ozone above 100 hPa. The result as shown in Figure 5-29 is that TES is biased somewhat high relative to MLS in the stratosphere, similar to what was seen in the July 2006 global survey.

Figure 5-30 to Figure 5-34 are scatter plots between the matched TES, OMI and TES, MLS data binned between 60-82°N, 30-60°N, 30°N-30°S and 30-60°S respectively for the time periods of this analysis. In all cases the correlations between TES and the other Aura instruments are reasonably good. In the case of the Southern polar region (Figure 5-34) the data had to be further screened to include only ocean scenes. The retrieval of TES data over continental Antarctica is currently problematic and is under investigation and as a result we filtered the southern polar data to use only measurements over the ocean. The correlation coefficients for the comparisons from the combined time period data, as well as the bias and standard deviation for the quantities (TES-OMI) and (TES-MLS) are summarized in Table 5-1 and Table 5-2. The results show that the column quantities calculated from the TES data correlate well with the quantities from OMI and MLS with TES biased high in all cases.

Table 5-1 The table provides a summary of the bias, standard deviation and correlation of the TES total ozone column relative to the OMI data for the time period January – March 2005, October 2005 and July 2006. The difference and standard deviation values are in Dobson units.

	Number of data points	Difference in the total column ozone (TES-OMI)	Standard Deviation (TES-OMI)	Correlation Coefficient TES, OMI
All Latitudes	10795	9.840	14.305	0.9645
60-82°N	1811	8.935	16.349	0.9384
30-60°N	2271	10.262	10.904	0.9720
30°N-30°S	4289	12.124	9.4495	0.8818
30-60°S	2424	5.393	10.902	0.9702
60-82°S	551	3.925	15.258	0.9384

Table 5-2 The table provides a summary of the bias, standard deviation and correlation of the TES total ozone column above 100 hPa relative to the MLS data for the time period January – March 2005, October 2005 and July 2006. The difference and standard deviation values are in Dobson units.

	Number of data points	Difference in column ozone above 100 hPa (TES-MLS)	Standard Deviation (TES-MLS)	Correlation Coefficient TES, MLS
All Latitudes	35267	2.644	13.212	0.9335
60-82°N	6443	0.928	11.203	0.9331
30-60°N	6632	3.313	9.923	0.9203
30°N-30°S	10097	4.618	5.698	0.9116
30-60°S	7340	0.873	10.994	0.9445
60-82°S	2174	2.502	26.469	0.9595

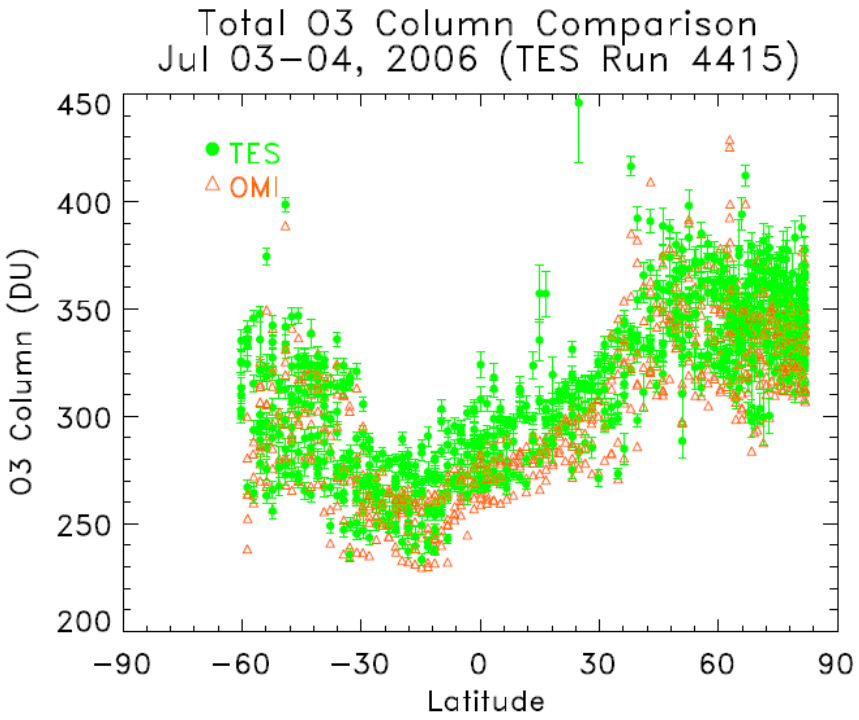

(a)

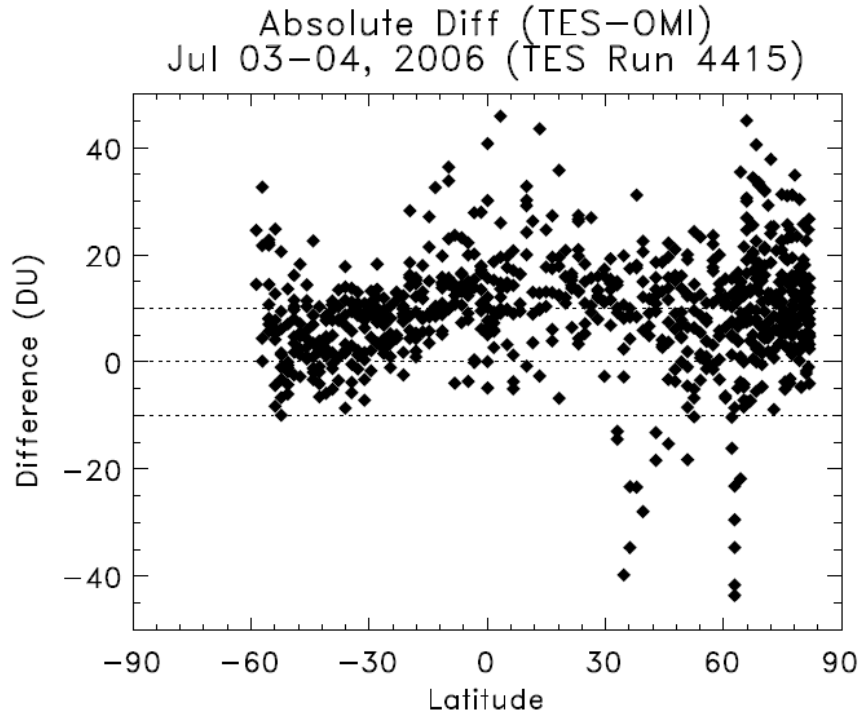

(b)

Figure 5-24 **(a)** TES and OMI total column ozone values for July 3-4, 2006 as a function of latitude. The error bars shown are the column error, as calculated using (Equation 5-6). **(b)** The absolute difference (in DU) between the TES and OMI measurements of the total ozone column as a function of latitude.

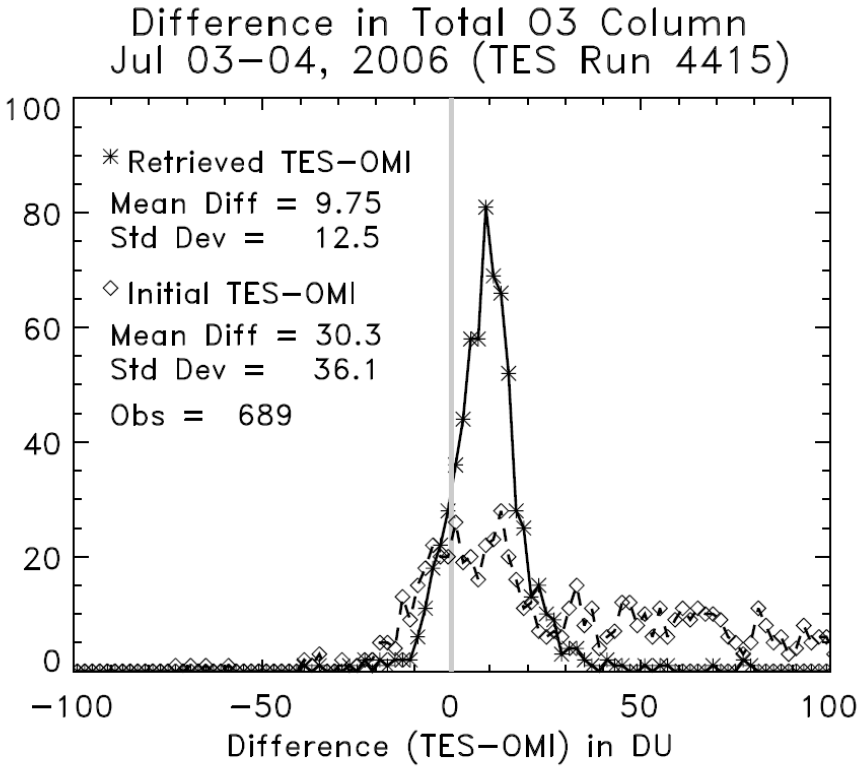

Figure 5-25 This figure shows a histogram of the absolute difference between TES and OMI column ozone data. The histogram with the solid line (*) shows that TES retrieved values for the column are biased high by nearly 10 DU. The histogram with dashed line (◊) shows difference calculated using the initial guess for the TES retrievals are biased by about 30 DU with a large tail in the distribution at large differences between initial TES value minus OMI. The improvement from the initial guess to the retrieved TES measurements suggests the TES retrieval is adding information and moving the data toward closer agreement with the OMI data.

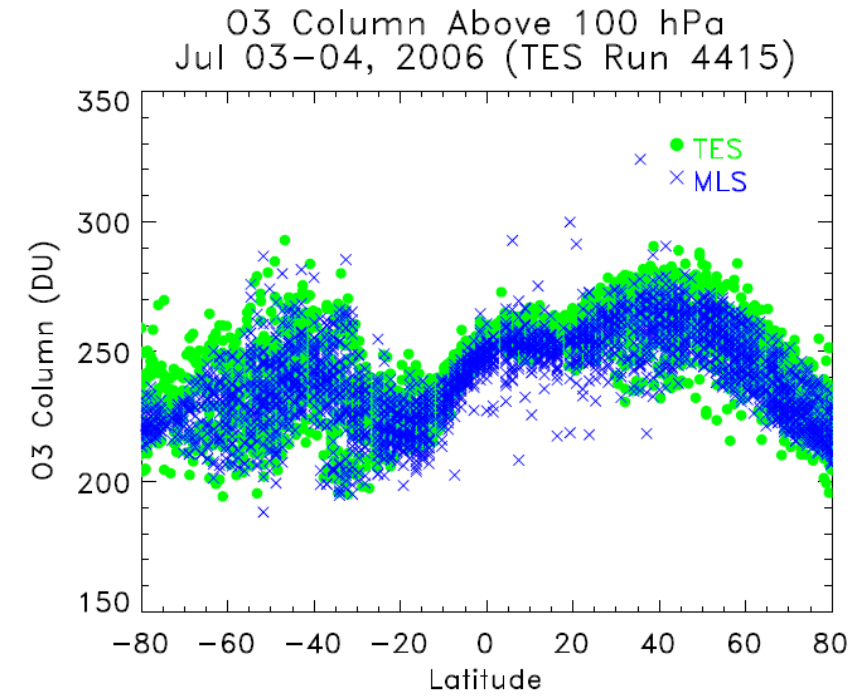

(a)

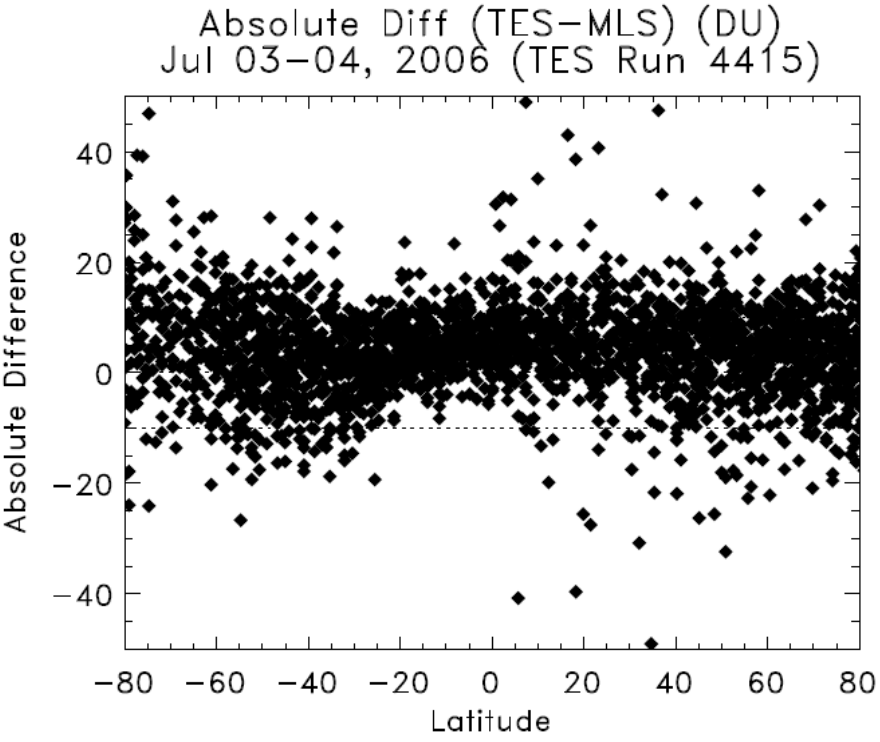

(b)

Figure 5-26 (a) The amount of ozone in the atmosphere above 100hPa as determined by TES and MLS for measurements on July 3-4, 2006. (b) The absolute difference (in DU) between the TES and MLS values for the ozone column above 100 hPa.

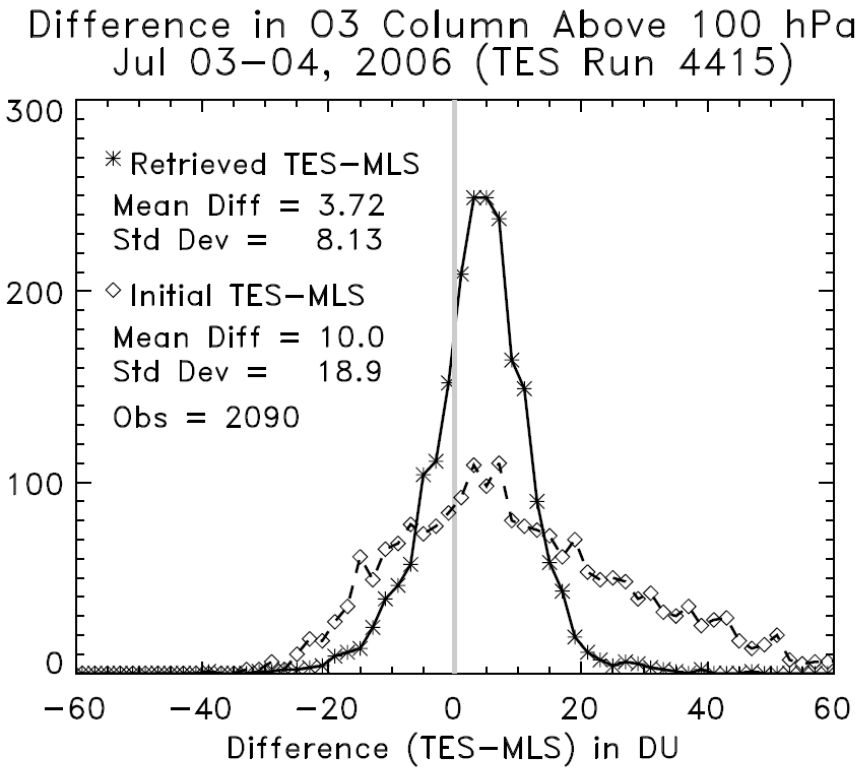

Figure 5-27 Similar to **Figure 5-25**, only showing the difference between TES and MLS column ozone above 100 hPa. The histogram with the solid line (*) shows that TES retrieved values for the column are biased high by nearly 4 DU. The histogram with dashed line (◊) shows difference calculated using the initial guess for the TES retrievals are biased by about 10 DU with a large tail. Again TES ozone column shows significant improvement over the initial guess.

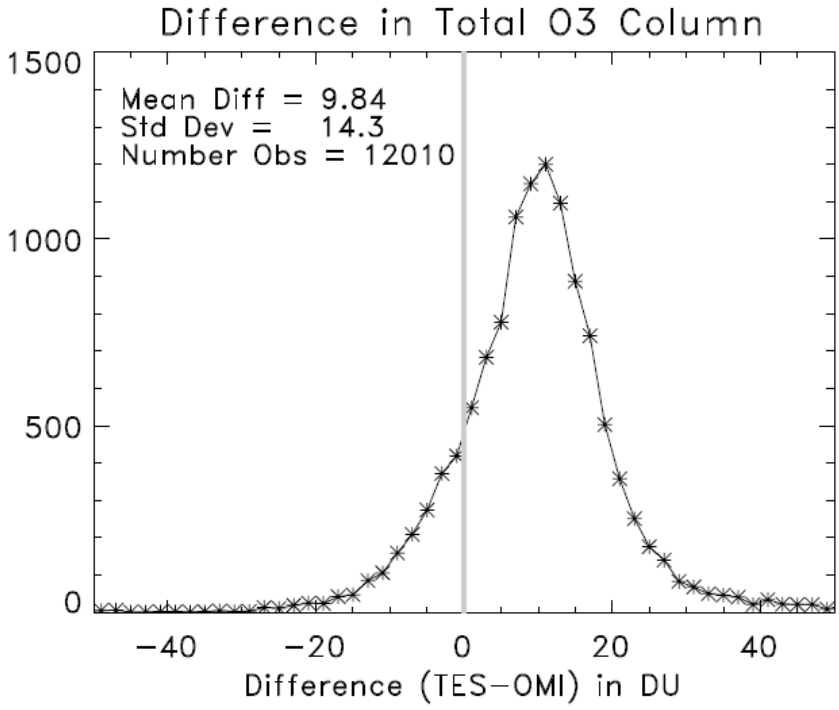

Figure 5-28 A histogram of the difference between TES and OMI for the January – March 2005 data, October 2005 and July 2006. TES is biased high by a value of 10.4 DU.

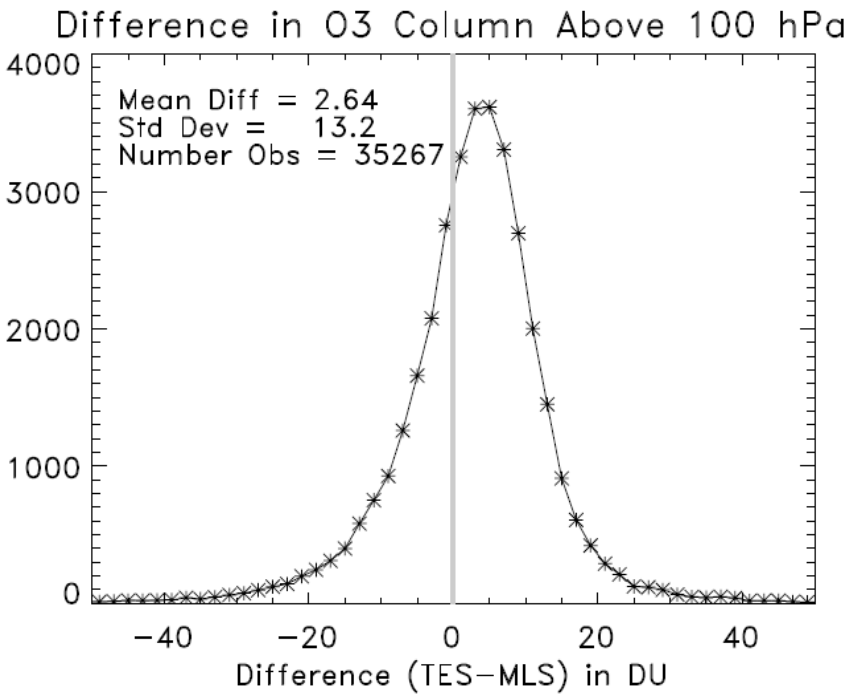

Figure 5-29 A histogram of the difference between TES and MLS for January – March 2005 data, October 2005 and July 2006. TES is biased high by a value of 2.2 DU in the stratosphere.

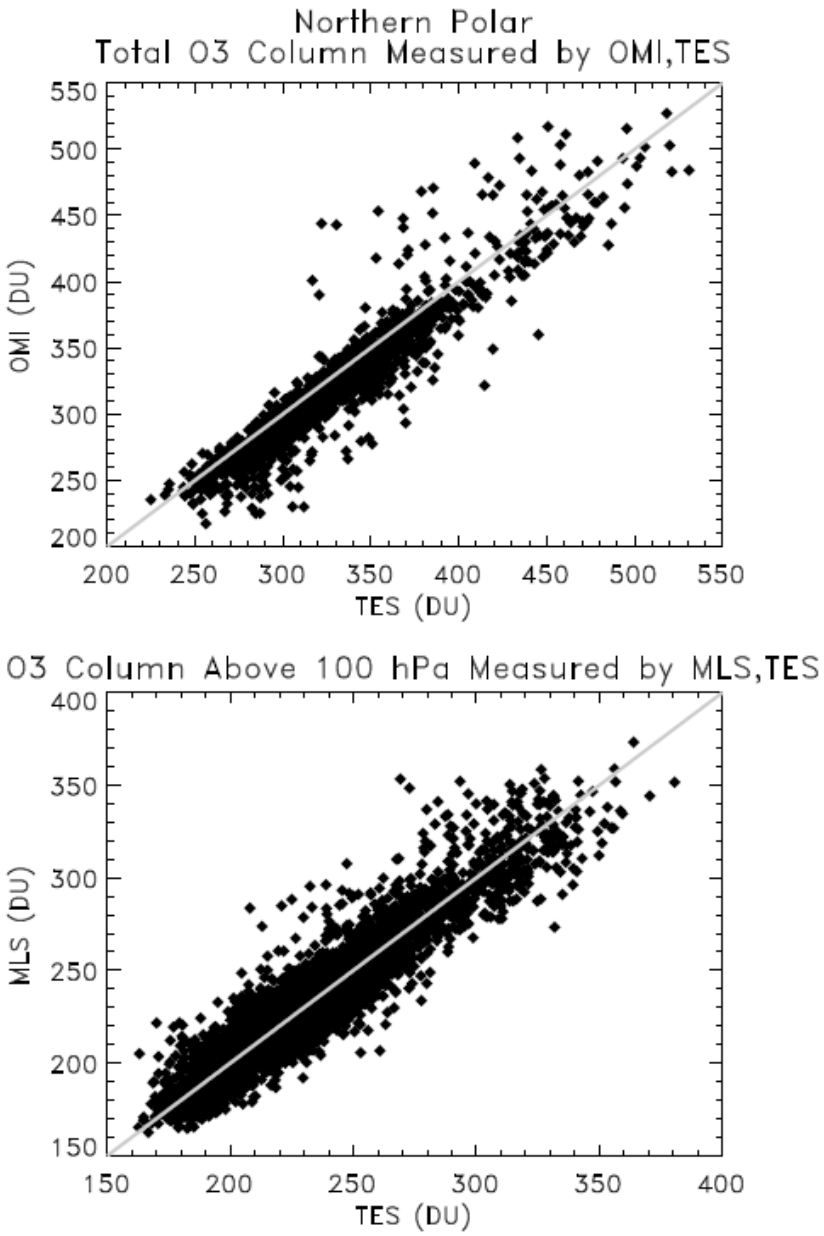

Figure 5-30 Scatter plot of the TES and OMI total column ozone values from 11 TES global surveys worth of data from January – March 2005, October 2005 and July 2006 (top). The plot shows only data from 60-82°N latitude. The correlation coefficient for this case is 0.9384. The bottom panel shows a scatter plot for the TES and MLS ozone column values above 100 hPa for the northern polar region. The correlation coefficient for the TES, MLS data is 0.9331.

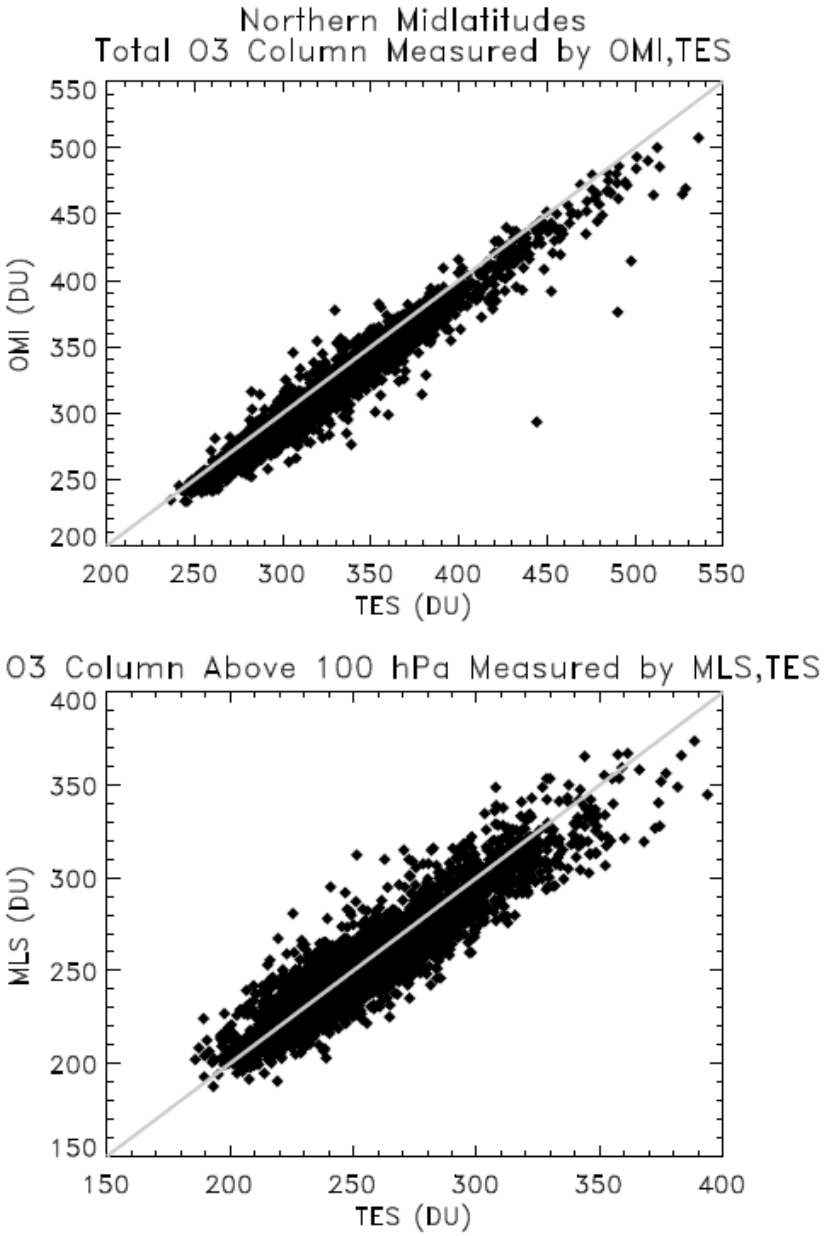

Figure 5-31 Similar to **Figure 5-30**, a scatter plot of the TES and OMI total column ozone values from 11 TES global surveys worth of data from January – March 2005, October 2005 and July 2006 (top). The plot shows only data from 30-60°N latitude. The correlation coefficient for this case is 0.9720. The bottom panel shows a scatter plot for the TES and MLS ozone column values above 100 hPa for the northern midlatitude region. The correlation coefficient for the TES, MLS data is 0.9203.

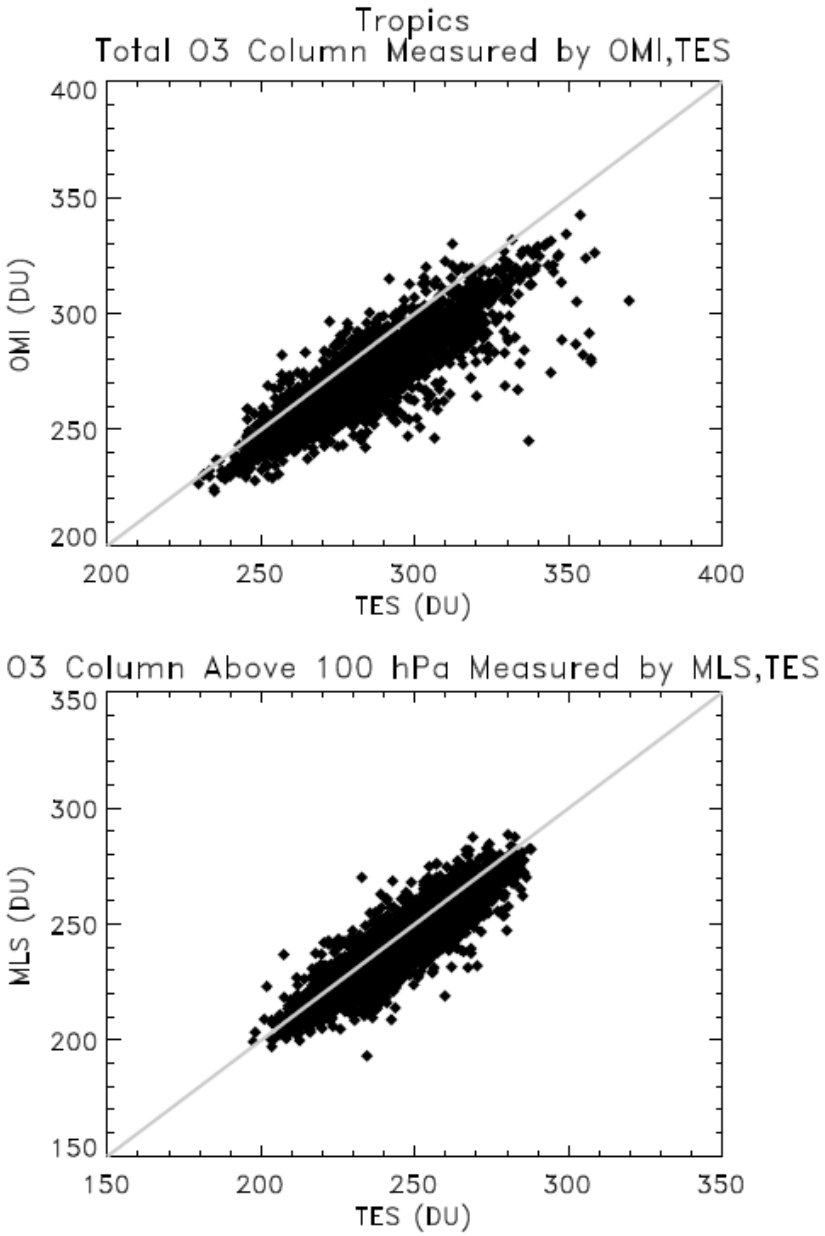

Figure 5-32 Similar to **Figure 5-31**, a scatter plot of the TES and OMI total column ozone values from 11 TES global surveys worth of data from January – March 2005, October 2005 and July 2006 (top). The plot shows only data from 30°N-30°S latitude. The correlation coefficient for this case is 0.8818. The bottom panel shows a scatter plot for the TES and MLS ozone column values above 100 hPa for the tropical region. The correlation coefficient for the TES, MLS data is 0.9116.

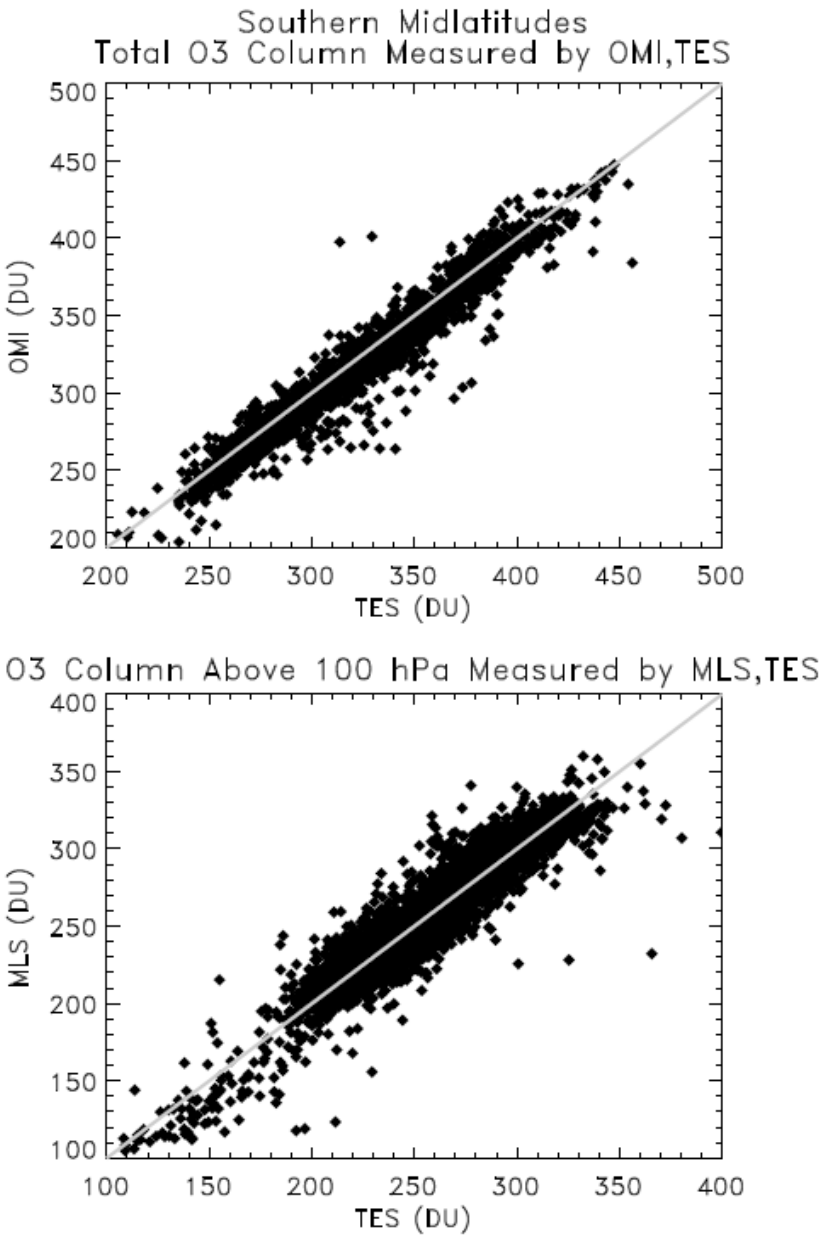

Figure 5-33 Similar to **Figure 5-32** a scatter plot of the TES and OMI total column ozone values from 11 TES global surveys worth of data from January – March 2005, October 2005 and July 2006 (top). The plot shows only data from 30-60°S latitude. The correlation coefficient for this case is 0.9702. The bottom panel shows a scatter plot for the TES and MLS ozone column values above 100 hPa for the southern midlatitude region. The correlation coefficient for the TES, MLS data is 0.9445

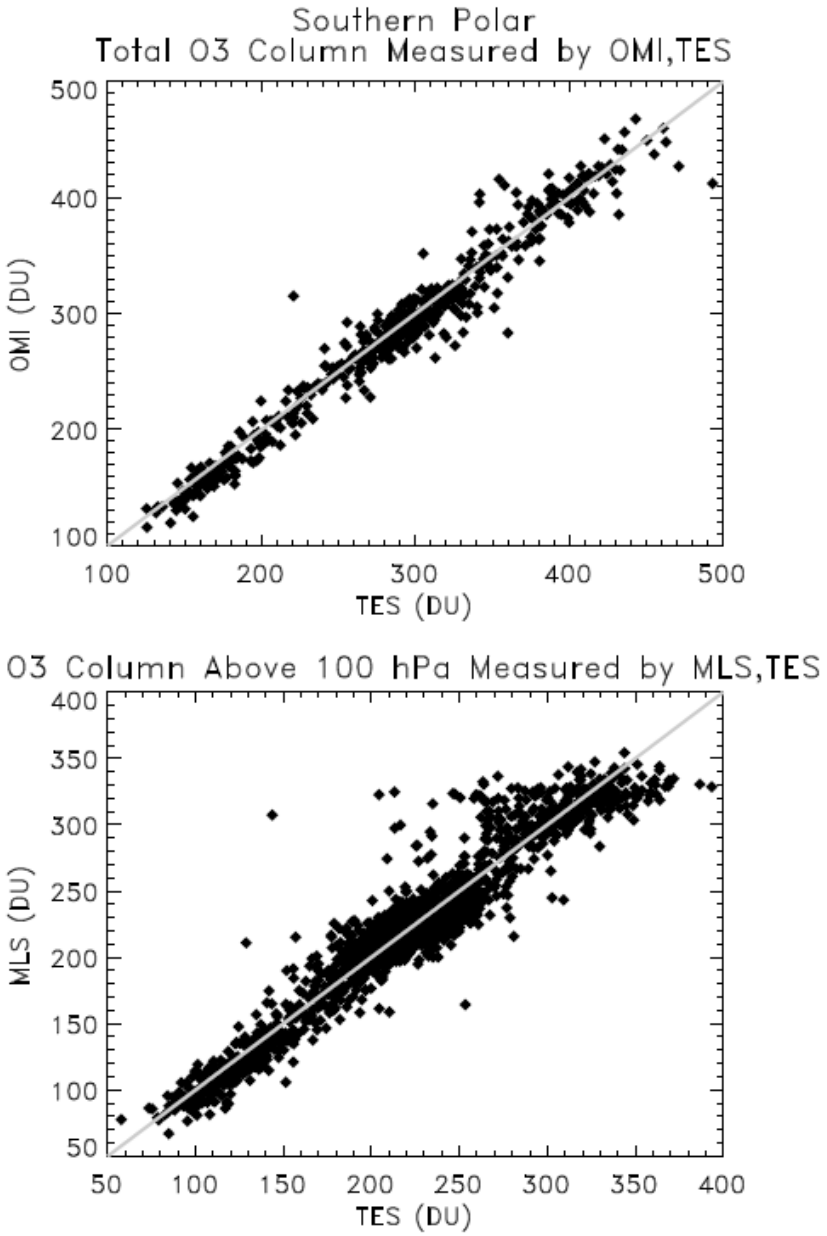

Figure 5-34 Similar to **Figure 5-33**, a scatter plot of the TES and OMI total column ozone values from 11 TES global surveys worth of data from January – March 2005, October 2005 and July 2006 (top). The plot shows only data from 60-82°S latitude. The correlation coefficient for this case is 0.9384. The bottom panel shows a scatter plot for the TES and MLS ozone column values above 100 hPa for the southern polar region. The correlation coefficient for the TES, MLS data is 0.9595. In this case the data was further screened to include only TES measurements over ocean.

5.5 References

[1] Beer, R., T.A. Glavich, D.M. Rider (2001), Tropospheric Emission Spectrometer for the Earth Observing System's Aura satellite, *Appl. Opt.,* 40, 2356-2367.

[2] Beer, R. (2006), TES on the Aura Mission: Scientific Objectives, Measurements and Analysis Overview, *IEEE Trans. Geosci. Remote Sensing*, *44* (No.5), 1102.

[3] Bloom, S., et al. (2005). Documentation and Validation of the Goddard Earth Observing System (GEOS) Data Assimilation System - Version 4. Technical Report Series on Global Modeling and Data Assimilation 104606, 26.

[4] K.W. Bowman, C. D. Rodgers, S. S. Kulawik, J. Worden, E. Sarkissian, G. Osterman, T. Steck, M. Lou, A. Eldering, M. Shepherd, H. Worden, M. Lampel, S. Clough, P. Brown, C. Rinsland, M. Gunson, R. Beer, "Tropospheric Emission Spectrometer: Retrieval Method and Error Analysis", *IEEE Trans. Geophys. Remote Sens.,* vol 44, no. 5, pp 1297-1307. May 2006.

[5] Brasseur GP, et al. (1998), MOZART, a global chemical transport model for ozone and related chemical tracers 1. Model description, *J. Geophys. Res.-Atmospheres, 103,* 28265-28289.

[6] Draxler, R.R. and Rolph, G.D. (2003), HYSPLIT (HYbrid Single-Particle Lagrangian Integrated Trajectory) Model access via NOAA ARL READY Website (http://www.arl.noaa.gov/ready/hysplit4.html). NOAA Air Resources Laboratory, Silver Spring, MD.

[7] Eldering, A. et al. (2007), Implementation of Cloud Retrievals for TES Atmospheric Retrieval – part 2: characterization of cloud top pressure and effective optical depth retrievals, *J. Geophys. Res.,* Submitted for this issue.

[8] Froidevaux, L., et al. (2007), Validation of Aura Microwave Limb Sounder stratospheric ozone measurements, *J. Geophys. Res.,* Submitted for this issue.

[9] Kulawik, S. S., et al. (2006), Implementation of cloud retrievals for Tropospheric Emission Spectrometer (TES) atmospheric retrievals: part 1. Description and characterization of errors on trace gas retrievals, *J. Geophys. Res.*, 111, D24204, doi:10.1029/2005JD006733.

[10] Jiang, Y. B., et al. (2007), Validation of Aura Microwave Limb Sounder Ozone by Ozonesonde and Lidar Measurements, *J. Geophys. Res.,* Submitted for this issue.

[11] Jourdain, L. et al. (2007), Tropospheric vertical distribution of tropical Atlantic ozone observed by TES during the Northern African biomass burning season, *Geophys. Res. Lett., 34*, L04810, doi:10.1029/2006GL028284.

[12] Levelt, P. F., et al. (2006a), The Ozone Monitoring Instrument, *IEEE Trans. Geophys. Remote Sens.*, 44(5), 1093– 1101.

[13] Levelt, P. F., et al. (2006b), Science objectives of the Ozone Monitoring Instrument, *IEEE Trans. Geophys. Remote Sens.*, 44(5), 1199–1208.

[14] Livesey N.J., et al. (2007), Validation of Aura Microwave Limb Sounder O3 and CO observations in the upper troposphere and lower stratosphere, *J. Geophys. Res.,* Submitted for this issue.

[15] Livesey, N. J., et al. (2007), EOS MLS version 2.2 Level 2 data quality and description document, *Tech. rep.*, Jet Propulsion Laboratory.

[16] Luo M., et al. (2007) Comparison of carbon monoxide measurements by TES and MOPITT the influence of a priori data and instrument characteristics on nadir atmospheric species retrievals, *J. Geophys. Res., 112*, D09303, doi:101029/2006JD007663.

[17] Nassar, R., et al. (2007), Validation of Tropospheric Emission Spectrometer (TES) Nadir Ozone Profiles Using Ozonesonde Measurements, *J. Geophys. Res.,* Submitted for this issue.

[18] Osterman, G.B. et al. (2006), Tropospheric Emission Spectrometer TES L2 Data User's Guide, version 2.00, 1 June 2006, Jet Propulsion Laboratory, California Institute of Technology, Pasadena, CA.

[19] Richards, N.A.D., et al. (2007), Validation of Tropospheric Emission Spectrometer (TES) Ozone Profiles with Aircraft Observations During INTEX-B, *J. Geophys. Res.,* Submitted for this issue.

[20] Osterman, G.B., S.S. Kulawik, H.M. Worden, N.A.D. Richards, B.M. Fisher, A. Eldering, M.W. Shephard, L. Froidevaux, G. Labow, M. Luo, R.L. Herman, K.W. Bowman (2007), Validation of Tropospheric Emission Spectrometer (TES) Measurements of the Total, Stratospheric and Tropospheric Column Abundance of Ozone, *J. Geophys. Res.,* Submitted.

[21] C. Rodgers and B. Conners, "Intercomparison of remote sounding instruments," *J. Geophys. Res.*, vol. 108(D3), p. 4119, 2003.

[22] C. Rodgers, *Inverse Methods for Atmospheric Sounding: Theory and Practice*. London: World Scientific, 2000, Hackensack, N. J..

[23] Schoeberl, M.R., et al. (2007), A Trajectory Based Estimate of the Tropospheric Column Ozone Column Using the Residual Method, *J. Geophys. Res.*, Submitted for this issue.

[24] Waters, J.W., et al. (2006), The Earth Observing System Microwave Limb Sounder (EOS MLS) on the Aura satellite, *IEEE Trans. Geosci. Remote Sens.*, 44(5), 1075-1092.

[25] Worden, H.M., et al. (2007), Comparisons of Tropospheric Emission Spectrometer (TES) ozone profiles to ozonesondes: Methods and initial results, *J. Geophys. Res*., 112, D03309, doi:10.1029/2006JD007258.

[26] Worden, J. et al. (2007), Improved Tropospheric Ozone Profile Retrievals Using OMI and TES Radiances, *Geophys. Res. Lett., 34*, L01809, doi:10.1029/2006GL027806

[27] Worden, J., S. S. Kulawik, M. Shepard, S. Clough, H. Worden, K. Bowman, and A. Goldman, "Predicted errors of Tropospheric Emission Spectrometer nadir retrievals from spectral window selection," *J. Geophys. Res*., vol. 109, no. D09308, May 2004.

[28] Ziemke, J.R., et al. (2006), Tropospheric ozone determined from Aura OMI and MLS: Evaluation of measurements and comparison with the Global Modeling Initiative's Chemical Transport Model, *J. Geophys. Res*., 111, D19303, doi:10.1029/2006JD007089.

6. Validation of TES Retrievals of Carbon Monoxide

In this section we briefly describe the TES instrument performance over two years on orbit and the effect of the optical bench warm-up conducted early Dec 2005 on filter 1A1 and the CO retrievals. A brief overview of the global distributions of TES CO measurements is given different seasons. We present comparisons of TES CO profiles with *in situ* measurements from several aircraft campaigns, including INTEX-B, AVE, and CR-AVE. Validation of TES CO data using MOPITT measurements, as well as comparisons in the upper troposphere of TES CO data to ACE (Atmospheric Chemistry Experiment) and MLS CO are shown. These comparisons not only offer good qualitative checks for TES data, *e.g.,* the characteristics of the CO global distribution or the shapes of their vertical profiles, but also offer quantitative validations of TES CO retrievals. An overview of the characterization of TES retrievals, including the roles of *a priori* profiles and the averaging kernels is also provided in this section.

TES Level 2 data are now being processed using to the F04_04 software (V003 data). In this validation report, most of the comparisons shown are for V002 data and the conclusions should are largely valid for V003 data as well. The differences in TES CO retrievals between V003 and V002 are small. The main differences are seen at high latitudes as a result of a relaxation of the a priori constraints.

6.1 Instrument performance before and after optical bench warm-up

The signal strength in TES 1A1 filter is not constant over time and the variation of the signal strength is reflected in the CO retrievals. Figure 6-1 displays the normalized integrated spectral magnitude (ISM) (top panel), beam splitter temperature (middle panel), and degree of freedom for signal (DOFS) for latitudes of 30°N-30°S as a function of time (Rinsland et al., 2006). The ISM is a sensitive indicator of the signal levels of the TES detectors and is calculated by integrating a spectrum over wavenumber. It is the primary quantity used to quantify and detect trends in the TES instrument alignment and performance. An overall trend of declining ISM with time and the measured beamsplitter temperature is apparent, with increases in beamsplitter temperatures when the detectors are de-iced periodically. The warming of the TES optical bench on November 29-December 2, 2005 improved the TES beamsplitter alignment, with an integrated spectral magnitude increase for the 1A1 filter by a factor of 3.4 as compared to the pre-warm up value.

Figure 6-2 shows the DOFS before and after optical bench warm-up. The average DOFS between 30°N-30°S was 0.72 prior to the TES optical bench warm up and then increased to 1.45 after the warm up. The latitudinal distributions of DOFS reflect the latitudinal distribution of the surface temperature. TES measurement signal to noise ratios are larger for scenes with higher surface temperatures, *e.g.,* tropics. In the high latitudes or for the scenes covered with clouds, TES CO profile retrievals have relatively less values.

Figure 6-3 illustrates the improvement in total retrieval error and the retrieval precision for TES CO at 511 hPa. In 30S – 30N, the averaged total error was reduced from 19 ppb to 11ppb, and the precision values were reduced from 10 ppb to 5 ppb.

In summary, TES retrievals of carbon monoxide are much improved after the optical bench warm up in early December 2005 as a result of the better alignment of the instrument and increased signal to noise.

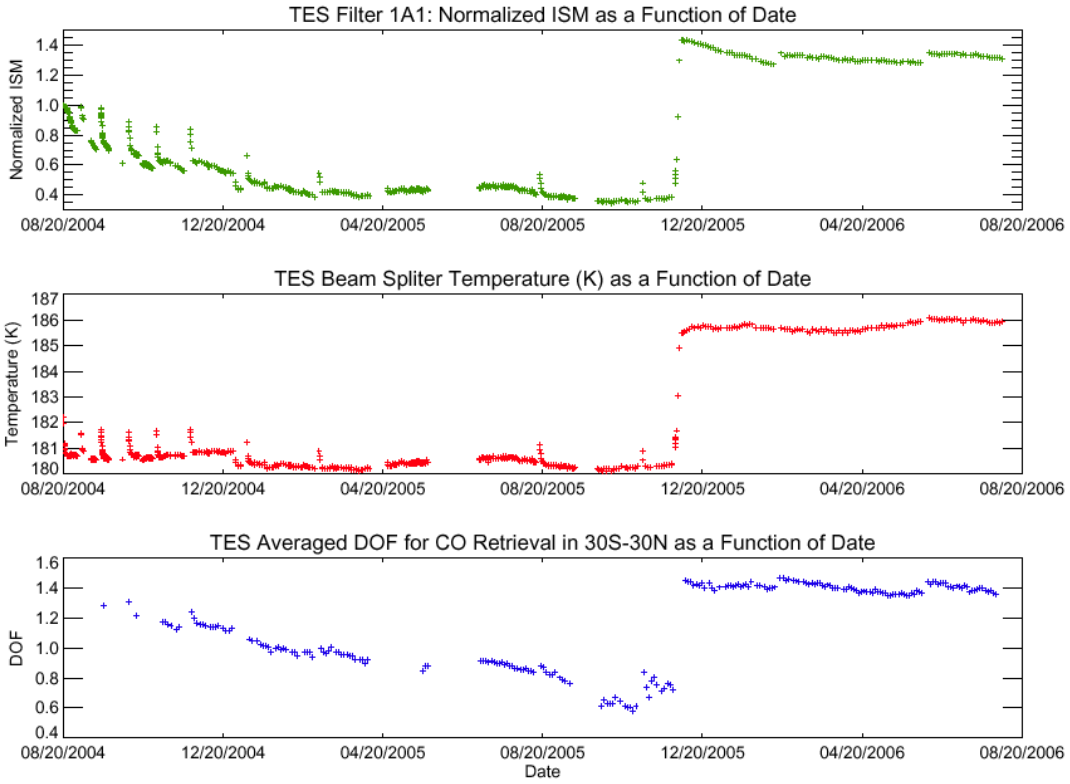

Figure 6-1 Time series of measured normalized Integrated Spectral Magnitude (ISM) (top panel), beamsplitter temperature (middle panel), and average DOFS for 30°N-30°S latitude. The ISM is normalized to 1.0 at the beginning of the time series. The ISM values stay stable for 2007.

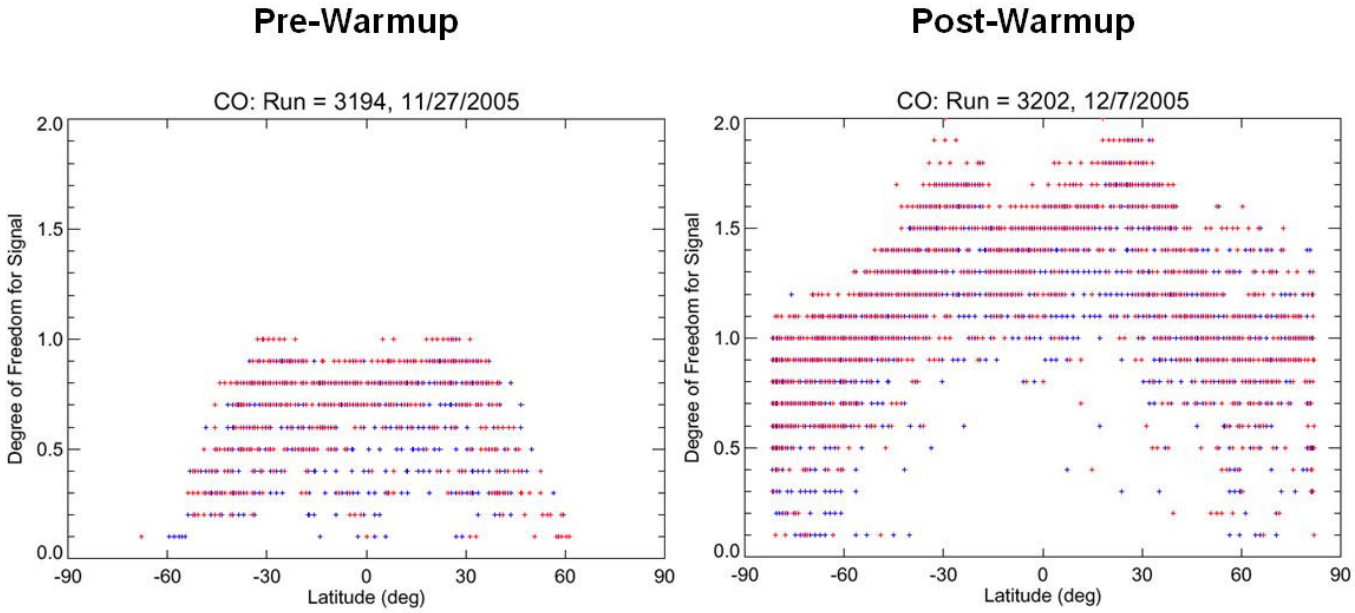

Figure 6-2 Latitudinal distributions of the degrees of freedom for signal (DOFS) of the TES CO retrievals for two global survey runs pre- and post optical bench warm up.

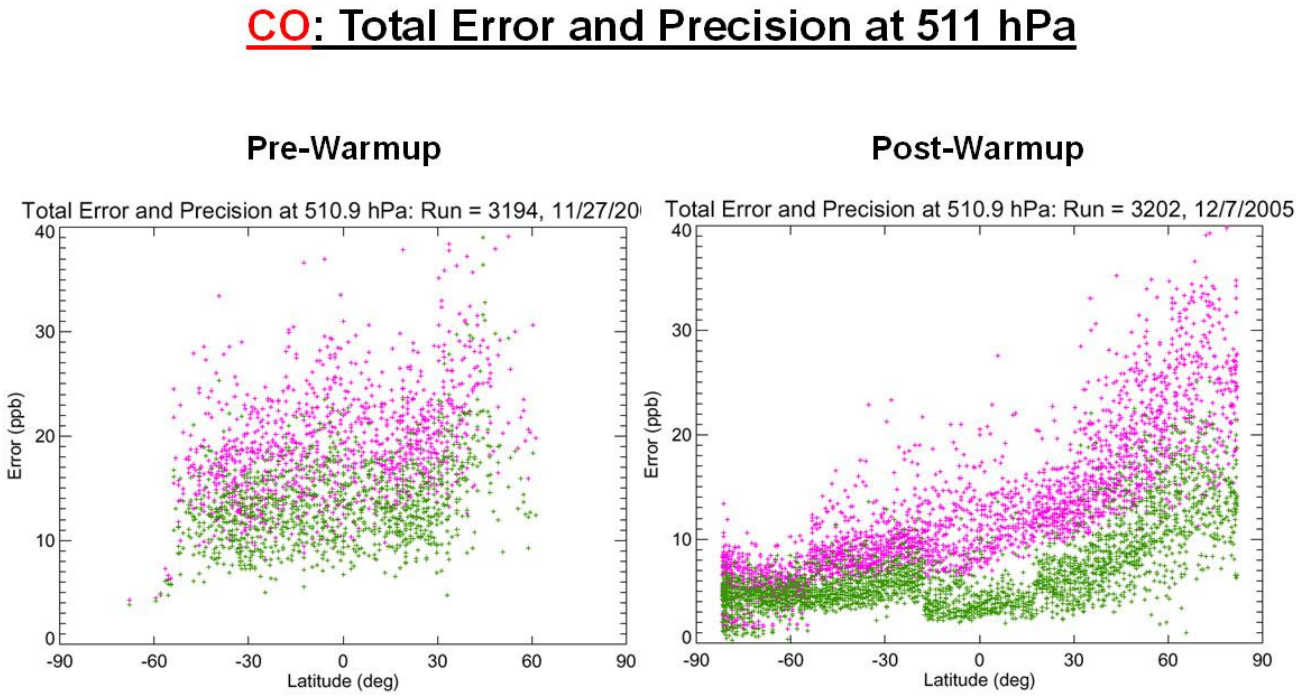

Figure 6-3 Latitudinal Distributions of the Total Errors and The Precisions for TES CO Retrievals in Two Global Survey Runs of Pre and Post Optical Bench Warm-up.

6.2 V003 vs V002

The major algorithm change for TES CO retrieval in V003 is the change of the a priori constraints in the high latitude bands, 54N-90N and 54S-90S. The constraints applied for these two latitude bands are now the same for those in 18N-54N and 18S-54S respectively; the change results more relaxed constraints compared to the values used for V002. The more relaxed constraints mean that the influence of the a priori profiles on the retrieved CO results can be less significant. This is illustrated in Figure 6-4 for the monthly means and 6-5 for a global survey. In Figure 6-4, TES CO in the northern high latitudes show larger variability and away from the a priori field (not shown). Figure 6-5 illustrates extra enhanced CO at high southern latitudes in V003 data compared to those in V002 data. The enhanced CO in this case is believed due to known Australian fires.

The two figures also illustrated that in the lower and mid-latitudes, there is very little difference between V003 CO and V002.

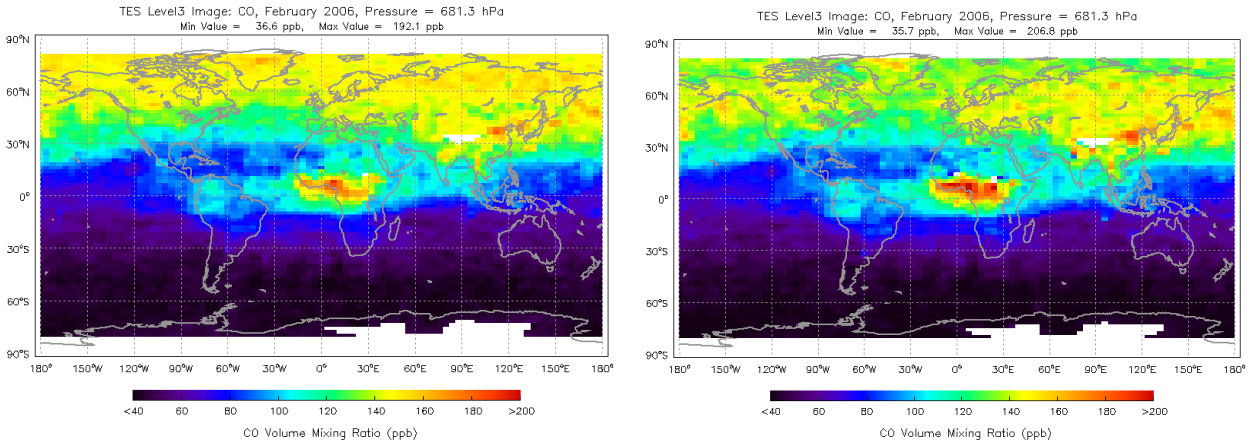

Figure 6-4 Comparison of TES CO data V003 (right) and V002 (left). Images are TES CO monthly means for February 2006 at 681.3 hPa.

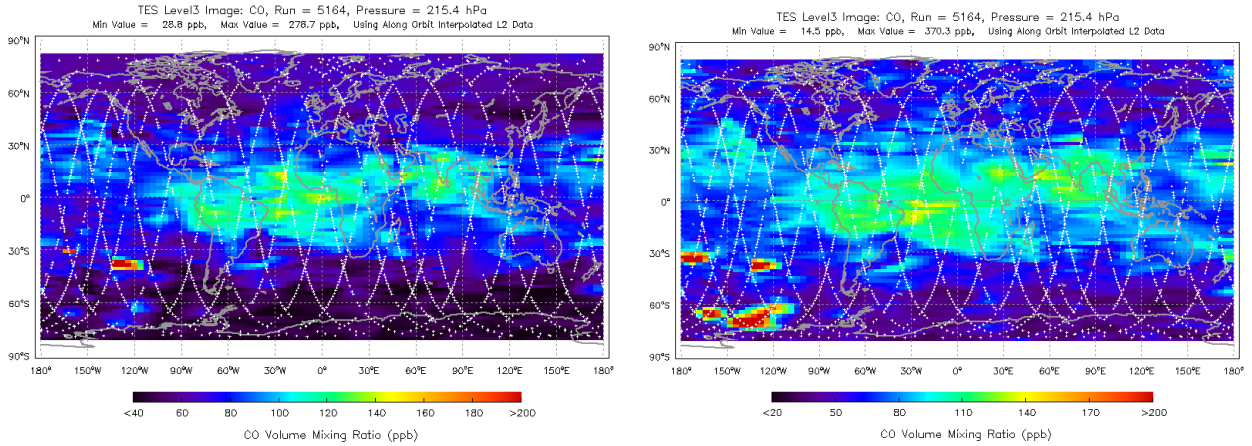

Figure 6-5 Comparison of TES CO data V003 (right) and V002 (left). Images are the horizontally interpolated TES CO values for Global Survey, Dec 16-17, 2006 at 215.4 hPa.

6.3 Global distributions of CO from TES measurements

Carbon monoxide is a by-product of incomplete combustion of fossil fuels and biomass, and is produced by oxidation of methane (CH_4) and other hydrocarbons. The global distributions of TES CO fields reflect this basic understanding, e.g., the enhanced CO regions and their seasonal variations are co-located with the known source regions. Figure 6-6 shows TES CO monthly mean distributions at 681.3 hPa for January, April, July and October 2006 (V003 data). In general, the northern hemispheric (and the tropics) show much more CO than the southern hemisphere due to the known distribution of natural and industrial sources. CO values in the winter/spring are larger than summer/fall due to the longer lifetime in seasons with less photochemical activity.

In central Africa, the enhanced CO corresponding to biomass burning occurs in two time periods, in Dec/Jan/Feb for latitudes north of the equator and in Jul/Aug/Sep south of the equator, corresponding to the local dry seasons. In South America, the biomass burning induced maximum in CO concentration occurred during Aug/Sep/Oct near equator. Enhanced levels of CO over E. China can be related local pollution and can be seen throughout the year in the TES observations. TES also observed enhanced CO over Siberian in July 2006 which is associated with the fire occurred in the last ten days of July as reported by the MODIS Rapid Response System (http://rapidfire.sci.gsfc.nasa.gov/gallery/?2006203-0722

and http://rapidfire.sci.gsfc.nasa.gov/gallery/?2006205-0724). The enhanced CO over Indonesian in Sept/Oct/Nov 2006 are due to intense fires under the very dry condition in a moderate El Nino period (Logen et al., 2007).

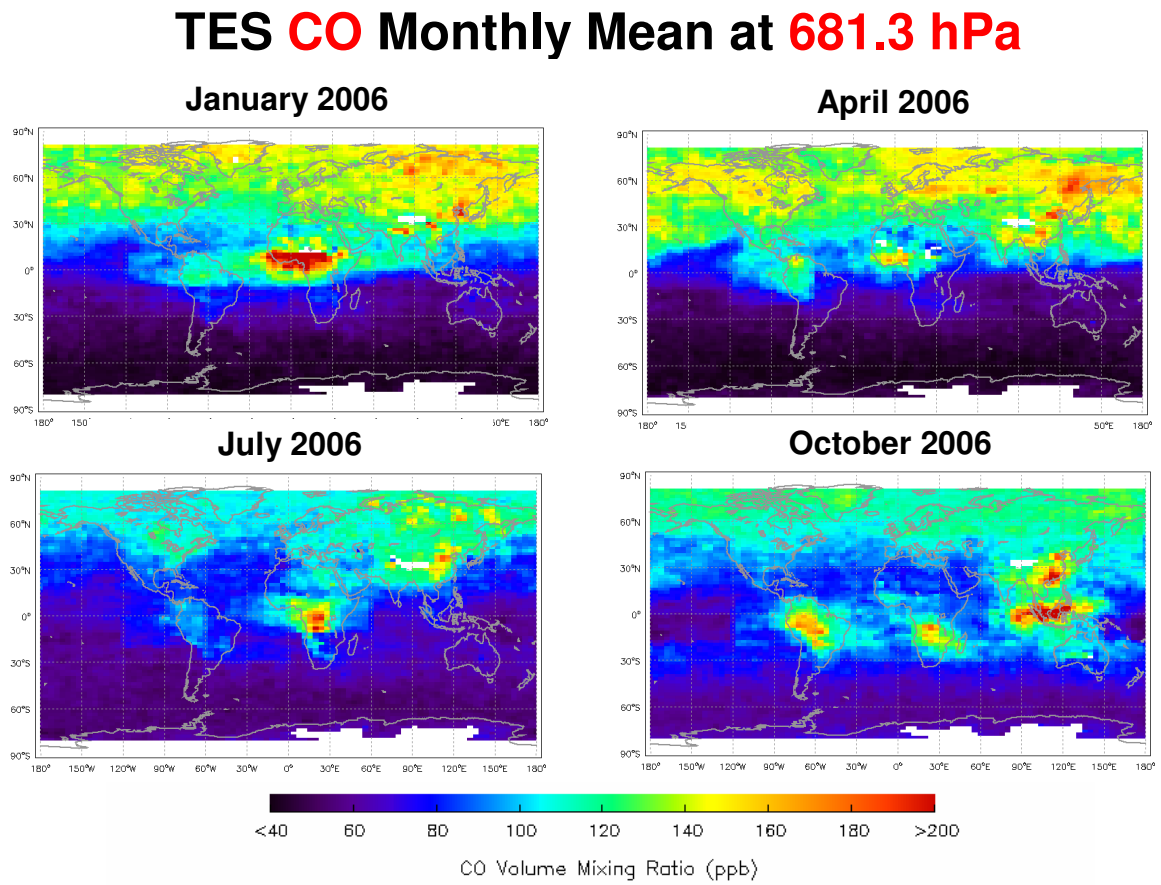

Figure 6-6 TES CO Global Distributions at 681.3 hPa for the Four Typical Months, Jan, April, July and October 2006.

6.4 CO validation: Comparisons to *in situ* Aircraft Measurement

During 2004-2006, several aircraft campaigns were conducted to study tropospheric chemistry and transport and to provide data for validation of the measurements made by the instruments on the Aura satellite. The TES team participated in the Aura Validation Experiment (AVE)

campaigns: Oct-Nov 2004 based near Houston, Jan-Feb 2005 based in Portsmouth, NH (PAVE), and in Jan-Feb 2006 based in Costa Rica (CR-AVE). TES also participated INTEX-B (International Chemical Transport Experiment) based which had deployments in Houston, Honolulu and Anchorage in March-May 2006. The TES CO data from the time periods of theses campaigns are compared with the *in situ* measurements for the aircraft flights when there are the best coincidences between TES measurement location and the aircraft CO profiles.

6.4.1 Comparisons to Argus CO Data in October-November 2004 AVE Aircraft Campaign

During the October-November 2004 AVE mission based in Houston, TX, TES made a series of step and stare nadir observations between equator and 60°N. TES CO validations using the in-situ measurements by the Argus instrument are documented in Lopez et al (2007).

In five days of aircraft flights, a total of 18 Argus CO profiles are compared with 4-6 TES CO profiles for each of them. As a standard process, the aircraft CO profiles are adjusted with applying TES a priori and averaging kernel profiles before comparing to the TES retrievals. Figure 6-7 shows the summary of the comparisons. On average, the TES CO in the mid troposphere is about 10% lower within TES retrieval errors and equivalent to CO spatial/temporal variability detected in both TES and Argus measurements.

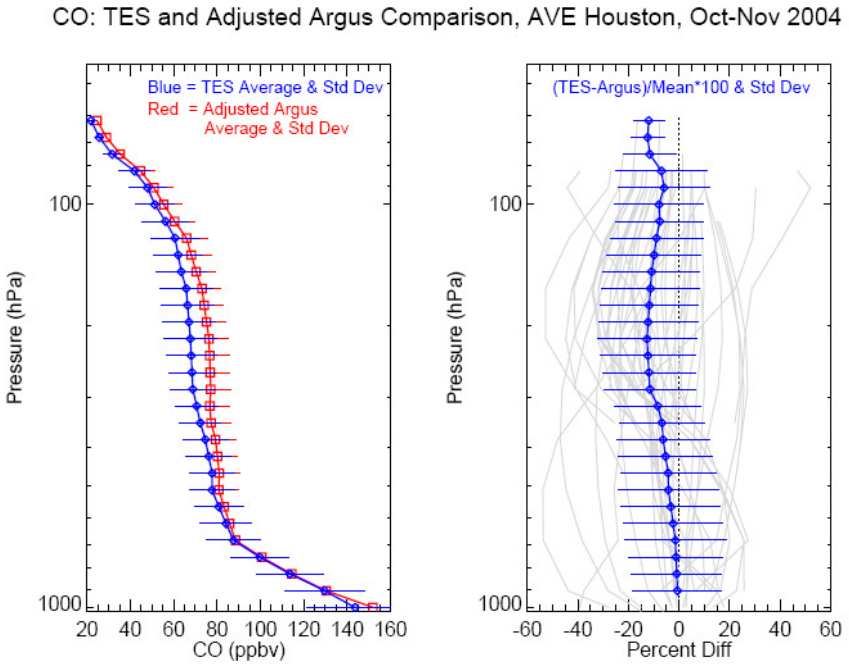

Figure 6-7 Averaged and the percent differences between TES and Argus CO Profiles from all Five Days of Measurements during AVE-04 WB-57 Campaign.

6.4.2 Comparisons to ALIAS CO Data in Jan-Feb 2006 CR-AVE Aircraft Campaign

The Aura Validation Experiment campaign in early 2006 was conducted from Costa Rica (CR-AVE). In addition to science objectives for the campaign, most WB-57 aircraft flights were planned for validations of the Aura measurements near tropical tropopause layer (TTL). The CO profiles measured by Aircraft Laser Infrared Absorption Spectrometer (ALIAS) and the Argus instrument during the take-offs and landings are compared to the TES CO profiles nearest to the airport. Most *in situ* measurements near the airport were far away from the TES footprints and the time differences were > 1 hr, and some of the comparisons were for next day. Total of 11 ALIAS profiles and 7 Argus profiles are used to compare to the TES CO profiles Most of the TES measurements were in near clear sky with effective cloud OD <0.1 and DOFs ~ 1.5. The results of these comparisons and the comparisons between the two aircraft measurements are documented by Lopez et al, 2007.

Figure 6-8 shows the averaged TES- ALIAS CO profile comparisons and the statistics. The two averaged CO profiles agree within 10% with TES being larger. The variability of the CO fields in the region from the two measurements is ~20%, in agreement with TES retrieval errors.

Figure 6-9 shows the averaged TES- Argus CO profile comparisons and the statistics. The two averaged CO profiles agree within 10% with TES being larger. The variability of the CO fields in the region from the two measurements is ~20%, in agreement with TES retrieval errors.

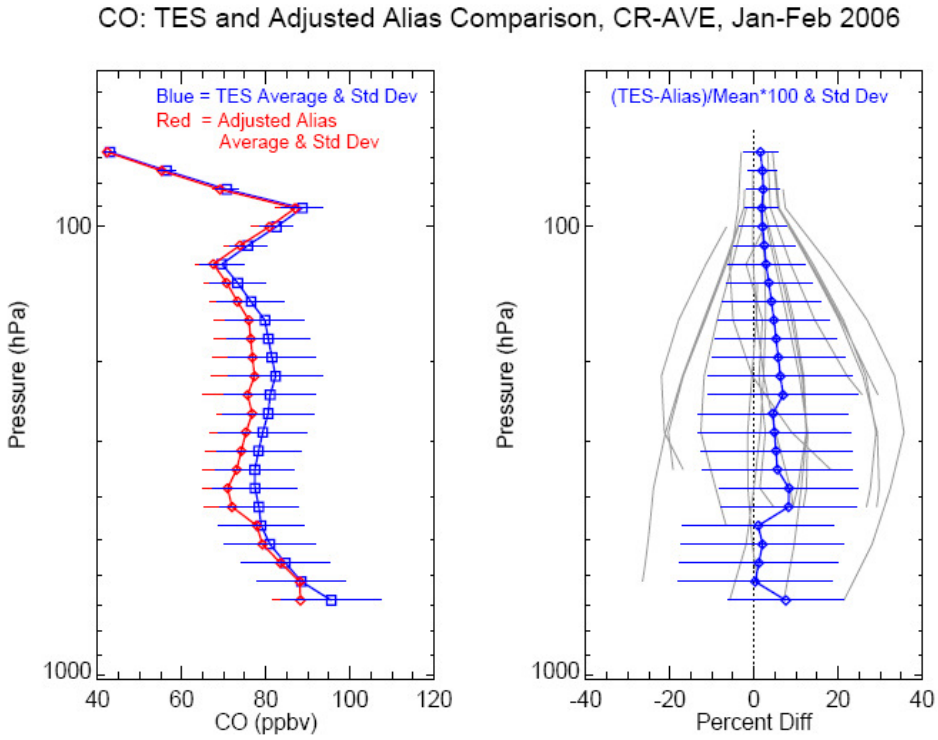

Figure 6-8 The Averaged CO Profiles of TES and ALIAS (Left Panel) and the Averaged Difference between TES and ALIAS CO Profiles (Right Panel).

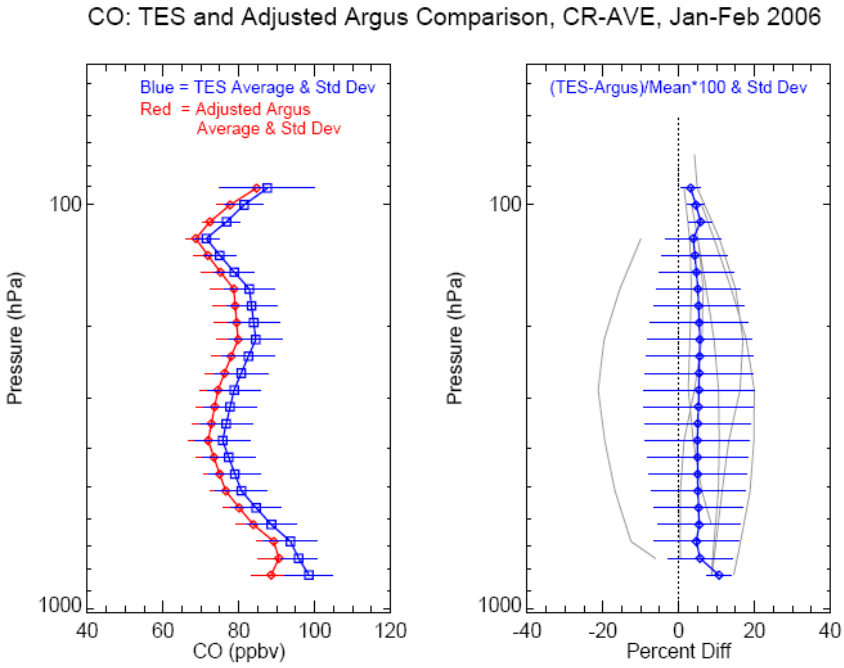

Figure 6-9 The Averaged CO Profiles of TES and Argus (Left Panel) and the Averaged Difference between TES and Argus CO Profiles (Right Panel).

6.4.3 Comparisons to DACOM CO Data in March-May 2006 INTEX-B Aircraft Campaign

During the INTEX-B campaign the DC-8 aircraft was flown out of Houston, Honolulu, and Anchorage. Many DC-8 flight plans were designed to include spirals near TES step and stare nadir observation footprints in order to provide opportunities for validation of TES carbon monoxide and ozone profiles. The total number of aircraft CO profiles collected by the NASA Langley Research Center DACOM instrument that are suitable for validation of TES CO measurements (0-100 km to the TES footprints) is 9 for Houston, 10 for Hawaii, and 1 for Anchorage. The TES CO validations with the DACOM data are documented in Luo et al., 2007b. TES V003 data are used.

Similar to previous comparisons of TES and aircraft *in situ* measurement of CO, we select 1-4 TES profiles closest to DACOM CO profiles, interpolate the DACOM profile to the TES pressure levels, extend the DACOM profile up and downward by scaled TES *a priori* profile, apply the TES averaging kernel and *a priori* to the DACOM profile, and calculate the differences between TES and the adjusted DACOM CO profiles. Figure 6-10 and Figure 6-11 show the summary of TES and DACOM CO profile comparisons for the Houston phase in March 2006. The correlation plots in Figure 6-10 include comparison for all coincident TES profiles, at all appropriate pressure levels and indicate the good agreement between TES and DACOM CO profiles with correlation coefficient of 0.87. If only a single TES profile is considered with its geolocation closest to the averaged DACOM locations, the correlation coefficient improved to 0.94. Figure 6-11 shows the comparisons of the averaged TES and DACOM CO profiles and their differences The difference between the averaged TES and DACOM profiles is much smaller than the variability in the measurements of the two instruments. The results of TES CO

being lower than the DACOM measurements by up-to 10% are in good agreement with the TES CO validation results of AVE-Oct 2004 in Houston area (6.4.1).

The comparisons of TES and DACOM CO measurements during INTEX-B Hawaii and Anchorage periods do not appear to be as good as those from the Houston flights. For example, the correlation coefficient between TES and DACOM profiles was only 0.55 in Hawaii and even worse for the Anchorage flight. Examination of the individual profiles of the DACOM *in situ* measurements indicate large CO values observed in vertical layers of the flight profiles. This is consistent with the understanding of sources of the CO plumes of and the transport patterns over Pacific Ocean in the spring. TES CO daily maps show much more variability in CO near Hawaii than seen near Houston in March. The large variability in the CO fields and the distance between the TES measurement location and the aircraft make comparisons more difficult for the Hawaii and Anchorage deployments.

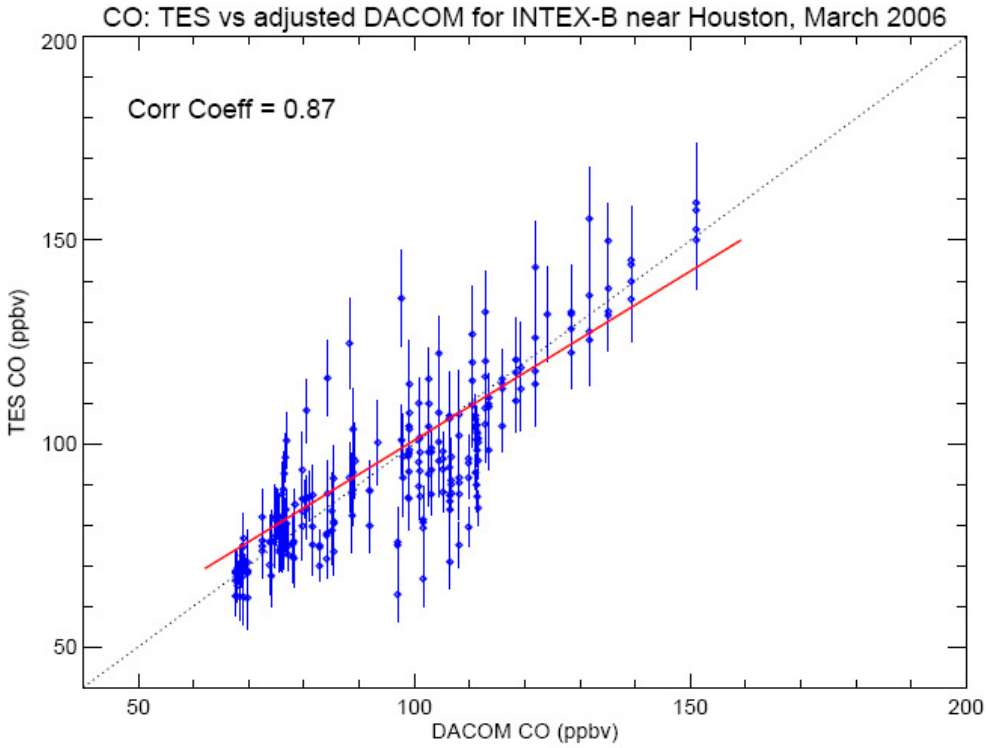

Figure 6-10 The Correlation Plot for TES and DACOM CO Profiles. Data are taken during 1st phase of INTEX-B campaign near Houston, March 2006.

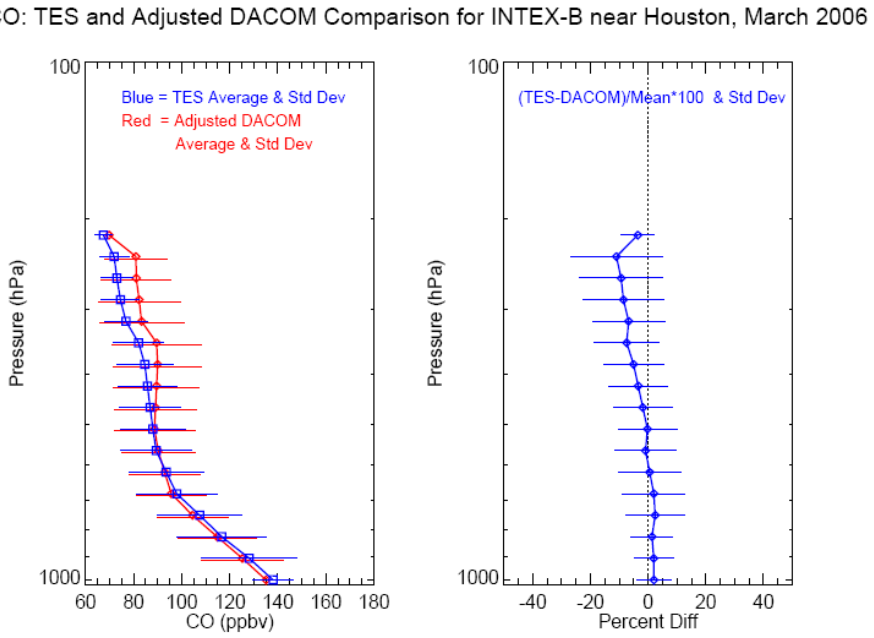

Figure 6-11 The average profiles of TES and DACOM are overlaid (left) and the averaged different between TES and DACOM CO profiles (right).

6.5 CO validation: comparisons to MOZAIC data set

The MOZAIC program (Measurements of Ozone and water vapor by In-service AIrbus aircraft, http://mozaic.aero.obs-mip.fr) collects CO *in situ* measurement during aircraft departure and arrival flight paths in many of the airports worldwide. Initially, measurements of CO made by MOZAIC aircraft from September 2004 to May 2005 are used for TES validation. Figure 6-12 shows the locations of the airports in the MOZAIC program and those with data used for TES CO comparisons.

For each airport and MOZAIC CO profile, all TES CO retrieved profiles within 250 km and within 24 hours are identified. Similar to the methods described in the previous section, the MOZAIC CO profiles were adjusted using the TES averaging kernel and *a priori*. Figure 6-13 through Figure 6-15 give results for comparisons between TES and MOZAIC profiles at the Munchen airport.

Table 6-1 gives summary of all comparisons for all MOZAIC locations. For most airports, TES and the adjusted MOZAIC profiles agree well. The best agreement is seen in European cities and cities with lower amounts of CO pollution. Those comparisons with poorer agreement are from cities known to be highly polluted and that are associated with larger variability in the CO profiles. We found that TES is generally lower (<10%) than MOZAIC at all pressures in most comparisons. Note that the time period for these comparisons is before the TES optical bench warm up that resulted in improved CO retrievals. Further comparisons between TES and MOZAIC CO data will be performed when the MOZAIC data become available.

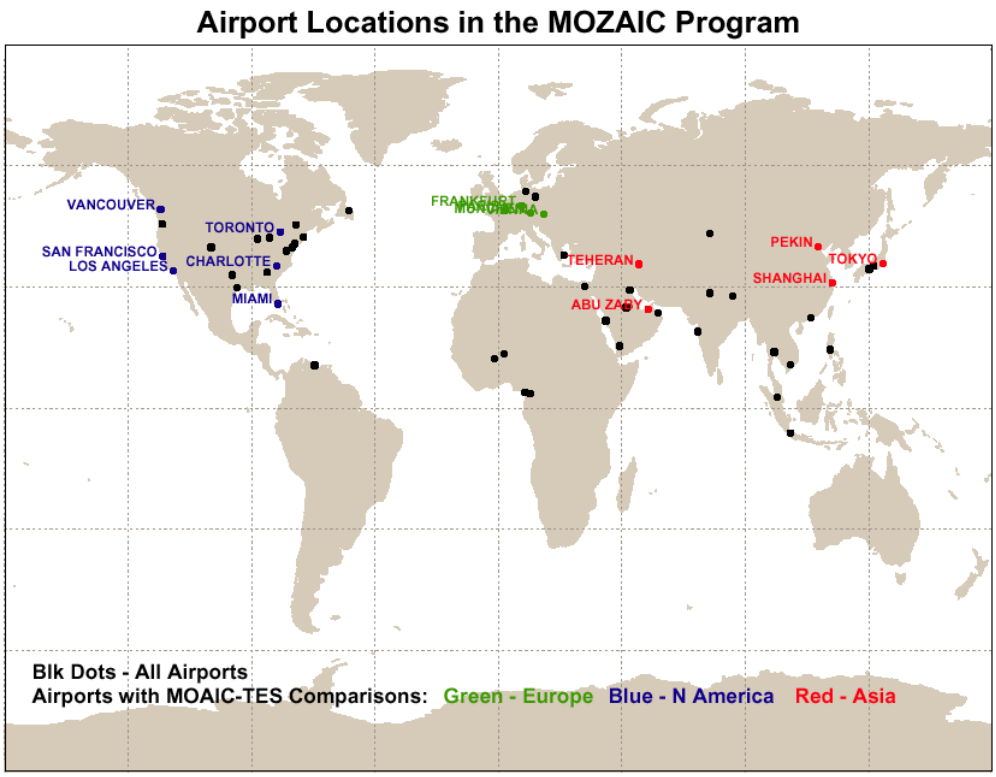

Figure 6-12 Airport Locations in the MOZAIC Program. The colored locations are those having TES coincidences.

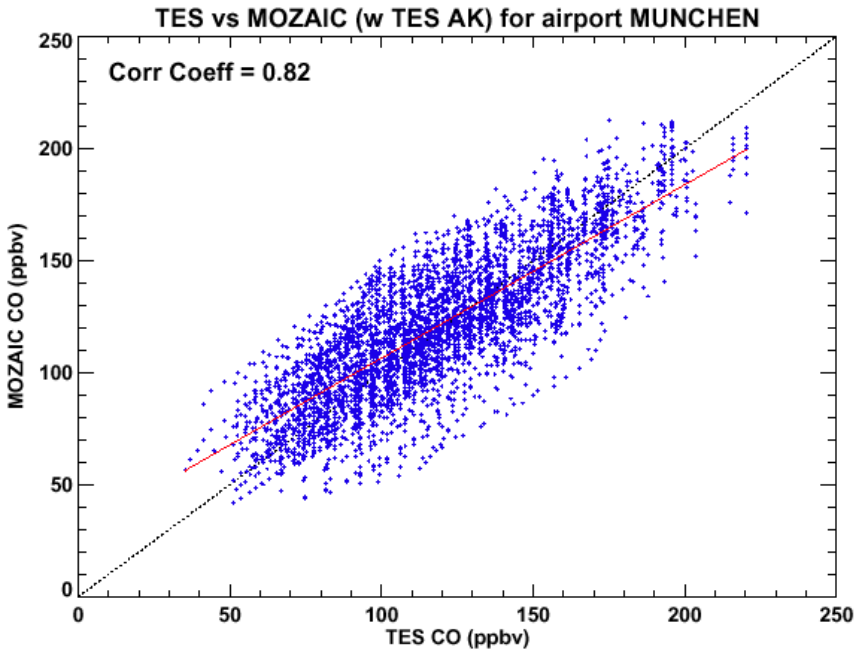

Figure 6-13 Correlation Plot of all TES and MOZAIC CO Comparison Profiles for Airport Munchen. The correlation coefficient is 0.82.

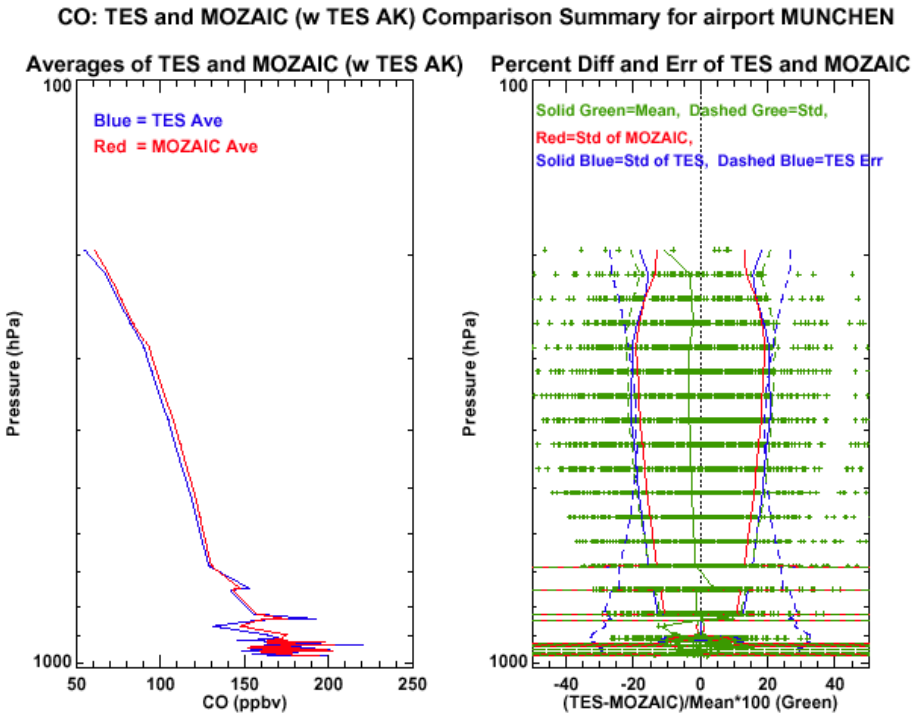

Figure 6-14 Same Data in Figure 5-15. Left panel shows the averages of the TES and MOZAIC CO profiles, and the right panel shows the difference, the standard deviations derived from the two data sets and the average for the TES retrieval errors.

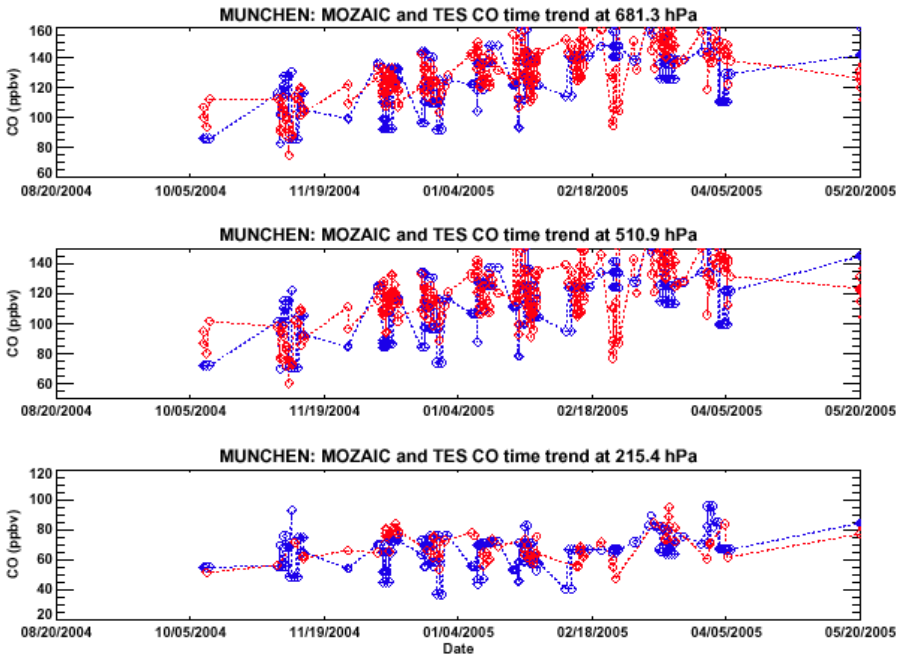

Figure 6-15 Same Data in Figure 5-15. The Time Trends of the TES and MOZAIC CO Data at Three Pressure Levels, 681.3, 510.9, and 215.4 hPa.

Table 6-1 Summary for TES-MOZAIC CO Comparisons, Sept 2004 – May 2005

Airport	Num TES-MOZ	Corr Coeff	TES-MOZ (%)	Sdv of MOZ (%)
PARIS	32	0.81	~ 5	15
FRANKFURT	93	0.85	<+/- 5	10-20
VIENNA	81	0.88	- (0-5)	10-15
MUNCHEN	193	0.82	< -5	10-20
TORONTO	49	0.81	-(5-10)	5-15
LOS ANGELES	27	0.63	- (0-5)	10-20
VANCOUVER	59	0.72	- (0-10)	10-20
SAN FRANCISCO	15	0.39	< 5	20-30
CHARLOTTE	12	0.78	< -5	5-15
MIAMI	8	0.81	- (0-10)	5-15
TOKYO	45	0.74	< -5	15-25
ABU ZABY	44	0.61	~ -5	10-20
TEHERAN	13	0.71	~ (-10)	10-15
PEKIN	14	0.81	- (0-10)	25
SHANGHAI	18	0.19	- (0-20)	15-50

Green – Europe, Blue - N America, Red - Asia

6.6 CO Validation: Comparisons to MOPITT Data

The retrieval results of TES 16-orbit global survey measurements in Sept 20-21, 2004 (Run ID 2147) have been examined extensively by the TES science team (M. Luo et al., 2006). Figure 6-16 illustrates CO total column amounts at TES nadir footprints for Run ID 2147. Over 70% of the profiles met the requirements for a successful retrieval according to the current quality criteria. In the future, TES Level 2 retrievals and column values will be mapped to a uniform latitude/longitude grid for each global survey (TES Level 3 products). An illustration of this is provided in Figure 6-17 for the CO column. Enhanced tropospheric CO is observed over parts of S. America and Africa, and along the east coast of Asia. These are associated with the well known seasonal biomass burning or pollution source regions. The degree-of-freedom for signal from TES CO retrievals are plotted as a function of latitude in Figure 6-18. Values for the *DOFS* of 0.5-2 are achieved, meaning TES measurements provide 0.5-2 pieces of independent vertical information for tropospheric CO. The better *DOFS* normally occurred for the daytime tropics with high surface temperatures and clear sky conditions where fewer scan signals were rejected due to clouds.

The CO profiles from MOPITT instrument on Terra are gathered for the same time period of the TES global survey on Sept.20-21, 2004. Figure 6-19 shows the MOPITT measurement of CO total column overlaid with TES geolocations. It is immediately realized that TES (Figure 6-16) and MOPITT (Figure 6-19) global CO agree well qualitatively, *e.g.,* they both detected enhanced CO near the polluted sources. In examining the model field of CO, *e.g.,* the MOZART

simulation used as *a priori* for TES CO retrievals, TES and MOPITT measurements revealed some more detailed CO distributions.

Figure 6-20 shows a comparison of the TES and MOPITT CO total column values as a function of latitude for the TES global survey time period in Sept.20-21, 2004. The reported percent errors for the two instruments are plotted as functions of latitude. The global averages of total column errors for CO are 8.7% for TES and 11.7% for MOPITT respectively. Again, we see general good agreement between the two instruments at most latitudes with the exception of southern high latitudes, where the column CO amounts measured by TES are slightly lower than that of MOPITT. This is believed to be due to the effect of the *a priori* in CO retrievals which will be demonstrated below for different pressure levels.

Quantitative comparisons between TES and MOPITT CO at low, mid and upper troposphere and total column for this day are presented in the paper M. Luo et al. 2007. Table 6-2 lists the comparison summary. Two steps are performed in the comparison, adjusting TES CO profiles to MOPITT *a priori* profile, and applying TES averaging kernels to MOPITT retrieved profiles. The final comparison is to compare TES retrieved CO profiles adjusted to MOPITT *a priori* and the MOPITT retrieved CO profiles adjusted to MOPITT averaging kernel. The agreement between the two CO fields becomes much better in all tropospheric levels and the total column, especially in the lower and upper troposphere where both instruments do not have much sensitivity in their measurements.

It is concluded in the paper (M. Luo et al., 2007) that no systematic differences are found as a function of latitude in the final comparisons between TES and MOPITT CO. These results show that knowledge of the *a priori* profiles, the averaging kernels, and the error covariance matrices in the standard data products provided by the instrument teams and understanding their roles in the retrieval products are essential in quantitatively interpreting both retrieved profiles and the derived total or partial columns for scientific applications

Table 6-2 Comparisons of Global Averages of TES and MOPITT Reported CO Volume Mixing Ratios at Three Pressure Levels and Total Column for Data taken in September 20-21, 2004.

	850 hPa		500 hPa		150 hPa		Total Column	
	% diff	% rms	% diff	% rms	% diff	% rms	% diff	% rms
Direct comparison of TES and MOPITT CO	-18%	36%	-3%	24%	-4.5%	35%	-11%	22%
TES CO adjusted to MOPITT *a priori* compared to MOPITT CO	-5%	35%	-3.8%	23%	-7%	24%	-5.4%	22%
TES CO adjusted to MOPITT *a priori* compared to MOPITT CO adjusted to TES averaging kernel	-0.2%	15%	-4%	23%	-4.8%	18.7%	-4.4%	16%

%diff is the global average of the differences between the matched TES and MOPITT points (TES minus MOPITT) divided by the average of the global averages of TES and MOPITT CO VMRs.

%rms is the root mean square (rms) of the differences between the matched TES and MOPITT points (TES minus MOPITT) divided by the average of the global averages of TES and MOPITT CO VMRs.

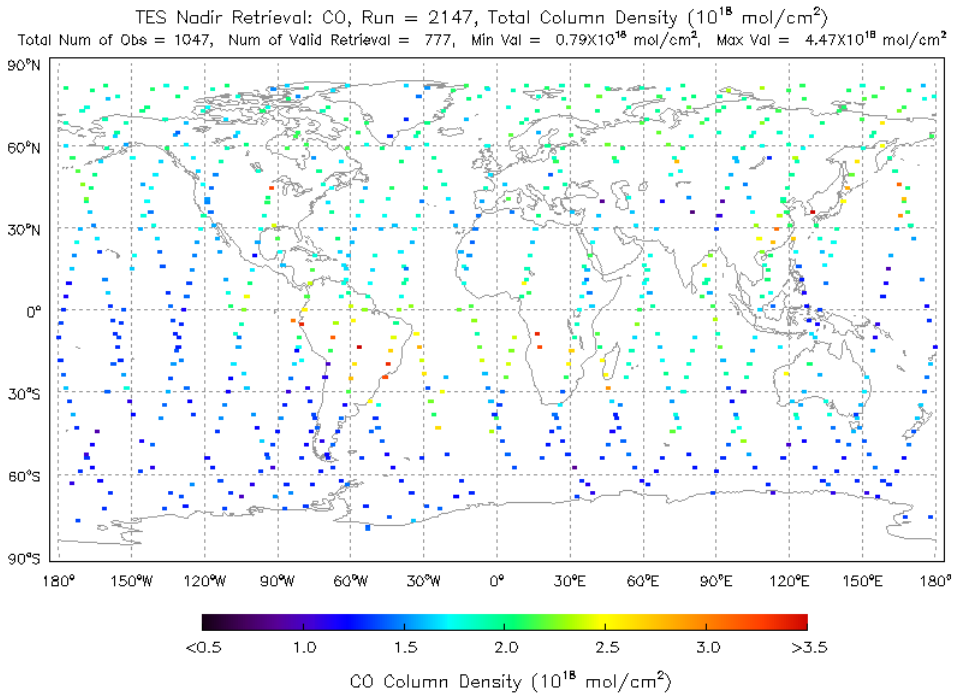

Figure 6-16 Total Column of TES CO shown as enlarged nadir footprints for TES Run ID 2147 (September 20-21, 2004). Elevated CO over and near the coasts of S. America and Africa are observed due to extensive biomass burnings in both regions. Larger CO values also showed up in expected pollution regions in E. Asia.

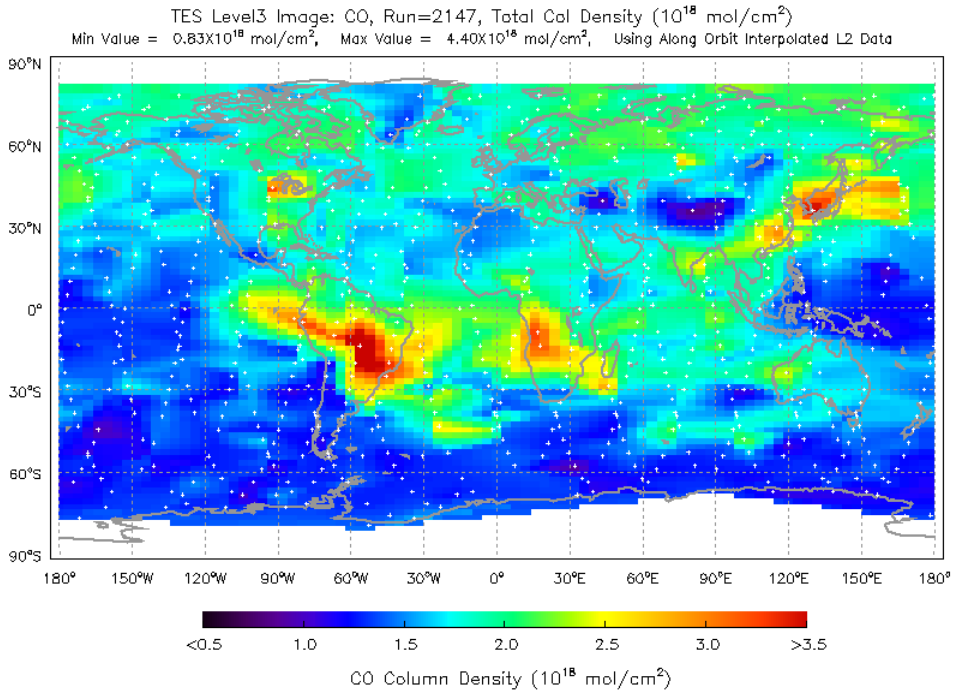

Figure 6-17 TES CO Column from **Figure 6-16** mapped to uniform grids in latitude and longitude, using Delaunay triangulations and the 2-D linear interpolation method. White marks are TES geolocations. The features in CO global distributions are more clearly displayed.

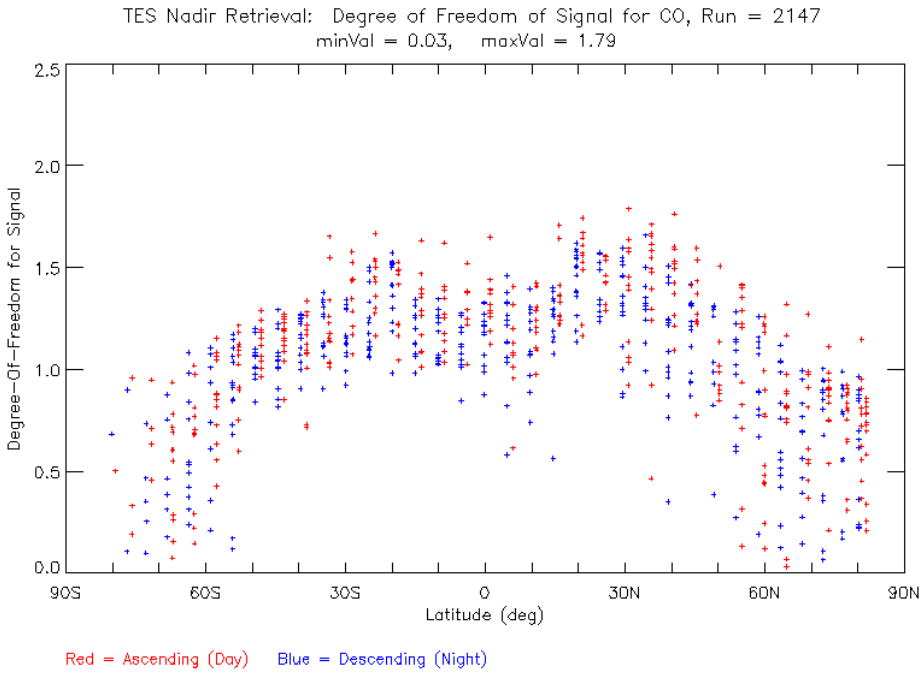

Figure 6-18 Degree of freedom for signal as a function of latitude for TES nadir CO retrieval on Sept. 20-21, 2004.

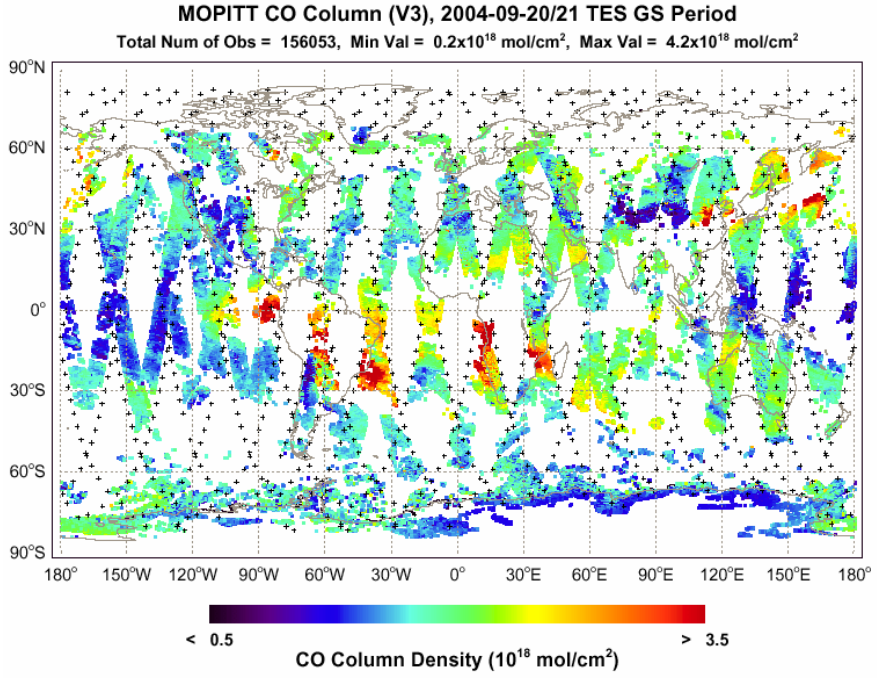

Figure 6-19 Terra-MOPITT CO total column observed in TES global survey period of Run ID 2147, Sept.20-21, 2004. Black marks are TES geolocations. Orbits of Terra and Aura have equator ascending crossing times of about 9:30 am and 1:45 pm respectively.

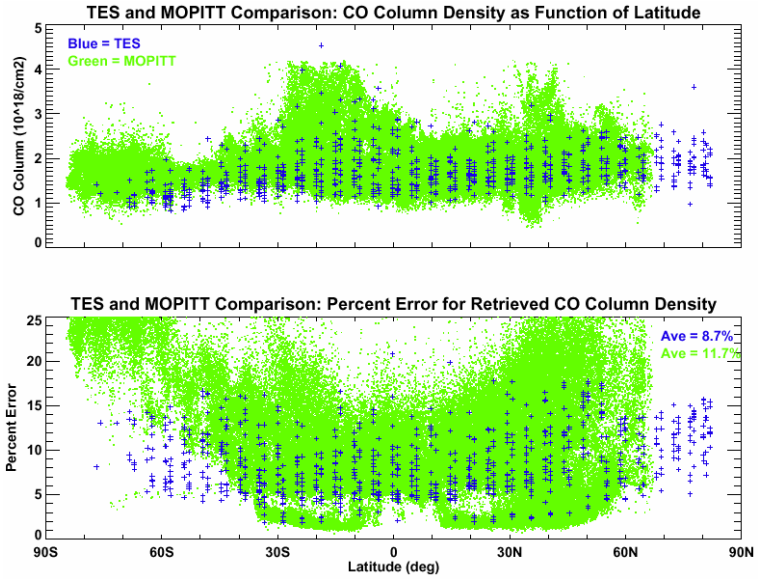

Figure 6-20 The top panel shows the comparisons of TES and MOPITT total CO columns as functions of Latitude for TES Run ID 2147, Sept.20-21, 2004. Note that TES CO column is visibly lower than that of MOPITT in Southern high latitudes. The bottom panel is the percent errors in TES and MOPITT CO columns. The global average values of their percent errors are 8.7% for TES and 11.7% for MOPITT, respectively.

6.7 CO validation: comparisons to ACE and MLS data

Both the Atmospheric Chemistry Experiment (ACE) and Microwave Limb Sounder (MLS) are limb viewing instruments and the sensitivity of the retrievals of CO by the two instruments are limited to the upper troposphere. Preliminary validation results between TES/ACE and TES/MLS are shown in the following section.

6.7.1 Comparisons to ACE

ACE is a Canadian satellite mission launched Aug 13, 2003. The ACE-FTS instrument operates primarily in solar occultation providing altitude profile information (typically 10–100 km) for temperature, pressure, and the volume mixing ratios of dozens molecules of atmospheric interest, as well as atmospheric extinction profiles over the latitudes 85°N to 85°S. Figure 6-21 gives the time trend of ACE latitude coverage for its sunrise and sunset measurements.

For each ACE CO profile, we select the corresponding TES CO profile within 24 hrs and closest in distance. Figure 6-22 shows some examples of the CO profile comparisons. Figure 6-23 illustrates time trend of the CO comparisons at 316.2 hPa for data between 30S and 30N latitude. These comparisons and those for other pressure levels (215.4 and 146.8 hPa) and latitudes indicate there is no obvious bias in the two CO data sets. The comparisons will be updated using more ACE and TES in the future.

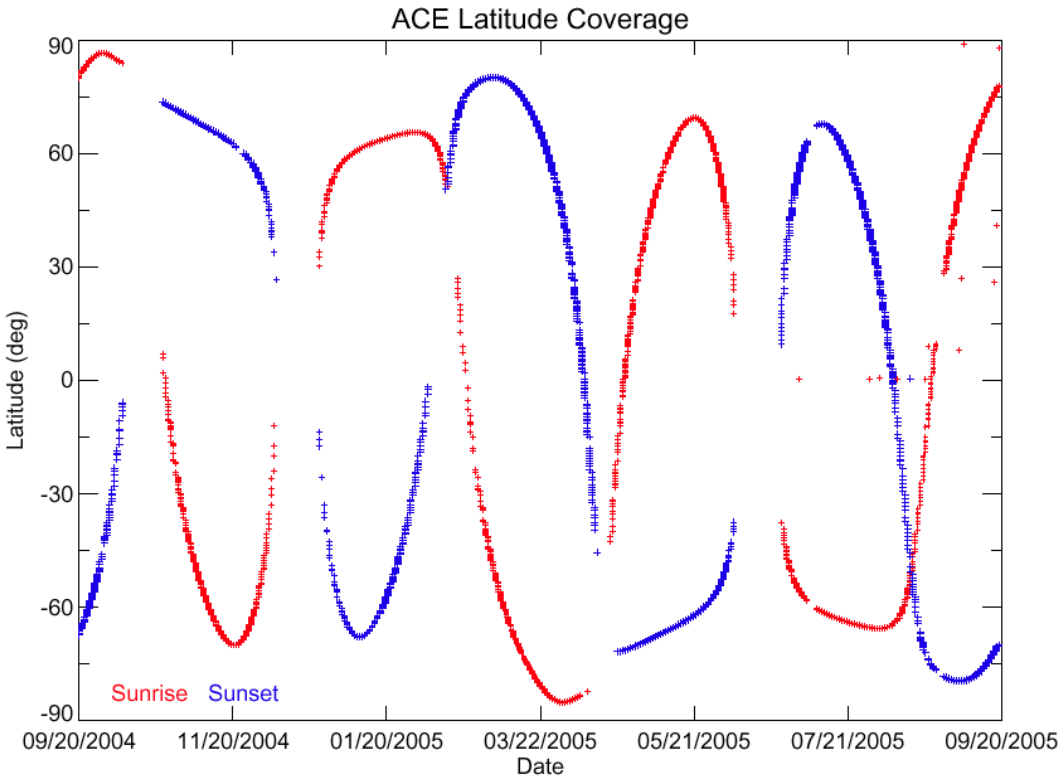

Figure 6-21 Time Trend of Latitude Coverage for ACE.

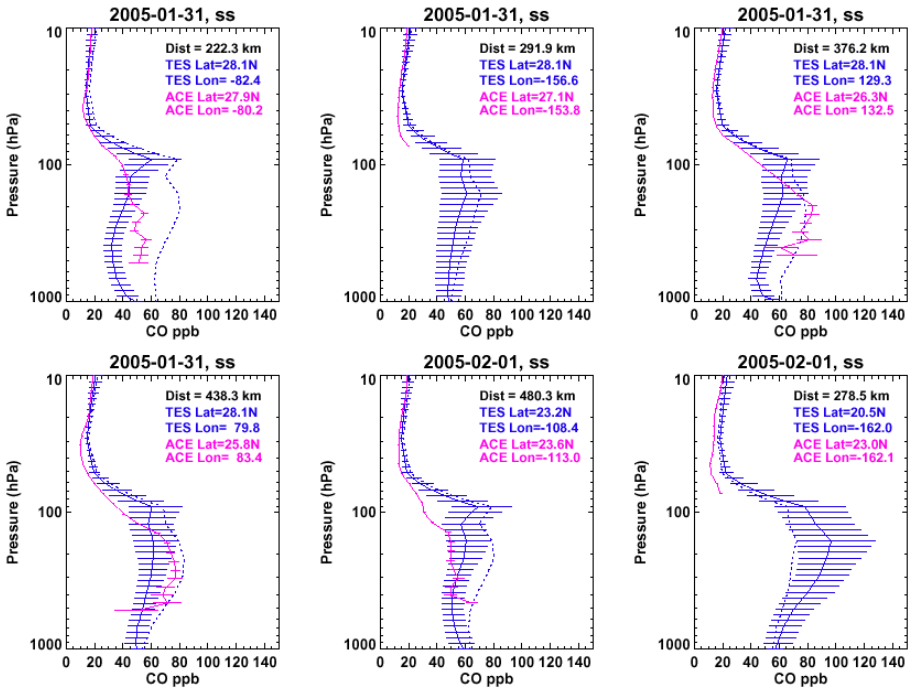

Figure 6-22 Examples of TES-ACE CO Profile Comparisons. Solid blue is TES retrieved profile and dotted blue is TES *a priori* profile. Solid magenta is ACE retrieved profile.

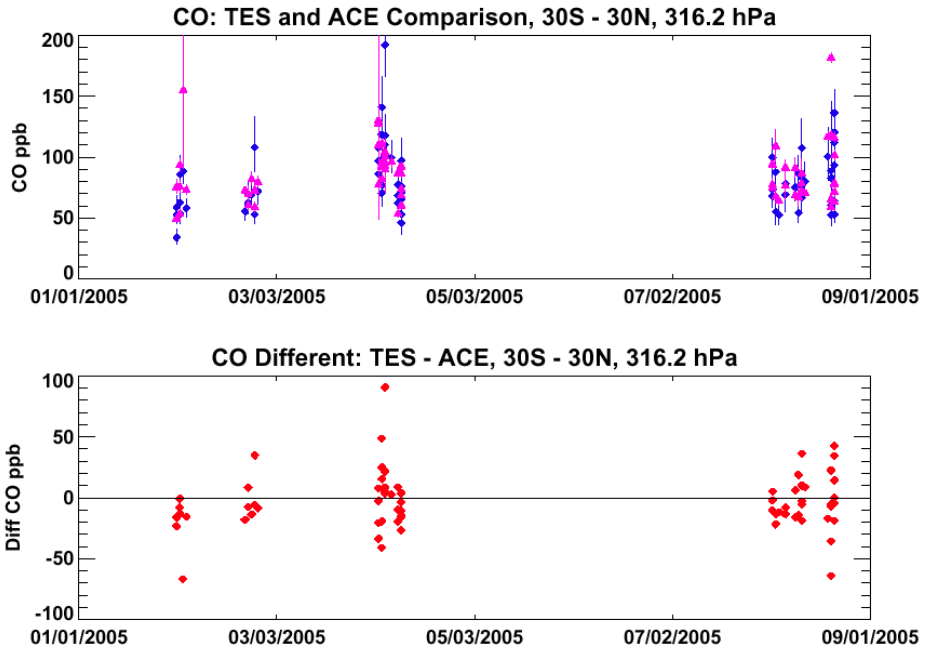

Figure 6-23 Time Trend of TES and ACE CO Comparisons at 316.2 hPa for Data in 30S-30N Latitude.

6.7.2 Comparisons to MLS

The JPL MLS instrument is a limb viewing instrument sensing the microwave thermal emissions in the atmosphere. The retrievals of CO profile from MLS measurements are available above the upper troposphere, for pressure levels < ~215 hPa. We made preliminary comparisons between TES V2 and MLS V1.5 CO data. This version of MLS CO data is too high relative to the aircraft measurements and model simulations (Filipiak et al., 2005). Figure 6-24 shows a side-by-side comparison of TES and MLS CO at 215.4 hPa. A new version of MLS data (V2) will be available in the near future and its comparison to TES CO is expected to be much improved.

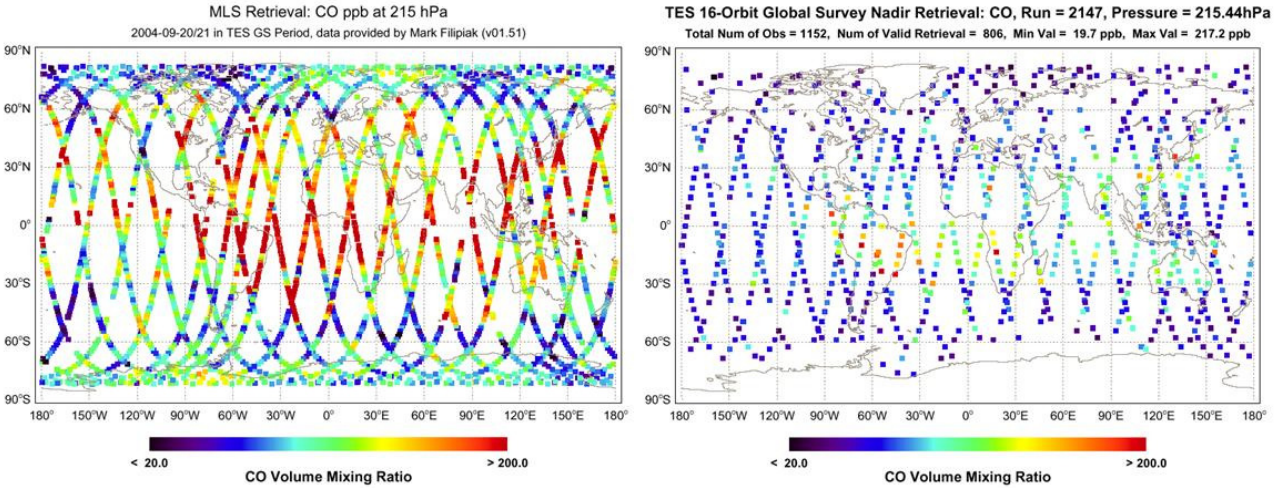

Figure 6-24 Comparison of TES and MLS Global Retrievals of CO at 215.4 hPa, September 20-21, 2004.

6.8 CO validation: summary and future works

Much progress has been made in validating TES CO profile retrievals. Table 6-3 gives a brief summary of the CO validation sources, the activities, and the preliminary conclusions. TES CO profiles are and will be compared to all satellite CO data from currently operating instruments, MOPITT, AIRS, ACE and MLS. These comparisons show general agreement in patterns of CO global distributions in the troposphere. The enhanced CO data in the lower troposphere can be closely related to the known burning or pollution sources. The direct comparisons of the retrievals from the remote sensing radiance measurements are not proper though, since the retrievals are influenced by the *a priori* assumptions used by different instrument teams. In comparisons to the MOPITT CO data, we illustrated the method of adjusting the comparison profiles with common *a priori* profiles and using the TES averaging kernels. This method will be used for future TES – AIRS CO comparisons.

The comparison of TES CO retrievals with *in situ* aircraft measurement cannot be made directly either. We presented that the TES CO averaging kernels and *a priori* profiles need to be applied to the *in situ* profiles before comparing to the TES retrieved CO profiles. Good agreement between the averaged *in situ* and TES CO profiles is obtained, within 10% and much less than the variabilities of TES and the aircraft CO measurements in the region. In general, the agreement is better for regions where CO fields have less variability. The MOZAIC data set includes a variety cities in different regions and for an extended term time period and therefore is potentially very valuable for validation of TES CO profiles.

Table 6-3 A summary list for TES CO validation activities. Red marks the future works.

Comparison Sources	Progress	Results / problems
MOPITT	• Data from Sept 20-21, 2004. JGR paper published (Luo et all., 2007) • Examine some CO enhancement events • Monthly	• Good agreement in global patterns • Influence of *a priori* constraints on CO retrievals of both instrument. The agreement much improved after adjusting the retrieval with *a priori* info. • MOPITT will release V4 data
ACE MLS AIRS	• Time trends with ACE data in upper trop and Indonesian fire event (Rinsland et al., Clerbaux et al., submitted 2007) • Four selected days to compare to MLS • AIRS retrieval w TES a priori (Warner et al., sumbitted 2007)	• Good agreement with ACE • MLS being too high but global patterns agree with TES. • Understand AIRS AK
AVE (Argus) CR-AVE (ALIAS/Argus)	• Comparisons made AVE-04 and CR-AVE-06 (Lopez et al, revision, 2007);	• TES CO lower by ~10% in mid-trop near Houston and higher by ~5% near Costa Rico. All agree within CO area variability and the estimated errors of 10-20%.

Comparison Sources	Progress	Results / problems
INTEX-B (DACOM)	• Comparisons made (Luo et al, in press 2007)	• TES CO lower by ~10% in mid_trop near Houston. All Agree within CO area variability and the estimated errors of 10-20%. Two large variability in CO in both aircraft and TES measurements in Hawaii and Anchorage.
MOZAIC	• Comparisons made Sept 04 – May 05	• Agreement within CO area variability and estimated errors of 10-20% in most airports. • Waiting for data after May 2005.

6.9 References

[1] Filipiak, M.J., R.S. Harwood, J.H. Jiang, Q. Li, N.J. Livesey, G.L. Manney, W. G. Read, M.J. Schwartz, J.W. Waters, D.L. Wu, "Carbon Monoxide Measured by the EOS Microwave Limb Sounder on Aura: First Results," Geophys. Res. Lett. 32, No. 14, L14825, doi:1029/2005GL022765, 28 July 2005

[2] C. P. Rinsland, M Luo, J. A. Logan, R. Beer, H. Worden, S. S. Kulawik, D. Rider, G. Osterman, M. Gunson, A. Eldering, A. Goldman, M. Shephard, S. A. Clough, C. Rodgers, M. Lampel, and L. Chiou, Nadir Measurements of Carbon Monoxide (CO) Distributions by the Tropospheric Emission Spectrometer (TES) Instrument onboard the Aura Spacecraft: Overview of Analysis Approach and Examples of Initial Results, Geophys. Res. Lett., 33, L2280610.1029/2006GL027000, 2006

[3] M. Luo, C. P. Rinsland, C. D. Rodgers, J. A. Logan, H. Worden, S. Kulawik, A. Eldering, A. Goldman, M. W. Shephard, M. Gunson, and M. Lampel, Comparison of carbon monoxide measurements by TES and MOPITT - the influence of a priori data and instrument characteristics on nadir atmospheric species retrievals, J. Geophys. Res., 112, D09303, doi:101029/2006JD007663, 2007.

[4] J. Logen et al., The effects of the 2006 El Nino on tropospheric composition as revealed by data from the Tropospheric Emission Spectrometer (TES), submitted to GRL, 2007.

[5] M. Luo, C. P. Rinsland, B. Fisher, G. Sachse, G. Diskin, J. Logan, H. Worden, S. Kulawik, G. Osterman, A. Eldering, R. Herman, and M. Shephard, TES carbon monoxide validation with DACOM aircraft measurements during INTEX-B 2006, in press, 2007.

[6] J. Lopez, M. Luo, L. Christensen, M. Loewenstein, H. Jost, C. R. Webster, and G. Osterman, TES carbon monoxide validation during two AVE campaigns using the Argus and ALIAS instruments on NASAs WB-5, submitted to JGR, 2007.

7. Validation of TES Nadir Retrievals of Temperature

7.1 Comparisons of TES Temperature with Sondes

Validation of TES temperature is important not only for its own merits, but also because ozone is retrieved jointly with temperature and water vapor. Retrieval improvements in any one of these species could impact the other two. This section focuses on v002 temperature retrievals with the standard retrieval quality flags. As discussed elsewhere in this validation report, the retrieval algorithm for TES v002 (R9) data has undergone significant improvements.

7.1.1 TES Temperature Comparisons with Sondes

During 2006, TES special observations were scheduled at the DOE Atmospheric Radiation Measurement (ARM) sites at Southern Great Plains, Oklahoma, the North Slope of Alaska, and the Tropical Western Pacific. With coincidence criteria of 2 hours and 250 km, these special observations were compared with radiosondes (RS90 and RS92 types). As shown below in Figure 7-1, a TES cold bias of ~1 K is seen in the upper troposphere relative to these sondes. In contrast, the bias between GMAO GEOS-4 and the sondes is much smaller.

Another set of sondes were launched from Heredia, Costa Rica, and San Cristobal, Galapagos, as part of the Ticosonde mission in January and February 2006. Figure 7-2 (a-c) shows comparisons between the closest sondes (with TES averaging kernel applied) and TES retrievals on three days. The comparisons on 22 January and 25 January both indicate a TES cold bias in the upper troposphere. On 7 February 2006, the temperature differences are greater, but so is the distance between the sonde and the TES retrieval.

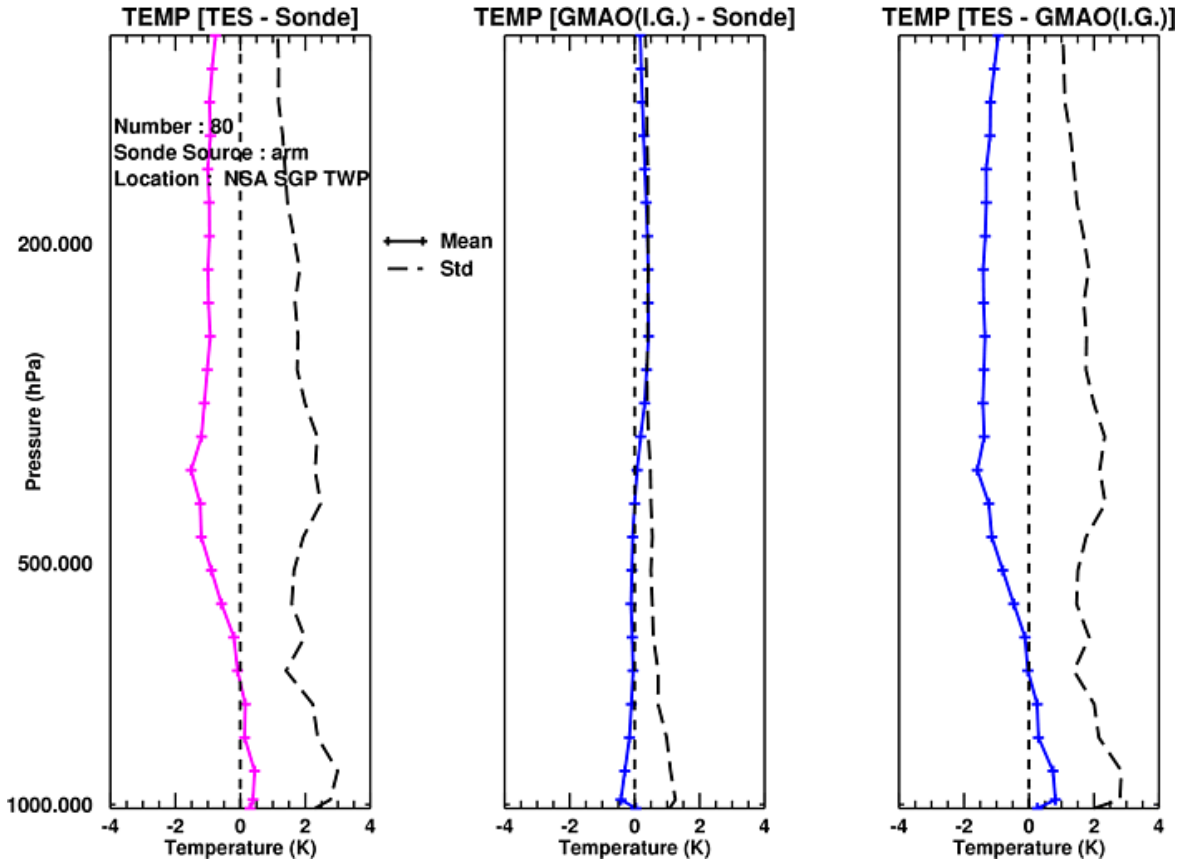

Figure 7-1 Comparison of TES Temperature Retrievals with ARM Site Radiosondes and GMAO GEOS-4.

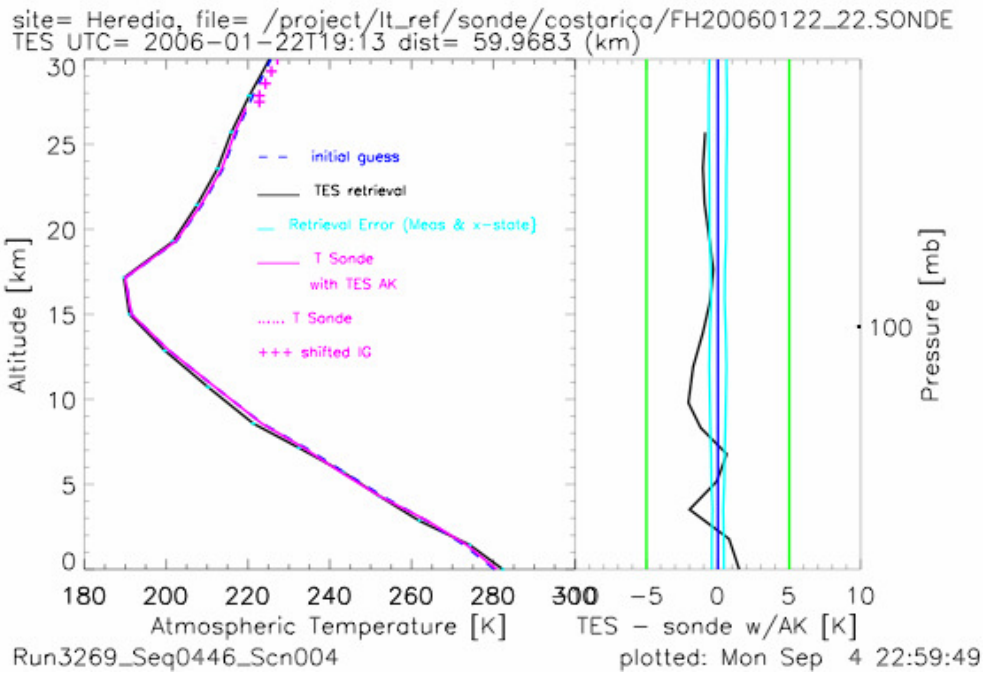

(a)

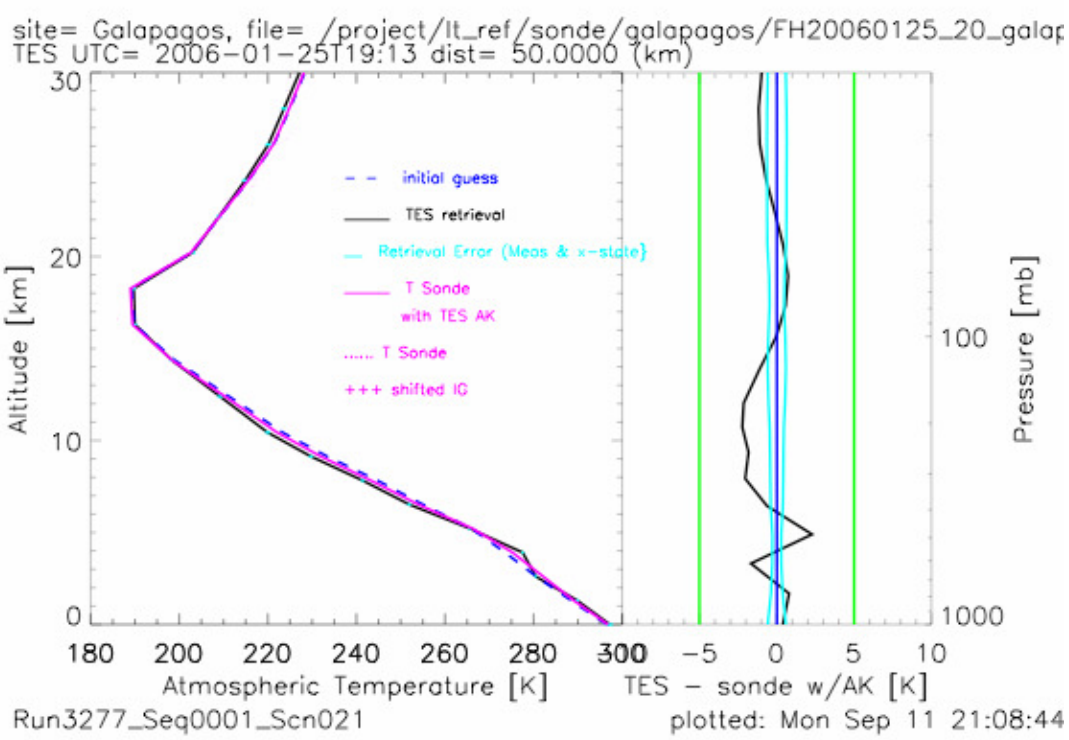

(b)

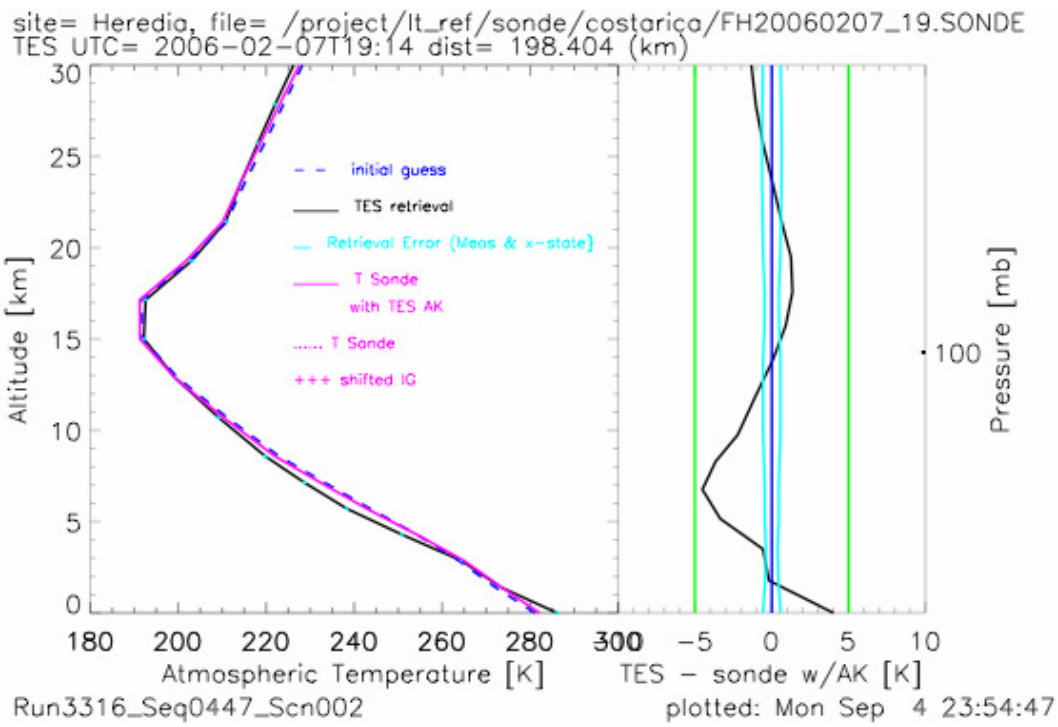

(c)

Figure 7-2 (a-c) Comparisons of TES Temperature Retrievals with Sondes launched during Ticosonde in Costa Rica and Galapagos.

7.2 Validation of TES Nadir Temperature Retrievals with Sondes

This is a summary of validation of v003 TES nadir temperature retrievals, and the differences between v002 and v003. Much of this work was reported by Herman et al. (2007). The previous TES version v002 (R9) temperature was retrieved from microwindows in the spectral bands of H_2O (2A1 filter) and O_3 (1B2 filter). Version v002 nadir temperature validation was covered by the TES version 2.0 validation report (Osterman et al., 2007). In version v003, temperature is now retrieved from these spectral bands and also from the CO_2 ν2 band (2B1 filter) at 650 to 800 cm^{-1}. As will be shown below, the addition of the CO_2 ν2 band has improved the TES temperature retrievals. We present here validation comparisons between TES v003 nadir temperature and sonde measurements, and their bias relative to GMAO GEOS-5.

TES retrieves temperature, ozone, and water vapor concurrently (Bowman et al., 2002, 2006; Worden et al., 2004). The initial guess in the TES retrieval algorithm is set equal to an *a priori* profile (constraint vector). The TES v003 *a priori* constraint vectors come from NASA's Goddard Earth Observing System (GEOS) data assimilation system GEOS-5 (Rienecker et al., 2007). These are produced by the Global Modeling and Assimilation Office (GMAO) at the NASA Goddard Space Flight Center (GSFC). GEOS-5 profiles are produced on a 0.625° longitude by 0.5° latitude grid. These profiles are interpolated to the locations and pressure levels of TES retrievals. The *a priori* covariance matrices used for retrieval regularization are described in Bowman et al. (2006). Previously, TES v002 temperature *a priori* constraint vectors came from GMAO GEOS-4 (Herman et al., 2007, and references therein).

GEOS-5 assimilates a wide range of operational satellite data, sonde measurements, et cetera. Sonde data are strong constraints on the thermal structure and winds throughout the troposphere, with an emphasis on continental regions where the observing network is denser. Space based observations include the High Resolution Infrared Sounders (HIRS) and Advanced Microwave Sounders (AMSU) instruments on National Oceanic & Atmospheric Administration (NOAA)'s operational sounders, which directly constrain temperature and moisture. GEOS-5 includes a direct assimilation of radiances from AMSU and HIRS in a three-dimensional variational assimilation, as well as radiances from the Advanced Infrared Sounder (AIRS) and AMSU instruments on NASA's EOS-Aqua platform (Zhu and Gelaro, 2007). The previous GEOS-4 assimilated observations of temperature and water vapor using a one-dimensional variational approach (Bloom et al., 2005), where a retrieval was made using a six-hour forecast as *a priori* state; the retrieved variables were assimilated.

7.2.1 NCEP sonde database compared with TES v003 Global Surveys

The National Weather Service's National Center for Environmental Prediction (NCEP) maintains the quality controlled Integrated Global Radiosonde Archive (IGRA) (Durre et al., 2006). The radiosondes (hereafter sondes) are typically launched four times daily (0, 6, 12, and 18 UT) at more than 800 sites around the globe. We utilize this database to find TES global survey observations coincident with sonde profiles at all latitudes. For a pair of observations to be considered coincident, we require sonde launch times and TES observation times within two hours, and sonde launch locations within 250 km of the nearest TES footprint. These criteria were chosen to try to balance the trade-off between co-located, simultaneous observations and the statistical need for a large number of comparisons. The standard quality flag was applied to the TES retrievals. Many types of sondes are included in the NCEP database. For the highest

accuracy, we focus exclusively on Vaisala RS-90 and RS-92 radiosondes, with a manufacturer's stated uncertainty of ±0.2°C (2σ) in the troposphere at night (Miloshevich et al., 2006).

Six TES global surveys from winter and spring 2006 have been compared with NCEP sondes. The TES retrievals have been filtered by the master quality flag (Osterman et al., 2007). Figure 7-3 and Figure 7-4 show comparisons of temperature profiles between sondes and TES v002 and v003, respectively. For these comparisons, we aggregate sonde data from all latitudes. The TES operator has been applied to the sonde profiles, and differences are shown as (T_{TES} - $T_{insituw/AK}$). Levels where TES has no sensitivity to temperature (i.e. where the sum of the row of the averaging kernel equals zero) are not included in the calculation of the mean difference. To improve the statistics, RS-90 and RS-92 sondes have been grouped together. These sondes are expected to exhibit similar temperature responses. Figure 7-3 shows that, relative to RS-90 and RS-92 sondes, TES v002 has a cold bias in the upper troposphere and lower stratosphere, with a maximum TES cold bias of 1.4 K peaking at 400 hPa pressure, and a slight warm bias in the lower troposphere. In contrast, TES v003 retrievals have significantly smaller temperature biases than v002 in the upper troposphere and lower stratosphere (<0.5 K absolute bias at 10-250 hPa), but little change with respect to sondes at pressures of 400 hPa and greater in the lower troposphere (Figure 7-4).

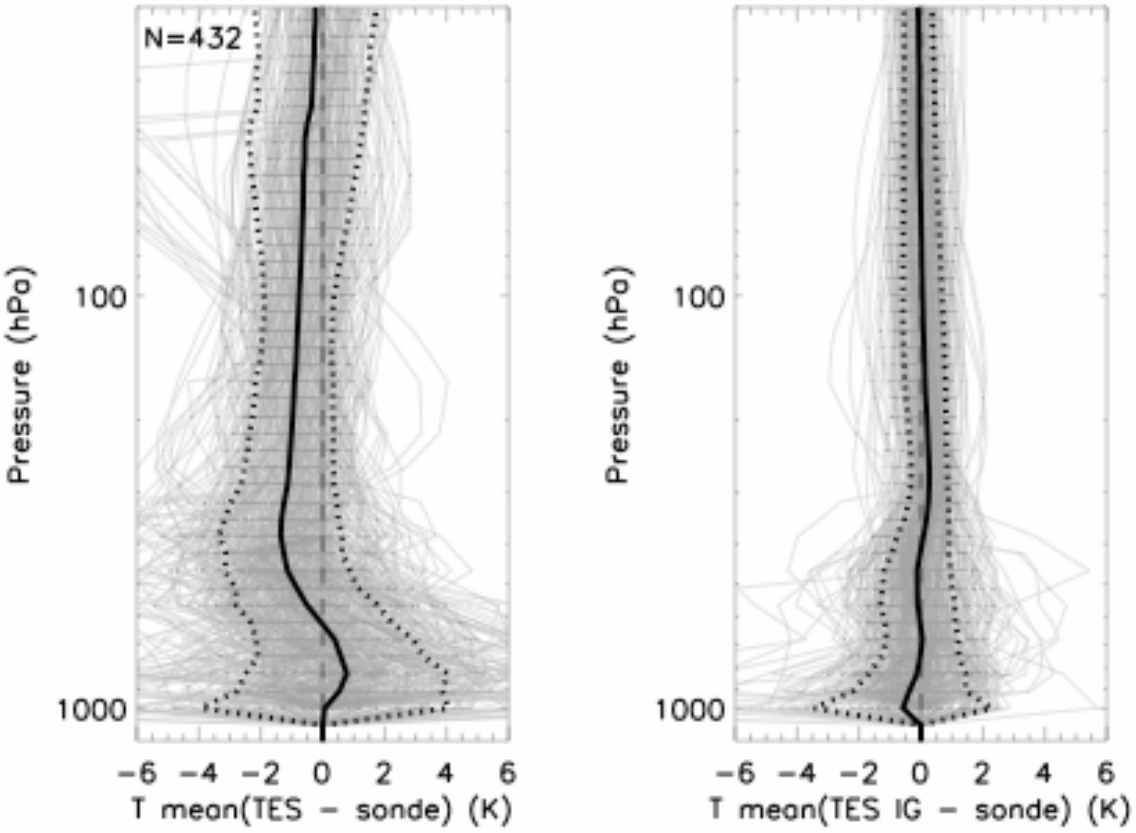

Figure 7-3 Temperatures from RS-90 and RS-92 sondes in the NCEP database compared with TES v002 global surveys (left) and the TES initial guess from GMAO GEOS-4 (right). For these comparisons, all latitudes are included. Shown are 432 individual temperature differences (thin grey lines), the mean difference (thick line) and 1σ (dotted lines). The TES operator has been applied to the sonde profiles, and differences are calculated as TES – sonde.

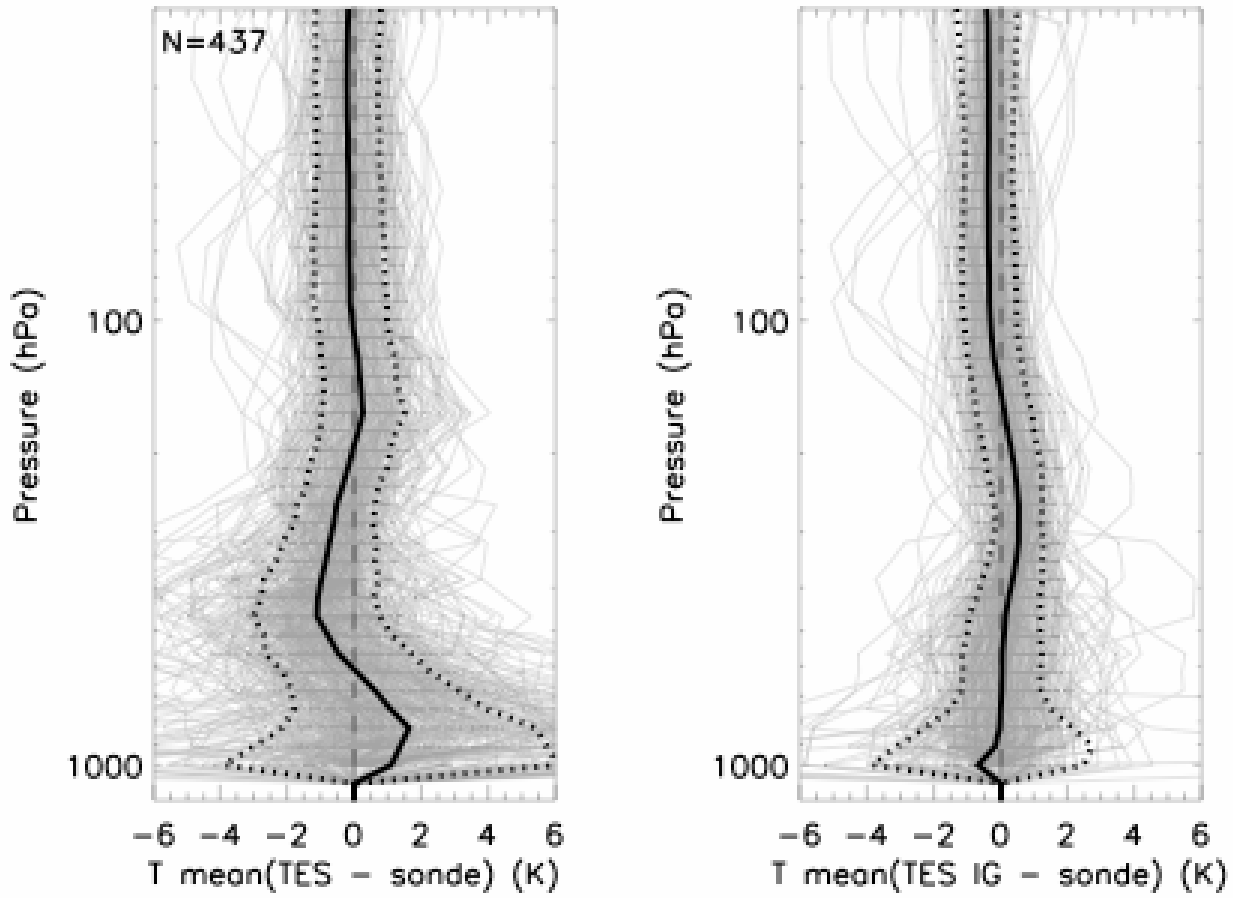

Figure 7-4 Temperatures from RS-90 and RS-92 sondes in the NCEP database compared with new TES v003 global surveys (left) and the TES initial guess from GMAO GEOS-5 (right). All latitudes are included. Shown are 437 individual temperature differences (thin grey lines), the mean difference (thick line) and 1σ (dotted lines). The TES operator has been applied to the sonde profiles, and differences are calculated as TES – sonde.

We also compare GMAO GEOS-4 and GEOS-5 with the sondes (right panels of Figure 7-3 and Figure 7-4) to assess how much the TES retrieval has moved from the initial guess. The TES operator is applied to the sonde profiles so that comparisons are made with the same vertical sensitivity and resolution as TES. It is seen that GEOS-4 and GEOS-5 have little bias relative to the sondes. This is not altogether surprising because GMAO assimilates data from sondes, especially over the continents where most of the sondes are launched. The largest differences between GEOS and sonde temperatures are seen in the lower troposphere, where there may be significant atmospheric variability. At 300 hPa in the upper troposphere, GMAO has a warm bias of 0.5 K for GEOS-4, and 1 K for GEOS-5. At 400 hPa and 800 hPa, TES temperature bias relative to sondes is significantly greater than GEOS-4 and -5 bias relative to sondes. With its 5.3 km by 8.5 km footprint, TES captures more small-scale variability than the GMAO analyses. This variability makes precise co-location critical for satellite-sonde comparisons. Below, sonde temperatures are compared with TES special observations for closer co-locations.

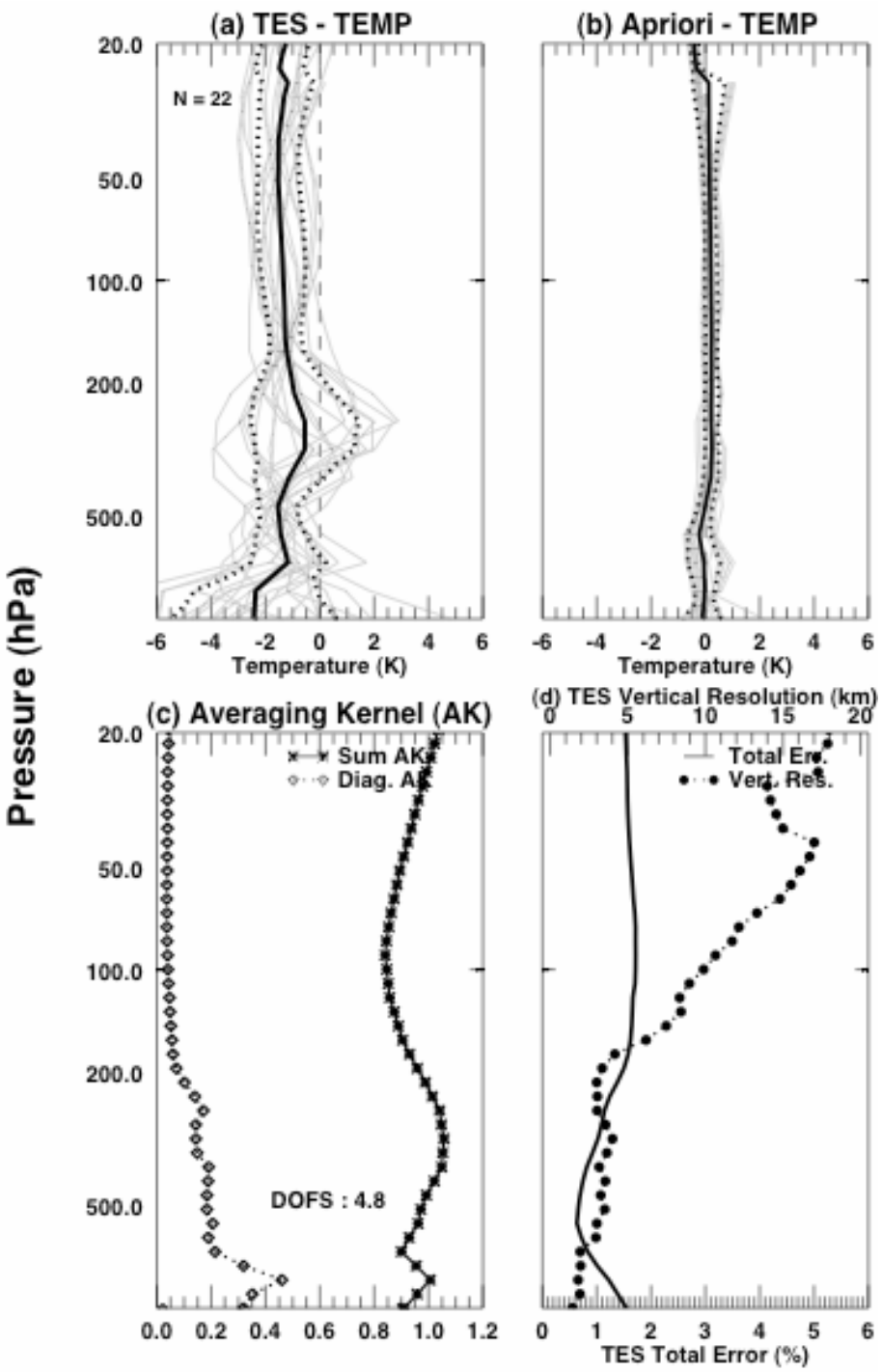

Figure 7-5 Temperatures from RS-92 sondes from the WAVES_2006 mission compared with TES v002 transects (panel a) and the TES initial guess (Apriori) from GMAO GEOS-4 (panel b). Panels a and b are plotted similar to Figure 7-3. Panel c shows the median values of the diagonals of the averaging kernel (open diamonds), which are measures of the degrees of freedom at each level. Panel c also shows the sums of the rows of the averaging kernels (x markers), which represent the fraction of the result that comes from the measurement and not from the initial guess. Panel d shows the median value of the estimated TES total error (solid

line), and the full width at half maximum of the rows of the averaging kernels (closed circles), which is a measure of the vertical resolution of TES temperature retrievals.

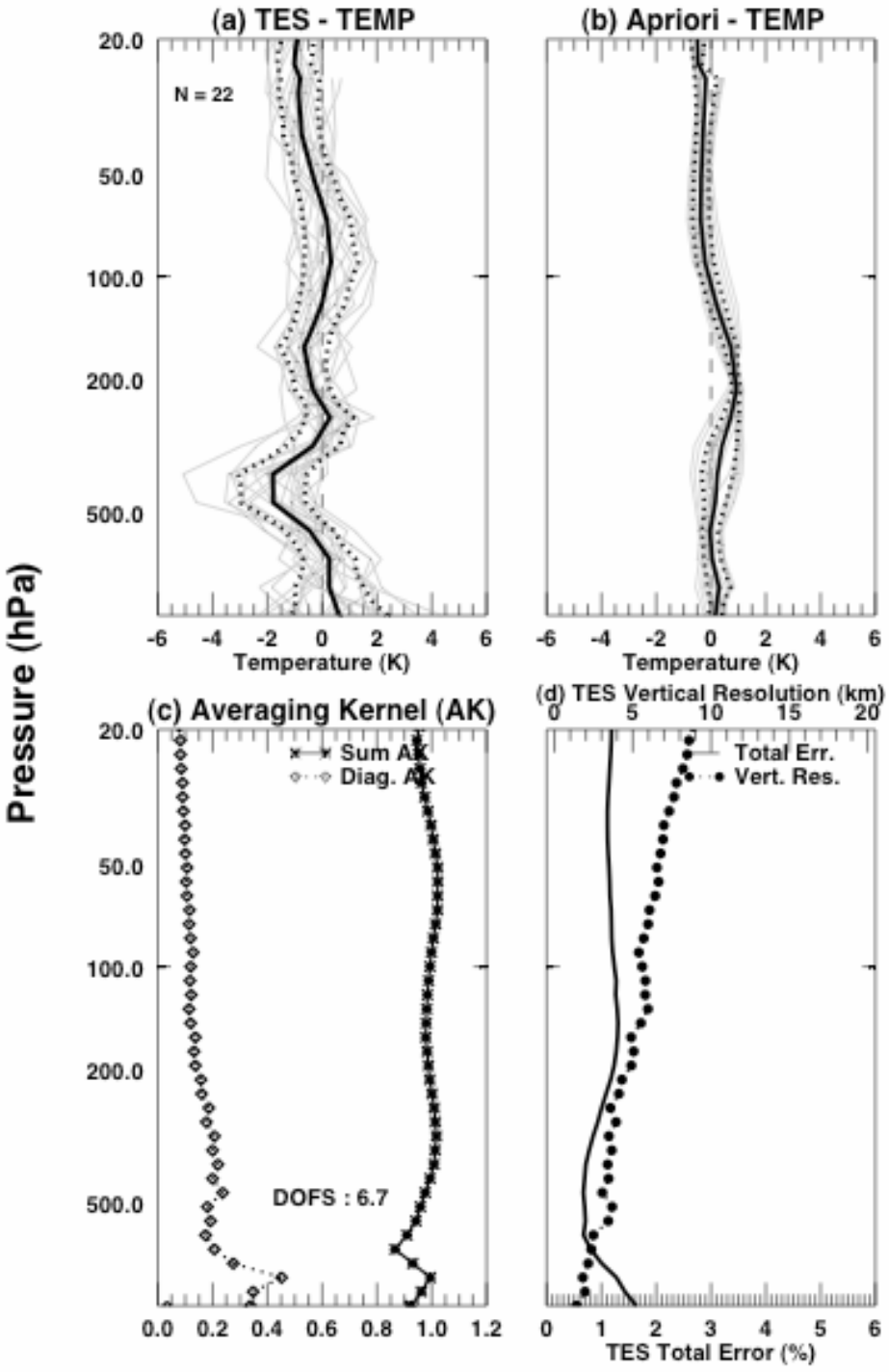

Figure 7-6 Temperatures from RS-92 sondes from the WAVES_2006 mission compared with TES v003 transects (panel a) and the TES initial guess (Apriori) from GMAO GEOS-5 (panel b). Panels c and d are plotted similar to Figure 7-5.

7.2.2 WAVES sondes compared with TES Special Observations

During summer 2006, TES transects were scheduled in coordination with RS-92 sonde launches during the Water Vapor Validation Experiment – Satellite/Sondes (WAVES_2006). This intercomparison campaign was located at the Howard University Research Campus in Beltsville, Maryland (39.0°N, 76.9°W). Figure 7-5 and Figure 7-6 show comparisons of the WAVES_2006 RS-92 sondes with TES v002 and v003, respectively, with coincidence criteria of 1.5 hours and 60 km. Although the number of comparisons (22) is small, the TES temperature bias relative to sondes is similar to the results shown above for TES global surveys. TES v002 has a 1 K cold bias relative to sondes in the upper troposphere and lower stratosphere (Figure 7-5, panel a). TES v003 has significantly improved temperature biases except at 400 hPa, where a cold bias remains (Figure 7-6, panel a). Sonde temperatures are in close agreement with GMAO GEOS-4 (Figure 7-5, panel b), but GEOS-5 appears to have a 1 K warm bias at 200 hPa (Figure 7-6, panel b). Even in the larger number of comparisons shown in Figure 7-4, GEOS-5 has a warm bias at 200-300 hPa. Panel c (Figure 7-5 and Figure 7-6) shows median values of the diagonals of the averaging kernel (open diamonds), which are measures of the degrees of freedom at each level. It is seen that, at 200 hPa and lower pressures, these median values are significantly larger for v003 temperature than v002. This means that v003 has greater sensitivity to temperature in the stratosphere. Panel d shows the full width at half maximum of the rows of the averaging kernels (closed circles), which is a measure of the vertical resolution of TES temperature retrievals. Figure 7-6, panel d, shows that TES v003 has significantly improved vertical resolution in the stratosphere.

7.2.3 References

[1] Bloom, S., A. da Silva, D. Dee, M. Bosilovich, J.-D. Chern, S. Pawson, S. Schubert, M. Sienkiewicz, I. Stajner, W.-W. Tan, M.-L. Wu, (2005), Documentation and Validation of the Goddard Earth Observing System (GEOS) Data Assimilation System – Version 4. Technical Report on Global Modeling and Data Assimilation 104606, 26. Available from http://gmao.gsfc.nasa.gov/pubs/docs/Bloom168.

[2] Bowman, K. W., J. Worden, T. Steck, H. M. Worden, S. Clough, and C. Rodgers (2002), Capturing time and vertical variability of tropospheric ozone: A study using TES nadir retrievals, J. Geophys. Res.-Atmos., 107, 4723.

[3] Bowman, K. W., C. D. Rodgers, S. S. Kulawik, J. Worden, E. Sarkissian, G. Osterman, T. Steck, M. Luo, A. Eldering, M. W. Shephard, H. Worden, M. Lampel, S. A. Clough, P. Brown, C. Rinsland, M. Gunson, R. Beer (2006), Tropospheric Emission Spectrometer: Retrieval Method and Error Analysis, IEEE Trans. Geosci. Remote Sensing, 44 (5), 1297.

[4] Durre, I., R.S. Vose, and D.B. Wuertz (2006), Overview of the integrated global radiosonde archive, J. Climate, 19(1), 53-68.

[5] Herman R.L., M. W. Shephard, B. M. Fisher, H. Vömel, T. P. Bui, L. M. Milosevich, D. N. Whiteman, R. Beer, K. Bowman, S. A. Clough, A. Eldering, M. R. Gunson, S. S. Kulawik, M. Luo, G. B. Osterman, D. Rider, H. M. Worden, and J. Worden (2007),

Validation of Tropospheric Emission Spectrometer temperature retrievals with aircraft and sondes, Submitted to J. Geophys. Res.

[6] Miloshevich, L. M., H. Vömel, D. N. Whiteman, B. M. Lesht, F. J. Schmidlin, and F. Russo (2006), Absolute accuracy of water vapor measurements from six operational radiosonde types launched during AWEX-G and implications for AIRS validation, J. Geophys. Res., 111, D09S10, doi: 10.1029/2005JD006083.

[7] Osterman, G. B., Editor (2007), TES Validation Report, Version 2.0, JPL document D33192, available at: http://tes.jpl.nasa.gov/docsLinks/documents.cfm.

[8] Rienecker, M. M., M. J. Suarez, R. Todling, J. Bacmeister, L. Takacs, H.-C. Liu, W. Gu, M. Sienkiewicz, R. D. Koster, R. Gelaro, and I. Stajner (2007), The GEOS-5 Data Assimilation System: A Documentation of GEOS-5.0 NASA TM 104606, 27, Technical Report Series on Global Modeling and Data Assimilation.

[9] Worden, J., S. S. Kulawik, M. Shephard, S. Clough, H. Worden, K. Bowman, and A. Goldman (2004), Predicted errors of Tropospheric Emission Spectrometer nadir retrievals from spectral window selection, J. Geophys. Res.-Atmos., 109(D09308).

[10] Zhu, Y., and R. Gelaro, Observation sensitivity calculations using the adjoint of the Gridpoint Statistical Interpolation (GSI) analysis system, Monthly Weather Rev., submitted (2007) - available from http://gmao.gsfc.nasa.gov.

8. TES Sea Surface Temperature Retrievals

8.1 Introduction to Sea Surface Temperature Validation

The TES sea surface temperature (SST) product, actually the TES surface temperature product filtered for scenes over water has undergone extensive validation analysis based on the V002 data. Sections 8.2 through 8.7 provide a discussion of the comparisons of TES data to other SST data sets. Another analysis has been developed (Tremblay et al., submitted 2007) which discuss a case study of look at the surface temperature of Lake Tahoe. This study also used V002 data and found that the TES observations of the water surface temperature compared to *in situ* buoys were biased high by 0.33 K. The study also updates some of the comparisons discussed below. The section below provides an excellent description of the methodology used in the SST comparisons.

The difference between the V002 and V003 SST retrievals is relatively small. A histogram of the difference between V003 and V002 (V003-V002) is shown in Figure 8-1. It shows that changes in the TES retrieval algorithm for the V003 data release have had relatively little effect on the TES SST product.

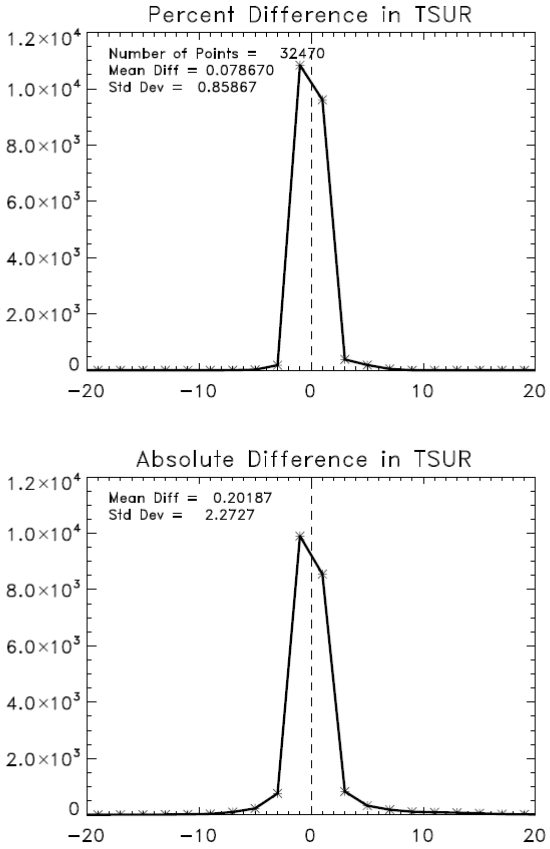

Figure 8-1 Histograms showing the difference between the V003 and V002 SST measurements from twelve global surveys taken through the TES data record.

8.2 Introduction to Version 002 Analysis

Although TES is focused on tropospheric chemistry, surface temperature (skin temperature) and emissivity measurements are essential elements of the nadir observations performed. Since ocean emissivity is known accurately (Masuda, *et al.* 1988), with respect to the TES calibration requirement and detector noise, retrievals of sea surface temperatures (SST) provide a useful method for assessing TES retrievals. The large percentage of observations partially or completely obscured by clouds makes it important to TES, and potentially to other remote sensing instruments, to characterize information that can be retrieved at different cloud effective optical depths. To this end, cloud optical depths (ODs) and the degrees of freedom of signal (DOFS) of the SST measurements are examined in conjunction with SST error estimates to assess the skill of TES retrievals in the presence of clouds. Global TES SST retrievals for Nov 4-16, 2004, are compared against the Reynolds Optimally Interpolated SST (ROI SST) (information on the Reynolds OI SST can be obtained from: http://podaac-www.jpl.nasa.gov/sst/) (Smith, *et al.,* 1994).

8.3 Data

There were seven TES global surveys Nov. 4-16, 2004 inclusive. SST differences are denoted as TES – ROI.

The TES 1B2 filter that spans the spectral range between 950 cm^{-1} and 1150 cm^{-1}, which encompasses the 9.6 μm ozone band, has been used with version 2 data (release 9 retrieval software) to retrieve surface temperature, emissivity (over land), atmospheric temperature, water vapor, and ozone. This spectral band is not optimal for retrieving temperature and water in general, however for the November data analyzed the signal to noise (NESR) in the pre-selected bands covered by the 2A1 and 2B1 filters (Worden, J., *et al*. 2006) was not sufficient to allow their use.

8.4 Clouds Optical Depth and Degrees of Freedom of Signal Distributions

The TES retrieval algorithm estimates an effective cloud optical depth for all target scenes. The November retrievals provide an initial look at cloud OD distribution data and the overall performance of the TES retrieval method. A study done by (Kulawik, *et al.* 2005) has shown that retrievals with effective cloud ODs less than 0.1 give essentially the same results for atmospheric profiles as cloud free retrievals, and that the information retrieved with clouds is still significant for effective OD up to ~1.

Table 8-1 Table showing Retrievals within Cloud Optical Depth Bins

Max Optical Depth	Number of clouds	Fraction of Clouds
0 - 0.05	1482	0.303
0.05 - .1	447	0.091
.1 - .2	153	0.031
.2 - .3	135	0.028
.3 - .4	104	0.021
.4 - .5	125	0.026
-.6	144	0.029
-.7	144	0.029
-.8	122	0.025
-.9	110	0.022
-1.0	101	0.021
-1.1	92	0.019
-1.2	93	0.019
-1.3	78	0.016
-1.4	71	0.015
-1.5	69	0.014
-1.6	61	0.012
-1.7	63	0.013
-1.8	56	0.011
-1.9	60	0.012
-2.0 or greater	1180	0.241

Degrees of freedom of signal for sea surface temperature has a very different distribution, see table below. The number of retrievals drops off with increasing DOFS from 0 to 0.6 and then goes up a bit, leveling off at ~6% per 0.1 DOFS bin.

Table 8-2 Table showing Retrievals within 0.1 DOFS Bins

DOFS SST	# Retrievals	Fraction Retrievals
0.0	1214.00	0.248313
0.1	908.000	0.185723
0.2	667.000	0.136429
0.3	309.000	0.0632031
0.4	247.000	0.0505216
0.5	212.000	0.0433627
0.6	208.000	0.0425445
0.7	224.000	0.0458171
0.8	302.000	0.0617713
0.9	301.000	0.0615668
1.0	297.000	0.0607486

The SST DOFS is a critical quantity because it encompasses both the information content of the SST retrieval and the sensitivity of the retrieval. This is because, as SST is a scalar quantity, the DOFS is both the averaging kernel and the trace of the averaging kernel. The estimate for SST can be written as:

$$SST_i = SST_a + DOFS*(SST_{True} - SST_a) + \varepsilon \qquad \text{(Equation 8-1)}$$

Where SST_i is the updated (optimal) estimate, SST_a is the *a priori* sea surface temperature, SST_{True} is the true SST, and ε is the error. Because SST defines the brightness temperature of the nadir absorption spectra (due to the well defined emissivity), SST provides a self-consistent verification of the information processing system from operation of the instrument through the radiative transfer model used by TES and the accuracy of the calibration algorithm. Because SST is a surface quantity the SST DOFS also serves as a measure of how well TES overall sees to the surface through the atmosphere including below clouds which have broad spectral features. Therefore, once we determine a level of SST DOFS that meets some sensitivity requirements, we can conclude that the sounding of atmospheric constituents both above and below the cloud contains useful information retrievable from the spectra observed.

8.5 Comparison to ROI Data

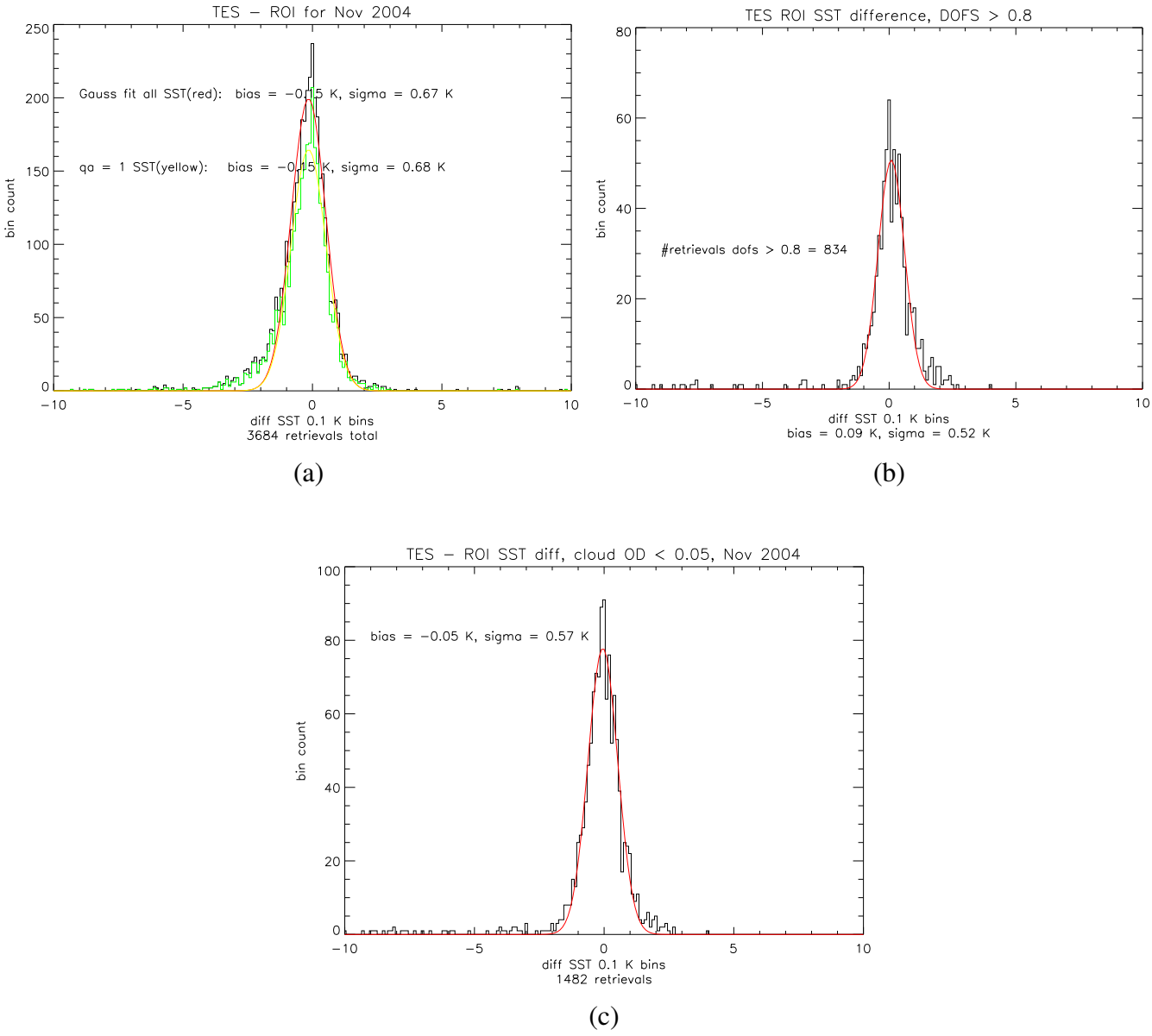

Figure 8-2 Histograms and Gaussian Fits to TES-ROI. (a) Black histogram is all Data - Fit by red Gaussian. Green Histogram is QA = 1 (good) fit by yellow Gaussian. (b) Histogram and Fit for DOFS > 0.8 (c) Histogram and Fit for Cloud OD < 0.05.

To understand the SST differences between TES and ROI we plot the histograms in Figure 8-2 which is the number of SST differences in 0.1 K bins. The distribution is strongly peaked near 0 K difference and can be fit reasonably well by a Gaussian distribution as shown in red. The key statistics TES - ROI, the RMS difference between TES and the comparison data set and the average temperature difference, or bias, are seen in Table 8-3, below.

Table 8-3 Bias, Sigma and RMS Statistics

Data	Bias (K)	Sigma (K)	RMS (K)	# Retrievals Compared
All data	-0.15	0.67	1.77	4625
Data w/QA = 1	-0.15	0.68	1.77	3684
Cloud OD < 0.05	-0.05	0.57	1.26	1482
DOFS ≥ 0.8	0.09	0.52	1.30	834

The hypothesis is that biases indicate simple systematic errors between the data sets, which can be subtracted out once they are documented, but the RMS differences contain both more complex systematic errors and uncorrelated errors due to instrument effects. Note that TES – ROI shows a slightly enhanced positive wing and a more enhanced negative wing in the histogram showing all data, Figure 8-2 (a), but for both filtering by DOFS and cloud optical depth the negative wings have been removed in Figure 8-2 (b and c).

Gaussian fits to the difference distributions have significantly smaller 1σ widths than the TES – ROI RMS widths as seen above in the table. Unsurprisingly the RMS is dominated by the outliers which the Gaussian fits have filtered out. DOFS of SST or cloud OD can be used as filters in preferentially reducing the outliers giving a physical basis for the non-normal statistics of the complete distribution.

In Figure 8-3 we see that the difference distributions do not have a significant latitudinal component between 60° S and 60° N. Therefore the temperature retrievals are not affected by latitudinal variations in calibration (due to instrument temperature drift from changing insolation), the SST itself, or variations of radiance over this range. Analysis of higher latitudes has not yet been done because the TES data sets do not flag sea ice.

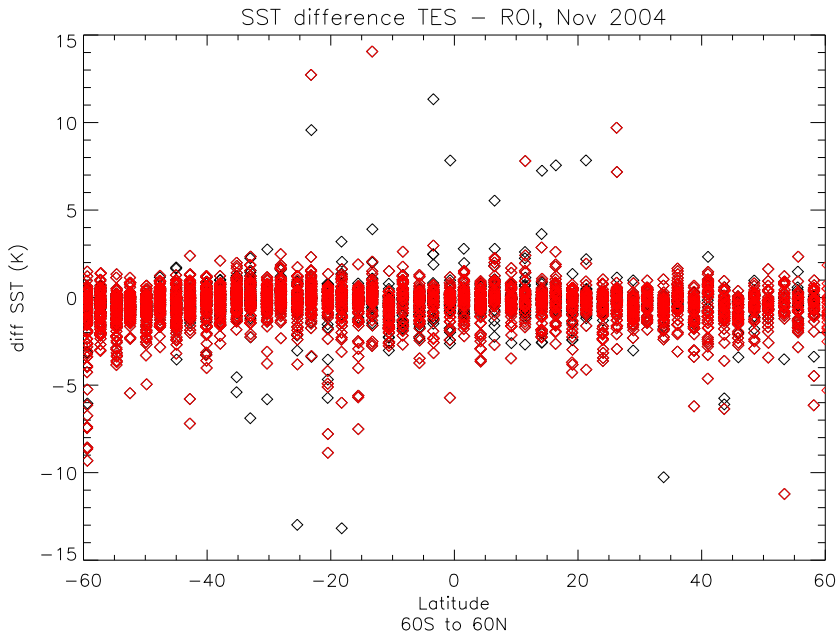

Figure 8-3 SST Differences vs. Latitude. Black shows all data, red shows data with QA = 1 (good).

8.6 Derived RMS SST Error from Comparison to AMSR-E

TES has a similar relative 1σ difference in temperature, on the order of 0.55 K for the most stringent filtering. If the 1σ width of the Gaussian is assumed to represent the RMS difference of uncorrelated measurements free of systematic errors and unaccounted for bias, then the 1σ width of the distribution, $diff_{RMS}$, is composed of the actual RMS errors of TES and ROI added in quadrature:

$$diff_{RMS} = \sqrt{TES_{RMS}^2 + ROI_{RMS}^2} \qquad \text{(Equation 8-2)}$$

Using this equation and taking the RMS error of ROI to be 0.4 - 0.5 K then the RMS error of TES is 0.23 - 0.38 K. The TES SST error is unlikely to be this small in reality. It is more likely that a high degree of correlation exists between ROI and TES. Further investigation will be required. Nonetheless it is reasonable to state that the overall RMS error of TES SST is about 0.5 K in line with the RMS error of ROI. Further, it is clear that TES does add information to the *a priori* in cases where Cloud OD < 0.05 or DOFS $\geq$ 0.8.

8.7 References

[1] Beer, R., 2006: TES on the Aura Mission: Scientific Objectives, Measurements and Analysis Overview, *IEEE Transactions on Geoscience and Remote Sensing* Special Issue on Aura, vol. 44, no. 5, May 2006.

[2] Masuda, K.T., Takashima and Y. Takayama, 1988: Emissivity of pure and sea waters for the model sea surfaces in the infrared window regions, Remote Sens. Environ, 24, 313-329.

[3] Bowman, K., et al. 2006: Tropospheric Emission Spectrometer: Retrieval Method and Error Analysis, *IEEE Transactions on Geoscience and Remote Sensing* Special Issue on Aura, vol. 44, no. 5, May 2006.

[4] Smith, T. M., R. W. Reynolds and C. F. Ropelewski, 1994: Optimal Averaging of Seasonal Sea Surface Temperatures and Associated Confidence Intervals (1860-1989). *J. Climate*, 7, 949-964.

[5] Worden, H. et al. 2006: TES L1 Algorithms: Interferogram processing, geolocation, radiometric and spectral calibration, *IEEE Transactions on Geoscience and Remote Sensing* Special Issue on Aura, vol. 44, no. 5, May 2006.

[6] Kulawik, S., et al. 2005: Implementation of Cloud Retrievals for Tropospheric Emission Spectrometer (TES) Atmospheric Retrievals – part I description and characterization of errors on trace gas retrievals, Submitted to *Journal of Geophysical Research - Atmospheres,* October 3, 2005

9. Comparison of TES Water Vapor with Sondes

A number of comparisons have been made between TES v002 water vapor and other data sources, including AIRS, aircraft, and sondes. The unique complication with water is variability over short distances. Therefore, the key to water validation is to perform statistics on large datasets to determine possible biases. The most mature of all these analyses is the comparison to sondes and that work is presented in this document. Comparisons between TES water vapor and AIRS and in situ aircraft measurements will be included in future versions of this report.

TES retrieves water vapor in the troposphere, with a sensitivity that decreases significantly at pressures less than 150 hPa, as shown below (Figure 9-1) in a plot of TES averaging kernels for water vapor. In the upper troposphere, TES has greater sensitivity to water in the tropics than at higher latitudes because the abundance of water is greater in the tropics (on a given pressure level).

For these comparisons, the TES retrievals were selected based on the recommended data quality screening. The following quality flags were applied specifically for TES water vapor retrievals:

SurfaceEmissMean_QA:	-0.1 to +0.1
KDotDL_QA:	-0.45 to +0.45
LDotDL_QA:	-0.45 to +0.45
CloudTopPressure:	90 to 1300 hPa
RadianceResidualMean:	-0.3 to +0.3
RadianceResidualRMS:	less than 1.4

TES water vapor is reported from the H_2O/HDO joint retrieval step, which comes after the O_3/H_2O/T joint retrieval step.

9.1 Comparison of TES Water Vapor with Sondes

A number of comparisons have been made between TES Level 2 v002 water vapor and other data sources, including AIRS, aircraft, and sondes, refer to Version 1 of the TES Validation Report for the TES v002 comparison results. The bulk of the more recent TES reprocessed v003 comparisons have been with radiosondes. The unique complication of water vapor comparisons is the variability over short distances. The following is a summary of the results presented in Shephard et al., (2007a).

TES retrieves water vapor in the troposphere in nadir viewing, with a sensitivity that decreases significantly at pressures less than ~200-300 hPa, as shown below (Figure 9-1) in a plot of TES averaging kernels for water vapor. In the upper troposphere, TES has greater sensitivity to water in the tropics than at higher latitudes because the abundance of water is greater in the tropics (on a given pressure level). The following comparison results and discussion are taken directly from Shephard et al., (2007a).

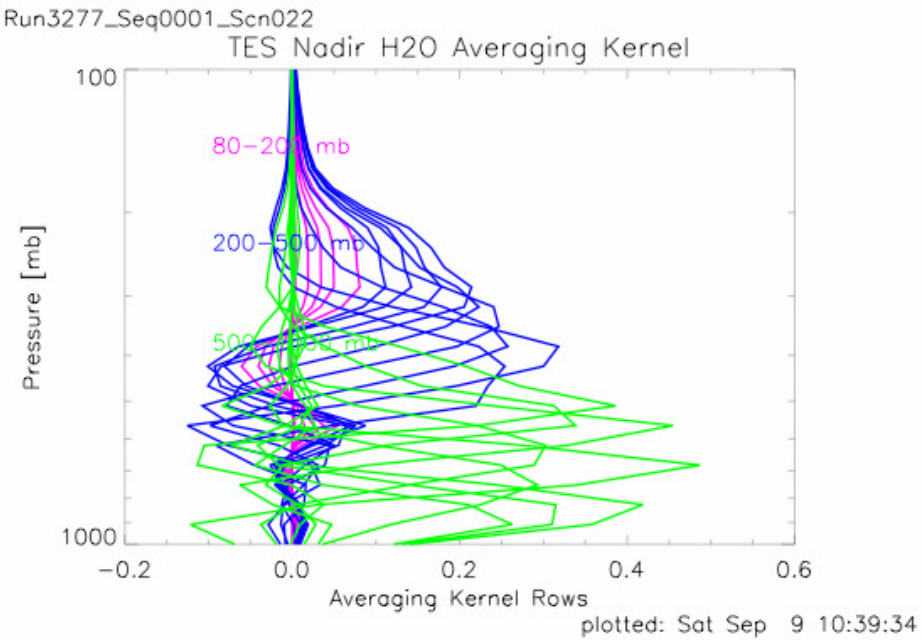

Figure 9-1 TES Nadir Water Vapor Averaging Kernel from a good Tropical Retrieval (Runid 3277, Sequence 1, Scan 022) Demonstrates Excellent Sensitivity and Vertical Resolution throughout the Troposphere, up to 150 hPa.

The main objective for obtaining satellite retrieved water vapor measurements has traditionally been to improve numerical weather prediction (NWP) (Smith, 1991). Providing water vapor profiles or spectral radiances for assimilation into NWP models is still the main objective of many current satellite sensors, for example AIRS (Tobin et al., 2006; Divakarla et al., 2006). However, for TES, the requirement is to obtain the most likely state of the atmosphere within the field-of-view of the measurement. This applies whether water vapor is a tracer of air mass, of chemical interest, or whether it is an interferent. The central objective of TES is the measurement of global profiles of tropospheric ozone and its precursors, of which water is a key one. Many validations of water vapor retrievals rely heavily on profiles obtained from radiosonde measurements.

In order to validate satellite retrieved profiles and investigate any systematic differences there are four critical elements that must be evaluated: (1) the accuracy of the spectral radiometric measurements; (2) the quality of the forward model calculations; (3) the role of the retrieval procedure (e.g. impact of uncertainties in the retrieved cloud and temperature); and (4) the accuracy of the characterization of the radiating atmospheres used in the validation (e.g. measurement uncertainties and error that occur from different spatial and temporal sampling of the atmosphere). To provide insight into the roles of these elements we consider each of these in turn by performing radiance closure studies. In particular we look in detail at the spectral radiances from selected cases from the WAVES_2006 campaign.

9.1.1 TES Retrieval Comparisons with *In situ* Sonde Measurements

Presented are results from TES retrievals versions V002, which have been available from the NASA Langley Distributed Active Archive Center (DAAC) since March 2006, and from newly released V003. The main differences between V002 and V003 that influence the TES water

vapor retrievals are: (i) improved TES temperature retrievals due to inclusion of the CO_2 ν2 spectral region with improved CO_2 forward model calculations (Shephard et al., 2007b); (ii) the migration of TES initial guess and *a priori* from GEOS-4 to GEOS-5; (iii) a lowered minimum value for the *a priori* cloud optical depth in order to better handle clouds with lower optical depths; and (iv) the addition of more surface microwindows to help characterize the surface.

9.1.1.1 Global Comparisons of TES Water Vapor Retrievals with Vaisala Radiosondes

Results from TES water vapor retrieval comparisons with global distributed National Weather Service's Centers for Environmental Prediction (NCEP) Vaisala RS90 and RS92 radiosondes are presented in Figure 9-2 and Figure 9-3. The coincidence criteria for matches between radiosonde launches and TES overpasses is within 3 hours and 100 km. Only the more accurate nighttime radiosondes measurements are used in the comparison. We also screened the comparison using the TES quality flag and eliminated scenes in which the TES cloud effective optical depths > 1.0. Additional plots are provide in Figure 9-2 and Figure 9-3 for a subset of comparisons where the TES cloud effective optical depths are less than or equal 0.1. Comparing Figure 9-2 and Figure 9-3 shows that in general there is about a 5% improvement in the mean differences below ~500 hPa in going from V002 to V003. TES V003 comparisons that include clouds with effective optical depths up to 1.0 have mean comparison differences of 5-10% in the lower troposphere (below 700 hPa) with the radiosonde being drier. This sonde dry bias compared with the TES observations increases to a maximum of ~20% in the middle-to- upper troposphere between ~300-400 hPa. The mean difference above ~300 hPa starts to decrease with decreasing TES water vapor retrieval sensitivity in the nadir. The TES V003 comparison in Figure 9-3 for the subset with reduce cloud influence shows steady decrease in the mean difference from the ~20% maximum at ~300 hPa to ~10% at ~400 hPa. From ~400 hPa down to the surface the difference remains relatively constant at ~10%.

The comparisons between the TES retrievals and the radiosondes show large variability in the differences. This is to be expected considering that there is no real "truth" due to known errors in the Vaisala RS90 and RS92 radiosondes, which had no corrections applied, and the inherent sampling errors of comparing point source observations with satellite observations that are not often observing the same air mass. Therefore, without additional information the conclusions that can be drawn about the performance of the TES water vapor retrieval from this type of general profile comparison of retrievals with radiosondes are limited as it difficult to analyze the potential causes for the comparison differences (e.g. measurement uncertainties, forward model error, retrieval errors, sampling errors, etc.). In order to approach a validation of the TES water vapor retrievals to obtain the most likely state of the water vapor field within the field-of-view of the TES observations, further steps have to be taken in order to characterize the systematic errors and ensure that the TES/sonde sampling error is minimized in the comparisons. The following section describes detailed comparisons where other coincident water vapor observations and radiance closure studies are used to select comparisons with sondes that better represent the true air mass being observed by TES.

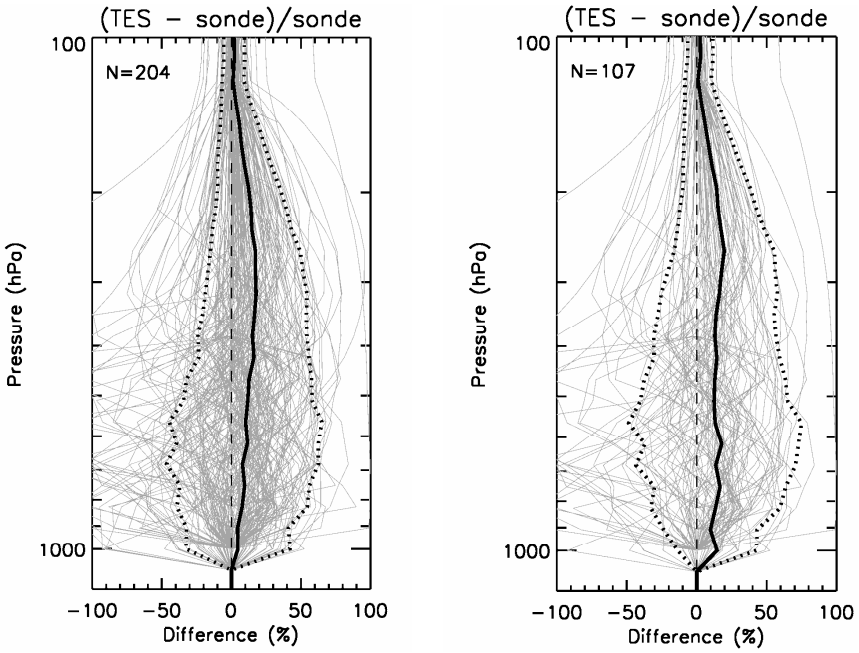

Figure 9-2 Global comparisons of TES V002 water vapor profiles with the Vaisala RS90 and RS92 radiosondes from NCEP. The coincidence criteria are within 100 km and 3 hours of a TES overpass. Only nighttime profiles are included. The dark solid lines are the mean differences and the dotted lines are the 1-sigma standard deviation. The thin grey lines are all the individual comparisons. A similar plot is also included on the right hand side that contains comparisons where the TES effective cloud optical depth is less than or equal to 0.1.

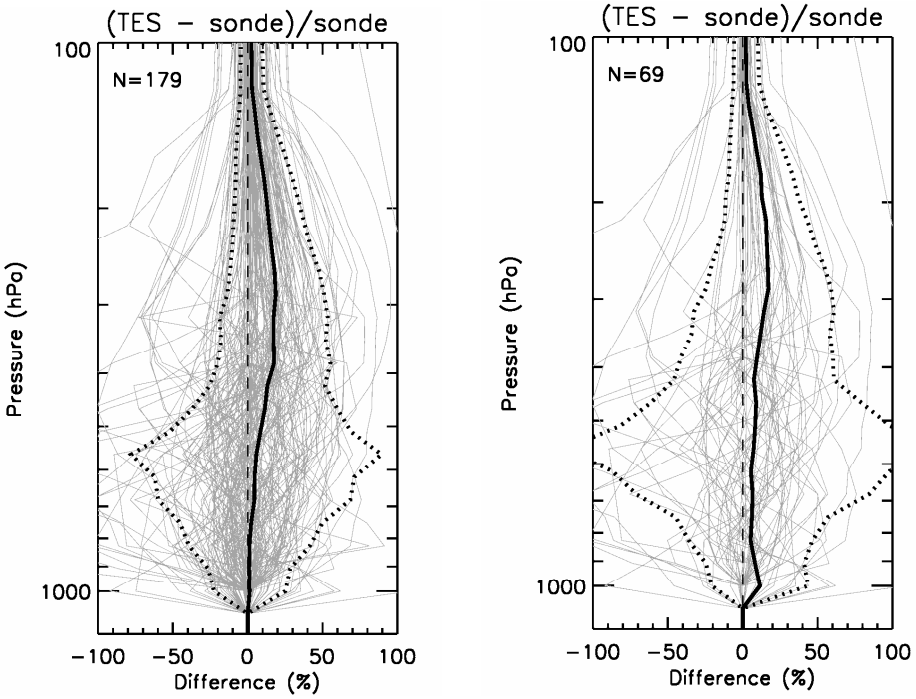

Figure 9-3 Similar plot as Figure 9-2, but for TES V003 retrievals.

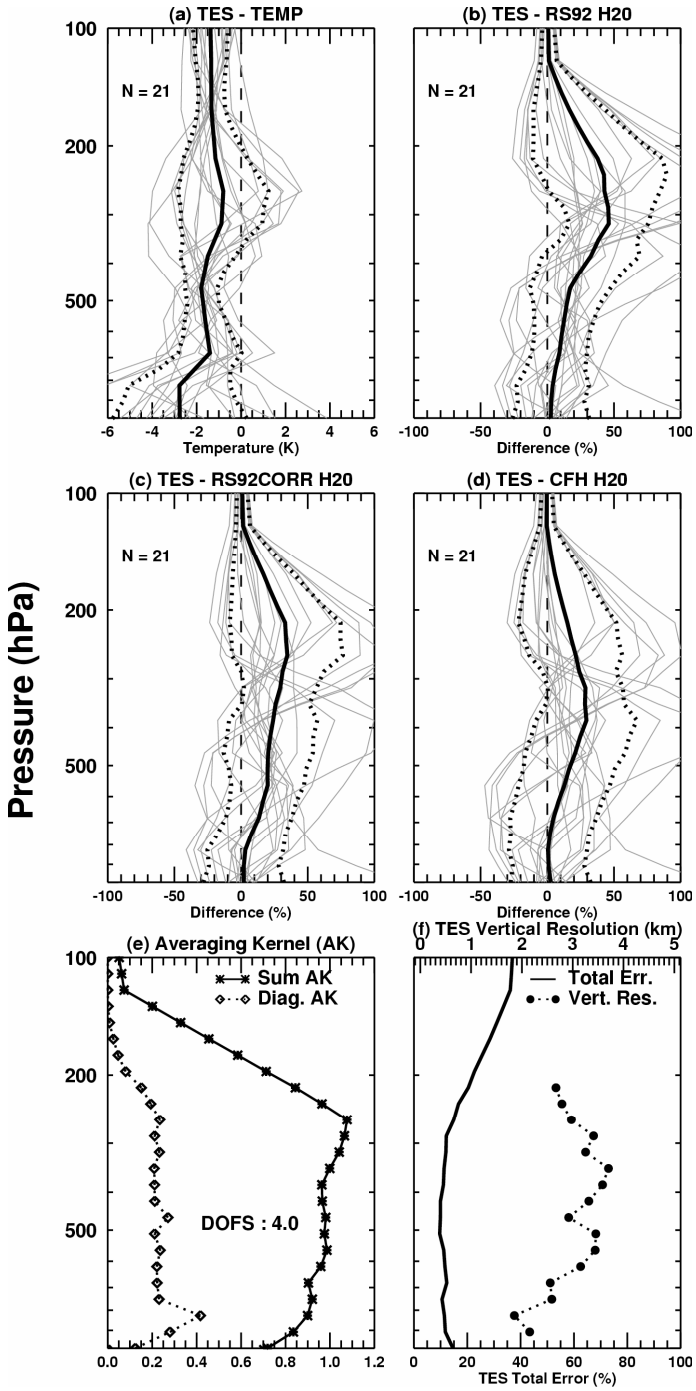

Figure 9-4 TES V002 comparison with sondes during WAVES_2006. The comparison consists of 21 nighttime match-ups that have a coincidence criteria of 60 km and 1.5 hours. The top four sets of plots compare the TES retrievals with the sondes. For these plots the solid lines are the mean difference, the dotted lines are the 1-sigma difference, and the thin grey lines are all the individual comparisons. Plots (a) is the RS92 temperature comparison, which is included for the purpose of determining its impact on the water vapor retrievals. Plots (b), (c), and (d) are the water vapor comparisons with the RS92, the RS92 with an empirical correction applied based on the CFH, and the CFH, respectively. Plot (e) shows the median value of the diagonal of the

averaging kernels and the sum of the rows of the averaging kernels of all 21 cases. The total degrees-of-freedom for signal (DOFS) is also labeled on Plot (e). Plot (f) shows the median value of the estimated TES Total Error generated from the square roots of the diagonal elements in the output total error covariance matrix, which includes systematic errors, measurement errors, and retrieval smoothing errors. Plot (f) also contains the vertical resolution of the TES water vapor retrieval plotted as a function of pressure, which is computed from the full-width-at-half-maximum of the rows of the averaging kernels.

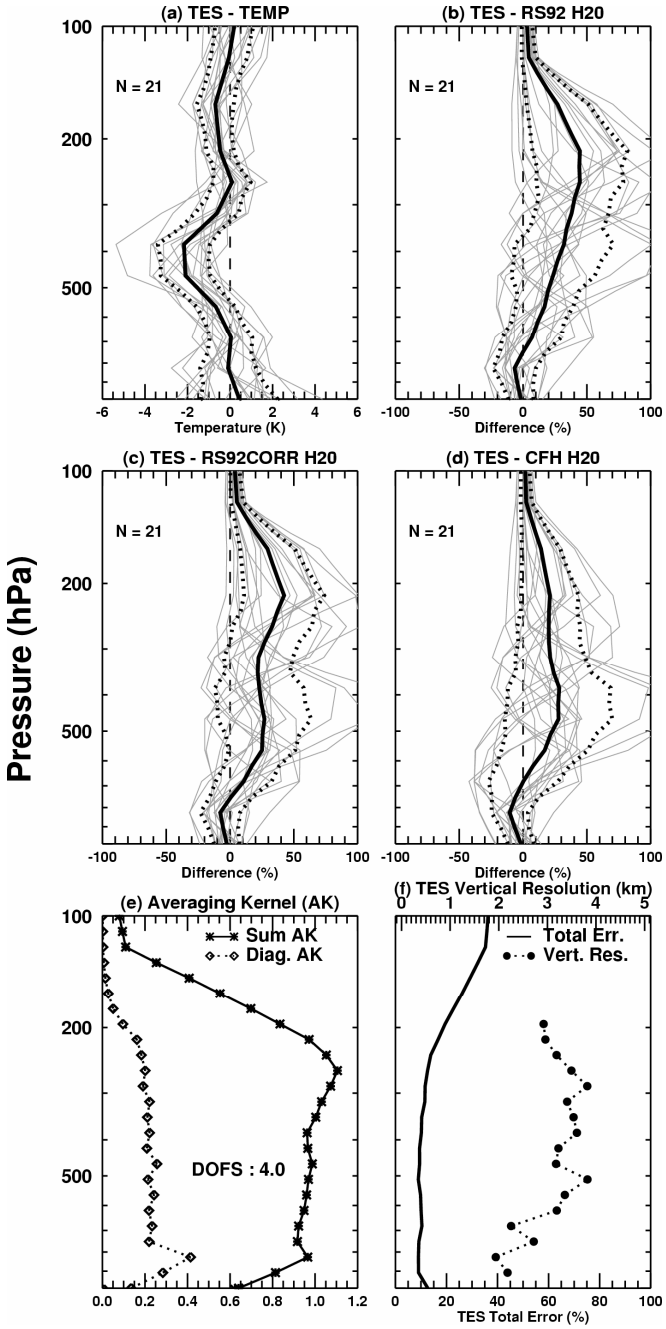

Figure 9-5 TES V003 comparison with sondes during WAVES_2006. The comparison consists of 21 nighttime match-ups that have a coincidence criteria of 60 km and 1.5 hours. The plotted convention is the same as Figure 9-4.

9.1.1.2 Detailed Comparisons of TES Water Vapor Retrievals with Sondes

In order to investigate the TES retrievals further we focused on water vapor measurements made during the WAVES_2006 campaign. During WAVES_2006 sondes were launched so that they were coincident and co-located with TES-Aura overpasses. To ensure better coincidences during this intensive water vapor measurement period, TES performed special observations in Transect viewing mode over the WAVES_2006 Beltsville, MD, USA site every other day. These Transects scans are spaced 12 km apart providing coverage that is much more dense than the routine TES Global Survey viewing mode. During this experiment Vaisala RS92 humidity sensors and the CFH were flown on the same balloon. This facilitated the comparison between the Vaisala RS92 and the CFH and the derivation of Miloshevich (2004, 2006) RS92 empirical correction. During WAVES there were 21 TES nighttime overpasses that were within 60 km and 1.5 hrs of a CFH launch. Figure 9-4 and Figure 9-5 show the comparison results for the 21 cases with both TES V002 and V003, respectively. The TES/RS92 comparisons are similar to the global NCEP comparisons in Figure 9-2 and Figure 9-3. TES/CFH comparisons are better in the upper troposphere (~300 hPa to the tropopause) than the TES/RS92 comparisons, which is expected since the CFH provides more accurate observations in the upper troposphere. However, the comparison differences between the TES water vapor retrievals and the sonde observations are large. To investigate this further, comparisons were selected from this set to study in detail using supporting WAVES_2006 water vapor observations and radiance closure studies.

On August 12, 2006 there was a CFH launch at 06:01 UTC and a TES Transect overpass an hour and 18 minutes later at 7:19 UTC. TES Run 4803, Sequence 0001, Scan 20 is selected as it was 0.45 km from this balloon launch site.

Figure 9-6 contains profile comparisons of the TES retrieved profile, the a priori (GMAO), and the RS92 with the CFH for Scan 20. Since the goal of this study is to validate TES retrievals, the TES averaging kernels and a priori were applied to the sondes. A radiance closure analysis is performed to provide more information on the differences.

The Line-By-Line Radiative Transfer Model (LBLRTM) is the forward model used by TES (Clough et al., 2005, 2006). LBLRTM was used to calculate radiances from the CFH, a priori (GMAO), RS92, and TES retrieval profiles. All the radiances were converted to brightness temperatures. Figure 9-7 is the radiance closure study for Scan 20. The highlighted red areas are the spectral regions to focus on in all the panels of Figure 9-7 as they are the TES microwindows used in the retrievals. The brightness temperature residuals corresponding to the profiles being compared in Figure 9-6 are shown in panels (a), (b), (c), and (d). Since the MODIS cloud fraction, the TES inter-pixel variability, and the lidar profiles suggest that there were no detectable clouds during the time of the TES overpass, the radiance calculations for the sonde profiles in panels (a), (b), and (c) were computed assuming there were no clouds. An important goal of these closure studies is to determine how well the sonde profiles sampled the true atmospheric state being observed by TES. If the sonde sampled the true atmospheric state being observed by TES then the brightness temperature residuals (TES observations - forward model calculations) would be no larger than the radiance contribution from the combined systematic errors from the forward model, TES instrument errors, the sonde water vapor and temperature measurement errors, and the cloud retrieval errors (if present). Negative (TES-Sonde) brightness temperature residuals in the water vapor lines greater than the systematic errors indicate that there is not enough water vapor in the part of the profile corresponding to that spectral region.

Conversely, positive residuals indicate that there is too much water vapor at these levels. Assuming that there are no clouds, the contribution to the brightness temperature residuals from the systematic errors due to uncertainties in the CFH measurements (Vömel et al., 2007b), the forwarded model error (Shephard et al., 2007c; Rothman et al., 2003; Gordon et al., 2007), and temperature retrieval errors (refer to Figure 9-5 (a) and the more detailed analysis in Herman et al., (2007)) are of the order of half a degree each (see Figure 9-7 (f)). The TES instrument measurement systematic error is determined from TES radiance validations (Shephard et al., 2007b) are on the order of tenths of a degree Kelvin. Note that it is difficult to compute a total systematic error value at this stage as the extent of the interdependence of the systematic errors is not known. (i.e. the systematic errors can only be additive if they are independent). However, even if all these errors were independent and additive then an estimate of the total systematic error would be on the order of ~1.0K (center of the water vapor lines).

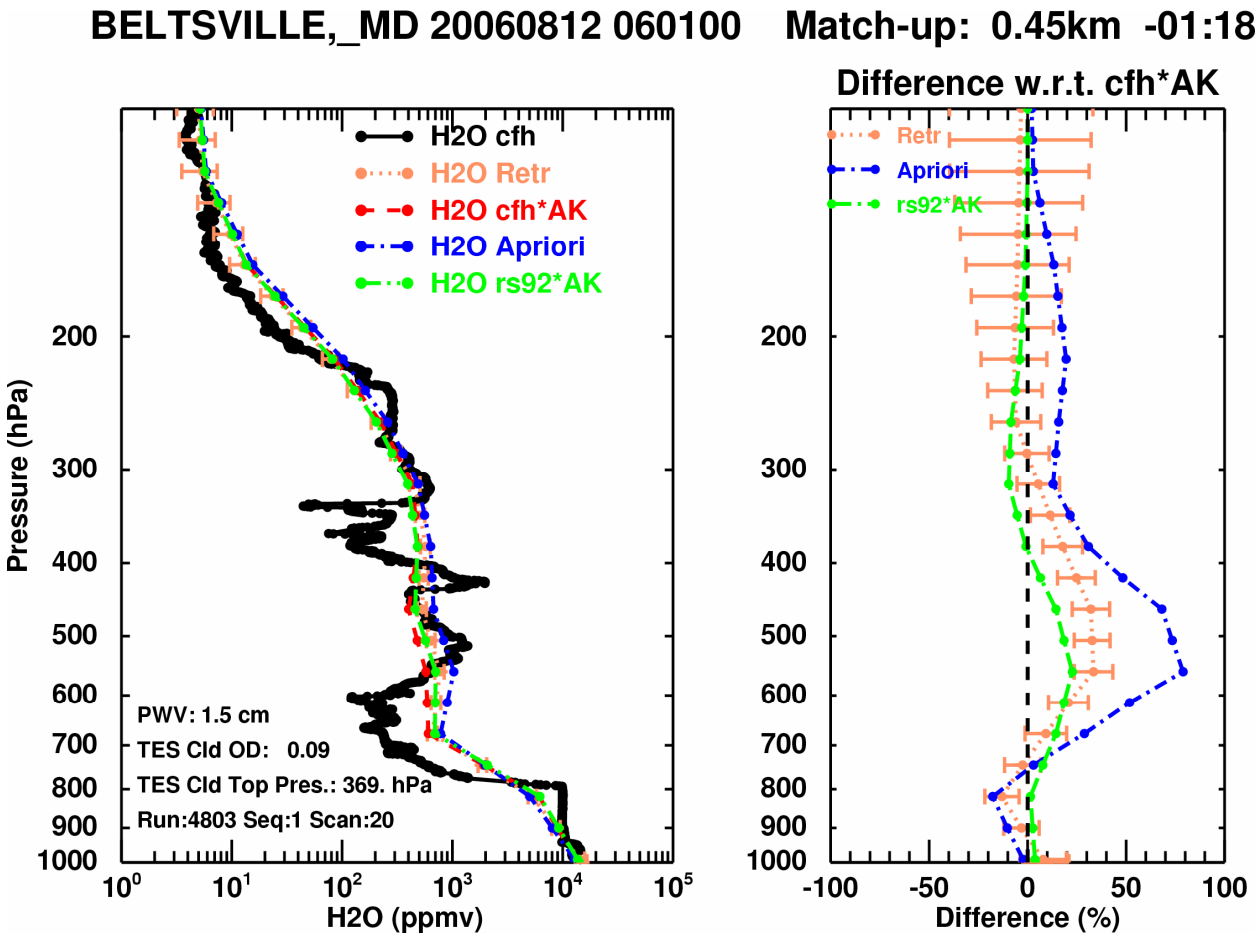

Figure 9-6 This is a CFH comparison plot on August 12, 2006 that corresponds to TES Scan 20. The CFH launch was launched 12.5 km away and an hour and 17 minutes before this TES scan. The left plot shows the observed CFH profile (black), the *a priori* profile (GMAO) (blue), the TES retrieved profile (salmon), and the CFH (red) and RS92 (green) profiles with the TES *a priori* and averaging kernels applied(AK). The right plot is the relative percent differences (Profile-CFH/CFH)x100 of the different profiles with respect to the CFH with the TES *a priori* and averaging kernel applied (dotted line at zero).

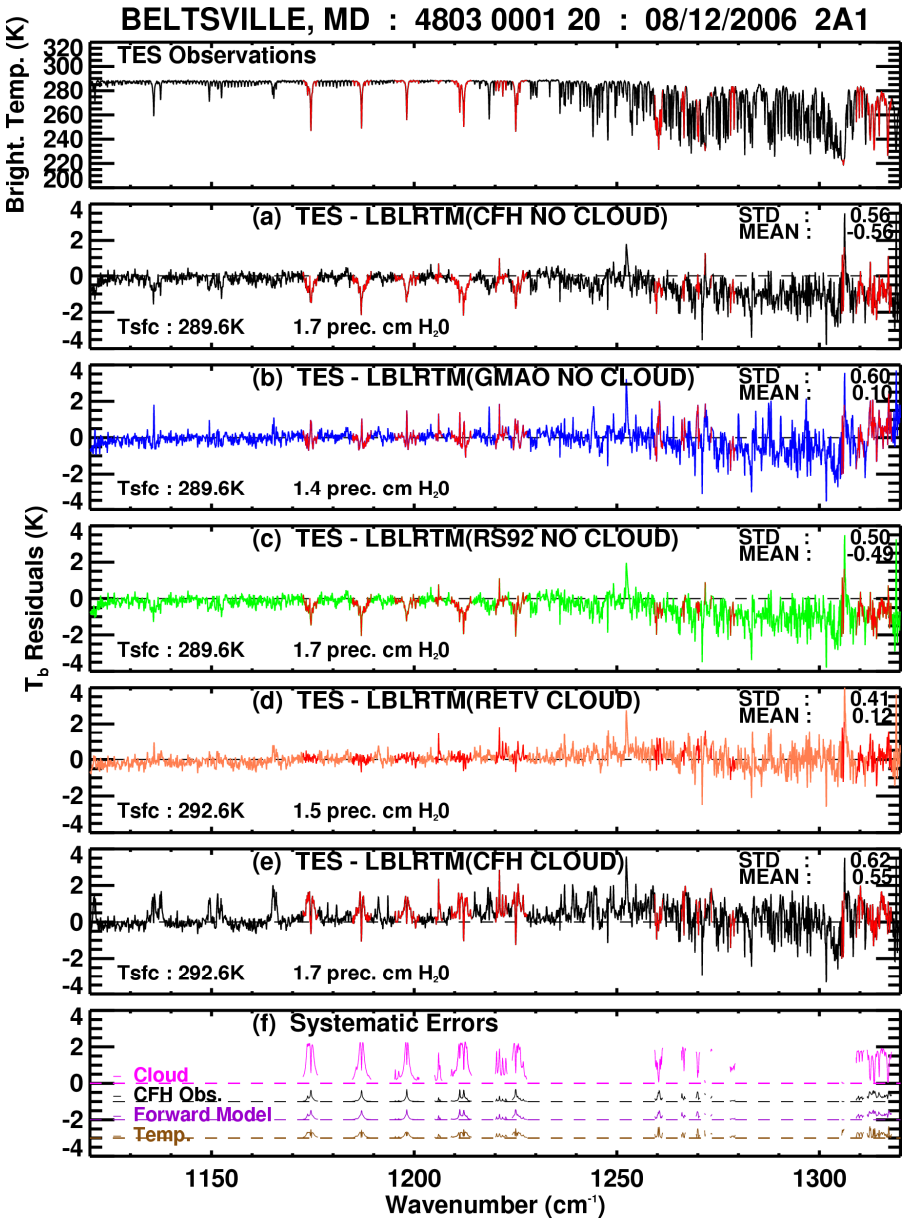

Figure 9-7 Radiance closure study for the WAVES_2006 comparison on August 12, 2006 of sondes with for TES Scan 20. The red in all the panels indicates the microwindows where the TES retrieval was performed. The top panel is a plot of the observed TES spectrum. The subsequent panels are residual plots of: (a) TES – LBLRTM calculated spectrum using the CFH specified atmosphere with no clouds, (b) TES – LBLRTM calculated spectrum using the TES *a priori* (GMAO) specified atmosphere with no clouds, (c) TES – LBLRTM calculated spectrum using the RS92 specified atmosphere with no clouds, (d) TES – LBLRTM calculated spectrum using the TES retrieved atmosphere including cloud optical depths (e) TES – LBLRTM calculated spectrum using the CFH atmosphere including TES retrieved cloud optical depths. The bottom panel (f) shows contributions in the TES microwindows from estimates of systematic errors in the retrieved cloud optical depths, uncertainties in the CFH observations (plotted with a –1K offset), forward model water vapor calculations (plotted with a –2K offset), and retrieved temperature profile (plotted with a –3K offset).

The negative residuals in Figure 9-7 (a) are a little larger than the estimated total systematic errors, which indicate that the CFH is a little drier than the atmosphere being observed by TES. The larger brightness temperature residuals of ~2K correspond to the middle troposphere (~500 hPa), which are where the profile differences in Figure 9-6 are the largest compared with the CFH. The positive residuals in Figure 9-7 (b) for the *a priori* (GMAO) profile are larger than the systematic errors, indicating that there is too much water vapor in the middle to upper troposphere levels of the profile. The small residuals from the spectral regions with the signal coming from the lower part of the troposphere (greater than ~800 hPa) indicate that the *a priori* profile agrees well with the TES observations in this part of the atmosphere. The negative residuals in Figure 9-7 (c) for the RS92 are a little smaller than the CFH, which shows that in this case the RS92 is a little closer to sampling the atmosphere being observed by TES. The magnitude and sign of brightness temperature residuals in Figure 9-7 panels (a), (b), and (c) are greater than the estimated total systematic errors and are consistent with profile differences between the TES retrieved profile and the other sondes. This suggests that the large profile comparison differences are due to the fact that the sondes are not sampling the same air mass as TES. Figure 9-7 (d) shows the residuals obtained by comparing the TES observations with the calculated radiances generated using the TES retrieved profile. This demonstrates that the TES retrieval was effective in minimizing the residuals.

The TES retrieved effective cloud optical depths are reported spectrally (Kulawik et al. 2006b; Eldering et al 2007) with an average value of 0.09 at a cloud top pressure of 369 hPa for Scan 20. This high altitude, optically thin cloud is assumed to be cirrus. This radiance closure study also provides valuable insight into the impact of clouds under these conditions. Forward model calculations with the CFH atmospheric state and retrieved cloud optical depths (Figure 9-7 (e)) are compared with the calculations without clouds (Figure 9-7 (a)). The results show that these cirrus type clouds have a significant impact on the water vapor residuals near the surface and the retrieved surface temperature (retrieved surface temperature difference is 3K). Since minimizing these residuals is the fundamental operation in the retrievals, it is important to reduce the retrieval uncertainty as much as possible under these conditions. Presently the TES operational retrieval of effective optical depths have large uncertainties for effective optical depths less than a few tenths and greater than two (Kulawik et al., 2006b). The radiance residuals from the TES reported uncertainties in the effective cloud optical depths are plotted in Figure 9-7 (f). Retrievals under these conditions are challenging and a number of refinements are being considered by the TES science team in order to reduce the uncertainty in the cloud retrievals. One possible approach would be to constrain the retrieval in such a way that the effective cloud optical depths represent the spectral signature of clouds, which will help distinguish retrieved clouds from other retrieved parameters (e.g. land surface emissivity). Another suggestion is to utilize more explicitly the TES inter-pixel variability in the retrieval process so that cloud-free cases can be more accurately identified, thus removing the impact of cloud uncertainty for these cases.

9.1.2 Discussion

Global comparisons of TES water vapor retrievals with nighttime NCEP Vaisala RS90 and RS92 radiosondes show a 5-10% bias in the lower troposphere (below 700 hPa) with the TES retrievals being moist with respect to the sondes. This sonde dry bias compared with the TES observations increases to a maximum of ~20% in the middle-to-upper troposphere between ~300-400 hPa. These global comparisons also show a significant variability in the comparisons of TES

retrievals with the *in situ* radiosonde measurements. This variability might be expected since water vapor is variable in the atmosphere over short distances and can change rapidly and balloon-borne *in situ* observations drift with the wind and take approximately an hour to ascend to their maximum altitude. This makes the use of *in situ* observations as truth to validate instantaneous satellite water vapor profiles challenging. Comparisons with *in-situ* water vapor measurements from sondes do help identify issues with satellite retrievals, but often the inherent sampling errors limit the degree to which the profiles alone can be used to validate TES water vapor retrievals. We demonstrated that even under relatively benign conditions where there is a "very good" coincidence between TES and the sonde (e.g. 12 km and 1 hour) there can be large differences many due to the fact the sonde is not sampling the same air mass as TES. The comparison results between TES and the CFH is 5-10% in the lower troposphere, and 5-40% in the middle troposphere (700-300 hPa). Radiance closure studies and a suite of water vapor observations were used to help characterize the water vapor variability along the TES transect and help better understand the TES–sonde profile differences. Results from the closure studies indicate that the estimated systematic errors from the forward model, TES measurements, CFH observations, and the retrieved temperature profile and clouds are likely not large enough to account for this TES/CFH systematic difference between 700-300 hPa with the TES observations being moist. Therefore, either there is additional systematic errors that are not being accounted for in the estimates (e.g. spectroscopic errors in the strong absorbing water vapor lines are larger than reported, uncertainties in the CFH observations are larger than documented, etc.), or the differences are due to sampling errors. Another result shown in the detailed comparison is that the retrieval of cloud optical depths under these conditions must be done accurately as high clouds with optical depths of ~10% can have a significant impact on the radiances used to retrieve the water vapor profile.

In order to rigorously validate the TES water vapor retrievals, further detailed comparison studies are needed in which accurate coincident profile observations are determined from using radiance closure studies and accompanied by a suite of other water vapor measurements that capture the water vapor variability and the clouds. The next step in the TES water vapor "validation" will be to perform water vapor comparisons with the purely vertical, remotely sensed profiles from the ground-based Ramon lidar during WAVES_2006 and the proposed air-borne Ramon lidar measurements for WAVES_2007 (Whiteman et al., 2006). In addition, any coincident and co-located retrieval from interferometer instruments will be used for validations.

9.1.3 References

[1] Clough, S. A., M. W. Shephard, E. J. Mlawer, J. S. Delamere, M. J. Iacono, K. Cady-Pereira, S. Boukabara, and P. D. Brown (2005), Atmospheric radiative transfer modeling: a summary of the AER codes, Short Communication, J. Quant. Spectrosc. Radiat. Transfer, 91, 233-244.

[2] Clough, S., M. Shephard, J. R. Worden, P. D. Brown, H. M. Worden, M. Lou, C. Rodgers, C. Rinsland, A. Goldman, L. Brown, A. Eldering, S. S. Kulawik, K. Cady-Pereira, G. Osterman, and R. Beer (2006), Forward model and Jacobians for Tropospheric Emission Spectrometer retrievals, IEEE Trans. Geosci. Remote Sens., 44(5), 1308–1323.

[3] Divakarla, M. G., C. D. Barnet, M. D. Goldberg, L. M. McMillin, E. Maddy, W. Wolf, and L. Zhou (2006), Validation of AIRS temperature and water vapor retrievals with

matched radiosonde measurements and forecasts, J. Geophys. Res., 111, D09S15, doi:10.1029/2005JD006116.

[4] Eldering A, S. S. Kulawik, J. Worden, K. Bowman, G. Osterman, S. A. Clough, M. Shephard (2007), Implementation of Cloud Retrievals for TES Atmospheric Retrievals – part 2: characterization of cloud top pressure and effective optical depth retrievals, Submitted to J. Geophys. Res., this issue.

[5] Gordon, I.E., L. S. Rothman, R. R. Gamache, D. Jacquemart, C. Boone, P. F. Bernath, M. W. Shephard, J. S. Delamere, S. A. Clough (2007), Current updates of water vapor linelist in HITRAN2004: A new "Diet" for air-broadened half-widths, J Quant Spectrosc Radiat Transfer, in press, doi:10.1016/j.jqsrt.2007.06.009.

[6] Herman R.L., M. W. Shephard, B. M. Fisher, H. Vömel, T. P. Bui, L. M. Milosevich, D. N. Whiteman, R. Beer, K. Bowman, S. A. Clough, A. Eldering, M. R. Gunson, S. S. Kulawik, M. Luo, G. B. Osterman, D. Rider, H. M. Worden, and J. Worden (2007), Validation of Tropospheric Emission Spectrometer temperature retrievals with aircraft and sondes, Submitted to J. Geophys. Res.

[7] JPL (2006), TES Level 2 Data User's Guide. Edited by G. Osterman.

[8] Kulawik S. S., G. Osterman, D. B. A. Jones, and K. W. Bowman (2006a), Calculation of altitude-dependent Tikhonov constraints for TES nadir retrievals, IEEE Trans. Geosci. Remote Sens., 44(5), 1334–1342.

[9] Kulawik, S.S., J. Worden, A. Eldering, K.W. Bowman, M. Gunson, G. Osterman, L. Zhang, S.A. Clough, M. W. Shephard, R. Beer (2006b), Implementation of Cloud Retrievals for Tropospheric Emission Spectrometer (TES) Atmospheric Retrievals - Part I description and characterization of errors on trace gas retrievals, accepted to J. Geophys. Res.-Atmospheres.

[10] Miloshevich, L. M., A. Paukkunen, H. Vömel, and S. J. Oltmans (2004), Development and Validation of a Time-Lag Correction for Vaisala Radiosonde Humidity Measurements, J. Atmos. Oceanic. Technol., 21, 1305-1327.

[11] Miloshevich, L. M., H. Vömel, D. N. Whiteman, B. M. Lesht, F. J. Schmidlin, and F. Russo (2006), Absolute accuracy of water vapor measurements from six operational radiosonde types launched during AWEX-G and implications for AIRS validation, J. Geophys. Res., 111(D09).

[12] Rothman LS, A. Barbe, D. C. Benner, L. R. Brown, C. Camy-Peyret, M. R. Carleer, K. V. Chance, C. Clerbaux, V. Dana, V. M. Devi, A. Fayt, J-M. Flaud, R. R. Gamache, A. Goldman, D. Jacquemart, K.W. Jucks, W.J. Lafferty, J-Y. Mandin, S. T. Massie, V. Nemtchinov, D.A. Newnham, A. Perrin, C. P. Rinsland, J. Schroeder, K. M. Smith, M. A. H. Smith, K. Tang, R. A. Toth, J. Auwera Vander, P. Varanasi, and K. Yoshino (2003), The HITRAN Molecular Spectroscopic Database: Edition of 2000 Including Updates through 2001, J. Quant. Spectrosc. Radiat. Transfer., 82, 5-44.

[13] Shephard M.W., R.L. Herman, B.M. Fisher, K.E. Cady-Pereira, S. A. Clough, V. H. Payne, D.N. Whiteman, J. P. Comer, H. Vömel, L.M. Milosevich, Ricardo Forno, M. Adam, G. B. Osterman, A. Eldering, J. R. Worden, L. R. Brown, H. M. Worden, S. S. Kulawik, D. M. Rider, A. Goldman, R. Beer, K. W. Bowman, C. D. Rodgers, M. Luo,

C. P. Rinsland, M. Lampel, M. R. Gunson, Comparison of Tropospheric Emission Spectrometer (TES) Water Vapor Retrievals with In Situ Measurements, submitted to J Geophys Res., 2007a..

[14] Shephard, M. W., H. M. Worden, K. E. Cady-Pereira, S. A. Clough, D. M. Rider, D. C. Tobin, H. E. Revercomb, H. H. Aumann, B. M. Fisher, K. W. Bowman, E. Sarkissian, D. Tremblay, M. Gunson, R. Beer, M. Luo, and G. B. Osterman, Tropospheric Emission Spectrometer Spectral Radiance Comparisons, Submitted to J. Geophys. Res., this issue, 2007b.

[15] Shephard, M. W., S. A. Clough, E. J. Mlawer, V. Payne, K. E. Cady-Pereira, and J. S. Delamere, Line-By-Line Radiative Transfer Model (LBLRTM) Improvements and Validations, in preparation, 2007c.

[16] Smith, W. L. (1991), Atmospheric soundings from satellites - False expectations or the key to improved weather prediction, Q. J. R. Meteorol. Soc., 117, 267-297.

[17] Tobin, C. D., H. E. Revercomb, R. O. Knuteson, B. M. Lesht, L. L. Strow, S. E. Hannon, W. F. Feltz, L. A. Moy, E. J. Fetzer, and T. S. Cress (2006), Atmospheric Radiation Measurement site atmospheric state best estimates for Atmospheric Infrared Sounder temperature and water vapor retrieval validations, J. Geophys. Res., 111, D09S14, doi:10.1029/2005JD006103.

[18] Vömel, H., D. E. David, and K. Smith (2007b), Accuracy of Tropospheric and Stratospheric Water Vapor Measurements by the Cryogenic Frost Point Hygrometer (CFH): Instrumental Details and Observations, J. Geophys. Res., 112, D08305, doi:10.1029/2006JD007224..

[19] Whiteman, D. N., F. Russo, L. Miloshevich, B. Demoz, Z. Wang, I. Veselovskii, H. Voemel, S. Hannon, B. Lesht, F. Schmidlin, A. Gambacorta, C. Barnet (2006), Analysis of Raman lidar and radiosonde measurements from the AWEX-G field campaign and its relation to Aqua validation, J. Geophys. Res., 111, D09S09, doi:10.1029/2005JD006429.

10. Validation of TES HDO/H_2O

TES is capable of measuring HDO in the troposphere from thermal infrared radiances between 1200 and 1350 cm^{-1}. Information on the simultaneous retrieval of HDO and H_2O is provided in Worden et al., 2006, including a description of error characterization and spatial and vertical sensitivities. The TES measurement of HDO is made in the nadir mode and is most sensitive in the region between 450 and 850 hPa.

There are few data sets that can be used for validation of measurements of HDO in the lower troposphere. Worden et al., 2006 provides information on comparison of the HDO/H_2O ratio to prior measurements and models. It has been determined that a bias of 5% may be seen in TES estimates of HDO. This bias could be largely the result of uncertainties in the HDO spectroscopic line strengths. Use of the ratio of HDO/H_2O in scientific analyses lessens the effects of this potential bias in the TES data. An example of an indirect validation of TES HDO is by comparing to the JPL aircraft *in situ* instrument ALIAS. Figure 10-1 shows a comparison of measurements of HDO from both TES and ALIAS from a flight of the NASA WB-57 aircraft near Costa Rica. The two measurements show very similar distributions for HDO.

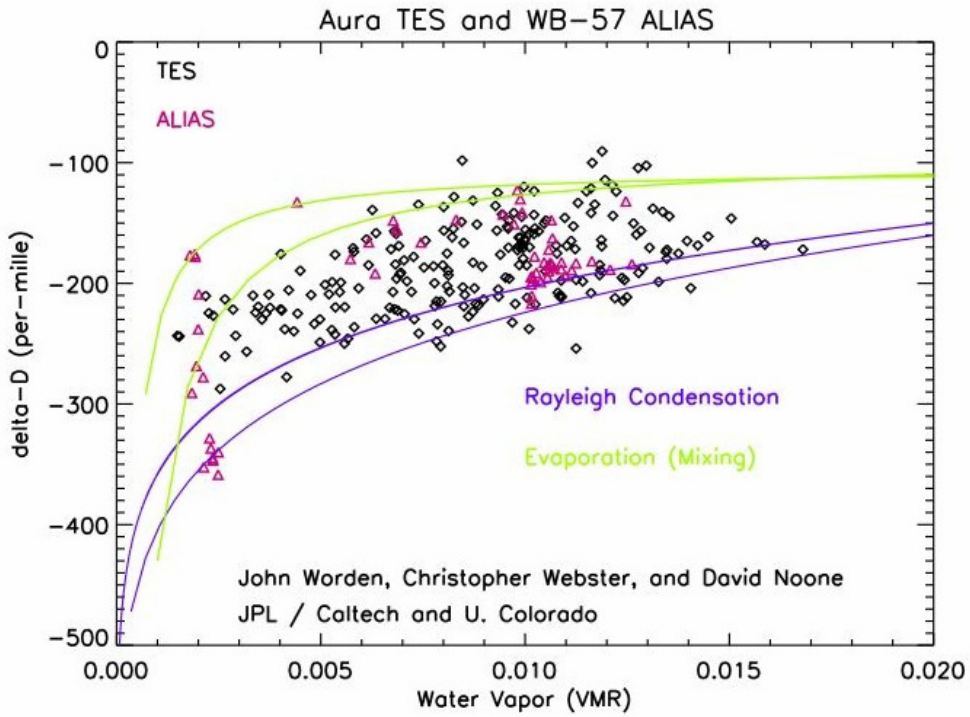

Figure 10-1 A comparison of the HDO/H_2O ratio as measured by TES and the JPL ALIAS instrument on a WB-57 flight from the Costa Rica Aura Validation Experiment.

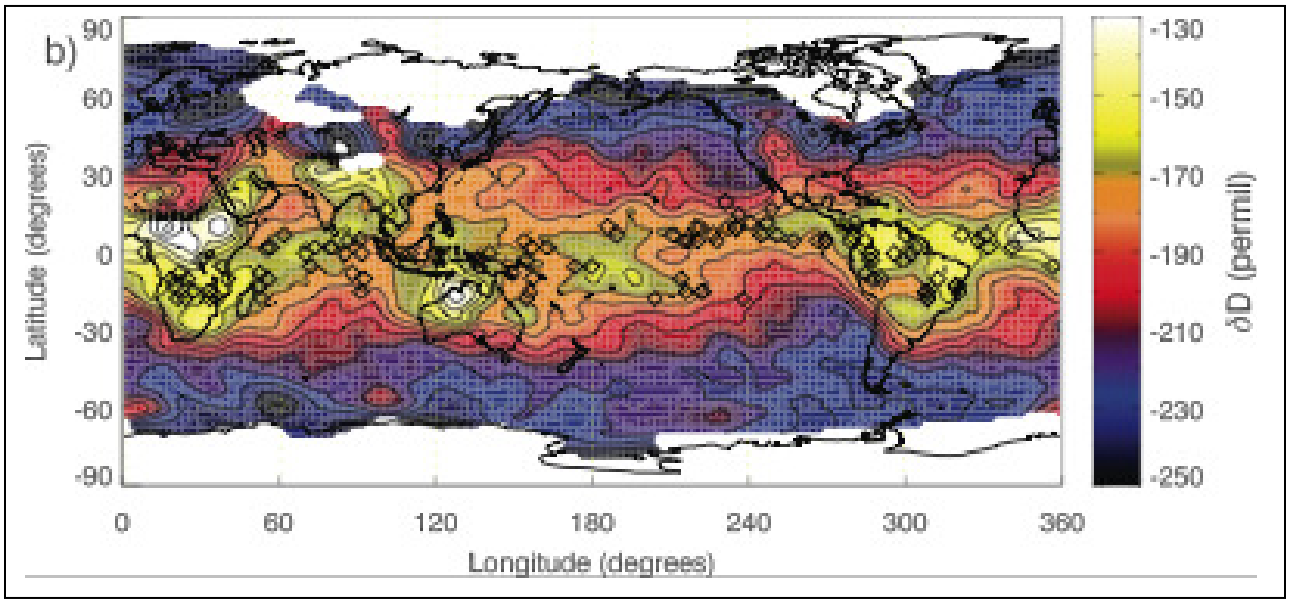

Figure 10-2 Global distribution of HDO/H_2O ratio in parts per thousand with respect to the ocean composition (δD) for the period between Sept 2004 and March 2005.

TES global observations of the HDO/H_2O ratio show expected features such as increasing depletion with latitude, relatively increased depletion inside large cloud systems, and less depletion in regions of convection (Lawrence *et al.*, 2004; Worden *et al.*, Nature 2007). For example Figure 10-2 shows the global distribution of the HDO/H_2O ratio in parts per thousand with respect to the ocean composition (dD) for the period between Sept 2004 and March 2005. This figure shows the latitudinal variation as well as less depletion over convective regions.

TES observations of the HDO/H_2O ratio are biased both by systematic errors such as calibration and spectroscopy as discussed earlier and also by the fixed *a priori* constraint vector which assumes tropical values for the HDO/H_2O ratio. Consequently, we suggest using only those data where the master quality flag is set to unity and only when the degrees of freedom for signal (DOFS) for the HDO retrieval is larger than 0.5 to reduce the effect of the *a priori* bias. Furthermore, one should consider the bias due to the constraint vector when comparing high-latitude regions with tropical regions and when comparing seasonal variations at high-latitude regions. For example, comparisons of seasonal variations at high latitudes will be biased towards the warmer parts of the cold season. Additional studies are needed to quantify the effect of this bias when comparing cold versus warm regions.

10.1 References

[1] Worden, J., K. Bowman, D. Noone, R. Beer, S. Clough, A. Eldering, B. Fisher, A. Goldman, M. Gunson, R. Herman, S. Kulawik, M. Lampel, M. Luo, G. Osterman, C. Rinsland, C. Rodgers, S. Sander, M. Shephard, and H. Worden, (2006), Tropospheric Emission Spectrometer observations of the tropospheric HDO/H_2O ratio: Estimation approach and characterization, *Journal of Geophysical Research, 111,* August 25, 2006, D16309, (doi:10.1029/2005JD006606)

[2] Lawrence, J.R.; Gedzelman, S.D.; Dexheimer, D.; Cho, H.-K.; Carrie, G.D.; Gasparini, R.; Anderson, C.R.; Bowman, K.P.; Biggerstaff, M.I. (2004), Stable Isotopic Composition of Water Vapor in the Tropics, *Journal of Geophysical Research-Atmospheres*, *109*, March 27, 2004, D06115, (doi:10.1029/2003JD004046).

[3] Worden, J., D. Noone, K. Bowman & TES science team and data contributors, (2007), Importance of rain evaporation and continental convection in the tropical water cycle, *Nature, 445,* 528-532, February 1, 2007 (doi:10.1038/nature05508).

11. TES Cloud Products

TES performs a retrieval of frequency dependent effective optical depth and cloud top pressure along with the trace gas retrievals. There are a number of fields the user might be interested in:

- CloudTopPressure,
- CloudTopPressureError,
- CloudEffectiveOpticalDepth (has frequency dependence),
- CloudEffectiveOpticalDepthError (has frequency dependence), and
- AverageCloudEffOpticalDepth.

11.1 Background

TES retrieves a cloud top pressure and cloud effective optical depth for each measurement. These data have error estimates, and based on those estimates and physics principles, we can make some statements about when TES has sensitivity to cloud parameters and when we do not. Figure 11-1 contains 2-D histograms of the cloud top pressure and effective cloud optical depth at 975 cm^{-1} for v002 and v003 of TES data. Figure 11-2 is a scatterplot of the cloud top pressure and effective cloud optical depth at 975 cm^{-1}. The error estimates are plotted over the data. These show that there is small uncertainty for moderate optical depths (1-10) and higher level clouds (pressures from 200-800mb). Error estimates on both effective optical depth and cloud top pressure tend to be large for clouds with optical depths less than a few tenths. For high effective optical depth clouds (greater than 10) at pressures between 800 and 1000mb), error estimates for cloud top pressure grow a bit larger again.

These error estimates are consistent with our expectations for TES – due to low thermal contrast, clouds near the surface are harder to characterize than clouds at high altitudes. Also, small effective optical depth clouds impart a small radiance change, and are harder to characterize than moderate optical depths. By time the effective cloud optical depth becomes larger than a few, the radiance change with change in optical depth is small, and characterization becomes more difficult.

11.2 Changes from v002 to v003

There are two changes between v002 and v003 that are expected to have some impact on clouds. One change was that the set of optical depths used for initial guesses was changed, and v003 contains initial guesses at smaller optical depths. This results in more retrieval values at low optical depth, some in cases where the retrieval makes no change from the initial guess. These changes are seen in the two panels of Figure 11-1.

The second change that impacts the clouds is the inclusion of filter 2B1 in the retrievals and the use of frequencies in the range of 671.32 - 901.48 cm^{-1}**.** This appears to have improved the characterization of the cloud top pressure for high clouds, as will be discussed in the section below.

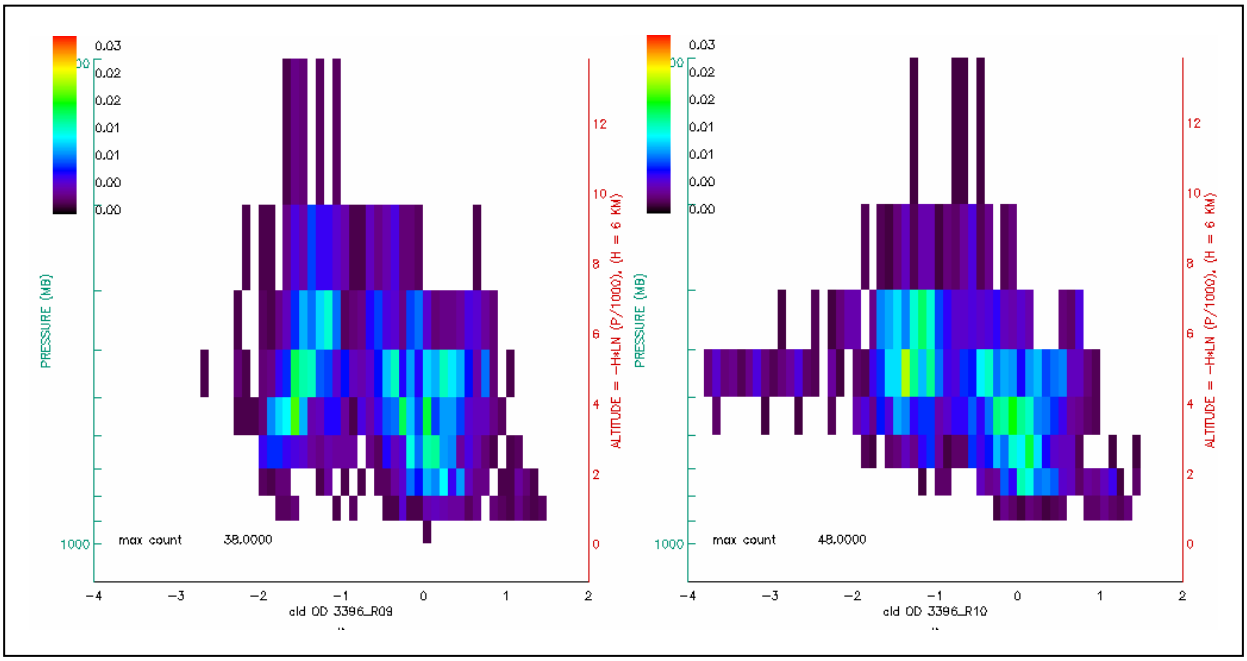

Figure 11-1 2-D histogram of TES retrieved cloud top pressure and cloud effective optical depth at 975 cm^{-1} for Global Survey runid 3396. The left panel shows the results for v002, and the right panel for v003. The color bar indicates the frequency of occurrence in fraction.

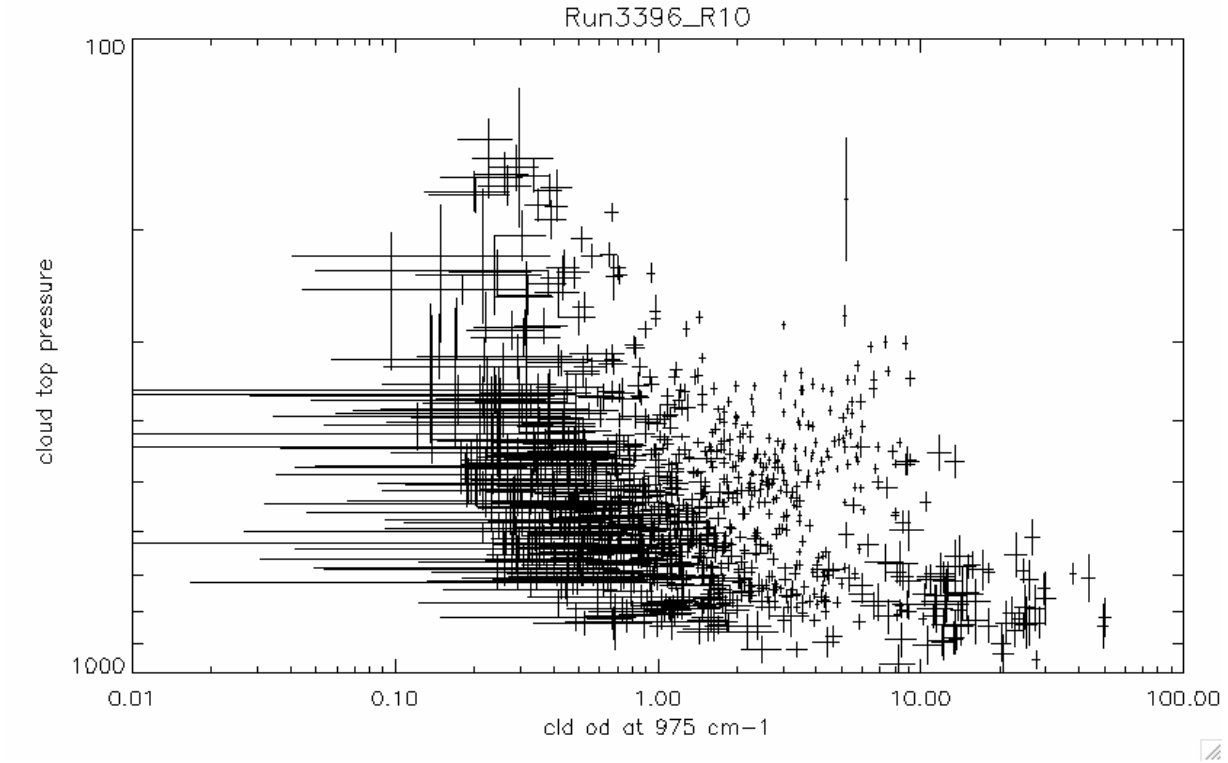

Figure 11-2 TES retrieved cloud top pressure and cloud effective optical depth at 975 cm^{-1} with error estimates for runid 3396.

11.3 Cloud Top Pressure

The cloud top pressure has been compared to MODIS and AIRS cloud top pressures. Only MODIS comparisons are presented in this version of the validation documents. For this comparison we use the MODIS cloud top pressure that is determined from the infrared retrieval technique from the MYD06 products. TES data are paired with the nearest neighbor of the MODIS 5km by 5km data products. There is always significant overlap of the TES and MODIS footprints. We select only the MODIS data that is confidently cloudy (cloud mask value 0). Figure 11-3 shows a histogram of the TES – MODIS cloud top pressure differences in mb for the complete set of clouds. Although the mean is reduced to 0.0mb in v003, from 48mb in v002, we still see that there are outliers with differences of greater than 300mb. Figure 11-3 is for a Global Survey, similar statistics are present in analysis of sets of step and stare runs.

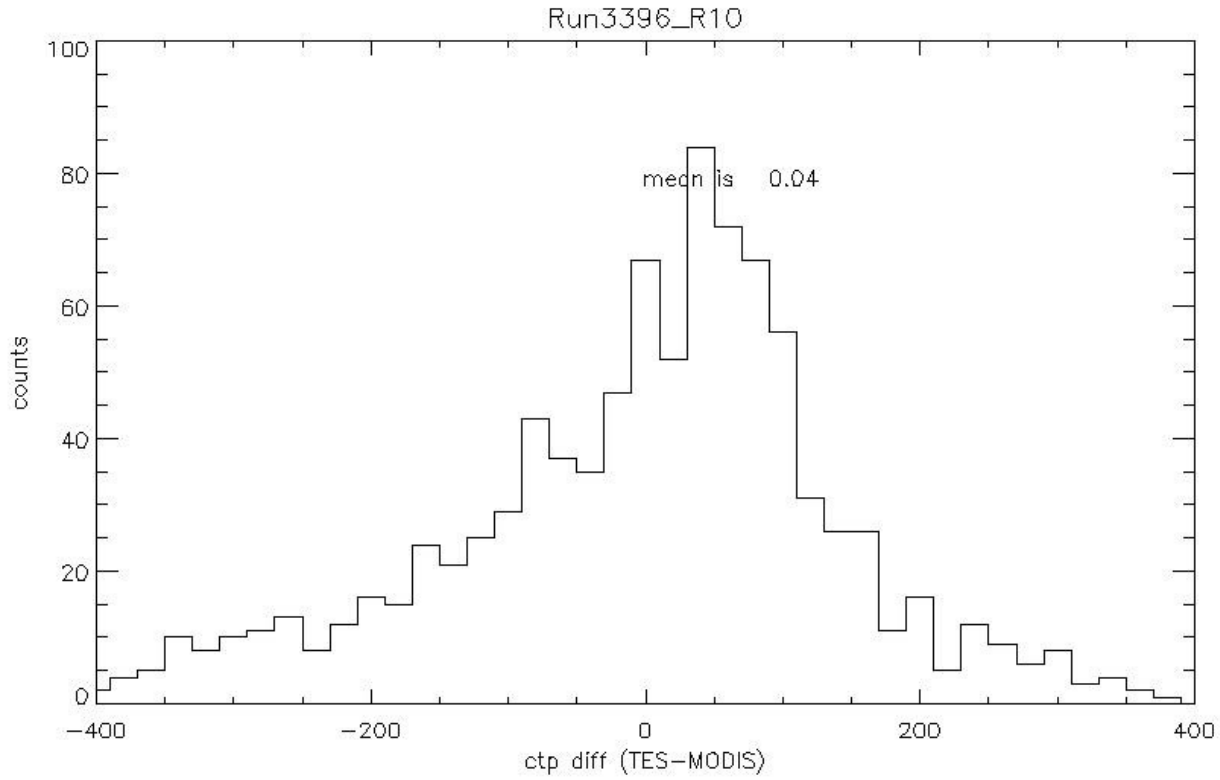

Figure 11-3 Histogram of Cloud Top Pressure Differences between MODIS and TES in mb.

To look into the cloud top pressure differences in a little more detail, statistics were developed after grouping data by cloud top pressure and cloud optical depth. The left hand column of Figure 11-4 shows data with effective optical depths less than 3, while the right hand column is all effective optical depths greater than OD 3.The lower panels are cloud top pressures greater than 700mb, while the upper panels are cloud top pressure less than 350 mb. We see that the histograms of cloud top pressure differences for clouds above 350mb are narrower. The lower optical depth clouds below 350mb have broad histograms although the mean differences are small. Further analysis shows that the large differences are related to the fact that TES's default initial guess for cloud top pressure is 500mb, while the MODIS first guess is closer to the surface pressure.

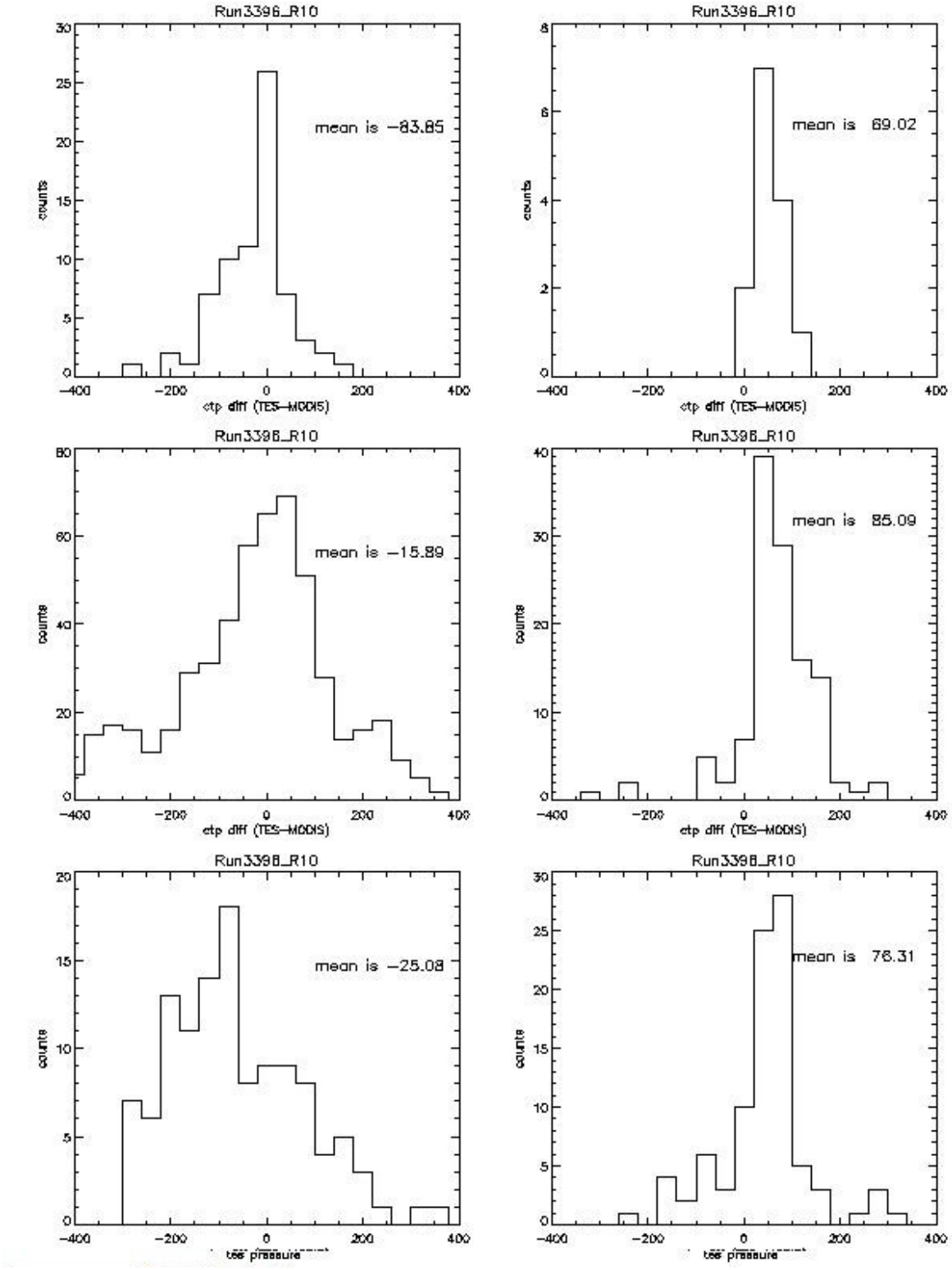

Figure 11-4 Histogram of TES-MODIS cloud top pressure differences. Left column is effective optical depth less than 3, right hand column greater than 3. Upper row is cloud top pressure less than 350 mb, bottom row is cloud top pressure greater than 700 mb.

Figure 11-5 illustrates the changes between v002 an v003 for the high and thinner clouds. The histogram of cloud top pressure is much more sharply peaked for v003 data, in response to the changes made in the initial guess and the inclusion of frequencies that have more sensitivity to cloud top height.

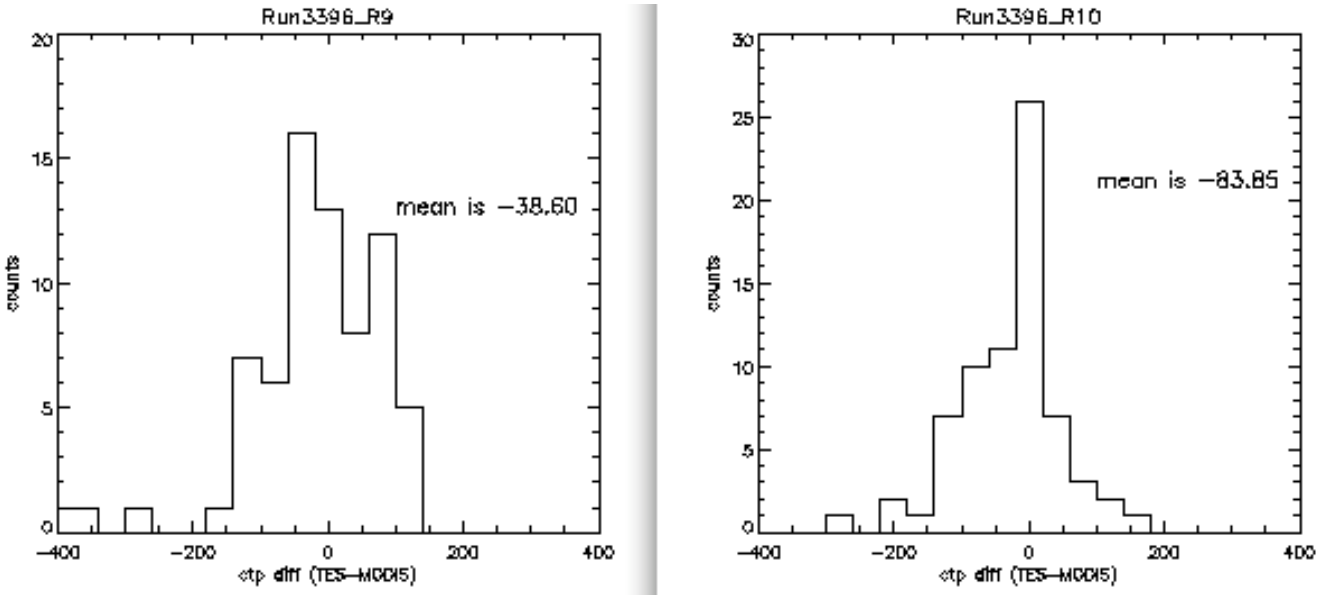

Figure 11-5 Comparison of histograms of cloud top pressure differences (TES-MODIS) for clouds with effective optical depth less than 3 and cloud top pressure less than 350 mb for voo2 (left panel) and v003 (right panel). The histogram for v003 is much more sharply peaked.

11.4 Cloud Effective Optical Depth

At present, we have limited correlative datasets for the validation of the effective cloud optical depth product from TES. For characterization purposes, we have compared MODIS visible optical depths to the TES effective cloud optical depths retrieved at 975 cm^{-1}. The average effective cloud optical depth is very well correlated to the effective cloud optical depth at 975 cm^{-1}, except at small effective optical depth, as shown in previous validation reports.

A scatterplot of TES effective cloud optical depth at 975 cm^{-1} and MODIS cloud optical depth is presented in Figure 11-6. The expected ratio of visible to infrared optical depth is dependent on the cloud particle sizes and shapes, and in thought to be on the order of 2. Figure 11-6 shows clearly that MODIS optical depths are larger than TES', but the scaling ranges from a factor of 10 to 1.

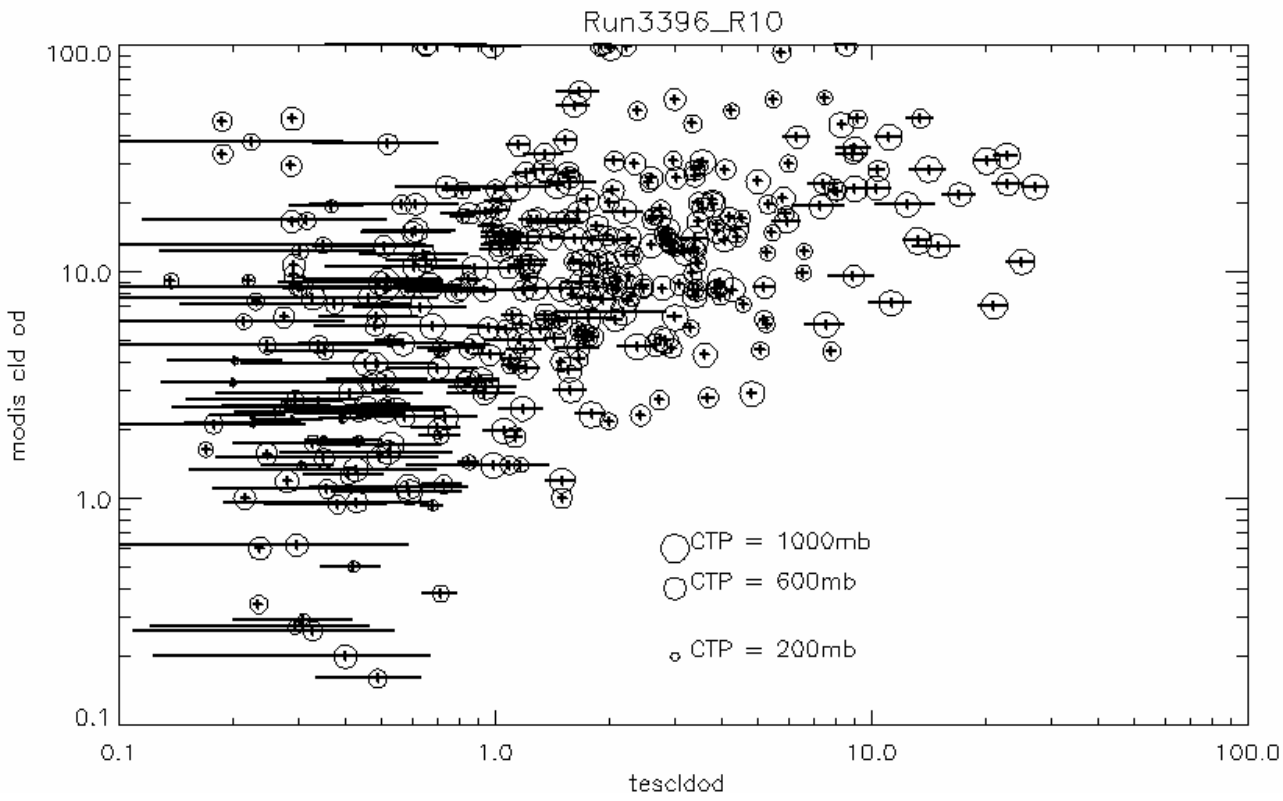

Figure 11-6 Scatterplot of MODIS visible cloud optical depth and TES effective cloud optical depth at 975 cm^{-1}.

12. Methane

For version V003 data, TES L2 methane retrievals are considered a beta level product, and thus should be used with great care. Validation efforts to date have focused on comparisons with methane column data from ground-based Fourier transform infrared spectrometer (FTIR) observations and on comparisons with in-situ aircraft-based observations.

12.1 Ground-based FTIR comparisons.

Ground-based FTIR data was obtained from publicly available international Network for the Detection of Atmospheric Composition Change (NDACC) data. Only a small sub-set of this data contains information about methane. Table 12-1 lists the NDACC sites with methane data available that overlaps in time with the TES data. It should be noted that the ground sites cover a large range of latitudes, but are concentrated at high latitudes.

Table 12-1 Ground Sites

Site	Latitude	East Longitude
Arrival Heights, Antarctica	77.825	166.65
Lauder, New Zealand	-45.038	169.684
Izana, Tenerife	28.3	343.52
Toronto, Canada	43.66	280.60
Bremen, Germany	53.107	8.854
Harestua, Norway	60.2	10.8
Kiruna, Sweden	67.84	20.41
Thule, Greenland	76.52	291.24
Ny-Aalesund, Norway	78.92	11.92
Eureka, Canada	80.05	273.58

To compare TES data to the ground-based FTIR column data, we have computed the total column from the TES retrieval and from the TES initial guess (IG). Since ground-based column data are daily averages and the methane column is not expected to vary strongly over short distances, we have used relatively relaxed coincidence criteria for these initial comparisons. A TES observation was considered coincident with the ground-based data if it was taken on the same day and was within 500 km of the ground site. All such TES observations meeting these criteria were averaged together for comparison with the FTIR data point. Using these criteria we found a total of 212 comparisons across all of the available NDACC sites. Note that since

processing of V003 data is not complete (particularly for 2005, where much of the publicly available FTIR data is concentrated), there may be additional coincidences not included in this work. As of this writing, no accommodation has been made for the elevation of the ground-based observatory.

Figure 12-1 shows histograms of the entire coincident data set. Figure 12-2 shows the same data as normalized differences between TES and the FTIR data. Examination of these two plots shows a ~5% high bias in the TES column with respect to the FTIR columns.

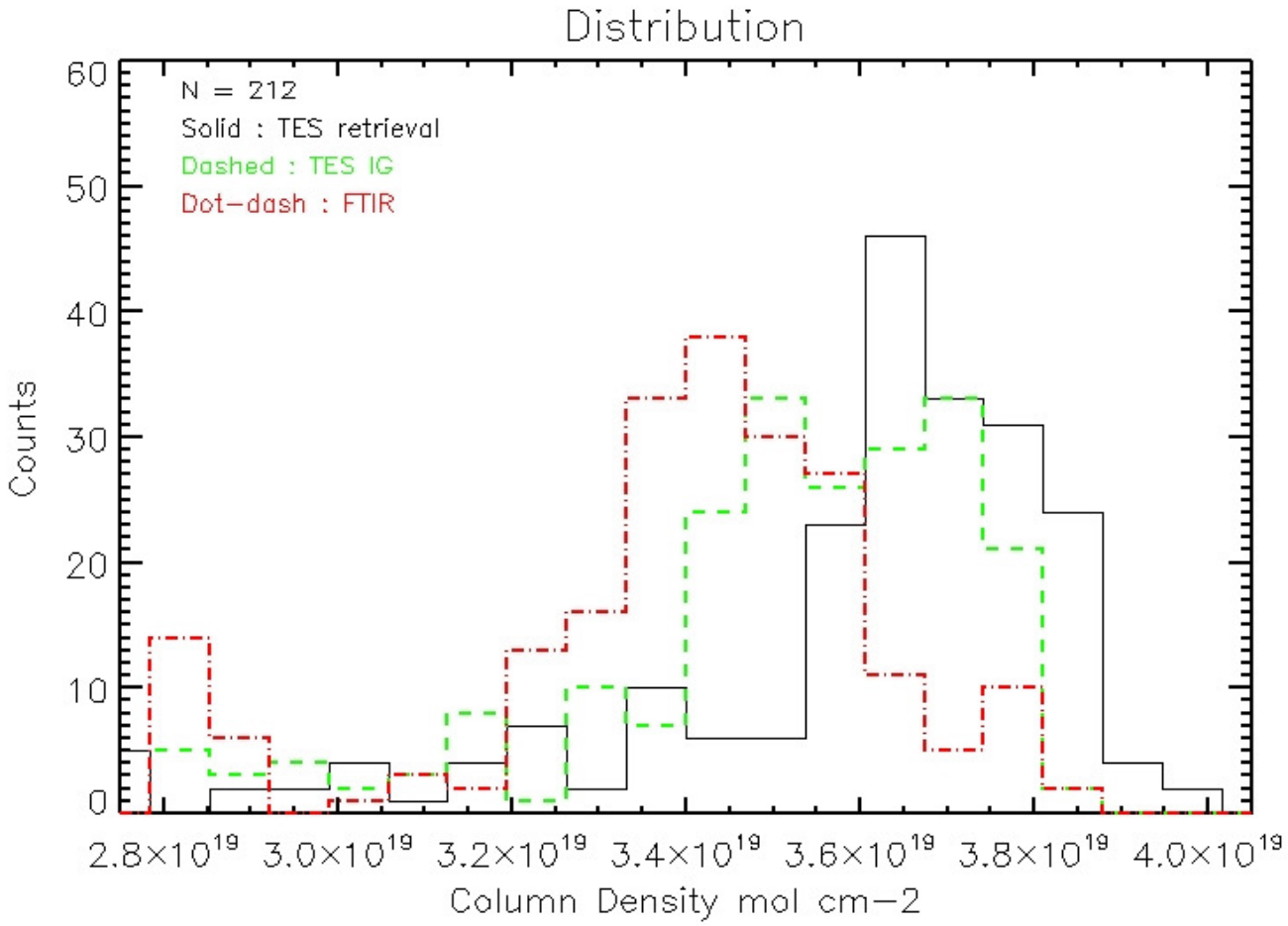

Figure 12-1 Histograms of CH_4 Column data.

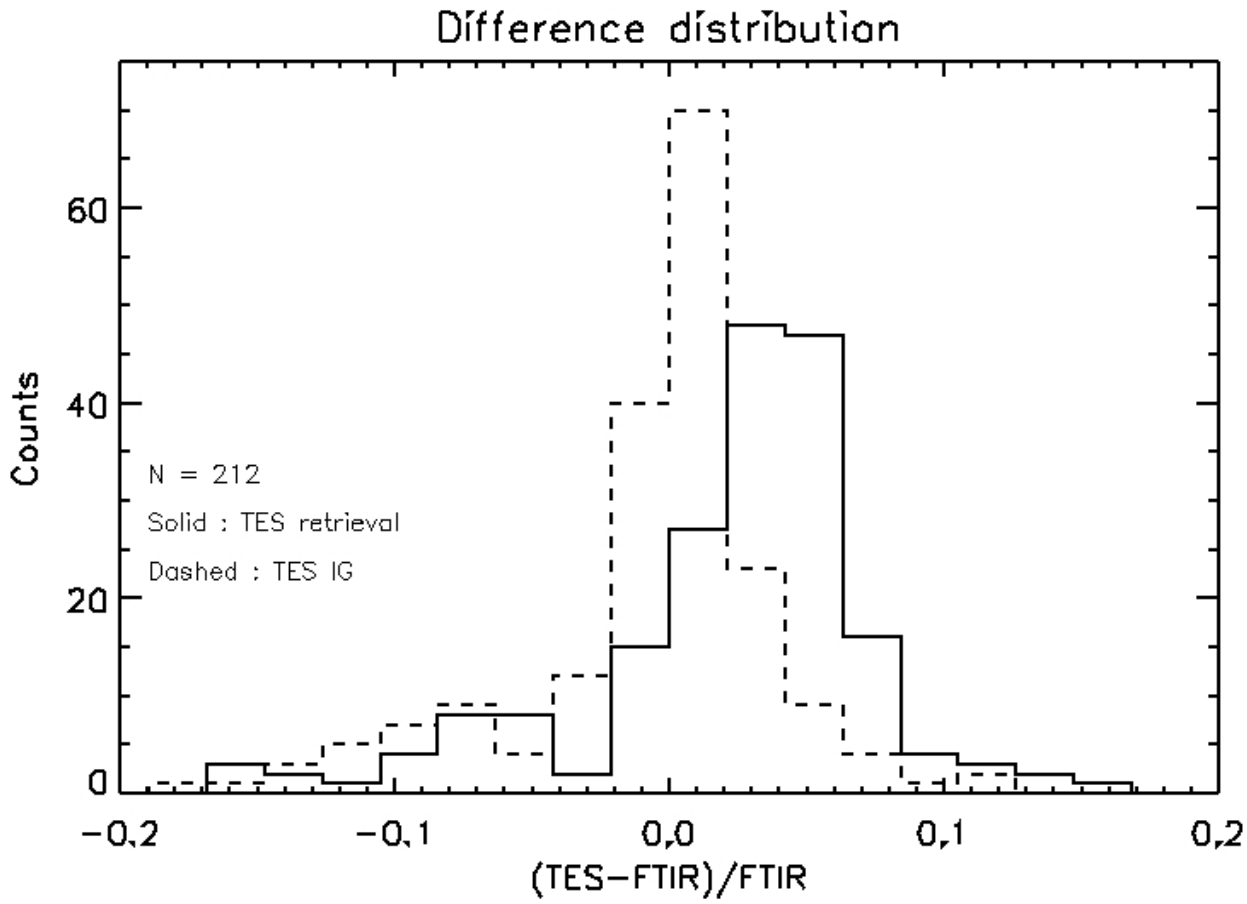

Figure 12-2 Normalized Histograms of CH4 column data

Since combining all of the data from such a wide range of latitudes, we have also plotted the sites separately. Figure 12-3 and Figure 12-4 show the three sets of column data overplotted as a function of time for 8 of the 10 sites. The two sites not shown only have one coincident point each and are consistent with data shown. These results show TES columns typically higher than the ground-based data, particularly at sites at high latitudes. The results shown from the Izana data are not understood at this point and are being further investigated. Interestingly, the Bremen and Thule data do not show much bias.

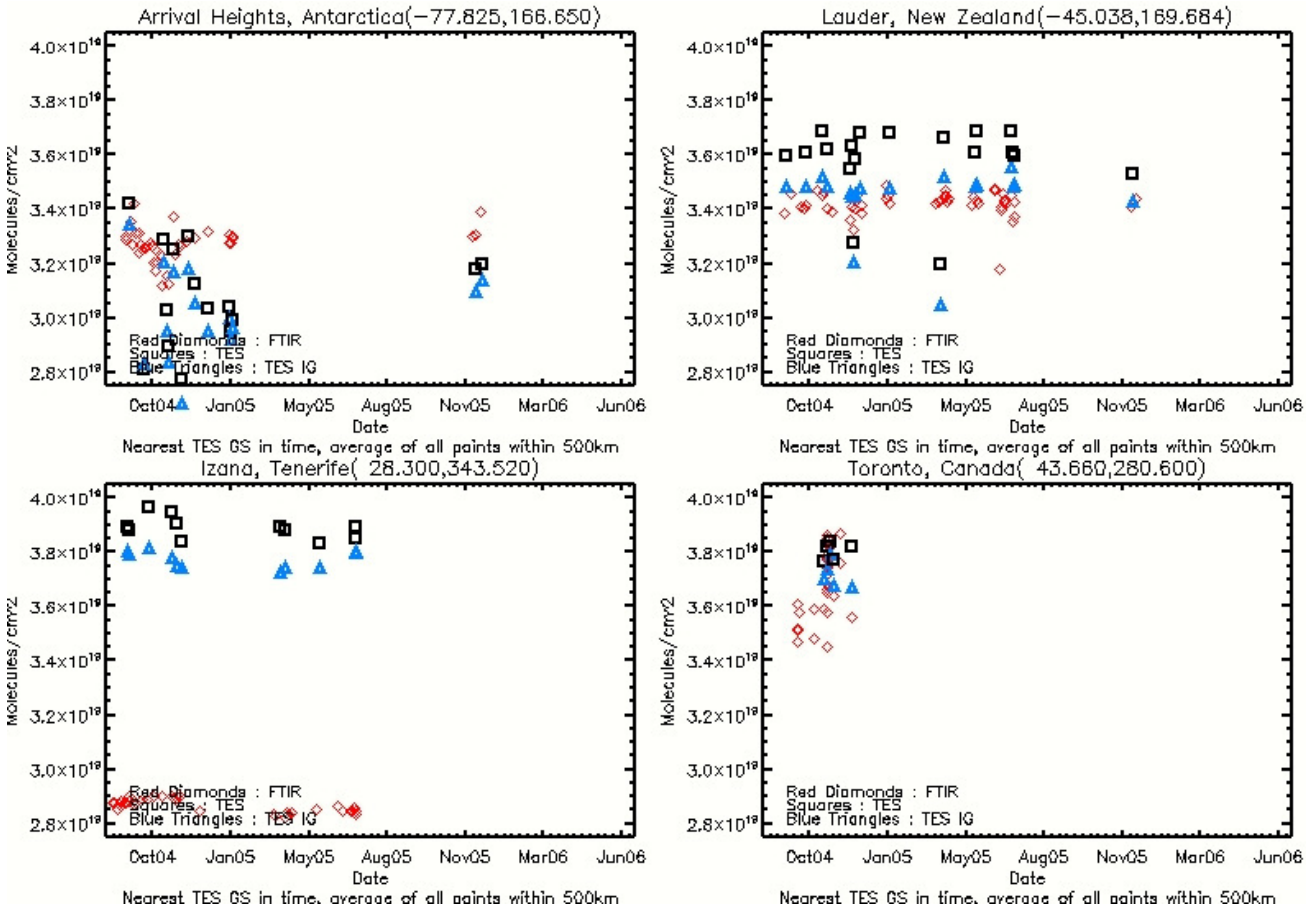

Figure 12-3 Column Comparisons

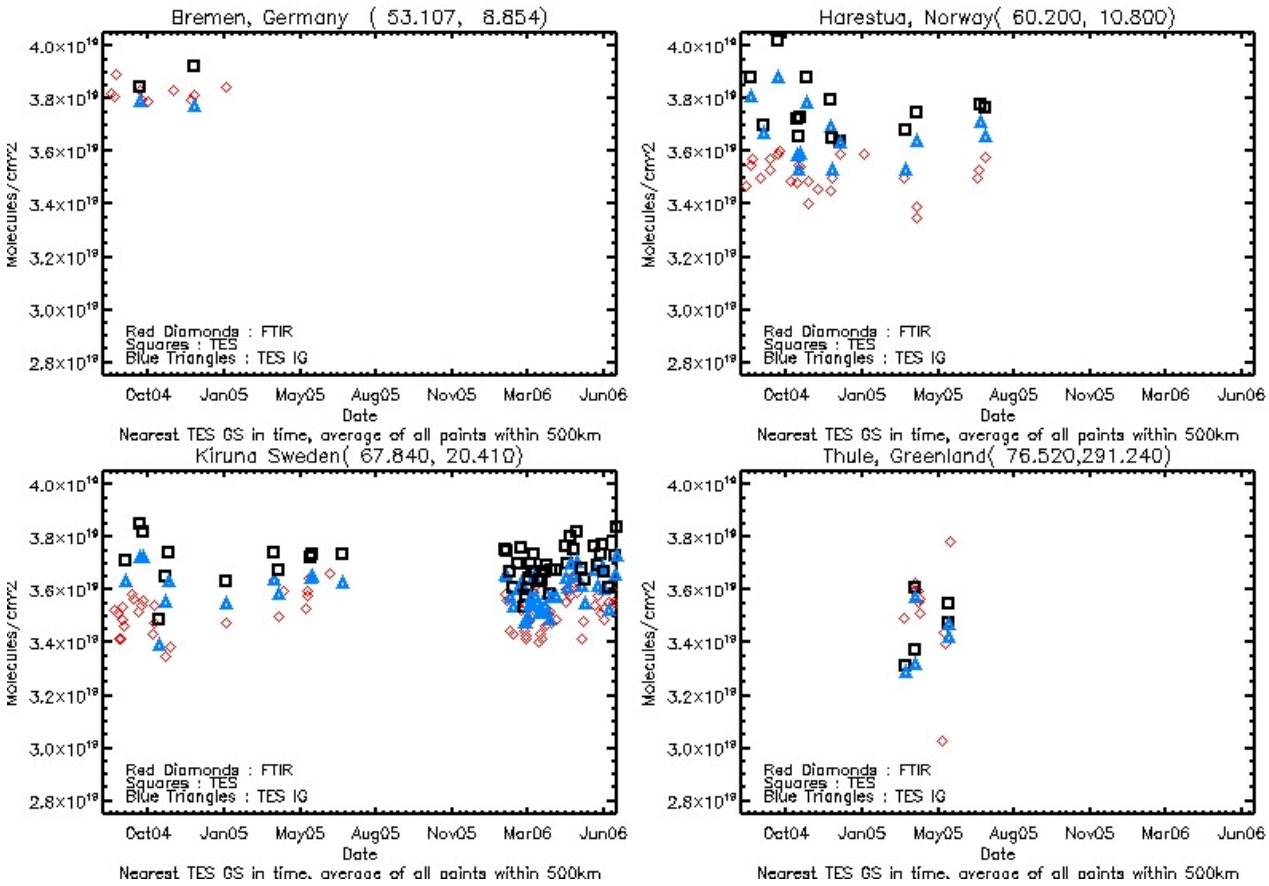

Figure 12-4 Column Comparisons

12.2 Comparisons with in-situ data

During the INTEX-B campaign, the NASA Langley Research Center aircraft instrument DACOM flying on the NASA DC-8 recorded in-situ methane measurements in the Houston, TX (http://code916.gsfc.nasa.gov/Public/Analysis/aircraft/tote/sachse.html) area in March 2006. Several flights were designed to align with TES observations, and a small number of close time and distance coincident comparison data sets are available. Figure 12-5 shows the details of one such flight with the associated TES footprint locations. The TES methane retrieval data are shown in Figure 12-6. Comparisons between the in-situ data taken during the first vertical aircraft sample and the four nearest (spatially) TES profiles are shown in Figure 12-7. As can be seen in Figure 12-7, TES exhibits an excess of methane in the retrieval in the middle troposphere from about 500-150 hPa. This pressure range aligns with the region of maximum sensitivity of the TES retrieval, as seen in the averaging kernels shown in the upper-right panel of Figure 12-7. This profile shape and bias was found in most of the comparisons with the in-situ data for this period whereas the in-situ data showed little variation across samples. The tropospheric bulge seen in these comparisons is likely the cause of the bias seen in the column data. The TES methane retrievals typically have ~1.5 degrees of freedom in this latitude range.

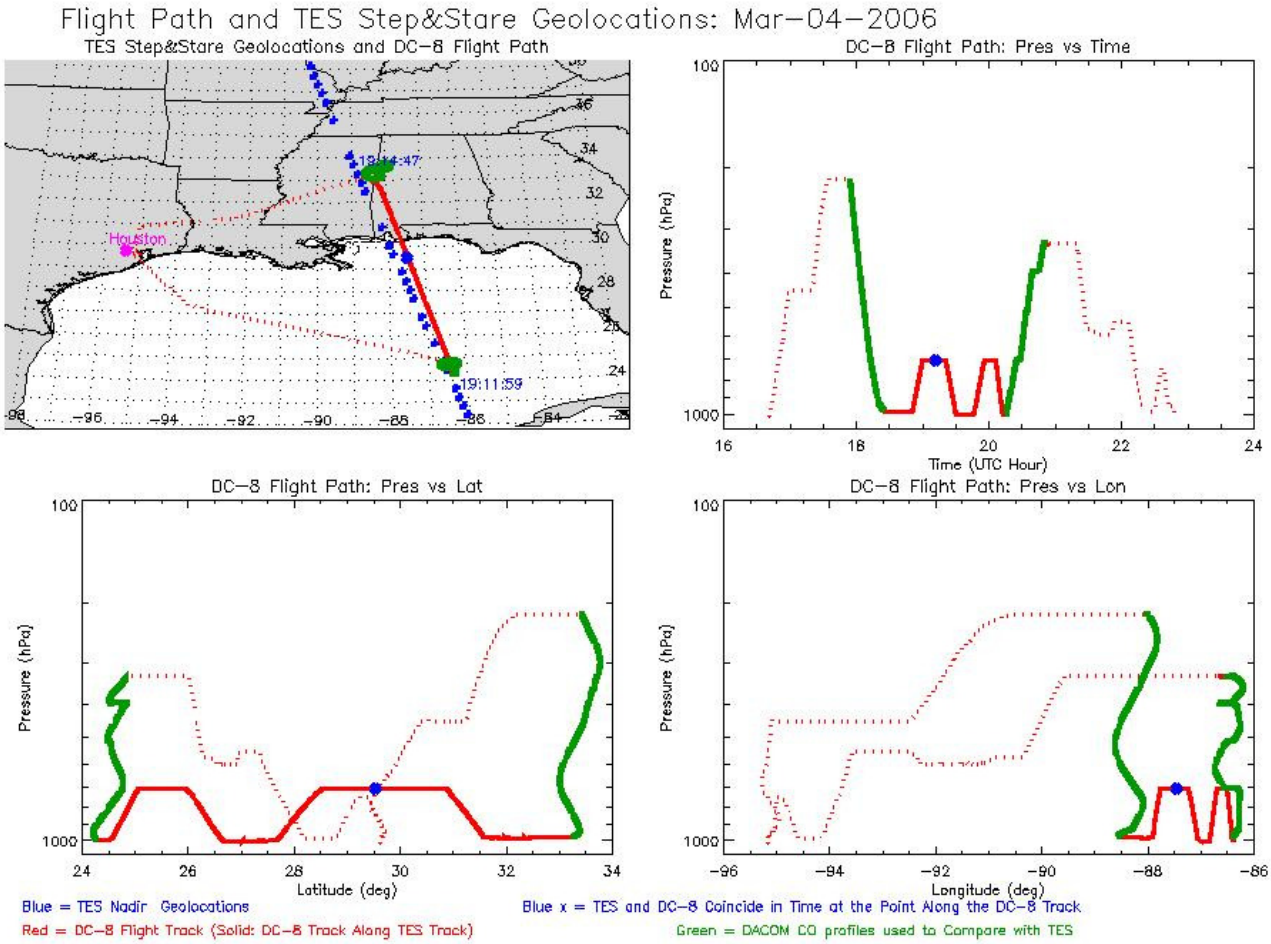

Figure 12-5 Flight Details

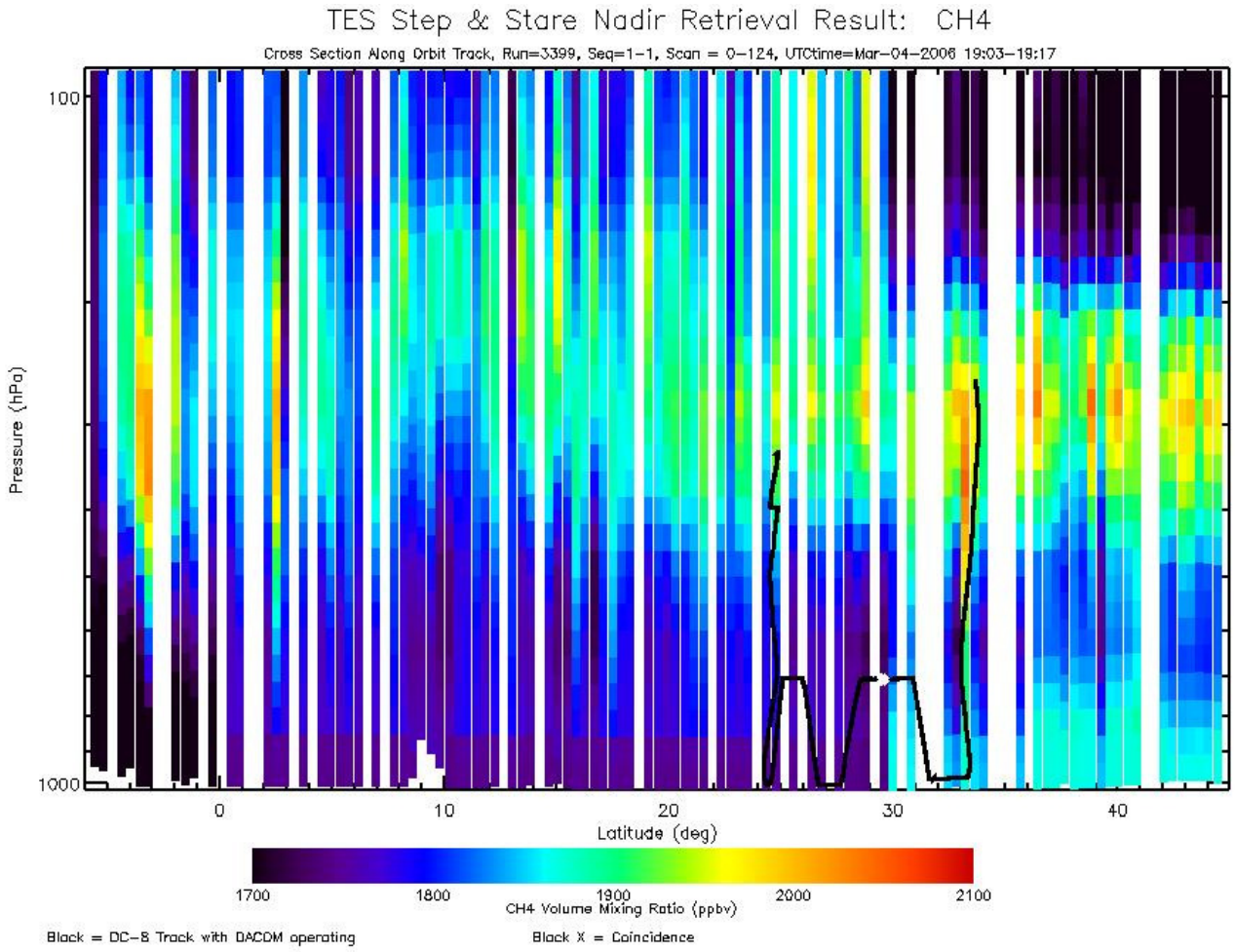

Figure 12-6 TES Curtain Plot

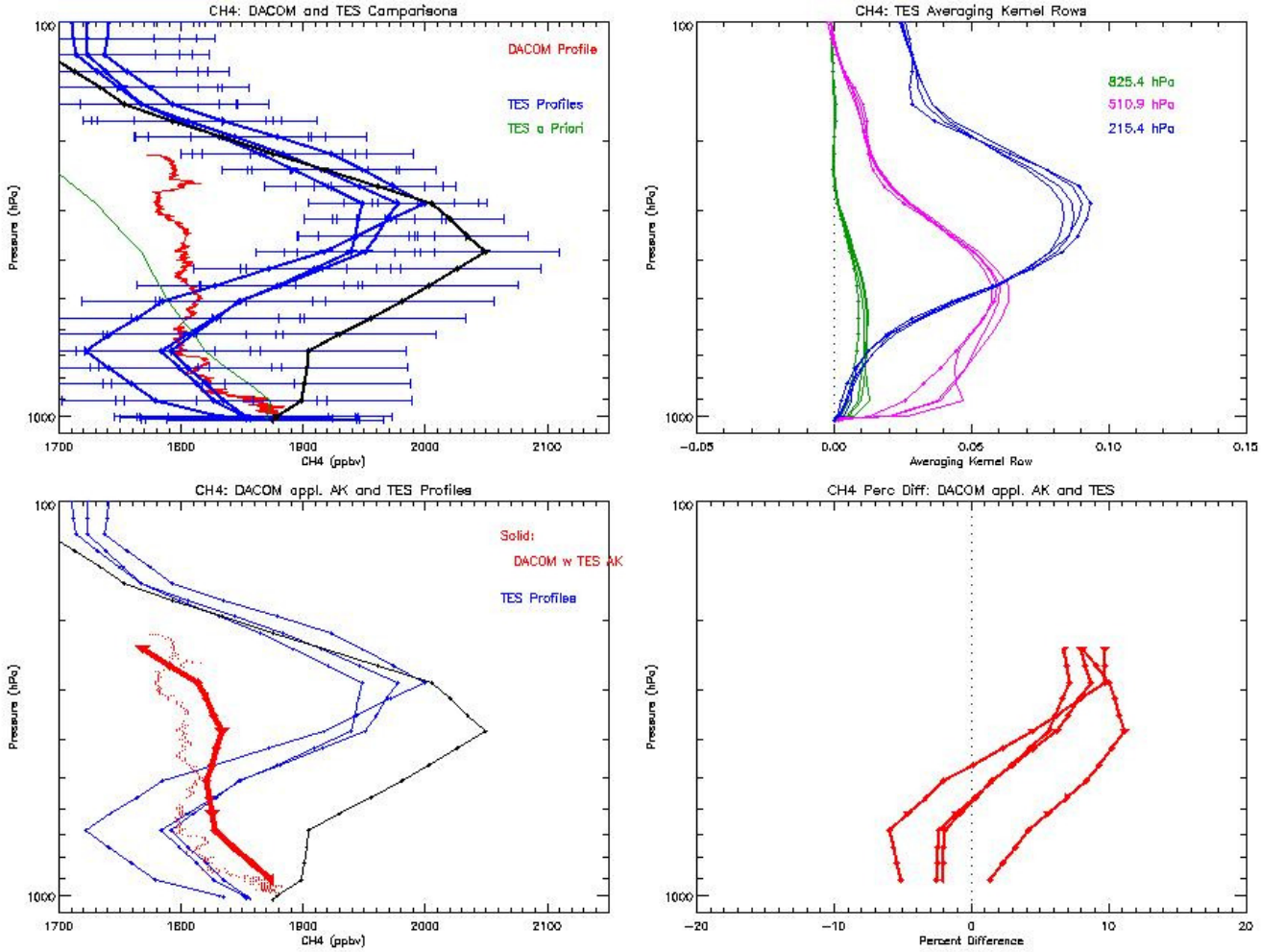

Figure 12-7 TES/DACOM Comparison

12.3 Conclusions

TES methane retrievals appear to have a high bias of ~5% of the total column. The profile information suggests this bias is primarily due to an overabundance (of up to 10-12%) in the middle and upper troposphere (approximately 500-150 hPa). These are only preliminary conclusions based on small samples and validation efforts are on-going as is work to improve the retrieval quality. Limited comparison data for methane in the free troposphere where TES is most sensitive will make robust statistical validation difficult. Comparisons with SCIAMACHY (SCanning Imaging Absorption SpectroMeter for Atmospheric CHartographY) data are planned, but the large differences in the sensitivities between TES and SCIAMACHY will make interpretation of such comparisons difficult.

13. Validation of TES Limb Nitric Acid Retrievals

V002 TES limb products are generally unvalidated and rarely contain useful information below the stratosphere. The V003 products are a significant improvement over the V002 products. TES V003 limb retrieves tropospheric data when the scene is cloud-free. Comparisons of TES V003 nitric acid retrievals to data from the SAGA (Jack Dibb, PI) and CIMS (Peter Popp, PI) aircraft instruments as well as to profiles from MLS have been performed. The F04_04 TES nitric acid product can be considered provisionally validated (see Table 1-1) between100 and 30 hPa. The TES team is continuing to try and improve the limb retrievals.

During INTEX-B the NASA DC-8 made two flights that included TES limb validation legs, (May 7 and 9, 2006), with the hope that data from the University of New Hampshire SAGA instrument could be used to evaluate TES retrievals. The MODIS image (Figure 13-1) from May 7, 2006 shows scattered clouds along the TES ground track, and currently the TES sensitivity will be limited to above the calculated cloud level. The flight track on May 9 also encountered heavy cloud cover.

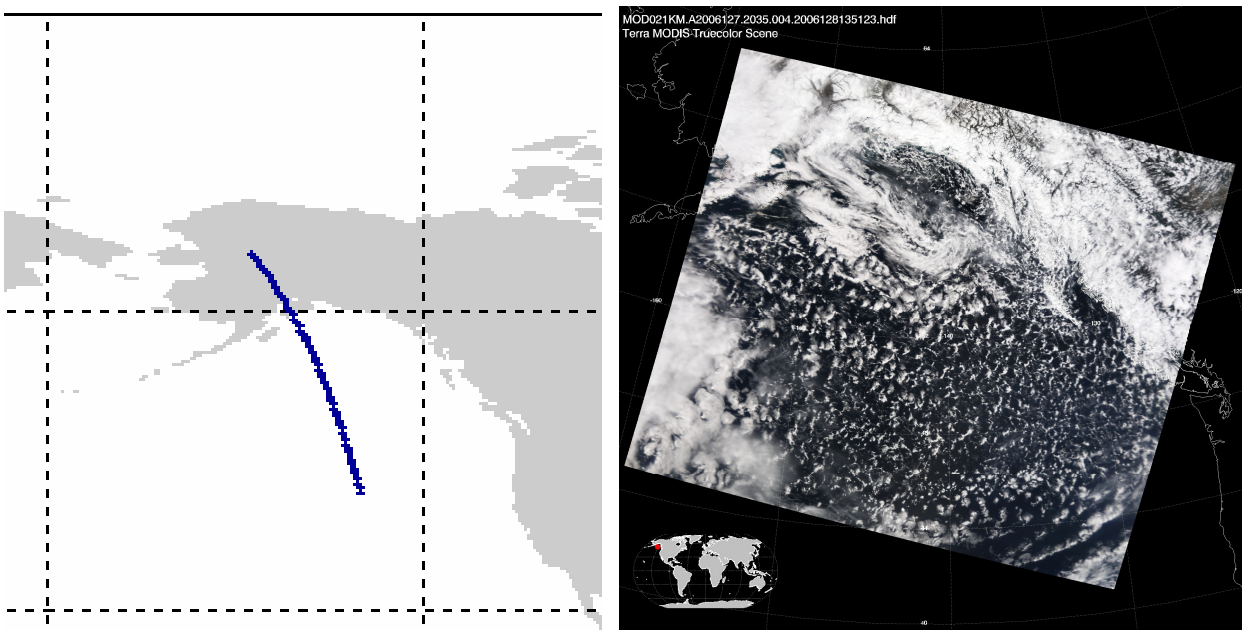

Figure 13-1 TES run 4113 ground track (left); MODIS image, 5/7/06 (right) with approximate TES ground track.

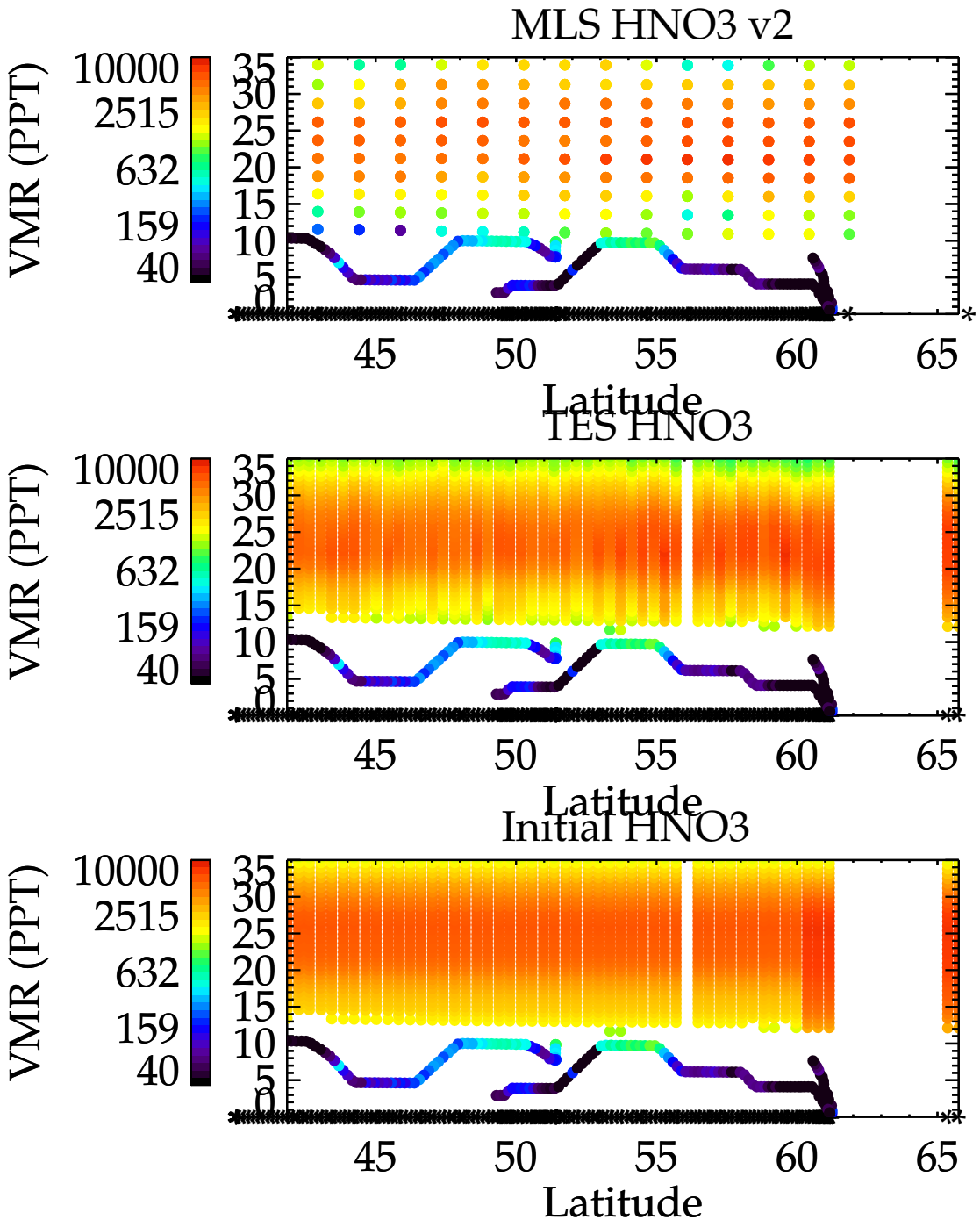

Figure 13-2 Plot comparing TES initial guess (bottom), results (middle) and MLS to SAGA data (Jack Dibb, PI) The TES data is only plotted to the lowest pressure levels at which there is sensitivity.

Figure 13-2 shows the TES nitric acid profiles nearest the DC-8 flight track, and compares that with the MLS data values and TES "initial" profiles. The profiles are not plotted below the

altitude where TES has sensitivity and. Figure 13-2 also shows the data from the SAG instrument from that day and it is apparent that the TES retrievals do not reach down to where the DC-8 measures. The comparisons to SAGA from INTEX-B indicate that TES cannot reach the SAGA validation data, because TES processing is cut off by the presence of clouds.

13.1 The CRAVE campaign – comparisons to CIMS, Peter Popp, PI

The flights of the NASA WB-57 during the Costa Rica Aura Validation Experiment (CRAVE) campaign did not match the dates of the TES limb observations. However, the variability and range of HNO_3 values is consistent between the CIMS HNO3 measurements and TES at 100 hPa as shown in Figure 13-3.

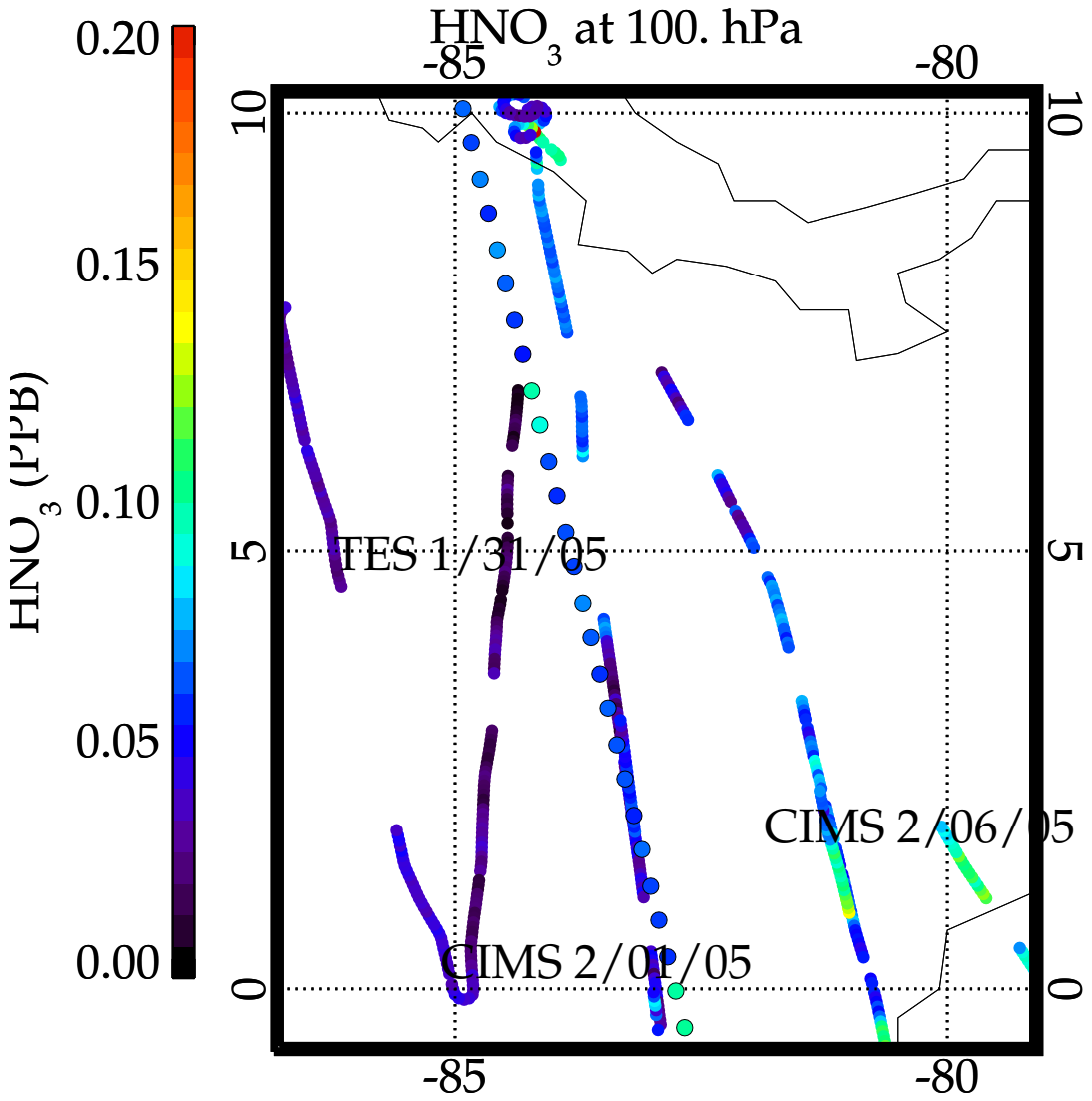

Figure 13-3 Comparison of TES and CIMS results near Costa Rica for late January, early February, 2006. The TES data, shown appears as evenly spaced circles, is in the vicinity of CIMS data, but for different dates and locations. The variability and range of values is consistent between the two instruments.

13.2 Global results and comparisons to MLS

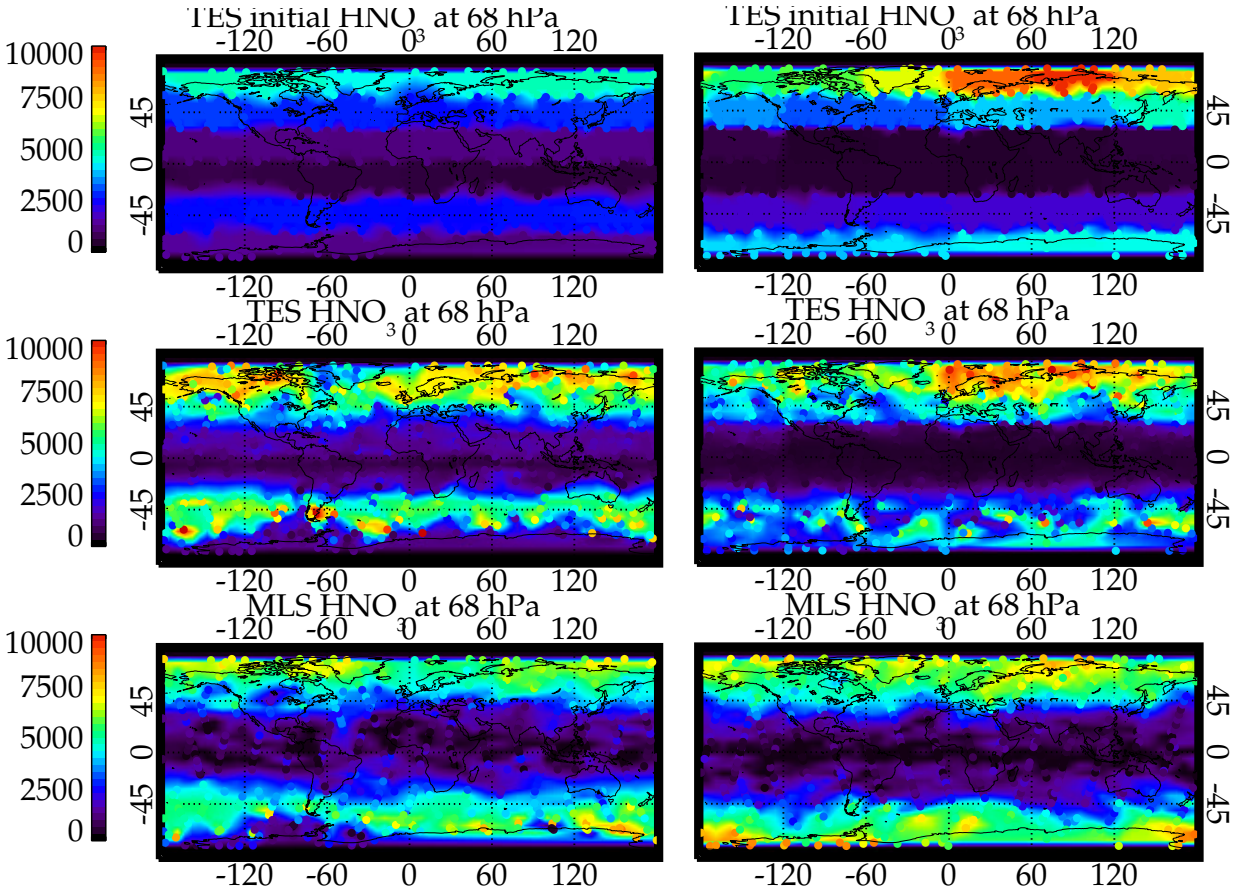

Figure 13-4 Global maps for September, 2004 (left) and April, 2005 (right). The top plots shows the TES initial guess; the middle plots show the TES result; and the bottom plots show MLS, all at 68 hPa**.**

Spatial maps of TES and MLS data show similar patterns between the two instruments, with increased stratospheric HNO_3 at both poles. The MLS and TES plots for September 20, 2004, show an important feature, which is the depletion of HNO_3 in the Antarctic polar winter.

Comparing to MLS statistically in the polar regions (45-90N and 45-90S), we find that the TES initial guess has rather large biases compared to the MLS result. The retrieved TES HNO_3 shows a markedly smaller bias, but a larger RMS compared to MLS, especially below 100 hPa.

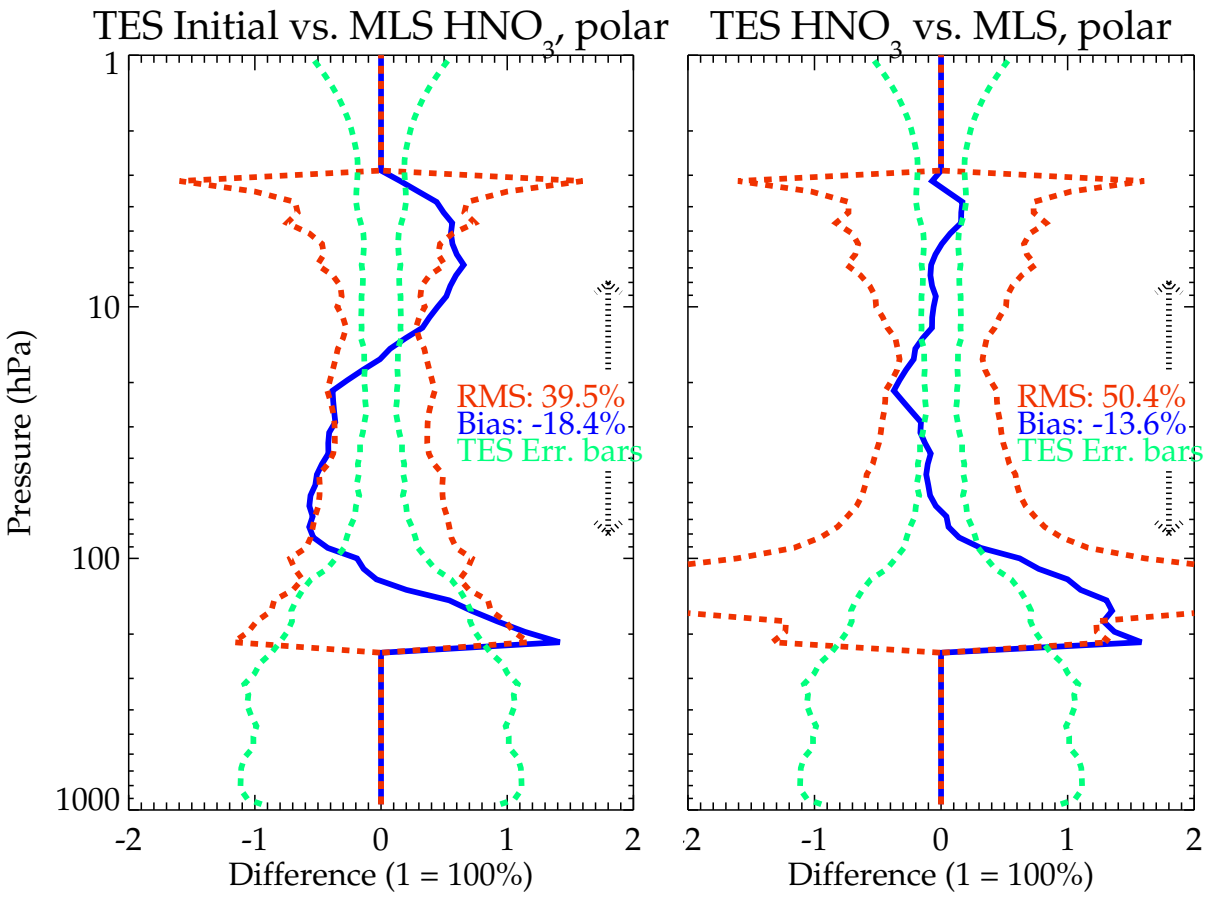

Figure 13-5 MLS compared to the TES initial guess (left) and TES results (right). The bias (blue, TES - MLS) is markedly improved by the TES retrieval between 30 and 100 hPa; however the RMS (red) increases following the retrieval, and is larger than the TES predicted errors (green).

14. Comparison of TES Limb Temperature with GMAO

Limb temperature is a product that has not received much attention to date. Up until 25 May 2005, the TES global survey consisted of 1152 sequences, each of which had two nadir and three limb scans. Limb scans were eliminated from the global survey to conserve TES instrument lifetime, but still are scheduled for special observations (most notably INTEX). For the TES v003 results presented here, it is important to note that temperature retrieval underwent a significant change. The previous TES version v002 (R9) temperature was retrieved from microwindows in the spectral bands of H_2O (2A1 filter) and O_3 (1B2 filter). In v003, temperature was retrieved from these spectral bands and also the CO_2 ν2 band (2B1 filter) at 650 to 800 cm^{-1}. As noted in the nadir temperature section, the addition of the CO_2 ν2 band has improved the TES temperature retrievals. We present here the first validation comparisons between TES v003 limb and nadir temperature, and their bias relative to GMAO GEOS-5.

Figure 14-1 shows the map of TES limb temperature retrievals at 46.4 hPa from Global Survey 2317 (12 November 2004). We focus on 46.4 hPa because the information content of limb temperature is found mainly in the stratosphere, as indicated by differences from the initial guess. At lower altitudes in the troposphere, limb temperature reverts to the initial guess due to high cloud opacity. Quality flags have not been applied to the limb data. For comparison, Figure 14-2 shows the TES nadir temperature retrievals from the same Global Survey. We note that all major features in the temperature field are reproduced in both limb and nadir.

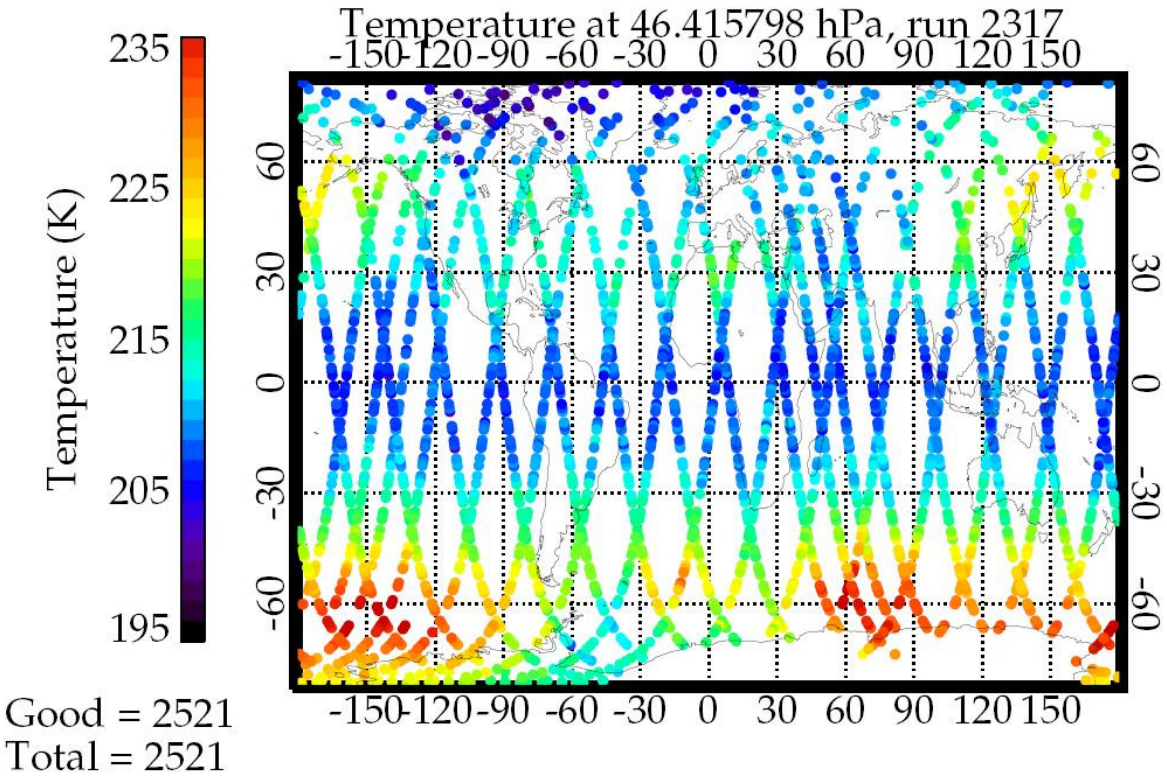

Figure 14-1 TES v003 limb retrievals of temperature at the 46.4 hPa pressure level from Global Survey run id 2317 (12 November 2004). There are a total of 2521 limb temperature retrievals in this Global Survey, with no filtering by quality flags.

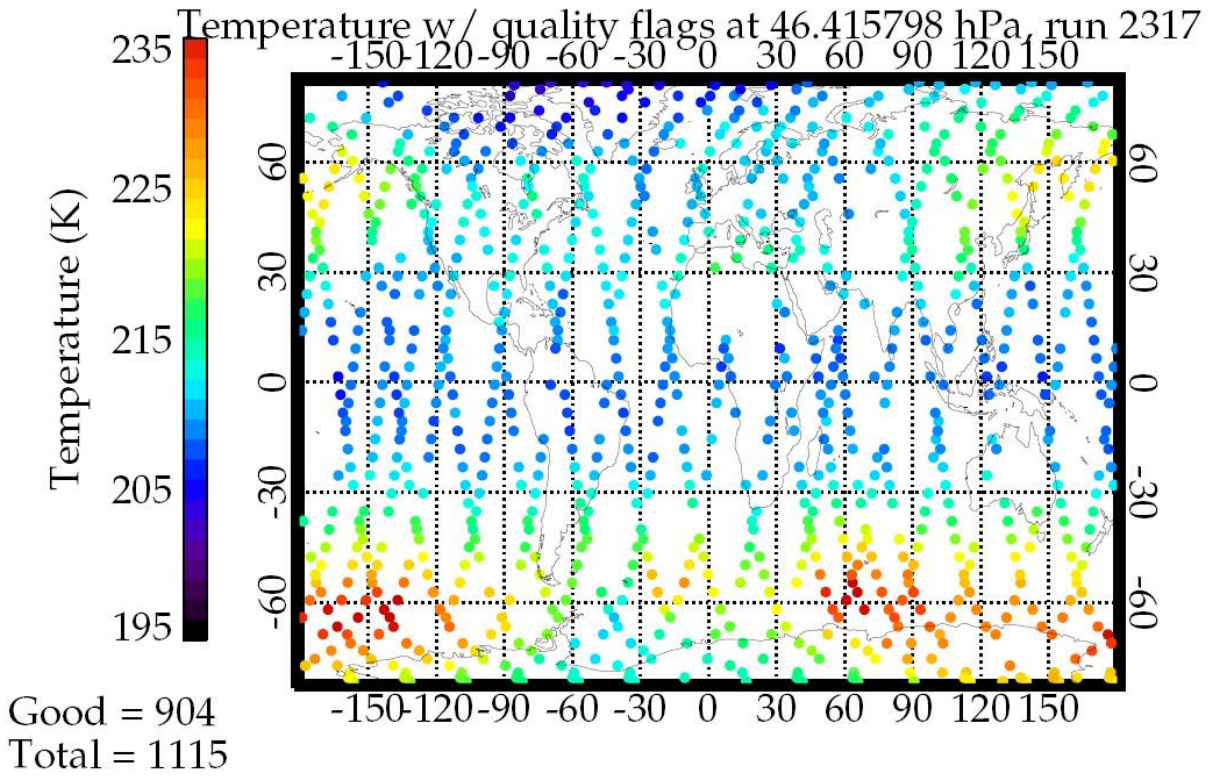

Figure 14-2 TES v003 nadir retrievals of temperature at the 46.4 hPa pressure level from Global Survey run id 2317 (12 November 2004). There are a total of 1115 temperature retrievals in this Global Survey, but only the 904 retrievals that satisfy the standard quality flag are shown. Note the similarity between nadir and limb temperature retrievals.

The initial guess in the TES retrieval algorithm is set equal to an *a priori* constraint. For temperature, the constraints are provided by the Goddard Space Flight Center (GSFC) Global Modeling and Assimilation Office (GMAO) (Rienecker et al., 2007). TES v003 retrievals use constraints from the GMAO Earth Observing System Data Assimilation System, Version 5 (GEOS-5). These analyses provide temperature profiles on a 0.625 degree by 0.5 degree grid, which are then interpolated to the location and pressure level of each TES retrieval. In Figure 14-3, we evaluate the bias of TES temperature by comparing it with GMAO GEOS-5. It is seen that limb retrievals (blue) and nadir retrievals (red) have sensitivities at different levels of the atmosphere, and different biases as well. For this particular global survey, nadir temperature biases relative to GMAO GEOS-5 are similar to the general pattern seen: TES cold bias at 400 hPa and TES warm bias at 800 hPa (see Nadir Temperature section). Limb temperatures show a smaller tropospheric bias relative to GEOS-5 because of lower sensitivity in the troposphere. Limb temperature has a warm bias relative to GEOS-5 in the stratosphere at pressures less than 100 hPa, and that bias increases with altitude.

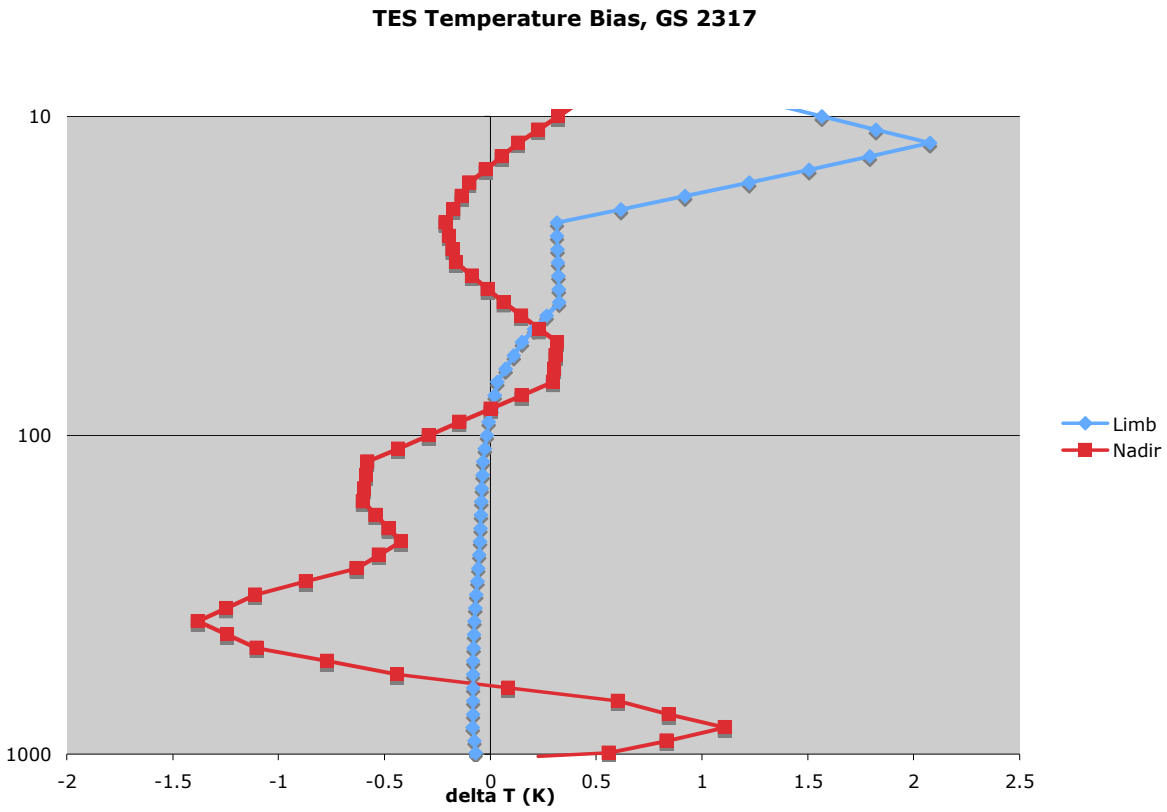

Figure 14-3 Mean bias of TES v003 temperature (Global Survey 2317) relative to the initial guess from GMAO GEOS-5. Nadir retrievals (red squares) and limb retrievals (blue circles) have sensitivities at different levels, and the biases are different also.

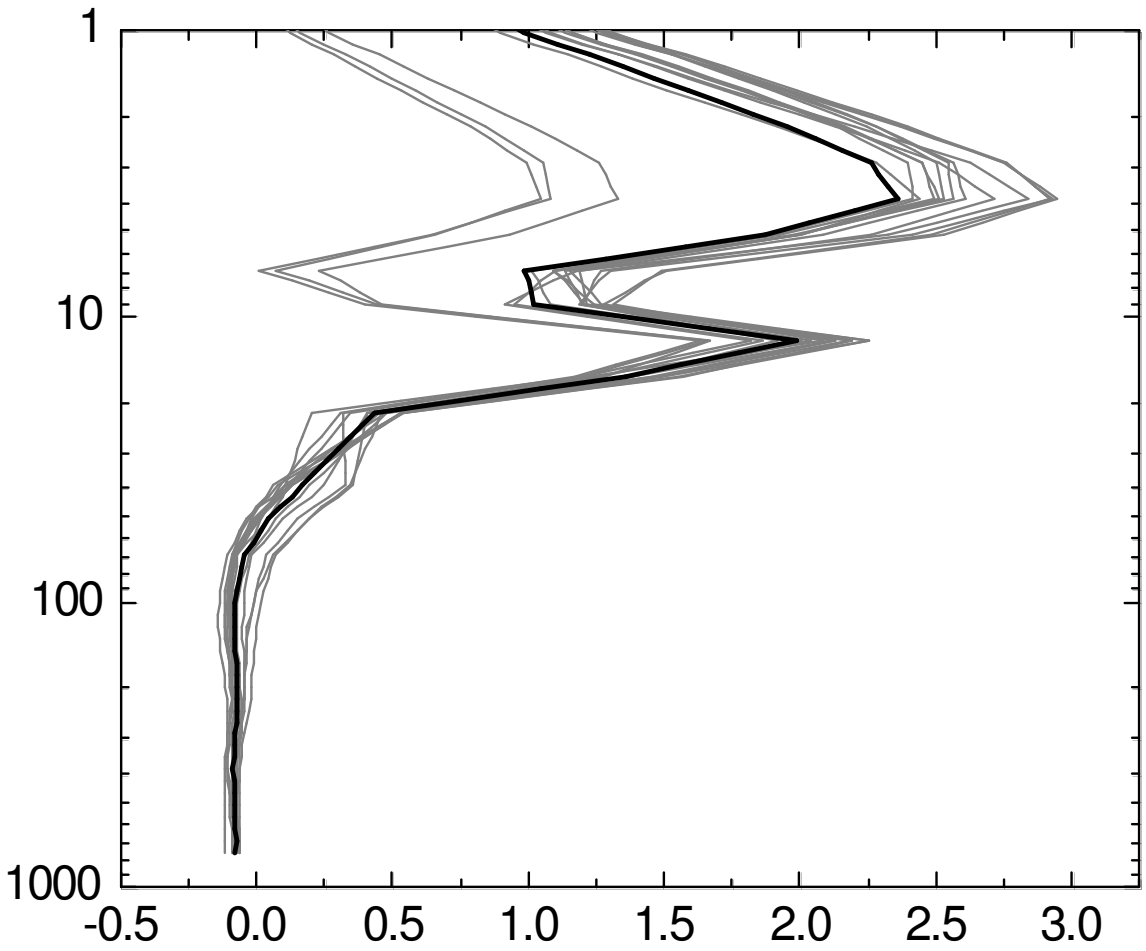

Figure 14-4 TES v003 temperature bias relative to the initial guess from GMAO GEOS-5 for fifteen global surveys (run ids 2317, 2328, 2336, 2345, 2352, 2377, 2805, 2810, 2815, 2820, 2825, 2833, 2841, 2846, 2856). At each pressure level, the mean bias from each global survey is shown in grey. The average for all 15 global surveys is the black line.

This analysis has been extended to a number of TES retrievals. Figure 14-4 takes the fifteen TES global surveys for which v003 limb temperature has been processed as of 12 September 2007 (run ids 2317, 2328, 2336, 2345, 2352, 2377, 2805, 2810, 2815, 2820, 2825, 2833, 2841, 2846, 2856), and compares them with GMAO GEOS-5. These results have been filtered for sensitivity by only considering retrievals and levels where the row of the averaging kernel is non-zero. At each pressure level, the global survey mean temperature bias (TES minus GEOS-5) is plotted in grey. In the troposphere, TES limb temperature has a cold bias of -0.08 K relative to GMAO GEOS-5. In the stratosphere, TES limb temperature typically has a warm bias that increases with altitude, up to +2 K at 12 hPa, and another maximum of greater than 2 K at 4 hPa. In Figure 14-4, three lines show much smaller temperature biases: these are the three most recent global surveys (run ids 2841, 2846, and 2856).

14.1 References

[1] Herman R.L., M. W. Shephard, B. M. Fisher, H. Vömel, T. P. Bui, L. M. Milosevich, D. N. Whiteman, R. Beer, K. Bowman, S. A. Clough, A. Eldering, M. R. Gunson, S. S. Kulawik, M. Luo, G. B. Osterman, D. Rider, H. M. Worden, and J. Worden (2007), Validation of Tropospheric Emission Spectrometer temperature retrievals with aircraft and sondes, Submitted to J. Geophys. Res.

[2] Osterman, G. B., Editor (2007), TES Validation Report, Version 2.0, JPL document D33192, available at: http://tes.jpl.nasa.gov/docsLinks/documents.cfm.

[3] Rienecker, M. M., M. J. Suarez, R. Todling, J. Bacmeister, L. Takacs, H.-C. Liu, W. Gu, M. Sienkiewicz, R. D. Koster, R. Gelaro, and I. Stajner (2007), The GEOS-5 Data Assimilation System: A Documentation of GEOS-5.0 NASA TM 104606, 27, Technical Report Series on Global Modeling and Data Assimilation.

15. Comparison of TES Limb Water with GMAO

TES limb water vapor retrievals have been relatively unexplored to date. Unlike TES nadir views, which have sensitivity to water throughout the tropopause (e.g. Shephard et al., 2007), TES limb retrievals are sensitive to water only at intermediate altitudes. In the stratosphere, there is low sensitivity due to the dryness of the air. At lower altitudes in the troposphere, limb water reverts to the initial guess due to high cloud opacity. We present here the first validation comparisons between TES v003 limb water and GMAO GEOS-5.

Figure 15-1 shows TES limb retrievals of water vapor for run id 2317 on the 421 hPa pressure level. These results have been filtered for sensitivity by only considering retrievals where the degrees of freedom for signal (DOFS) is greater than 1.0 and levels in which the row of the averaging kernel is non-zero. Quality flags have not been applied to the limb data. Justification for the DOFS > 1 criterion is apparent from Figure 15-2, which plots limb water DOFS versus latitude for the same run id. It is seen that only a small fraction of limb retrievals have good values of DOFS for water.

The initial guess in the TES retrieval algorithm is set equal to an *a priori* constraint. For water, the constraints are provided by the Goddard Space Flight Center (GSFC) Global Modeling and Assimilation Office (GMAO) [Rienecker et al., 2007]. TES v003 retrievals use constraints from the GMAO Earth Observing System Data Assimilation System, Version 5 (GEOS-5). These analyses provide water vapor profiles on a 0.625 degree by 0.5 degree grid, which are then interpolated to the location and pressure level of each TES retrieval. In Figure 15-3, we evaluate the bias of TES water by comparing it with GMAO GEOS-5. This analysis has been extended to fifteen TES global surveys (run ids 2317, 2328, 2336, 2345, 2352, 2377, 2805, 2810, 2815, 2820, 2825, 2833, 2841, 2846, 2856). At each pressure level, the global survey fractional water bias (TES minus GEOS-5)/TES is plotted in grey, and the mean is plotted in the thick black line. TES limb water has a dry bias relative to GEOS-5 in the upper troposphere, peaking at 4.6% dry at 261 hPa. Above and below this altitude, the fractional difference between TES and GEOS-5 is smaller because TES has lower sensitivity to limb water. An ongoing investigation will characterize TES limb water more fully.

15.1 References

[1] Osterman, G. B., Editor (2007), TES Validation Report, Version 2.0, JPL document D33192, available at: http://tes.jpl.nasa.gov/docsLinks/documents.cfm.

[2] Rienecker, M. M., M. J. Suarez, R. Todling, J. Bacmeister, L. Takacs, H.-C. Liu, W. Gu, M. Sienkiewicz, R. D. Koster, R. Gelaro, and I. Stajner (2007), The GEOS-5 Data Assimilation System: A Documentation of GEOS-5.0 NASA TM 104606, 27, Technical Report Series on Global Modeling and Data Assimilation.

[3] Shephard, M. W., et al., (2007), Comparison of Tropospheric Emission Spectrometer (TES) Nadir Water Vapor Retrievals with In Situ Measurements, Submitted to J. Geophys. Res.

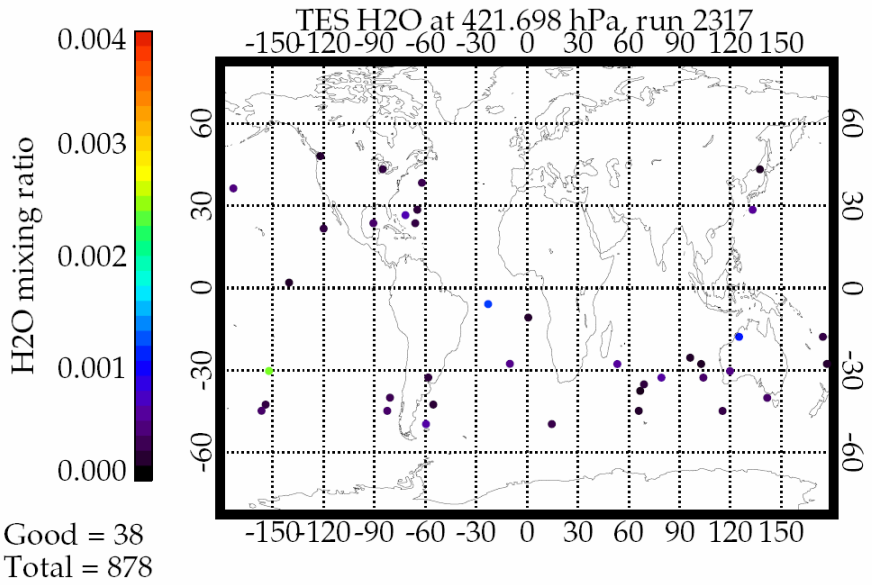

Figure 15-1 TES v003 limb water retrievals for run id 2317 at the 421 hPa pressure level. Only 38 out of 878 retrievals have degrees of freedom for signal (DOFS) > 1.0.

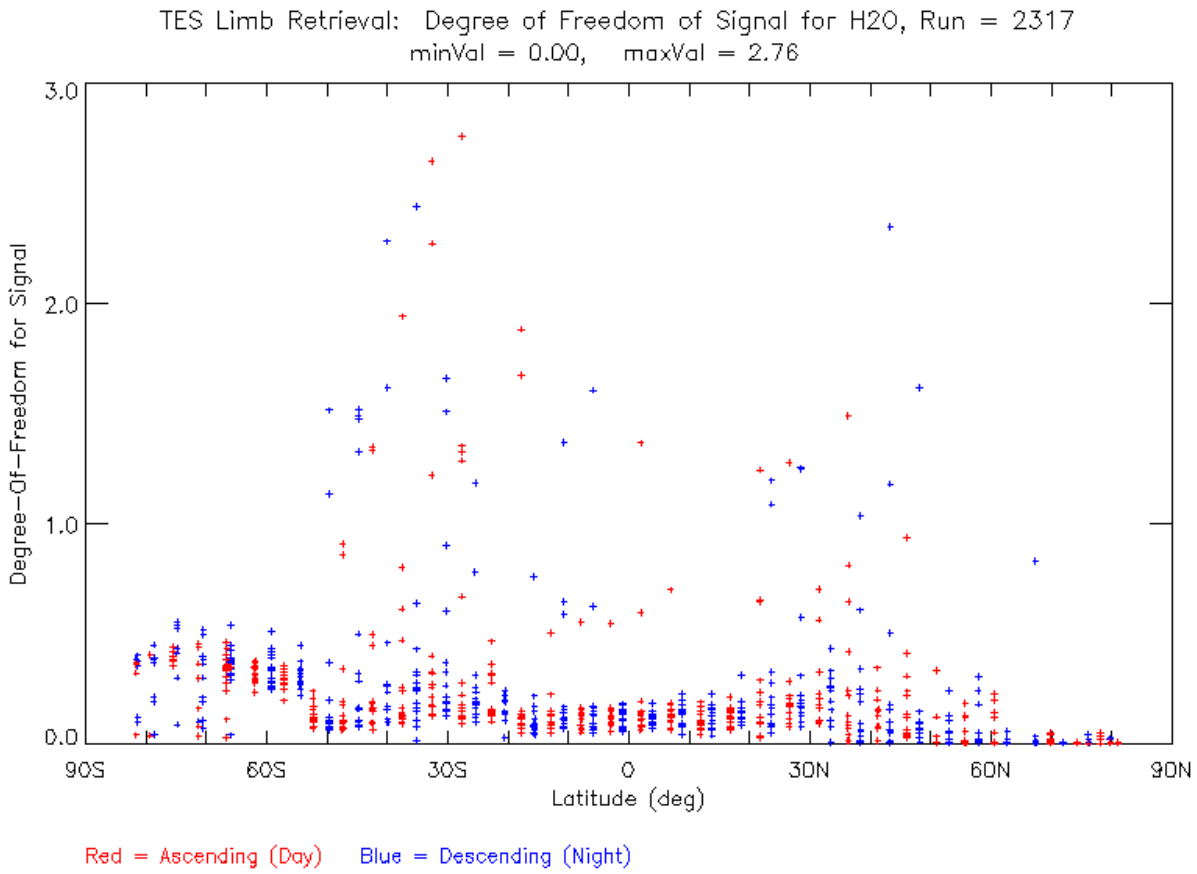

Figure 15-2 Latitudinal distribution of DOFS for TES v003 limb water, run id 2317, shows that most limb retrievals have poor sensitivity to water vapor.

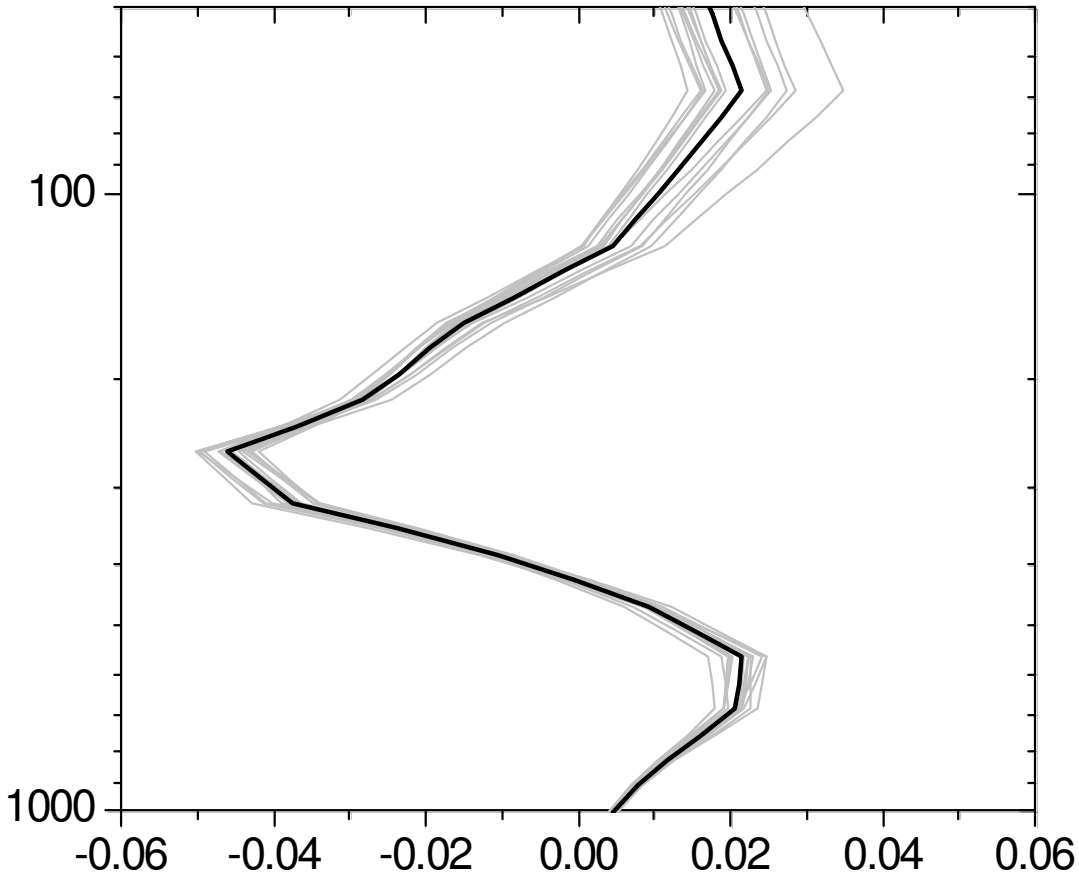

Figure 15-3 TES v003 limb water bias relative to the initial guess from GMAO GEOS-5 for fifteen global surveys (run ids 2317, 2328, 2336, 2345, 2352, 2377, 2805, 2810, 2815, 2820, 2825, 2833, 2841, 2846, 2856). At each pressure level, the mean bias from each global survey is shown in grey. The average for all 15 global surveys is the black line.

Appendices

A. Acronyms

ACE	Atmospheric Chemistry Experiment
AIRS	Atmospheric Infrared Sounder
ALIAS	Aircraft Laser Infrared Absorption Spectrometer
AMSR	Advanced Microwave Scanning Radiometer
AMSU	Advanced Microwave Sounding Unit
ASDC	Atmospheric Science Data Center
ARM	Atmospheric Radiation Measurement
ARM-SGP	Atmospheric Radiation Measurement – Southern Great Plains
AVE	Aura Validation Experiment
CFH	Cryogenic Frostpoint Hygrometer
CH_4	Methane, Natural Gas
CIMS	Chemical Ionization Mass Spectrometers
CO	Carbon Monoxide
CO2	Carbon Dioxide
CR-AVE	Costa Rica Aura Validation Experiment
DACOM	Differential-Absorption Carbon Monoxide Monitor
DIAL	Differential Absorption Lidar
DOE	Department of Energy
DOF	Degrees of Freedom
DOFS	Degrees of Freedom for Signal
DPS	Data Products Specification
EOS	Earth Observing System
FTIR	Fourier Transform Infrared Spectrometer
FTS	Fourier Transform Spectrometer
GEOS	Global Earth Observing System
GMAO	Global Modeling Assimilation Office
GSFC	Goddard Space Flight Center
H_2O	Dihydrogen Monoxide (Water)

HDF	Hierarchical Data Format
HDO	Hydrogen Deuterium Monoxide (“Heavy Water”)
HIRDLS	High Resolution Dynamics Limb Sounder
HIRS	High Resolution Infrared Sounders
HIS	High-Resolution Interferometer Sounder
hPa	Hectopascal, a unit used for air pressure
HYSPLIT	Hybrid Single-Particle Lagrangian Integrated Trajectory
IEEE	Institute of Electrical and Electronics Engineers
IG	Initial Guess
IGRA	Integrated Global Radiosonde Archive
ILS	Instrument Line Shape
INTEX	International Chemical Transport Experiment
IONS	INTEX Ozonesonde Network Study
ISM	Integrated Spectral Magnitude
JPL	Jet Propulsion Laboratory
K	Kelvin
L1	Level 1
L1B	Level 1B
L2	Level 2
LBLRTM	Line-by-Line Radiative Transfer Model
MISR	Multi-angle Imaging SpectroRadiometer
MLS	Microwave Limb Sounder
MODIS	Moderate Resolution Imaging Spectroradiometer
MOPITT	Measurement Of Pollution In The Troposphere
MOZAIC	Measurement of OZONE on Airbus In-service Aircraft
NASA	National Aeronautics and Space Administration
NATIVE	Nittany Atmospheric Trailer and Integrated Validation Experiment
NCEP	National Centers for Environmental Prediction
NDACC	Network for the Detection of Atmospheric Composition Change
NESR	Noise Equivalent Source Radiance, Noise Equivalent Spectral Radiance
NH	New Hampshire
NOAA	National Oceanic & Atmospheric Administration

O3	Ozone
OD	Optical Depth
OMI	Ozone Monitoring Instrument
PAVE	Polar Aura Validation Experiment
PI	Principal Investigator
PNNL	Pacific Northwest National Laboratory
Ppbv	Parts per billion by volume
RMS	Root-Mean-Square
ROI	Reynolds Optimally Interpolated
Run ID	TES run identification number
SAGA	Soluble Acidic Gases and Aerosol
SAUNA	Sodankyla Total Column Ozone Intercomparison
SCIAMACHY	SCanning Imaging Absorption SpectroMeter for Atmospheric CHartographY
SHADOZ	Southern Hemisphere Additional Ozonesondes
SHIS, S-HIS	Scanning HIS
SST	Sea Surface Temperature
STD	Standard Deviation
TES	Tropospheric Emission Spectrometer
TOMS	Total Ozone Mapping Spectrometer
TTL	Tropical Tropopause Layer
TX	Texas
VMR	Volume Mixing Ratio
WOUDC	World Ozone and Ultraviolet Radiation Data Centre